TESIS DE LA UNIVERSIDAD DE ZARAGOZA

2024

98

EMILIO PLUMED VELILLA

Coupled Inductors Applied to Domestic Induction Heating.

Director/es

Acero Acero, Jesús

Lope Moratilla, Ignacio

ISSN 2254-7606

Prensas de la Universidad Universidad Zaragoza

Universidad de Zaragoza
Servicio de Publicaciones

ISSN 2254-7606

Universidad Zaragoza
1542

Tesis Doctoral

COUPLED INDUCTORS APPLIED TO DOMESTIC INDUCTION HEATING.

Autor

EMILIO PLUMED VELILLA

Director/es

Acero Acero, Jesús
Lope Moratilla, Ignacio

UNIVERSIDAD DE ZARAGOZA
Escuela de Doctorado

Programa de Doctorado en Ingeniería Electrónica

2022

PhD Dissertation

Coupled Inductors Applied to Domestic Induction Heating

Author

Emilio Plumed Velilla

Advisors

Jesús Acero Acero

Ignacio Lope Moratilla

Universidad Zaragoza

Departamento de Ingeniería Electrónica y Comunicaciones

Escuela de Ingeniería y Arquitectura

Universidad de Zaragoza

Zaragoza, November, 2021

Tesis Doctoral

Coupled Inductors Applied to Domestic Induction Heating

Memoria presentada por

Emilio Plumed Velilla

Grado en Ingeniería de Tecnologías Industriales por la Universidad de Zaragoza

Máster en Ingeniería Industrial por la Universidad de Zaragoza

Para la obtención del título de

Doctor por la Universidad de Zaragoza

Directores

Jesús Acero Acero

Ignacio Lope Moratilla

Departamento de Ingeniería Electrónica y Comunicaciones

Escuela de Ingeniería y Arquitectura

Universidad de Zaragoza

Zaragoza, November, 2021

To my family

Acknowledgements

Early 2016, when I was offered the topic for my Master's Thesis, I had no idea what I was getting into. At first I was reluctant, "electromagnetic fields simulations? that sounds complicated!", I thought. But I was intrigued, so up the stairs I went, along the corridor to the furthest corner of the Ada Byron building, where my life took an entirely new direction.

I have the utmost gratitude for my PhD advisors, Prof. Jesús Acero and Dr. Ignacio Lope, who managed to hook me in and never let go. Their wealth of knowledge, constant motivation, and indefatigability have provided unending inspiration and support throughout.

I would like to thank Prof. José Miguel Burdío for his warm welcome into the research group and his support. Moreover, I would like to thank Dr. Óscar Lucía and Dr. Hector Sarnago for their expert electronics knowledge.

I am very grateful to my labmates, Dr. Mario Pérez, Javier Serrano, Jorge Villa, Borja López, Pablo Guillén, Alexis Narváez and Alberto Pascual for their camaraderie and insight.

The close collaboration with BSH Home Appliances has allowed me to meet and work alongside many wonderful people. I would like to thank Tomás Cabeza as main purveyor of most electronics used in the dissertation and great Matlab coding know-how. His toolboxes and repositories have simplified countless hours of work. Moreover, I would like to thank Manuel Almolda for his excellent and numerous inductor prototypes, as well as Jorge Felices and Izaskun Jaca for their expertise in prototyping other complex pieces. Additionally, I am deeply grateful to Pablo Hernández, Jorge Pascual, Alberto Domínguez, Francisco Villuendas, Manuel Fernández and everyone else who contributed in any measure to this work and my own personal growth.

The financial support received during the dissertation have helped me along immensely, and I would like to thank the DGA for its doctoral student grants, the numerous projects from MINECO and MICINN and BSH Home Appliances.

I would be very remiss if I did not mention my family. My mother's love and care,

my father's good nature and biting humor and my sister's cheerful and supporting nature have provided a strong foundation to weather any storm. My aunt Manuela often says with a wink and a smile that she wished there was an inventor in the family. I got here thanks to all of you.

As I finish writing these words all of the troubles and tribulations slip from my mind and only the good times remain. Finally I thank you, dear reader, for your interest in my dissertation, please enjoy reading!

Agradecimientos

A principios de 2016, cuando me propusieron mi tema para el TFM, no tenía ni idea de dónde me estaba metiendo. Primero tenía mis reservas, y pensé: "¿simulaciones electromagnéticas? ¡parece muy difícil!". Pero tenía curiosidad, así que subí al piso más alto y al despacho más recóndito del edificio Ada Byron, donde mi vida dio un giro inesperado.

Tengo la más sincera gratitud por mis directores de tesis, Prof. Jesús Acero y Dr. Ignacio Lope, que consiguieron agasajarme y convencerme para seguir. Su vasto conocimiento, motivación constante e incansabilidad me han otorgado inspiración inagotable y apoyo constante durante todo el proceso.

Me gustaría agradecer a Prof. José Miguel Burdío por su cálida bienvenida al grupo de investigación y su apoyo. Además, me gustaría agradecer a Dr. Óscar Lucía y Dr. Héctor Sarnago por su experto conocimiento en electrónica.

Estoy muy agradecido de mis compañeros de laboratorio, Dr. Mario Pérez, Javier Serrano, Jorge Villa, Borja López, Pablo Guillén, Alexis Narváez y Alberto Pascual por su camaradería y perspicacia.

La estrecha colaboración con BSH Electrodomésticos me ha permitido conocer y trabajar junto con mucha gente maravillosa. Me gustaría darle las gracias a Tomás Cabeza como principal proveedor de la mayor parte de componentes electrónicos usados en la tesis y su gran conocimiento de programación en Matlab. Sus herramientas y repositorios han simplificado incontables horas de trabajo. Además, me gustaría agradecer a Manuel Almolda por los excelentes y numerosos prototipos de inductores, así como a Jorge Felices e Izaskun Jaca por su experiencia para desarrollar otras piezas complejas. Adicionalmente, estoy profundamente agradecido a Pablo Hernández, Jorge Pascual, Alberto Domínguez, Francisco Villuendas, Manuel Fernández y todos aquellos que han contribuido en alguna medida a este trabajo y a mi crecimiento personal.

El apoyo financiero recibido durante el desarrollo de la tesis ha sido una ayuda inmensa, por lo que me gustaría agradecer a la DGA por sus becas predoctorales, a los numerosos proyectos del MINECO y MICINN y a BSH Electrodomésticos.

Sería muy negligente por mi parte si no mencionase a mi familia. El amor y el cariño de mi madre, la jovialidad y humor mordaz de mi padre y la naturaleza alegre y alentadora de mi hermana son fuertes cimientos para aguantar cualquier tormenta. Mi tía Manuela suele decir con un guiño y una sonrisa que le gustaría tener un inventor en la familia. He llegado aquí gracias a todos vosotros.

Mientras termino de escribir estas palabras, todos los problemas y malos momentos se evaporan de mi mente, dejando sólo los buenos tiempos. Finalmente te agradezco a ti, querido lector, por tu interés en mi tesis, por favor, ¡disfruta de la lectura!

Index

Abstract **15**

Nomenclature **19**

Acronyms **27**

1 Introduction **29**

1.1 Domestic induction heating 31

1.1.1 Physical phenomenology 31

1.1.2 History of induction heating's practical application 33

1.1.3 General characteristics of induction heating cooktops 34

1.1.4 Components of induction heating system 35

1.1.4.1 Power electronics 36

1.1.4.2 Control electronics 37

1.1.4.3 Inductor-load system 38

1.1.5 Typical commercial induction heating layouts and models . . . 40

1.2 Dissertation motivation and objectives 41

1.2.1 Motivation 41

1.2.2 Objectives 43

1.3 State of the art review 44

1.3.1 Induction heating systems 45

1.3.1.1 Ideal inductor-load system modelling 46

1.3.1.2 Winding losses modelling 47

1.3.1.3 Induction heating system design and resonant inverter topologies and control 48

1.3.1.4 Radiated near field 49

1.3.2 Inductive wireless power transfer modelling 50

1.3.2.1 Ideal wireless power transfer (WPT) inductors modelling 50

1.3.2.2 Windings' losses modelling 51

1.3.2.3 Topologies and system design 51

1.3.2.4 Radiated near field . . . 53
1.3.3 Coupled IH-WPT modelling . . . 54
1.3.3.1 Mutual impedance modelling and calculation . . . 54
1.3.3.2 Inductively coupled heating system design . . . 54
1.3.4 Bibliography summary . . . 54
1.4 Dissertation Organization . . . 57

2 Single-inductor induction under worktop . . . 59
2.1 Introduction . . . 61
2.2 Modelling . . . 62
2.2.1 Assumptions and simplifications . . . 63
2.2.2 Total impedance and induction impedance . . . 64
2.2.3 Litz winding losses . . . 66
2.3 Design parameters . . . 69
2.3.1 Delivered power . . . 70
2.3.2 Power factor . . . 70
2.3.3 Inductor to load efficiency . . . 71
2.3.4 Power distribution in the load . . . 71
2.3.5 Emitted near field . . . 72
2.4 General design process . . . 73
2.4.1 FEA simulations . . . 73
2.4.2 Selection of winding turns, resonant capacitor and cable . . . 75
2.5 Inductor to load distance analysis . . . 76
2.5.1 Geometry and design . . . 76
2.5.2 Effects on the design parameters . . . 77
2.5.2.1 Inductive power factor . . . 77
2.5.2.2 Efficiency and losses density . . . 78
2.5.2.3 Power distribution . . . 79
2.5.2.4 Emitted near field . . . 80
2.5.3 Safe zone of operation . . . 81
2.6 Ferrite volume analysis . . . 82
2.6.1 Impact on the relevant parameters . . . 83
2.6.2 Pareto representation . . . 84
2.7 Prototypes and experimental measurements . . . 84
2.7.1 Prototype description . . . 84
2.7.2 Measurements . . . 86

2.7.2.1 Low signal regime . . . 86
2.7.2.2 Full power regime . . . 87
2.8 Conclusion . . . 89

3 Inductively Coupled Heating . . . 91
3.1 Introduction . . . 93
3.2 Modelling . . . 93
3.2.1 Total impedance and induction impedance . . . 94
3.2.2 Load impedance through Poynting's vector . . . 95
3.2.3 Winding losses . . . 96
3.2.4 Matrix representation . . . 98
3.3 Two-inductor ICH system . . . 99
3.4 Design parameters . . . 101
3.4.1 Geometry . . . 101
3.4.2 Goal parameters . . . 101
3.4.3 Dimensionless design parameters . . . 103
3.5 inductively coupled heating (ICH) system design process . . . 104
3.5.1 Resonant frequencies . . . 104
3.5.2 Selection of winding cable . . . 105
3.5.3 Impedance simulations . . . 108
3.6 Same-diameter prototype . . . 111
3.6.1 Low signal regime . . . 111
3.6.1.1 Prototype description . . . 111
3.6.1.2 Measurements . . . 111
3.6.2 Full signal regime . . . 113
3.6.2.1 Design and prototype . . . 113
3.6.2.2 Measurements . . . 114
3.7 Conclusion . . . 115

4 Large diameter load adaptation to a smaller primary inductor . . . 117
4.1 Introduction . . . 119
4.2 System simulation and design . . . 120
4.2.1 Score definition . . . 123
4.2.2 Simulation results . . . 124
4.3 Viability of the design and comparison with IH . . . 128
4.3.1 Distance comparison with IH . . . 128
4.3.2 Lateral misalignment . . . 132

4.4 Experimental measurements . . . 135
4.5 Conclusion . . . 139

5 Multiple loads with a single transmitter. . . . 141
5.1 Introduction . . . 143
5.2 System model and design . . . 144
5.2.1 ICH system model . . . 144
5.2.2 System design and relevant parameters . . . 150
5.3 Experimental measurements . . . 156
5.3.1 Small signal regime . . . 156
5.3.2 Full power regime . . . 158
5.4 Conclusion . . . 164

6 Small receiver ICH system . . . 165
6.1 Introduction . . . 167
6.2 System analysis and design . . . 168
6.2.1 Inductor-load system . . . 168
6.2.2 Capacitor location and orientation . . . 171
6.2.3 Induced voltage and track twinning . . . 173
6.2.4 Individual track routing . . . 174
6.3 Experimental results . . . 176
6.3.1 Electrical measurements . . . 176
6.3.2 Thermal measurements . . . 180
6.4 Conclusion . . . 182

7 EMI reduction of ICH systems . . . 183
7.1 Introduction . . . 185
7.2 Measuring procedures and methods . . . 185
7.3 EMI FEA simulations . . . 186
7.3.1 Conventional IH systems . . . 186
7.3.2 ICH systems . . . 187
7.4 Experimental results . . . 191
7.5 Conclusion . . . 195

8 Conclusion . . . 197
8.1 Summary . . . 199
8.2 Conclusion . . . 201

8.3 Future research 202

Appendices 203

A Electromagnetic theory 205

A.1 System electromagnetic modelling 205

A.2 Magneto quasi static (MQS) approach 206

B Twisted strands simulations. 209

B.1 Litz wire description 209

B.2 Mathematical description 211

B.2.1 Nomenclature, definitions and assumptions 211

B.2.2 Mathematical description of bundle trajectories 214

B.2.3 Collision detection methods 216

B.2.3.1 Three dimensional method 217

B.2.3.2 Two dimensional method 220

B.2.4 Method comparison for the simulations at hand 222

B.3 Simulation model 223

B.4 Simulation results 225

C Measurement post processing. 229

D Experimental results comparison 235

D.1 Experimental setups 235

D.2 Equivalent impedance measurements 237

D.3 Power and current measurements 239

E List of contributions 243

E.1 Conference papers 243

E.2 Journal articles 244

E.3 Patents 245

Bibliography 247

Abstract

This research work examines the viability of induction heating (IH) systems with very high inductor to load distance. Figures of merit (FoMs) such as efficiency, power factor and power distribution are considered.

As a starting point, modifications to conventional IH systems are proposed. Limits are established according to each FoM. Higher diameter inductors can reach further distances than smaller ones without going over the limits. Prototypes are proposed and built, and the agreement between simulations and experimental results is tested. However, conventional IH systems are still somewhat limited in their maximum distance.

Then, inductively coupled heating (ICH) technology is considered. First, a secondary inductor with a resonant capacitor in series is placed beneath the ferromagnetic load. Optimal system design is able to significantly improve FoMs at higher distances. Prototypes to verify the modelling and design are tested. Afterwards, different variations of ICH are proposed and tested.

Second, a big secondary inductor and load are adapted to a smaller primary inductor, designed by applying a scoring system using the FoMs. The system and its power distribution are verified with electrical and thermographic measurements.

Third, two ferromagnetic loads are heated from a single primary inductor by connecting a third inductor in series with the secondary winding. The design can be optimized to maximize power transferred to the uncoupled load. The system is verified with electrical and thermal measurements.

Fourth, a small ferromagnetic load is adapted with a small secondary winding. The resonant capacitors are housed beneath the winding, and simulations are carried out to determine optimal position and orientation of said capacitors. The PCB layout is also considered to minimize proximity losses. The system is verified with electric and thermal measurements.

Magnetic flux emissions are compared between equivalent IH, and ICH. It is found in simulation and experimental measurements that optimum designs are able to minimize inductively coupled heating emissions, particularly at higher distances.

Resumen

Este trabajo de investigación examina la viabilidad de sistemas de calentamiento por inducción IH con gran distancia entre inductor y carga. Se utilizan figuras de mérito FoMs tales como la eficiencia, factor de potencia y distribución de potencia.

Como punto de partida se proponen modificaciones a sistemas IH convencionales. Se establecen límites acordes a cada FoM. Inductores de gran diámetro pueden alcanzar mayores distances que los pequeños sin sobrepasar los límites. Se proponen y construyen prototipos para verificar la adecuación de la simulaciones a los resultados experimentales. Sin embargo, los sistemas IH convencionales aún están algo limitados en su distancia máxima.

Después se considera la tecnología de calentamiento inductivamente acoplado (ICH). Primero, un inductor secundario con condensador en serie se coloca debajo de la carga. Un óptimo diseño del sistema es capaz de mejorar significativamente las FoMs a grandes distancias. Se testean prototipos para verificar su modelado y diseño. Después se proponen y verifican diferentes variaciones de sistemas ICH.

Segundo, un inductor secundario y carga grandes se adaptan a un primario más pequeño, diseñado mediante un sistema de puntuación basado en FoMs. Se verifican el sistema y su distribución de potencia con medidas eléctricas y termográficas.

Tercero, se calientan dos cargas ferromagnéticas desde un único primario, conectando un tercer inductor en serie con el inductor secundario. Se puede optimizar el diseño para maximizar la potencia entregada a la carga no acoplada. Se verifica el sistema con medidas eléctricas y termográficas.

Cuarto, se adapta una pequeña carga ferromagnética con un secundario pequeño. Los condensadores de resonancia se sitúan debajo del inductor, y se realizan simulaciones para determinar su posición y orientación óptima. También se considera la distribución de la PCB para minimizar las pérdidas de proximidad. Se verifica el sistema mediante medidas eléctricas y térmicas.

Se comparan las emisiones de flujo magnético entre sistemas IH e ICH equivalentes. Los diseños ICH óptimos son capaces de minimizar las emisiones tanto para simulaciones y resultados experimentales, especialmente a grandes distancias.

Nomenclature

$\mathbf{A}$	Magnetic vector potential (V s/m)
$\hat{\mathbf{b}}$	Unitary binormal vector to a trajectory
$\mathbf{B}$	Magnetic flux density vector (T)
B_{e_i}	Magnetic flux density in the direction of $\hat{e}_i$ (T)
$\overline{B_{i,e_j}}$	Shortened version of $B_{i,e_j,\text{p.t.},\text{p.A.}}$ (T/A)
$B_{i,e_j,\text{p.t.},\text{p.A.}}$	Per-turn, per-ampere magnetic flux density of the ith inductor in the direction of $\hat{e}_j$ (T/A)
b_l	Bundle level
B_{meas}	Probe-measured magnetic flux density (T)
$\mathbf{B}_{\text{p.t.},\text{p.A.}}$	Magnetic flux density vector generated per turn and per Ampere (T/A)
B_φ	Magnetic flux density in the azimuthal direction (T)
B_r	Magnetic flux density in the radial direction (T)
$\mathbf{B}_{\text{rms}}$	Root mean square magnetic flux density vector (T)
$\mathbf{B}_{\text{rms}}$	Root mean square magnetic flux density vector norm (T)
B_{sim}	Simulated probe magnetic flux density (T)
B_z	Magnetic flux density in the vertical direction (T)
C	Compensation capacitor (F)
c_{fer}	Ferrite coverage, expressed as a percentage.
C_i	Compensation capacitor in series with the ith inductor (Ω)
$C_{i,\text{p.t.}}$	Mathematical per-turn compensation capacitor in series with the ith inductor (F)
C_{snub}	Snubber capacitance (F)
$\mathbf{D}$	Electric displacement field vector (C/m^2)
d_{fer}	Distance between winding and ferrite (m)
dl	Length differential (m)
d_{load}	Distance between winding and load (m)
d_{loads}	Vertical distance between loads (m)

dS	Surface differential (m^2)
d_{sh}	Distance between ferrite and aluminum shielding (m)
∂t	Time differential (s)
d_{wij}	Vertical distance between the ith inductor and the jth inductor (m)
d_{wil}	Total vertical distance between the ith inductor and the load (m)
$\mathbf{E}$	Electric field vector (V/m)
$\hat{\mathbf{e}}_i$	Generalized unitary vector that forms an orthogonal coordinate systems with $\{\hat{\mathbf{e}}_1, \hat{\mathbf{e}}_2, \hat{\mathbf{e}}_3\}$
$\mathbf{E}_i$	Electric field vector generated by the ith inductor (V/m)
$\mathbf{E}_{i,\text{p.t.,p.A.}}$	Electric field generated per winding turn and per Ampere (1/m)
E_ϕ	Electric field, azimuthal component (V/m)
f	Frequency (Hz)
$f_{0,\text{eq}}$	Resonant frequency of the equivalent impedance (Hz)
$f_{0,i}$	Resonant frequency of the ith inductor and capacitor (Hz)
GS	Global score to determine design suitability, including PR, PF, PD and η
$\mathbf{H}$	Magnetic field strength vector (A/m)
$\mathbf{H}^*$	Magnetic field strength vector complex conjugate (A/m)
h_{fer}	Ferrite thickness (m)
$\mathbf{H}_i$	Magnetic field vector generated by the ith inductor (A/m)
h_{load}	load thickness (m)
$\mathbf{H}_{\text{p.s.,p.A.}}$	Magnetic field generated per winding turn and per Ampere (1/m)
$\bar{\mathbf{H}}$	Shortened version of $\mathbf{H}_{\text{p.s.,p.A.}}$ (1/m)
h_{sh}	Shielding thickness (m)
h_w	Winding thickness (m)
h_{wi}	Thickness of the ith inductor (m)
$\mathbf{I}$	Current vector for multiple inductor systems
I	Electric current (A)
I_i	Electric current circulating through the ith inductor (A)
I_{rms}	Root mean square current (A)
$\mathbf{J}$	Electric current density (A/m^2)
J_i	Bessel function of the first kind and ith order

J_w	Winding losses volumetric density (W/m^3)
$J_{w,i}$	Volumetric losses density of the ith inductor (W/m^3)
$J_{w,\text{limit}}$	Winding losses density limit (W/m^3)
$k_{L,ij}$	Inductive coupling factor between inductors i and j
K_p	Cable packing factor
$k_{R,ij}$	Resistive coupling factor between inductors i and j
K_Z	Ratio between mutual impedance, Z_{12}, and secondary self-impedance, Z_{22}
L'	Reflected inductance to the primary side (H)
L_eq	Winding equivalent inductance (H)
$L_\text{eq,p.t.}$	Per-turn equivalent impedance (H)
L_{ij}	Inductance due to field generated in the ith inductor measured in the jth inductor (H)
$L_{ij,\text{p.t.}}$	Per-turn inductance generated by the ith inductor measured in the jth inductor (H)
L_ind	Winding ideal inductance due to electromagnetic induction (H)
$L_{\text{ind},ij}$	Ideal inductance due to field generated in the ith inductor measured in the jth inductor (H)
$L_{\text{ind},ij,\text{p.t.}}$	Ideal per-turn inductance due to field generated in the ith inductor measured in the jth inductor (H)
$L_\text{ind,p.t.}$	Per-turn induction inductance (H)
L_rec	Receiver-side inductance made up of its elements in series (H)
$l_{t,\text{mean}}$	Winding mean turn length (m)
n_b	Number of layers in a bundle
$\hat{\mathbf{n}}$	Unitary normal vector to a specified surface, or to a trajectory
$\mathbf{N}_l$	Vector containing the number of sub-bundle of each layer in a larger bundle
n_s	Inductor number of strands
$n_{s,i}$	Number of strands of the ith inductor
n_t	Inductor number of turns
n_{t_i}	Number of turns of the ith inductor
$(n_{t,i}n_{s,i})$	Total strands of the ith inductor
$(n_{t,i}n_{s,i})_{\eta_\text{max}}$	Number of total strands of the ith inductor that produces maximum

	efficiency
$(n_{t,i}n_{s,i})_{\text{opt}}$	Optimum number of total strands of the ith inductor according to (3.81) and (3.82)
$(n_t n_s)_{\max}$	Maximum number of total strands that can fit in a given winding geometry
$(n_t n_s)_{\text{opt}}$	Optimum number of total strands
P	Electrical power (W)
P_{cond}	Conduction power losses (W)
PD	Power distribution, calculated as the normalized standard deviation of Poynting's vector in the target surface
PF	Power factor
PF_{ind}	Inductive power factor
P_i	Electrical power in the ith surface (W)
P_{load}	Power dissipated in the ferromagnetic load (W)
$P_{\text{load,bottom}}$	Power delivered to the bottom load (W)
$P_{\text{load,top}}$	Power delivered to the top load (W)
$P_{\max}$	Maximum power (W)
P_{prox}	Proximity power losses (W)
PR	Power reach score, calculated as the ratio of the maximum power achieved by the system with the desired maximum power
pr_n	Pitch ratio between the nth layer sub-bundle and the global wire pitch
PR_{top}	Ratio of power delivered to the top load with the total power
P_{sh}	Power dissipated in the shielding (W)
P_w	Winding power losses (W)
Q_{ij}	Quality factor of impedance element ij
$\Re$	Symbol that denotes the real component of a complex number
R'	Reflected resistance to the primary side (Ω)
r_b	External bundle radius (m)
R_{cond}	Winding conduction losses resistance (Ω)
$R_{\text{cond},ii,\text{p.t.,p.s.}}$	Conduction per-turn, per-strand resistance in the ith inductor (Ω)
$R_{\text{cond},ii,s}$	Shortened version of $R_{\text{cond},ii,\text{p.t.,p.s.}}$ (Ω)
$R_{\text{cond},ij}$	Conduction resistance due to field generated in the ith inductor

	measured in the jth inductor (Ω)
$R_{\text{cond,p.t.,p.s.}}$	Per-turn, per-strand winding conduction losses resistance (Ω)
R_{eq}	Winding equivalent resistance (Ω)
$r_{\text{fer,ext}}$	Ferrite external radius (m)
$r_{\text{fer,int}}$	Ferrite internal radius (m)
R_i	Induction resistance in the ith surface, either load or shielding (Ω)
R_{ij}	Resistance due to field generated in the ith inductor measured in the jth inductor (Ω)
$R_{ij,\text{p.t.}}$	Per-turn resistance generated by the ith inductor measured in the jth inductor (Ω)
R_{ind}	Winding ideal resistance component due to electromagnetic induction (Ω)
$R_{\text{ind},ij}$	Ideal resistance due to field generated in the ith inductor measured in the jth inductor (Ω)
$R_{\text{ind,p.t.}}$	Per-turn induction resistance (Ω)
R_{load}	Winding resistance component due to the ferromagnetic load (Ω)
r_{load}	Load radius (m)
$R_{\text{load},ij}$	Load resistance due to field generated in the ith inductor measured in the jth inductor (Ω)
$R_{\text{load},ij,\text{p.t.}}$	Load per-turn resistance due to field generated in the ith inductor measured in the jth inductor (Ω)
$R_{\text{load,p.t.}}$	Per-turn load resistance (Ω)
$r_{\text{pos},n}$	Position radius of the nth bundle or sub-bundle (m)
R_{prox}	Winding proximity losses resistance (Ω)
$R_{\text{prox,p.t.,p.s.}}$	Per-turn, per-strand winding proximity losses resistance (Ω)
$R_{\text{prox},ij}$	Proximity resistance due to field generated in the ith inductor measured in the jth inductor (Ω)
$R_{\text{prox},ijk}$	Proximity resistance due to field product generated in the ith inductor and the jth inductor and measured in the kth inductor (Ω)
$R_{\text{prox},ijk,s}$	Proximity per-turn, per-strand resistance due to field product generated in the ith inductor and the jth inductor and measured in the kth inductor (Ω)

R_{rec}	Receiver-side resistance made up of its elements in series (Ω)
r_s	Cable strand radius (m)
R_{sh}	Winding resistance component due to electromagnetic shielding (Ω)
r_{sh}	Shielding radius (m)
$R_{\text{sh},ij}$	Shielding resistance due to field generated in the ith inductor measured in the jth inductor (Ω)
$R_{\text{sh},ij,\text{p.t.}}$	Shielding per-turn resistance due to field generated in the ith inductor measured in the jth inductor (Ω)
$R_{\text{sh,p.t.}}$	Per-turn shielding resistance (Ω)
R_w	Winding total losses resistance (Ω)
$R_{w,ij}$	Losses resistance due to field generated in the ith inductor measured in the jth inductor (Ω)
$r_{\text{w,ext}}$	Inductor external radius (m)
$r_{\text{w,int}}$	Inductor internal radius (m)
$\mathbf{S}$	Poynting's vector (electromagnetic power flux density) (W/m^2)
S_{cable}	Cable section area (m^2)
S_i	Surface of the ith volume, where i is either load, or sh for the shielding (m^2)
$\mathbf{S}_{ij}$	Poynting's vector generated by the interference of the electric field generated by the ith inductor and the magnetic field generated by the jth inductor (W/m^2)
S_{load}	Poynting's vector component normal to the load (W/m^2)
$\overline{S}_{\text{load}}$	Mean Poynting's vector component normal to the load (W/m^2)
S_{loop}	Field probe loop area (m^2)
S_s	Strand section (m^2)
S_w	Winding section area (m^2)
$S_{w,i}$	Winding section area of the ith inductor (m^2)
$\hat{\mathbf{t}}$	Unitary tangential vector to a trajectory
T	Temperature (°C)
t_l	Bundle twisting level
$\mathbf{V}$	Voltage vector for multiple inductor systems
$V_{C,i}$	Voltage in the ith capacitor (V)
V_D	Voltage of two inductors in series with direct connection (V)

V_I	Voltage of two inductors in series with inverse connection (V)
$V_{i,\text{rms}}$	Root mean square of the ith inductor voltage (V)
V_{ind}	Ideal inductor voltage (V)
$V_{\text{ind},ij}$	Ideal voltage due to field generated in the ith inductor measured in the jth inductor (V)
V_{loop}	Induced voltage in a probe loop (V)
V_{mains}	Mains voltage (V)
$V_{\text{mains,rms}}$	Root mean square mains voltage (V)
V_{rms}	Root mean square voltage (V)
V_w	Winding volume (m^3)
X_{ii}	Reactance of the series ith inductor and capacitor (Ω)
$X_{ii,\text{p.t.}}$	Per-turn reactance of the series ith inductor and capacitor (Ω)
x_{wij}	Horizontal offset between the ith inductor and the jth inductor (m)
Z_{eq}	Equivalent impedance (Ω)
Z_{ij}	Impedance due to field generated in the ith inductor measured in the jth inductor (Ω)
$Z_{ij,\text{p.t.}}$	Per-turn impedance due to field generated in the ith inductor measured in the jth inductor (Ω)
Z_{ind}	Winding ideal impedance component due to electromagnetic induction (Ω)
$Z_{\text{ind},ij}$	Ideal impedance due to field generated in the ith inductor measured in the jth inductor (Ω)
$\angle$	Symbol that denotes the phase angle of a complex number
δ	Skin depth, penetration depth of electromagnetic fields (m)
η	Efficiency
η_{max}	Maximum efficiency
λ	Linear helix pitch
λ	Angular helix pitch
μ	Relative magnetic permeability
∇	Vector differential operator used to calculate gradients ($\nabla\mathbf{A}$), divergences ($\nabla \cdot \mathbf{A}$) and curls ($\nabla \times \mathbf{A}$)
ω	Angular frequency (rad/s)
$\omega_{0,\text{eq}}$	Resonant angular frequency of the equivalent impedance (rad/s)

$\omega_{0,\text{rec}}$	Receiver-side angular resonant frequency (rad/s)
$\omega_{0,i}$	Resonant angular frequency of the ith inductor and capacitor (rad/s)
ϕ	Scalar electric potential (V)
Φ_{cond}	Frequency-dependent conduction losses function
Φ_{prox}	Frequency-dependent proximity losses function
σ	Electric conductivity (S/m)
σ_{Al}	Aluminum conductivity (S/m)
σ_{Cu}	Copper conductivity (S/m)
$\varnothing_{\text{load}}$	Load diameter (m)
$\varnothing_{\text{sh}}$	External aluminum shielding diameter (m)
$\varnothing_{\text{fer,ext}}$	External ferrite diameter (m)
$\varnothing_{\text{fer,int}}$	Internal ferrite diameter (m)
$\varnothing_{w,\text{ext}}$	External winding diameter (m)
$\varnothing_{wi,\text{ext}}$	External diameter of the ith inductor (m)
$\varnothing_{wi,\text{int}}$	Internal diameter of the ith inductor (m)
φ	Phase angle difference between the inductor currents (rad)
φ_i	Phase angle of the current of the ith inductor (rad)

Acronyms

AC	alternating current
ADC	analog to digital converter
ASIC	application specific integrated circuit
BSH	Bosch and Siemens home appliances
DC	direct current
EMC	electromagnetic compatibility
EMI	electromagnetic interference
DFT	discrete Fourier transform
FFT	fast Fourier transform
FDM	finite difference method
FEA	finite element analysis
FEM	finite element method
FoM	figure of merit
GaN	gallium nitride
IBC	impedance boundary condition
ICH	inductively coupled heating
ICNIRP	International Commission on Non-Ionizing Radiation Protection
IEC	International Electrotechnical Commission
IGBT	insulated-gate bipolar transistor
IH	induction heating
IuW	induction under worktop
MLCC	multi-layer ceramic capacitor
MoM	method of moments
MQS	magneto quasi static
PDM	pulse density modulation
PPS	polyphenylene sulfide
PS	phase shift
PWM	pulse width modulation
PEEC	partial element equivalent circuit
rms	root mean square
SiC	silicon carbide

WPT wireless power transfer

ZVS zero voltage switching

Chapter 1

Introduction

This chapter introduces the physical phenomena of domestic induction heating and its evolution throughout recent history. In addition, the main characteristics and components of domestic induction heating systems are described, including some commercial models. The new trend of using induction heating through the kitchen worktop and the challenges it entails for the inductor vessel system are at the core of the motivation for the current dissertation. The current state of the art of electromagnetic modeling of induction heating systems at a conventional and increased distance, as well as wireless power transfer systems and coupled induction heating systems are reviewed. Finally, the dissertation organization is outlined.

Table of contents

1.1 Domestic induction heating. . . . 31
1.1.1 Physical phenomenology . . . 31
1.1.2 History of induction heating's practical application . . . 33
1.1.3 General characteristics of induction heating cooktops . . . 34
1.1.4 Components of induction heating system . . . 35
1.1.4.1 Power electronics . . . 36
1.1.4.2 Control electronics . . . 37
1.1.4.3 Inductor-load system . . . 38
1.1.5 Typical commercial induction heating layouts and models . . . 40
1.2 Dissertation motivation and objectives. . . . 41
1.2.1 Motivation . . . 41
1.2.2 Objectives . . . 43
1.3 State of the art review . . . 44
1.3.1 Induction heating systems. . . . 45
1.3.1.1 Ideal inductor-load system modelling . . . 46
1.3.1.2 Winding losses modelling. . . . 47
1.3.1.3 Induction heating system design and resonant inverter topologies and control . . . 48
1.3.1.4 Radiated near field . . . 49

1.3.2 Inductive wireless power transfer modelling 50
1.3.2.1 Ideal WPT inductors modelling 50
1.3.2.2 Windings' losses modelling 51
1.3.2.3 Topologies and system design 51
1.3.2.4 Radiated near field 53
1.3.3 Coupled IH-WPT modelling 54
1.3.3.1 Mutual impedance modelling and calculation 54
1.3.3.2 Inductively coupled heating system design 54
1.3.4 Bibliography summary 54
1.4 Dissertation Organization 57

1.1 Domestic induction heating

Domestic IH provides contactless heating of conductive media, which enabled different applications according to their power requirements and materials. Industrial applications are associated with the highest power ratings, mostly for heat treatments of metallic billets, ranging from full volume to only surface treatments [1]. Medical applications generally need low power and they often involve hyperthermia of organic tissue for tumor treatment [2, 3]. Domestic appliances have a medium power requirement and they usually focus on ferromagnetic vessels [4], though there are successful all metal applications [5].

1.1.1 Physical phenomenology

The fundamental operation of IH is the driving of an alternating current through an inductor placed near a conductive material. This current generates an alternating magnetic field which generates heat in the workpiece through two main mechanisms [6]:

- *Induced currents*: The magnetic field induces eddy currents in the conductive material.
- *Hysteresis losses*: In ferromagnetic materials, the magnetic field also reorients the magnetic domains in the material.

An alternating current in an inductor generates an alternating magnetic field which is intrinsically linked to an electric field. Through Faraday's law of induction, said magnetic field generates an electromotive force in a medium. That law states that the electromotive force is given by the rate of change of the magnetic flux that flows through the load surface, where the magnetic flux is the surface integral of the $\mathbf{B}$ field. The electromotive force causes induced currents due to the material's conductivity, which directly generate heat due to its skin depth, which depends on the material's resistivity and magnetic permeability, as well as the fields' frequency. Generally, these Joule losses are the main contribution to total losses in the medium. The phenomenon is exemplified in Fig. 1.1.

The induced currents produce several effects:

- Resistive Joule losses due to the material conductivity and magnetic permeability.
- An electromagnetic field oposing the one generated by the inductor, reducing

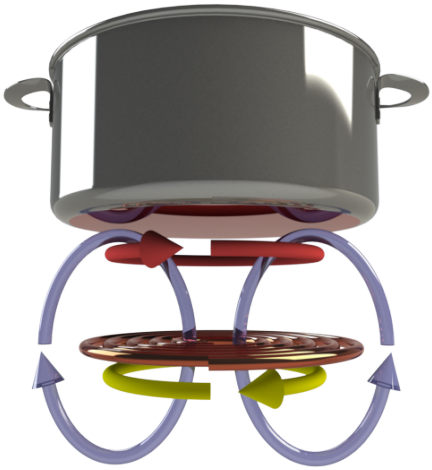

Figure 1.1: Induced Currents.

the radiated field farther away from the system.

- The opposing fields generate forces between inductor and material.

Ferromagnetic materials are divided into regions or domains in the microscopic level. These regions consist of sets of magnetic dipoles whose internal fields are aligned. The regions are also the cause of magnetic remanence and hysteresis. When a ferromagnetic material is immersed in an external magnetic field intensity, **H**, these domains experience magnetic forces to orient themselves to the external field and generate magnetic flux density, **B**, growing in the process. The stronger the **H** field, the more domains are reoriented and grow and the stronger **B** becomes. Due to the irreversible nature of this process, heat is dissipated, though it is usually smaller than the Joule losses contribution. Once all domains are aligned, the material is saturated, and **B** can only grow with the air permeability.

As the external excitation is removed, the material's reaction can be classified as soft, if the domains revert to their original state, or hard, if the domains retain their new orientation, keeping a remanent **B**. This magnetic remanence is associated with power losses, since more energy has to be spent in order to change the domains' magnetic orientation [7].

In order to represent the material's magnetic behavior, the quasi-stationary **B** response to a periodic **H** excitation is plotted, which is commonly called the hysteresis loop, as shown in Fig 1.2.

Considering that most ferromagnetic materials used as IH vessels are relatively soft, hysteresis losses are only the second biggest contribution to domestic induction

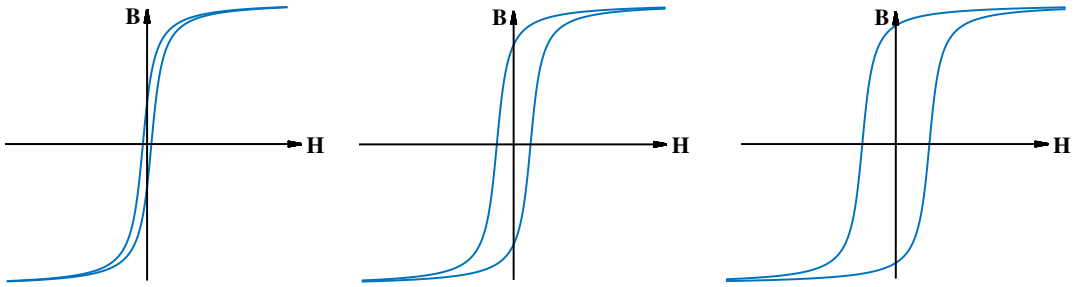

Figure 1.2: Hysteresis loops of increasing hardness.

heating (IH).

1.1.2 History of induction heating's practical application

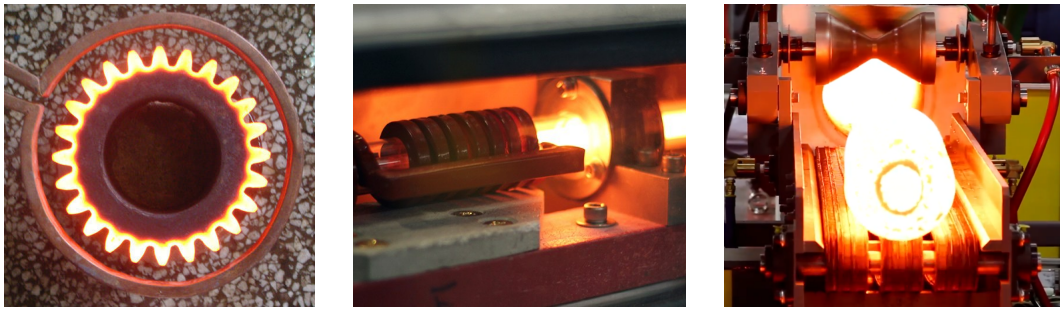

(a) (b) (c)

Figure 1.3: Industrial applications of IH. (a) Hardening. (b) Annealing. (c) Heating prior to forging.

The first industrial applications of IH appeared around the end of the 19th century, as a new way to apply heat treatment to steel parts, such as hardening and annealing or preparation for forging as depicted in Fig. 1.3. Originally the systems operated at or near the mains frequency, between 50-60 Hz, which was a very limiting operating condition. As vacuum valves were introduced and developed throughout the first half of the 20th century, IH systems were able to increase their operating frequency up to 100 kHz with some major limitations [8].

In the 60s, solid-state semiconductors propelled the technology forward, introducing it to other fields, such as the automotive and food industries. At this point however, IH struggled to compete with other technologies in terms of efficiency, cost, and volume.

In the 70s, American and Japanese companies patented their first domestic IH devices [9, 10]. Nevertheless, at that point those prototypes were still expensive,

inefficient and voluminous, so only a few Japanese products ever went to market.

In the second half of the 1980s, the development of insulated-gate bipolar transistors (IGBTs) enabled IH systems to be more efficient and cost-effective. This improvement allowed IH to directly compete with well established traditional heating systems.

Throughout the 90s, consumer interest in the products kept growing, and by the year 2000 they became a standard in the white goods industry. At this time researchers started looking into biomedical applications of IH beyond sterilization and manufacturing of medical equipment. The most prominent topic was the heating of ferromagnetic micro or nano-particles to produce local hyperthermia in cancerous tissue.

Originally, IH appliances were designed as direct substitutes of gas cookers and resistive glass-ceramic hobs, with the limitation of only being able to use ferromagnetic vessels. This kind of appliance is still the most popular in the European market, with Germany, France and Spain as main consumers. The Asian market, led by Japan and China, is currently the biggest. The Asian market also consumes the kind of appliance described earlier, but low-power "rice cookers" and all-metal appliances are considerably more popular. The different customer preferences have kept the markets apart, allowing the manufacturers little overlap outside their original location.

In terms of manufacturers and suppliers, the European market is mostly provided by Bosch and Siemens home appliances (BSH), Brandt, EGO, Electrolux and the American Whirpool, whereas the Asian market is mainly supplied by Midea, LG, Panasonic and Samsung.

For over thirty years, the University of Zaragoza has closely collaborated with BSH's Montañana Development Center in Zaragoza. Montañana being the sole IH research center in the entire company is therefore a testament to their ingenuity.

1.1.3 General characteristics of induction heating cooktops

The main differences between IH and conventional gas and radiating cooktops are described below. On the one hand, the main advantages are [11]:

- *Swiftness*: The heat is directly generated in the vessels, without intermediate conduits and hence, no delays.

- *Safety*: In radiating glass ceramic cooktops, the glass is heated up to 500ºC in order to heat the vessels, while in IH the glass ceramic is at most at the same temperature as the vessel. In gas cooktops, the flame does not extinguish if the vessel is removed, while in IH the appliance can no longer deliver power in the same circumstance.
- *Efficiency*: The heat transfer mechanism and the resonant power electronics technology minimize IH losses. In radiating glass ceramic appliances, the glass itself dissipates heat in the surrounding environment, while in gas cookers, fuel combustion produces air convection and radiation losses.
- *Cleanliness*: The only surface susceptible to dirt is the planar glass ceramic, and the low temperature compared to radiant cooktops ensures that spills can not burn and prevents their strong adhesion.
- *Control*: Power delivery can be adjusted instantly and precisely to the desired level, thanks to the power electronics.

On the other hand, the most significant drawbacks are:

- *Higher cost*: Domestic IH is more technologically complex than most other cooking methods, requiring more expensive electronics and materials. This can be overcome by the additional functionality. The consumer can be convinced to buy a more expensive appliance when the added value is worth the cost.
- *Vessel limitation*: Most IH appliances outside the Asian market are limited to ferromagnetic vessels. In Europe, vessel manufacturers eventually adapted to IH by using ferromagnetic materials at the vessel's bottom. Conversely, in Asia, IH appliances adapted to the existing vessels using more complex power electronics and control strategies and reducing performance in some cases.

1.1.4 Components of induction heating system

The main elements present in a IH cooktop are shown in Fig. 1.4. The inductors are driven by the power electronics, which are in turn operated by the control electronics. Users only have direct access to the ceramic glass and its user interface, which gives commands to the control electronics.

In terms of functionality, the appliance can be divided into 3 distinct parts:

- Power electronics.

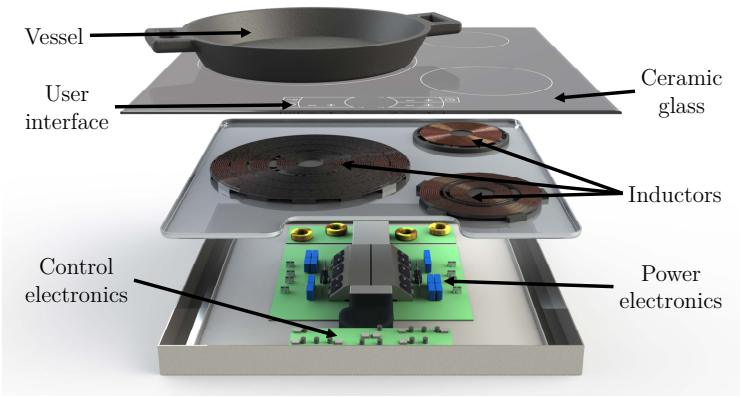

Figure 1.4: IH cooktop components

- Control electronics.
- Inductor-vessel system.

Basically, the control electronics sends activation signals to the power electronics. Then, the power electronics inject medium frequency current into the inductors. Finally, the inductors generate magnetic fields that heat up the vessels.

1.1.4.1 Power electronics

The main function of the power electronics is to convert the mains electrical energy, increasing its frequency, to be usable by the inductor system. Additionally, the power electronics have to comply with electromagnetic compatibility (EMC) regulations in order to avoid interfering with nearby components of the electrical grid. The typical power electronics construction for a single IH load is shown in Fig. 1.5. The outlined blocks can be described as:

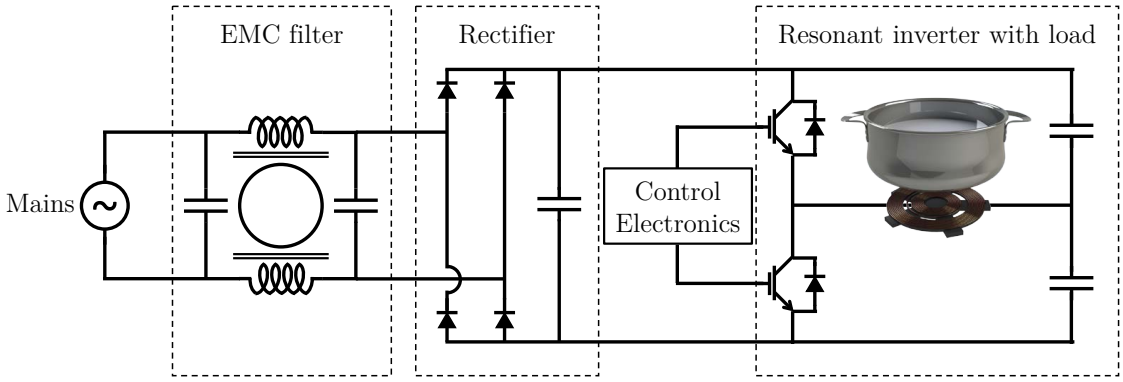

Figure 1.5: IH power electronics main blocks.

- *EMC filter*: The filter is an elaborate composition of differential and common mode chokes, as well as filter capacitors. It blocks unwanted harmonics and

high frequency noise from going into or coming out of the appliance, complying with EMC restrictions.

- *Rectifier*: A four diode bridge is used to fully rectify the mains wave. This stage also includes a direct current (DC) bus capacitor, which has a low enough value to ensure the bus keeps the mains frequency in order to achieve a high power factor.

- *Resonant inverter*: The inverter itself can be arranged by means of different topologies according to the number of switching devices and the type of transistors themselves. Fig. 1.5 represents the IH power electronics of a relatively simple IGBT series resonant half-bridge. Activated by the control electronics, the inverter switches the bus voltage at a medium frequency (20-100 kHz). The inverter output voltage feeds the resonant tank composed of the inductor-vessel inductive load and resonant capacitors.

Each inverter topology has different impedance load requirements, dictating the inductor system design. The inverter topologies that most manufacturers use are resonant or quasi-resonant, achieving high efficiency and power-volume density. Single-switch topologies are the cheapest, but their power is limited by high voltages, making them ideal for the low power "rice cookers" characteristic of the Asian market. Half-bridge inverters are relatively cheap and have a positive influence on EMC, usually making them the most cost-effective for applications up to 5 kW and the standard in European markets. Full bridge inverters are relatively expensive, but they have the least voltage stress and the most modulation options and strategies that can be implemented, making them necessary for high power applications, such as industrial IH.

1.1.4.2 Control electronics

The control electronics are entrusted to follow the user's instructions and ensure the safe and efficient operation of the appliance. It can be divided into three distinct blocks:

- *User Interface*: the user is able to select cooking zones' power or temperature via capacitive sensors, or less commonly with knobs and buttons. The interface can inform the user of a target temperature being reached, a cooking zone that is too hot or about incompatible vessels. The interface sends and receives these messages to and from the control block.

- *Measurement system*: the system acquires voltages, currents and temperatures in relevant locations by means of sensors and analog to digital converters (ADCs). Digital processors are used to obtain composite variables and indirect mesurements. All the data is sent to the control block to be processed.
- *Control system*: the system sends activation signals to the inverters according to the interface's commands and the information acquired by the measurement block. When necessary, it also sends information back to the interface. Considering the operating frequency range, the control system needs to be fast, so most implementations use powerful microcontrollers. BSH is the only manufacturer known to use application specific integrated circuits (ASICs). In order to achieve more versatility, the ASIC is partnered with a slower microcontroller, which takes care of the high level, low speed tasks, while the ASIC manages the low level, high speed tasks.

1.1.4.3 Inductor-load system

The inductor-vessel system, and more generally, the inductor-load system, is able to wirelessly transform the electrical energy provided by the power electronics and turn it to heat in the vessel. In circuit terms, it can be associated with a frequency dependent equivalent impedance, with real and imaginary components. The compound name alludes to the intrinsic link between its inductor and load, because the equivalent impedance is dependent on the entire system geometry, as well as their materials.

Considering that most cooking vessels are round, the typical domestic IH inductor winding is planar and circular. The main system components are pointed out in Fig. 1.6 [12]:

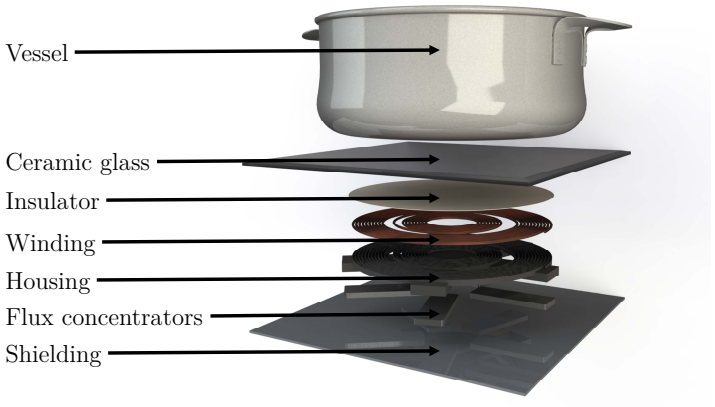

Figure 1.6: Inductor-vessel system components.

- *Vessel*: The power transfer concentrates in the bottom of the conductive load due to the materials' skin depth. This fact gives a lot of flexibility to vessel construction. Many manufacturers use a multi-layer structure, with a ferromagnetic disc at the bottom and heat conductive materials on top.

- *Ceramic glass*: As a material with very good thermal properties, IH appliances inherited the ceramic glass from conventional radiating cooktops. A 4 mm thickness is typically used to separate inductor from load.

- *Insulator*: A thin slice of heat and electrical insulating material is placed between inductor and glass for added safety. A layer of mica thinner than 0.5 mm is rather common.

- *Winding*: The inductor coil is arranged as a planar spiral of high conductivity cable. Copper and aluminum are the most frequent materials, copper being the most efficient and aluminum a cheaper alternative. Multi-stranded litz wire is commonly used to minimize losses.

- *Housing*: The housing contains the inductor winding, giving it its shape and acting as an electrical insulator toward the flux concentrators and magnetic shielding.

- *Flux concentrators*: The flux concentrators channel the magnetic flux, partially shielding the elements below and redirecting the flux toward the vessel and thus increasing efficiency and power factor. The concentrators need high permeability and low losses, and ferrite fulfils both requirements.

- *Electromagnetic shielding*: In order to nullify the magnetic field that could interfere with the electronics placed below, a conductive layer is used. At the interest frequency range, this layer's skin depth needs to be lower than its thickness to be fit for purpose. Typically, a 2 mm thick layer of aluminum is more than enough to completely shield the electronics.

The intrinsic relation between inductor and load makes the power electronics quite hard to design. After all, there can be as many equivalent impedances as vessel materials, sizes and arrangement configurations.

Figure 1.7: Four hobs induction cooktop.

1.1.5 Typical commercial induction heating layouts and models

Originally, domestic induction heating appliances used similar hob layouts to traditional radiating and gas cooktops, either three or four round burners of different diameter, as shown on Figs. 1.4 and 1.7. The adaptation of hobs' diameters to the vessels is even more important in IH, because of the need to achieve good power distribution and adequate performance. Consequently, as IH appliances evolved, there was a push towards more adaptable cooking surfaces, where size and position were less restricted. These newer layouts, shown in Fig. 1.8, are described below, in increasing complexity:

- *Concentric windings*: A big inductor is divided into two or three sections that can be activated independently, in order to adapt to several diameters.

- *Flexible layouts*: These layouts are created with several inductors close together, activating them according to the overlap with the vessels above. Considering that a low number of inductors is preferred, other shapes than circles are often used. These flexible layouts are not big enough to cover the entire cooktop, so several of them can be used in each appliance.

- *Total active surface*: Total active surfaces are an extension of the flexible layout concept to the entire cooktop. In order to have better vessel adaptation and fill the entire surface, small circular inductors are used.

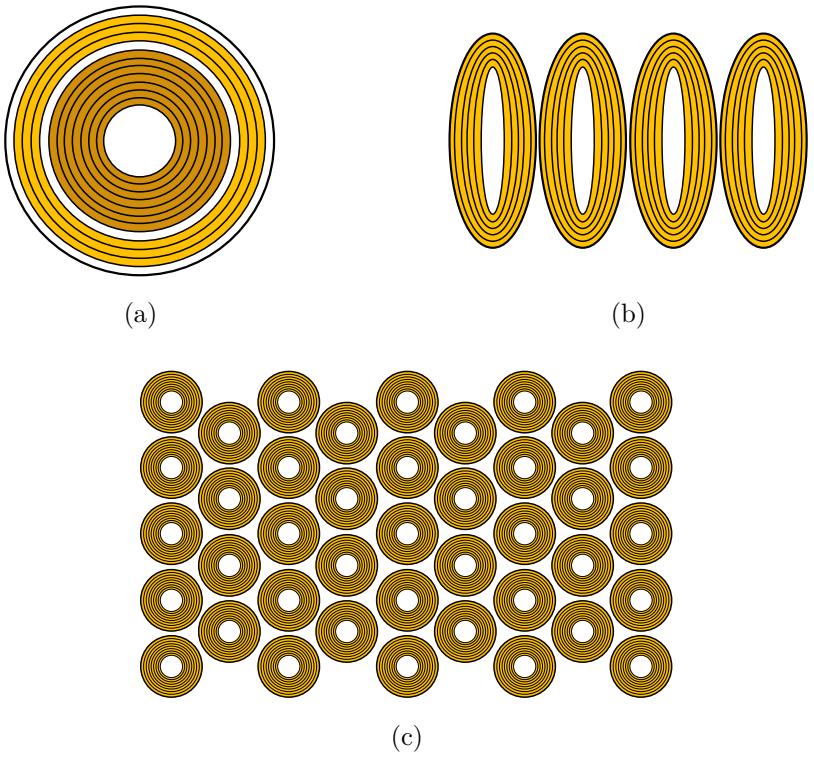

Figure 1.8: Adaptative inductor layouts. (a) Concentric winding inductor. (b) Flexible inductor layout. (c) Total active surface.

1.2 Dissertation motivation and objectives

1.2.1 Motivation

In recent years, interest has been growing over IH appliances whose surface became the kitchen worktop itself, a concept that has no consensual name yet, but throughout the dissertation it will be referred as induction under worktop (IuW). The motivation behind switching the ceramic glass for a kitchen worktop is aesthetic and functional: the cooktop is seamlessly integrated in the worktop, extending the available space for everyday chores, preparing dishes and facilitating easier cleaning, as depicted in Fig. 1.9. An important aspect to consider is that the IuW concept can only be realized with technology that does not require direct contact between the source and destination of the energy transfer. In other words, gas and radiant cooktops are unsuitable for IuW.

In order to realize this concept, a significant limitation needs to be overcome. Conventional IH systems have always used their ubiquitous ceramic glass, ensuring small distances between inductor and load (4 mm) that provide high efficiency and good coupling. Barring a few exceptional cases, kitchen worktops need to be relatively thick, 10 mm at least, and more commonly between 20 and 30 mm.

(a)

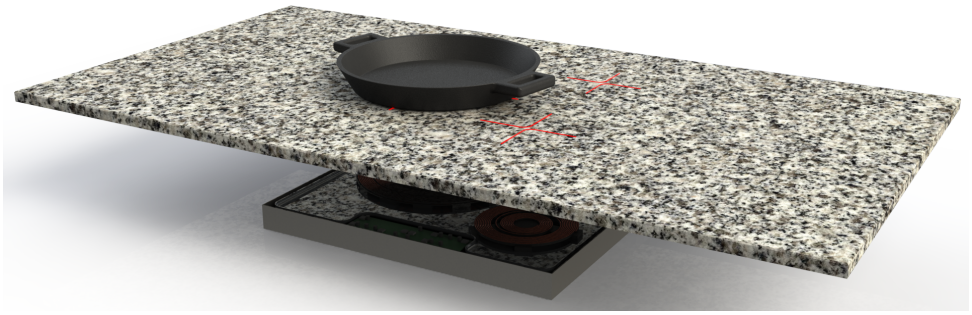

(b)

Figure 1.9: (a) Conventional IH encastre. (b) IuW system.

This is mainly due to the mechanical and thermal stresses that a normal worktop should be able to withstand. These stresses include static loads from food, beverages and small appliances, dynamic loads from food preparation (chopping, kneading, accidental drops, and so on) and high temperatures from vessels that have been removed from a cooktop. Moreover, if the worktops are to become the surface where vessels are heated, then they should be able to weather even higher temperatures and thermal shock, justifying even further the need for worktop thickness.

Proof of this can be found in current commercial applications of IuW, such as TPB Tech or CooKingRAK, shown on Fig. 1.10, where the inductors are placed in drilled holes inside the worktop in order to minimize the distance between inductor and load. These systems can be prone to breaking their surface on and around the inductors due to reduced thickness, mostly under thermal shock conditions or several slower temperature cycles.

Bearing in mind that worktop thickness can only be reduced so much, a different option is to adapt the IH systems to be able to operate at higher distances. On a first approach, the inductors and resonant inverter can be directly redesigned to work at their new distances, making them as efficient as possible and try and determine their limits.

(a) (b)

Figure 1.10: (a) TPB Tech (b) CooKingRAK.

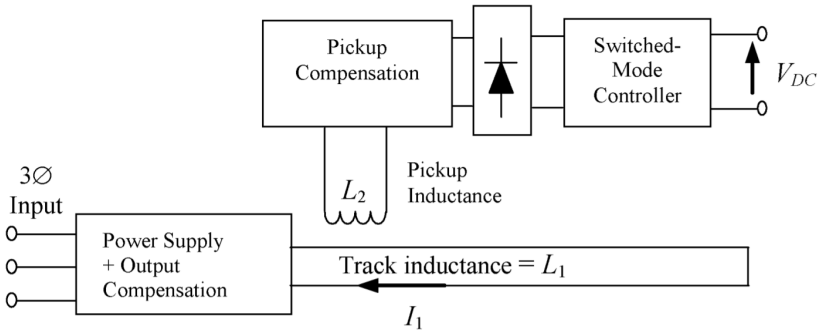

Figure 1.11: General arrangement of a WPT system [13].

A different solution presents itself when examining an application similar to IH, namely, wireless power transfer (WPT). Inductive WPT uses inductors as transmitters and receivers in order to send power between them without electrical contacts, schematically represented in Fig. 1.11. Physically, they use the same phenomenon as IH to transfer power. Therefore, an option to improve the power transfer between inductor and load may be to add more inductors to act as energy bridges to the load.

Given all of the above, the main motivation of this dissertation is finding the optimum realizations of the IuW concept with either a single or multiple inductors.

1.2.2 Objectives

This dissertation's goal is to find solutions for the distance problem in IuW from the perspective of the inductor-load system design and eventually from the resonant inverter perspective. It is expected that single inductor systems will be suitable as long as the ratio between distance and inductor-load diameter is relatively small. For higher distances and smaller diameters, coupled inductor systems akin to those of

WPT seem promising. In order to realize the IuW concept, the following objectives are set:

1. Determine the distance limit of single inductor IH systems for each diameter according to efficiency, coupling between inductor and load, ability to deliver sufficient power, heat distribution in the load and magnetic flux emissions. IH system simulations with different configurations, diameters and increasing worktop thickness will be carried out.

2. Explore the possibility of adding a second inductor attached to the load, acting as an energy bridge between the primary inductor and the vessel, which is called inductively coupled heating (ICH) in this dissertation.

3. Analyze different ICH configurations to study their possibilities. Feeding loads of different size, horizontal offset or vertical offset with the same primary inductor or feeding loads connected in series are possible applications.

4. Establish figures of merit or scores able to determine design suitability of ICH systems and allow for their optimization. The scores should include aspects such as efficiency, stress of electronic components, the ability to reach the desired power and the heat distribution in the load.

5. Prototype and build the most promising IH and ICH systems. Test these prototypes in low signal conditions for impedance measurement, and in high signal conditions for full power delivery measurements. The results will be compared with the corresponding simulations, determining their validity and accuracy.

1.3 State of the art review

The previous section outlined the need for magnetic modelling, design and test of IH systems, particularly at higher distances, WPT systems, and systems that combine the two technologies. According to these needs, the current state of the art is examined to determine the knowledge that can be used as is, and the areas that need further development to achieve the stated goals. Consequently, the review is focused into three broad topics:

- *Induction heating systems*: Analytical, numerical and analytical-numerical methods used to obtain inductor impedances with ferromagnetic loads, as well as winding losses are examined. Inductor and resonant tank design will also be

surveyed, with particular attention to systems with high gap between inductor and load. Some consideration will also be given to magnetic field emissions of IH systems, which are likely to increase with inductor-load distance.

- *Inductive wireless power transfer modelling*: The simulation methods to obtain inductor impedances will be reviewed, with a careful consideration of mutual impedance, and emphasizing the differences and similarities with IH modelling to determine what can be reused for ICH. Moreover, compensation techniques and inverter topologies are also examined. Similarly, magnetic field emissions are also considered.
- *Coupled induction heating modelling*: Mutual impedance calculation and ICH system design will be examined. Care will be taken to ascertain the validity of directly translated WPT design.

1.3.1 Induction heating systems

The electromagnetic modelling and system design of conventional IH systems can be divided into:

- *Ideal inductor-load modelling*: The driving current is assumed filamentary or uniform, the inductor winding is considered lossless, and the impedance is given by all other surrounding media, such as the ferromagnetic load, flux concentrators, magnetic shielding, and others. The impedance can be divided into series resistance and inductance, where the resistance represents the power dissipated in the media and the inductance represents the accumulated magnetic energy. The contributions to the resistance element are usually separated to differentiate between the heated elements.
- *Winding losses modelling*: It calculates the losses in the inductor winding. These losses are usually separated into conduction losses and proximity losses, which captures their physical origin and determines the calculation methodology. Generally, conduction losses can be calculated analytically, and proximity losses usually need a mixed numerical-analytical calculation. The equivalent losses resistance adds to the series inductor impedance.
- *Induction heating system design and resonant inverter topologies and control*: System design usually entails the selection of the winding number of turns, the cable number of strands, and resonant capacitor. The most common topology is the half-bridge inverter, though other topologies are used for

different purposes.

- *Radiated near field*: As the health and safety of people and other near electronic devices are a major concern, EMC regulations are strict, and IH manufacturers are compelled to take electromagnetic emissions into account in the design of their products. From the perspective of the inductor-load system, near-field emissions are the most important to watch out for.

1.3.1.1 Ideal inductor-load system modelling

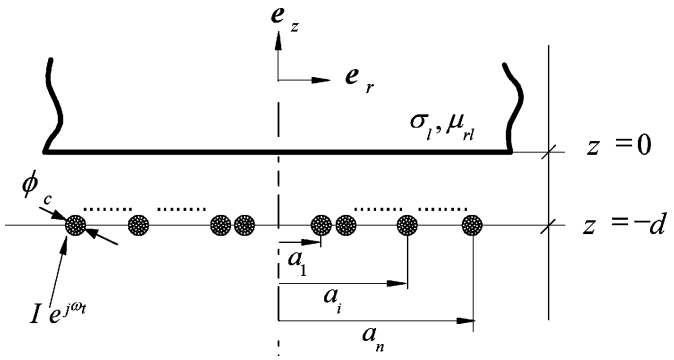

Figure 1.12: 2D IH system geometry [14].

Electromagnetic modelling is approached by solving Maxwell's equations [15] to obtain the magnetic and electric fields [16, 17] and obtain the relevant parameters, which are impedance values in this case [6]. Usually the impedance is obtained as the voltage induced in a winding divided by the input current. These calculations are generally complicated, as the geometries, materials and boundary conditions involved usually prevent easy solutions. Consequently, both analytical and numerical methods have been used to solve electromagnetic problems since their inception. Because of this, analytical solutions focus on geometries with higher symmetry, such as axisymmetry [18–21], as the one depicted in Fig. 1.12. The numeric methods are applied using either the differential or integral formulation of Maxwell's equations [22, 23]. The method of moments (MoM) and partial element equivalent circuit (PEEC) method use the integral formulation [24], the finite difference method (FDM) uses the differential formulation and the finite element method (FEM), also known as finite element analysis (FEA), can use either [25–28]. Problems involving magnetic fields and induction currents in particular can use the magnetic vector potential formulation, which is useful to analytical [21] and numerical methods [29] alike. Currently FEM is widely adopted due to its versatility and the abundance of effective computer software that uses it, such as COMSOL and ANSYS Maxwell.

In the literature there are very few works that focus on extending IH distance [30], which is not surprising, since it reduces efficiency and inductor-load coupling and the new market trend has not been popularized yet. The IuW concept does requires a significant distance increment, and a viable solution is yet to be reported. Fortunately, the methods previously reported can be used to analyze the bigger distance cases.

1.3.1.2 Winding losses modelling

Losses in inductor windings are caused by the currents circulating through them due to the cable material's conductivity. The total current can be separated into the intended current driven through the winding and the unintended circulating current caused by external magnetic fields, and so the losses are separated into conduction losses and proximity losses [31]. Conduction losses are caused by a longitudinal electric field, where the DC component makes use of the full cable cross-section and the alternating current (AC) component takes into consideration the skin effect, which entails that the time-varying electric field pushes the current density to the edges of the conductor, reducing the effective cross-section. The magnetic fields that cause proximity losses can be caused internally, by different strands of the same cable or externally, by other turns of the winding or other inductors.

Cable construction is also important. Cables can be composed of a single conducting strand or multiple strands. Multi-stranded cables can have their strands parallel to one another, simply twisted, or in litz configuration. Litz strands are usually considered equivalent, while strands of other configurations are not. For losses calculations, the cable cross section is considered homogeneous for the single conductor and litz wire cases [32] and non-homogeneous for other multi-stranded cables [33–35].

Due to the orthogonality of conduction and proximity fields, the losses they cause can be separated [36–38], and analytical solutions are more readily available. Conduction effects in isolated round wires can be accurately calculated with 1D approximations, and their proximity effects have been successfully approached with 1D and 2D approximations [14,39], such as the example in Fig. 1.13. Foil windings in transformers also have simple solutions at low frequency, and many efforts were devoted to find equivalences between different cable shapes so that foil winding expressions could be applied to those other cross-sections [31,40–48]. These methods work at low frequency, though some have tried to extend the frequency range using

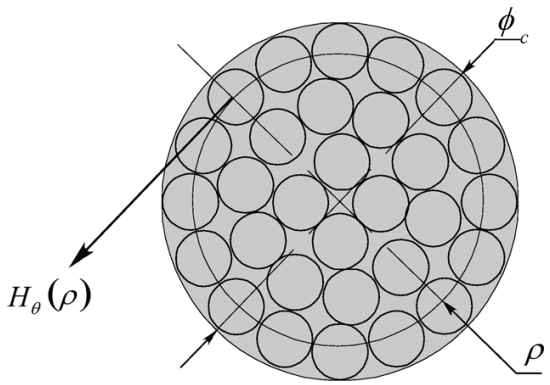

Figure 1.13: Magnetic field generated in litz wire strands that cause proximity losses [14].

complex permeability, with mixed success [49]. Accurate results for proximity losses usually require the calculation of the full magnetic field over the inductor, which can be achieved analytically in axisymmetric and infinite 2D geometries [14, 50–52].

Numerical analysis is typically used to calculate the external field that causes proximity losses [53, 54], though there are methods that combine analytical and numerical calculations and purely numerical methods. Numerical calculations are sometimes used to adapt a simpler analytical model to a 2D or 3D field problem [55–57]. Numerical methods are also used to calculate 2D fields for non-round wires at higher frequencies [58–61]. Lately, with the rapid improvement of computing power, FEM and PEEC methods have been used to obtain losses directly from 3D simulations of the cable structure [62–67].

Regardless of the method, many authors provide optimization guidelines for the inductors, considering strand diameter, number of strands, frequency, etc [39, 46, 47, 54].

For the purposes of this work, the losses will be calculated analytically considering field orthogonality, using magnetic field information from numerical FEM simulations.

1.3.1.3 Induction heating system design and resonant inverter topologies and control

Once impedance and losses are calculated, IH design entails choosing operation frequency, number of turns and capacitors according to the impedance results in order to meet power requirements and limitations of current and voltage [4, 19, 68]. Similarly, as mentioned previously, the winding's cable can be optimized to maximize efficiency by selecting the appropriate strand diameter, number of strands and

operating frequency. When power distribution is focused in the design, individual placement of inductor turns can be carefully selected [69], or an arrangement of multiple smaller inductors can be constructed [70]. The frequency dependency of impedance parameters is sometimes expressed as networks of fixed impedance values to achieve better approximations in time-domain simulations [71].

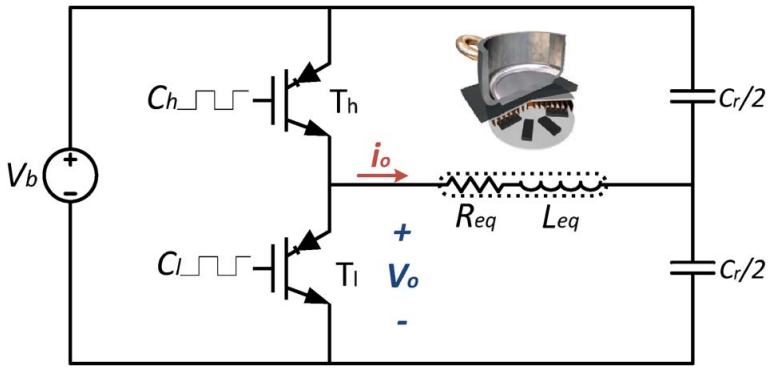

Figure 1.14: Half-bridge IH circuit [72].

Impedance requirements are also directly related to the inverter topology [73,74]. In domestic IH, the most prevalent topologies are the half-bridge inverter, like the one shown in Fig. 1.14, and single-switch inverters in the European and Asian markets respectively [4, 11, 75]. With the advent of newer technology and appliances functionality, other devices [72] and topologies have gained popularity. Silicon carbide (SiC) and gallium nitride (GaN) devices allow for faster switching speeds and reduced losses [76]. Double half-bridge topologies allow for phase-shift control [77, 78], full bridges increase modulation possibilities [68, 79] and matrix topologies allow operation of multiple resonant tanks with reduced number of devices [80,81]. Sometimes the resonant tank itself has internal switches that change the resonant capacitors and/or snubbers in order to adapt to extreme inductor impedance changes [5, 82].

Although frequency control, duty cycle and pulse density modulation (PDM) are common control methods for half-bridge inverters [4, 68, 78–80, 83], some variations are sometimes used to achieve particular purposes [84].

1.3.1.4 Radiated near field

There are numerous studies [85–88] that establish the health effects of magnetic and electric fields and their safe limits as guidelines. These effects are usually limited to Joule heating, nerve stimulation and changes in cell membrane permeability.

Regulations [89, 90] use these guidelines to establish the upper limits of the fields that an appliance can emit to its surroundings according to the exposure to the general public. Investigations have been carried out in recent years to determine and verify the effects of different design considerations on these emissions [91, 92]. Distance increases would likely increase the radiated field, though no specific study has been carried out yet.

1.3.2 Inductive wireless power transfer modelling

The review of WPT systems is separated into:

- *Ideal WPT inductors modelling*: Magnetic simulation of WPT systems is similar to IH systems', without the ferromagnetic loads. Much emphasis is placed upon mutual impedance, which can be calculated as the induced voltage in a winding due to an excitation current in another winding.
- *Windings' losses modelling*: Winding losses calculations are very similar to IH windings, with the caveat that multiple inductors add more components to proximity losses calculations.
- *Topologies and system design*: Generally full bridges are employed, with input and output voltage control using buck or buck-boost converters, compensation topologies in resonant tanks of series-series capacitors, series-parallel, and other combinations.
- *Radiated near field*: Similar to IH systems, WPT have to mitigate their emissions when people and other devices can be in their proximity.

1.3.2.1 Ideal WPT inductors modelling

Considering that inductive WPT systems are essentially loosely coupled transformers, much of the simulation and design process of these systems are based on the same principles [93, 94]. The growing interest in electric vehicle chargers has motivated researchers to develop and improve wireless charging methods, which has also generated interest for applications in all power ranges [13, 95–97], with numerous contributions. In simulations, Maxwell's equations are used to calculate the electromagnetic fields generated by each inductor and be able to determine their self and mutual impedances [98]. As with IH, WPT systems can be simulated analytically or numerically, though the FEM is the most common [99]. It is worth noting that the most common inductor geometry is rectangular [13] to mitigate

misalignment problems. Aside from minor differences of geometries and materials, simulation methods for WPT system are the same as coupled IH systems.

1.3.2.2 Windings' losses modelling

Inductor windings in both IH and WPT are constructed with the same range of conductive materials and cable configurations. Litz wires are preferred up to 0.1 - 1 MHz due to their small losses [98]. Solid wires and hollow litz, [100], are used in the megahertz range because of their smaller proximity losses. Therefore, the calculation of losses and efficiency in WPT systems is nearly identical to that of IH systems, as well as the strand number and diameter selection [101–103]. Nevertheless, the grouping of several inductors causes additional terms in proximity losses. In simple terms, the magnetic field generated in one inductor causes proximity losses both on itself and the other inductor. These additional proximity losses are usually small compared with the other loss mechanisms, which may be the reason they are rarely reported in the literature [104, 105]. Even though most authors choose to calculate cable losses using mainly analytical methods [106–110], separating the cable calculations from the rest of the system, some authors prefer to model everything at once, simulating the skin and proximity effects with equivalent, homogenized cable properties, [111–113]. The requirements for low coil resistance have made some researchers re-evaluate how ideal litz wires are, using mostly numeric calculations to determine the effect cable construction has on losses [114–118]. The winding losses modelling for WPT is also valid for coupled IH and ICH.

1.3.2.3 Topologies and system design

Reactance compensation and impedance matching are very important in WPT systems. Without resonant tanks, the transmitter and receiver inductors would cause the systems' impedance to be highly inductive, with barely any power transferred. Each coil can form its resonant tank with capacitors and additional inductances in series and/or parallel [119]. Depending on the desired behaviour of the system impedance and whether the power source is either a voltage source or a current source, different tank topologies will be desired [120]. The most common are series capacitors in either side, S/S, for voltage sources and parallel capacitor on one side and series in the other, P/S, for current sources [13, 96, 121]. This is due to the fact that they are the cheapest compensations with only two capacitors, their resonant frequencies are independent of mutual impedance, and the system

control is simple. Generally, the most beneficial approach is to set the resonant frequency of both transmitter and receiver sides on the same value [120]. Adding another capacitor to the primary side in a SP/S or PS/S configuration can make the output current independent from mutual inductance. Additional inductors are included in the compensation [122] when load independent output current is desired, where elements are placed alternately in series and parallel, where the last element is usually in series LCL/P, LCC/P, CLC/P, LLCL/P, LCL/LCL [119], as depicted in Fig. 1.15.

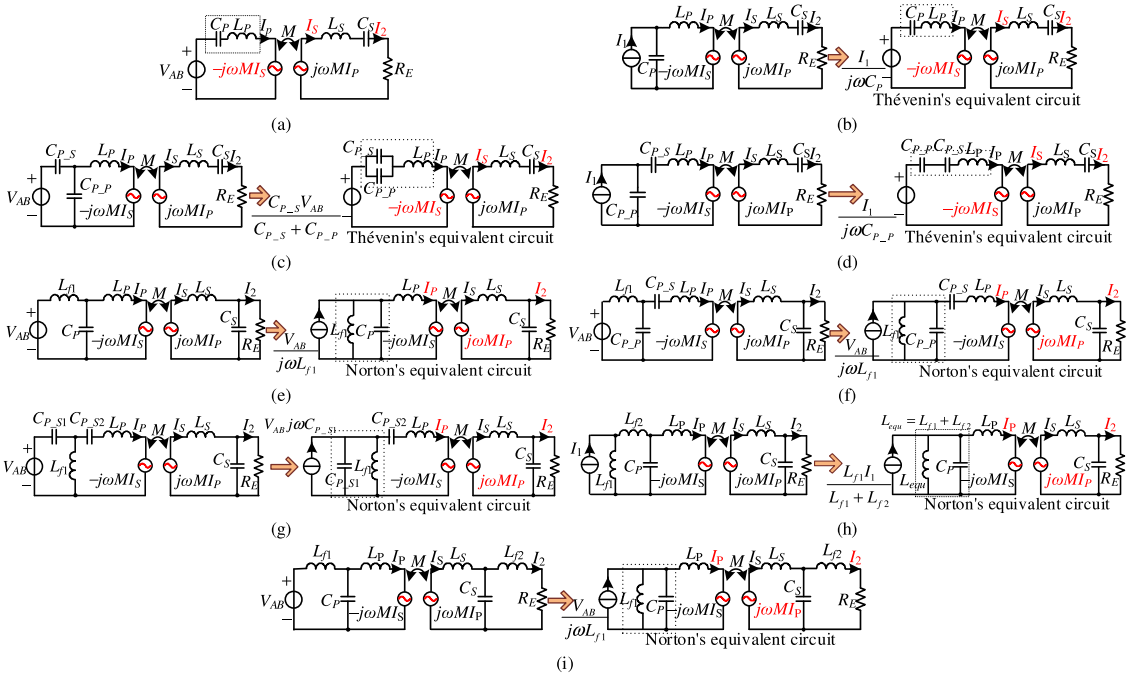

Figure 1.15: WPT compensations. (a) S/S, (b) P/S, (c) SP/S, (d) PS/S, (e) *LCL*/P (f) *LCC*/P (g) *CLC*/P (h) *LLCL*/P and (i) *LCL*/*LCL* [119].

The primary resonant tank is predominantly fed by full bridge inverters due to their control possibilities and reduced component stress [95]. The secondary voltage is usually rectified to a DC bus in order to feed the load. Sometimes, a DC-DC converter is placed before the load to decouple the required load voltage from the optimal operation point of the WPT system [123], as there are efficiency and power optimal load resistances for most WPT systems.

Considering the fact that there are at least two resonant tanks in each system, the optimal operating point is their resonant frequency [98], with sharp decreases in performance at different frequencies. Therefore, the tanks are mostly designed to have the same resonant frequency, which the controls use as the operating point. The power delivery is controlled by other means, such as duty cycle, phase

shift (PS) control, pulse width modulation (PWM), PDM or DC-DC converters for input or output voltage. Moreover, the phenomenon known as pole-splitting [124] also discourages frequency control. Depending on the proportions between impedance elements, two LC resonant tanks with their resonant frequency on the same value can create three zero crossing points for the global impedance's angle. Consequently, there are four regions of operation, a capacitive region for frequencies below the first zero crossing point, inductive between the first point and global impedance, capacitive between global impedance and the third point and inductive for frequencies above the last point. Equivalent system resistance also changes with frequency, achieving its absolute maximum in a single peak at the resonant frequency.

The complexity of the systems due to the additional coil in WPT with respect to IH gives additional degrees of freedom in the design that need to be accounted for to achieve adequate and efficient products [125]. Similarly, control methods have to account for more variables, some of which are across inaccessible air gaps [126]. Systems with active control components in both sides usually requires fast communication to transmit control variables. Some authors avoid the need for fast links by estimating the required parameters from the opposite side [127]. Many works focus on in-transit operation of elecric vehicles' WPT systems, with specific coil designs and control techniques [128]. Some works offer both IH and WPT functionality independent of one another [129].

Over time, WPT systems have increased their efficiency, gaps and delivered power, mostly due to advances in power electronics and control [130].

1.3.2.4 Radiated near field

The general public may have access to the vicinity of WPT systems, as is the case with domestic IH systems. Regulations and standards are in place to ensure that no potentially harmful electromagnetic field manages to affect the general public [87, 131], limiting the emissions from appliances.

Therefore, some effort has been directed to determine radiated magnetic flux, mainly with FEA simulations, [132–136]. The simulations are used to understand the field's source characteristics, system shielding elements, and generate solutions to mitigate emissions to better comply with the regulations.

1.3.3 Coupled IH-WPT modelling

The examination of coupled IH systems is divided into:

- *Mutual impedance calculation*: Mutual impedance in coupled IH applications is similar to WPT, though the resistive component is usually non-zero.
- *Inductively coupled heating system design*: The existing resistive component of mutual impedance prevents the secondary impedance to be reflected in phase to the primary side, eliminating suppositions that are true in WPT, such as identical global and local resonant frequencies.

1.3.3.1 Mutual impedance modelling and calculation

Induction heating (IH) systems with coupled inductors can be calculated with the same methods of WPT, with the difference that mutual impedance has a significant resistive component [137–139]. This mutual resistance causes an impedance phase shift that nullifies the simple design rule to match the resonant frequency on the transmitter and receiver side [140–142]. The phase shift between inductor currents can be used to change power distribution in the IH loads [143–146]. Though there already are some ICH applications [147–149], their modelling is not entirely clear as they do not give values for mutual impedance or "load coil" impedance and neither do they show experimental results of impedance of any kind.

1.3.3.2 Inductively coupled heating system design

ICH system design is still in its infancy. Works found in the literature [147–149] do not seem to have a systematic approach yet, because there is barely any discussion on parameters that can be influenced by design or the different ways that the system could be optimized. The effects of mutual resistance in system resonance and pole-splitting, considerations about performance such as power distribution or power factor are not present in these works.

1.3.4 Bibliography summary

The methods used to calculate ideal inductor impedances and winding losses can be directly applied to high distance systems. However, system design requires more care, due to the reduction in efficiency and inductor-load coupling, which can cause over-currents, over-voltages and excessive losses where there were no issues before. Similarly, the radiated magnetic field will probably increase, and steps will have to be taken to minimize the emissions and comply with EMC regulations.

Table 1.1 summarizes the main contributions to IH systems in terms of load impedance calculation, winding losses, system design and magnetic flux near-field emissions according to the distance between inductor and load.

Table 1.1
Bibliography related to IH modelling and analysis

Inductor-load distance	Ideal inductor-load model	Winding losses	System design	Near-field emissions
$\leq 10\,\mathrm{mm}$	[18, 19, 21, 29]	[14, 32, 44, 47, 57]	[4, 54, 68, 69]	[91, 92]
$> 10\,\mathrm{mm}$			–	–

As can be inferred from Table 1.1, low distance, planar IH systems have been thoroughly investigated. However, very few contributions deal with high distance systems, given that increased distance is quite detrimental and the IuW concept is the only one where increased distance is required. The lack of works on high distance IH systems justifies the objective to explore them in this dissertation.

WPT is quickly becoming a mature technology, with many contributions to coil simulation and design, system topology and control.

The application of WPT concepts to IH is fairly recent, and very few works have been published to this date. Many assumptions have been carried over. Several authors model IH loads as virtual inductors coupled with the physical ones, where otherwise mutual resistances are not represented as such, but their effects are the same.

Table 1.2 summarizes the bibliography contributions to planar coupled IH systems, WPT systems and ICH systems, according to mutual impedance calculation, winding losses, system design and magnetic flux near-field emissions. As seen in the table, there are few contributions related to ICH. Although some works have already started exploring ICH systems, there are no authors that have tried to apply it to IuW. Moreover, the characterization of the systems is usually addressed from the WPT point of view, carrying over several assumptions, such as the erroneous simplification that mutual impedance remains purely inductive in the presence of a lossy medium.

As seen in Table 1.2, winding losses in ICH systems have not been explored yet.

Table 1.2
Bibliography related to ICH modelling

System	Mutual impedance calculation	Winding losses	System design	Near-field emissions
Coupled IH	[138, 139]	[143, 144]	[138, 146]	–
WPT	[93, 94]	[104, 105, 113]	[95, 119]	[133, 135, 136]
ICH	[149]	–	[147, 148]	–

No publications have tackled the optimization of efficiency with respect to winding cable characteristics, litz or otherwise.

It is remarkable that there are no works related to near-field emissions of coupled IH systems. Current EMC regulations' test conditions only require a single load to be heated at a time, which usually means that a single inductor needs to be activated. Moreover, no works have been found involving multiple inductors to heat a bigger load with a focus on their magnetic flux emissions.

Table 1.3 classifies the contributions according to the power delivered and transfer distance. This examination reveals that none of the existing works related to ICH deliver more than 300 W.

Table 1.3
Bibliography related to IH and ICH system design according to power rating and inductor to inductor distance.

Type of system	$\leq 300\,\mathrm{W}$ $\leq 10\,\mathrm{mm}$	$\leq 300\,\mathrm{W}$ $> 10\,\mathrm{mm}$	$> 300\,\mathrm{W}$ $\leq 10\,\mathrm{mm}$	$> 300\,\mathrm{W}$ $> 10\,\mathrm{mm}$
IH	[54]	–	[4, 68, 69, 138, 146]	–
WPT	[95, 119]		[121, 122]	[13]
ICH	–	[147, 148]	–	–

There is a clear gap in contributions regarding high power ICH systems shown in Table 1.3. The small amount of power and the general lack of knowledge due to the dearth of investigations in ICH systems are the perfect motivation to thoroughly study them.

1.4 Dissertation Organization

The dissertation is organized in 7 Chapters and 5 Appendices. In this first Chapter, the principles and history of IH have been introduced, the motivation and objectives of the dissertation itself have been outlined, and a state-of-the-art review has been carried out, highlighting the lack of works related to IuW and ICH.

Chapter 2 develops the basis for IH simulation and design, focusing on single inductor systems at higher distances in order to implement the IuW concept. Interesting designs are developed as prototypes and tested to verify the simulations.

Chapter 3 explores ICH systems, their modelling, losses calculations and system design, using the previously established IH and WPT works. As in the previous chapter, interesting designs are developed as prototypes and tested.

Chapter 4 develops an ICH system with a large secondary inductor and load, keeping the same primary inductor used to heat a same-diameter load. The system is optimized to maintain good parameters for all considered distances. A prototype is built and tested, obtaining satisfactory results where the performance of large-distance cooking is improved.

Chapter 5 introduces an ICH system with a third inductor connected in series with the receiver secondary inductor, which is able to heat two loads simultaneously. The system is designed to maximize power transferred to the second load, which is uncoupled from the primary and secondary inductors. A prototype is built and tested.

Chapter 6 presents an ICH system with a small secondary inductor and load. In addition to the electromagnetic design, the resonant capacitors are housed beneath the secondary capacitor and the design focuses on minimizing capacitor heating. Prototypes of the electromagnetic system and of different PCB's to house the capacitors are built and tested.

Chapter 7 examines the magnetic field emissions of IH and ICH systems of comparable geometry. Design guidelines to minimize ICH emissions are also considered.

Chapter 8 summarizes the contents of the dissertation, draws relevant conclusions and outlines the possible avenues of future research.

Appendix A elaborates on the electromagnetic theory fundamentals that are used

in the FEA simulations. Appendix B examines the structure of multi-stranded cables and their approximation to the litz wire ideal with microscopic FEA simulations of conduction and proximity losses in the strands. Appendix C explains the different methods to process oscilloscope measurements and obtain impedance results. Appendix D compiles a list of all experimental setups shown throughout the dissertation for ease of comparison. Appendix E lists the contributions made in terms of conference papers, journal articles and patents.

Chapter 2

Single-inductor induction under worktop

This chapter develops the inductor-load system of the IuW concept, particularly the electromagnetic simulation and impedance design. The simulations are used to explore the worktop thickness limits in terms of electronics stress, efficiency, ability to deliver sufficient power, heat distribution and magnetic flux emissions. Technically viable simulations will be chosen to develop as prototypes, which will be used to validate the simulations and generally demonstrate the capabilities of IuW.

Table of contents

2.1 Introduction . . . 61
2.2 Modelling . . . 62
2.2.1 Assumptions and simplifications . . . 63
2.2.2 Total impedance and induction impedance . . . 64
2.2.3 Litz winding losses . . . 66
2.3 Design parameters . . . 69
2.3.1 Delivered power . . . 70
2.3.2 Power factor . . . 70
2.3.3 Inductor to load efficiency . . . 71
2.3.4 Power distribution in the load . . . 71
2.3.5 Emitted near field . . . 72
2.4 General design process . . . 73
2.4.1 FEA simulations . . . 73
2.4.2 Selection of winding turns, resonant capacitor and cable . . . 75
2.5 Inductor to load distance analysis . . . 76
2.5.1 Geometry and design . . . 76
2.5.2 Effects on the design parameters . . . 77
2.5.2.1 Inductive power factor . . . 77
2.5.2.2 Efficiency and losses density . . . 78
2.5.2.3 Power distribution . . . 79
2.5.2.4 Emitted near field . . . 80
2.5.3 Safe zone of operation . . . 81

2.6 Ferrite volume analysis 82
2.6.1 Impact on the relevant parameters 83
2.6.2 Pareto representation 84
2.7 Prototypes and experimental measurements 84
2.7.1 Prototype description 84
2.7.2 Measurements 86
2.7.2.1 Low signal regime 86
2.7.2.2 Full power regime 87
2.8 Conclusion 89

2.1 Introduction

The IuW concept has already made its way into the market, but it is currently a very niche product. This is not due to its lack of widespread appeal, as many people agree that the concept has many benefits. Aesthetically, the integration of IH technology beneath the kitchen worktop results in a seamless surface without fissures or holes. Functionally, the zone that could be exclusively used to heat pots and pans is now multi-purpose, as is the whole worktop. Moreover, the surface will be easier to clean due to the lack of gaps or joints.

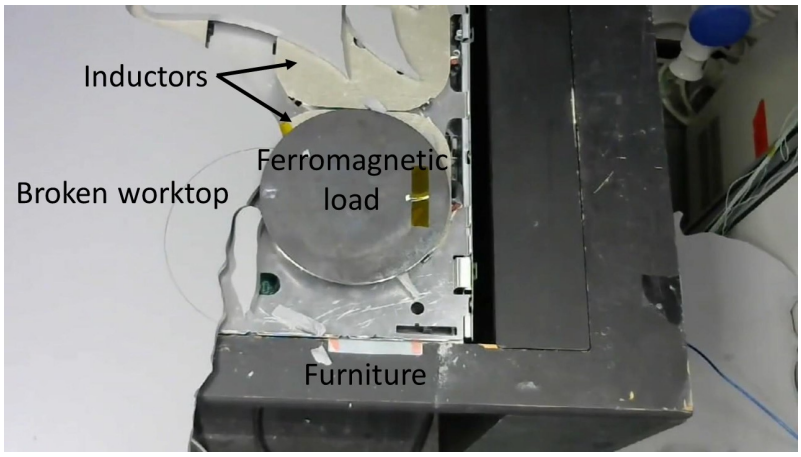

Figure 2.1: Low thickness worktop breaking under thermal stress.

The main disadvantage of current IuW implementations is the lack of standardization, which increases its cost significantly. Each appliance must be custom-built into each individual worktop. This is due to the fact that the inductors are housed inside blind holes drilled below the worktop itself. The holes are used to reduce the inductor-load distance and keep it as similar as possible to conventional IH systems, reusing the same electronic technology. Moreover, the holes cause further problems for the worktops. The very area with the thinnest section has the most thermal stress and mechanical stress due to the heating and placing/removing of cookware. The high stresses in such weak areas can cause early fatigue failures in the worktop and spectacular cracking of its surface due to thermal shock and stress, as shown in Fig. 2.1.

In addition to its technical problems, the current approach requires that the appliance and the worktop be completely integrated, which from a business point of view demands a close relationship between the appliance manufacturer and worktop manufacturer, driving costs higher, and making the IH-manufacturer rely on an undesired external factor. Given that the worktop is the most "important"

(a) (b)

Figure 2.2: Visual representation of IuW systems: (a) commercially available, (b) proposed structure.

component of the combined product, the worktop manufacturer would have the most advantageous position in the partnership.

Manufacturers of IH technology could benefit greatly from IuW cooktops able to work at an ample range of distances, without the need to house the coils inside the worktop. That way, the installation would only require the fixation of the appliance to the bottom of the worktop, regardless of thickness, make and size, allowing for a standard model. Fig. 2.2 shows a schematic representation of available commercial applications and the proposed structure. For this ideal to be realized, the technical distance limits must be determined to know how feasible it is, as conventional IH design warns that high distances are to be avoided [6].

In order to determine the relevant design parameters such as the current, efficiency, power distribution and magnetic field emissions of IuW systems, this chapter first introduces the modelling for IH systems. Then, it describes the involved parameters and the design process. These tools are used to analyze the effects of distance increase on the system and determine the feasible distances.

2.2 Modelling

The electromagnetic simulations are carried out in the commercial FEA tool COMSOL Multiphysics, which solves Maxwell's equations applying the magnetic vector potential [15], explained further in Appendix A. Simplified systems will be modelled as 2D geometries with axial symmetry, while some complete systems will be simulated in full 3D geometry. The FEA tool will be used to obtain impedances, magnetic fields for proximity losses calculations and magnetic flux densities for EMC norm measurements. In post-processing, the winding losses are calculated.

Conduction losses use purely analytical expressions, and the formula for proximity losses uses the magnetic field extracted from the finite element simulation.

2.2.1 Assumptions and simplifications

For the purposes of simulation and calculations, appropriate assumptions are adopted. The assumptions lead to several simplifications. Their purpose is to reduce complexity and computational costs of the calculations, without sacrificing accuracy and reliability. They are listed below:

- *Magneto quasi static (MQS) approach*: The displacement field is assumed constant or slowly changing, meaning that there is no accumulation of charge [16]. Therefore, closed-loop currents are sufficient sources to calculate winding resistance and inductance.
- *Linear magnetic flux and magnetic field relation*: Magnetic permeability is considered constant and does not depend on magnetic field strength [6]. This generally necessitates different permeabilities for ferromagnetic materials at low and high magnetic field strength regimes.
- *Sinusoidal regime and first order harmonic*: Despite the fact that often the input voltage is a square-wave, the resulting current is usually nearly sinusoidal, and the higher order harmonics have very little, or no contribution to power delivery. Consequently, the FEA simulations and most circuit calculations are carried out in the frequency domain, disregarding higher order harmonics. Some frequency-domain incompatible effects become relevant in some scenarios, such as snubber capacitor charging, which can be taken into account by carrying out time-domain circuit simulations.
- *Ideal litz wire*: For the calculations, it is assumed that all winding strands have regular radial and angular transposition, ensuring equivalence between strands. Strand equivalence simplifies losses calculations and minimizes induced current effects of electromagnetic fields in the inductor [14]. Appendix B closely examines strand equivalence in practical cable structures.
- *Winding modelled as a uniform current density*: In simulation, the exact inductor geometry is substituted by a lossless, ideal disk, which carries a uniform current density. The simplification is valid when enough of the disk is filled with the real winding and the cable ensures a near uniform current distribution, as is the case with litz wire.

- *Zero ferrite losses*: In the kilohertz range, ferrite power losses due to induced currents and hysteresis are negligible. In the simulations, the ferrite material uses zero conductivity to enforce this assumption.

- *Disregard of longitudinal proximity losses*: Azimuthal magnetic field is small, and its effect on proximity losses is also smaller than those of perpendicular magnetic field. Therefore, longitudinal proximity losses can be discounted from the calculations.

- *Symmetry*: Geometries with circular inductors, loads and ferrites can be directly represented in 2D enforcing full rotational symmetry. Geometries with discrete axial symmetry, such as when the ferrite is distributed in evenly spaced bars, the discrete axial symmetry can be represented as a 3D spherical wedge. If the loads or inductors are misaligned along a single axis, a vertical symmetry plane can be applied. In any other scenario, geometry simplifications would incur significant errors, which can only be avoided by representing the full 3D geometry.

- *Low skin depth of fields in dissipative media*: The high conductivity and sometimes permeability of the heated materials ensures that the electromagnetic fields are confined to the materials' surface. This phenomenon allows to move the low penetration current densities to the boundary itself, applying the impedance boundary condition (IBC), and avoid meshing and calculating in the volume beyond the boundary.

2.2.2 Total impedance and induction impedance

The inductor-load system is most commonly represented as an equivalent impedance [54], composed of a series resistance and inductance. The impedance depends on the system geometry, the materials of the load, shielding and flux concentrators, and the frequency. Fig. 2.3 (a) represents the IH system schematically.

Fig. 2.3 (b) shows the equivalent circuit of the inductor-load impedance with a voltage generator and compensation capacitor. The equivalent resistance, R_{eq}, includes contributions from the induction heating system with ideal inductor, R_{ind}, and winding losses, R_w. The ideal induction heating resistance comprises the contribution of the load, R_{load}, and shielding, R_{sh}. Winding losses are separated into conduction losses, R_{cond}, and proximity losses, R_{prox}. The equivalent inductance is entirely made up of the ideal induction inductance, $L_{\text{eq}} = L_{\text{ind}}$. Elements with

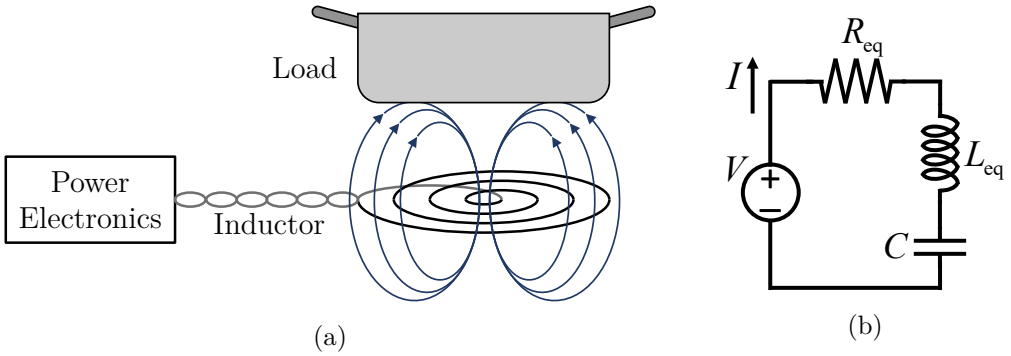

Figure 2.3: (a) Schematic representation of IH systems, (b) IH equivalent circuit.

the ind, load and sh subscripts are obtained from FEA simulations, whereas the losses, with cond and prox subscripts, are calculated in post-processing. These considerations are encapsulated in the following equations:

$$R_{\text{eq}} = R_{\text{ind}} + R_w, \tag{2.1}$$

$$R_{\text{ind}} = R_{\text{load}} + R_{\text{sh}}, \tag{2.2}$$

$$R_w = R_{\text{cond}} + R_{\text{prox}}. \tag{2.3}$$

In the simulation, the system is excited by driving a known current through the inductor, $I = 1\,\text{A}$. The ideal induced voltage in the inductor, V_{ind}, is calculated from the electric field:

$$V_{\text{ind}} = -\oint E_\phi dl, \tag{2.4}$$

where E_ϕ is the electric field's azimuthal component. The impedance can be calculated by dividing the induced voltage by the input current:

$$Z_{\text{ind}} = \frac{V_{\text{ind}}}{I}. \tag{2.5}$$

The real part of the impedance corresponds with the induction resistance, R_{ind}, and the imaginary part is the equivalent inductance's reactance, ωL_{ind}:

$$Z_{\text{ind}} = R_{\text{ind}} + j\omega L_{\text{ind}}. \tag{2.6}$$

In order to separate the elements of R_{ind}, the contribution to the power losses in each material need to be obtained separately. Poynting's vector, $\mathbf{S}$, represents the electromagnetic surface power density:

$$\mathbf{S} = \mathbf{E} \times \mathbf{H}^*, \tag{2.7}$$

where $\mathbf{E}$ is the electric field vector and $\mathbf{H}^*$ is the complex conjugate of the magnetic field vector.

Its integration over a surface yields the total power transmitted through said surface. If the integration surface is the closed boundary of a volume, such as the load or shielding, the integration accounts for the total power dissipated (or generated, in the case of the inductor) in the volume, P_i, where the subscript i denotes the target surface, which can be load or sh for the shielding:

$$P_i = \int_{S_i} \mathbf{S}\hat{\mathbf{n}} dS_i, \tag{2.8}$$

where S_i is the volume's surface and $\hat{\mathbf{n}}$ is its normal unitary vector. A resistance value, R_i, can be obtained from the power and input current:

$$R_i = \frac{P_i}{I_{\text{rms}}^2}, \tag{2.9}$$

where I_{rms} is the root mean square (rms) of I.

2.2.3 Litz winding losses

Winding conduction losses, R_{cond}, as the name suggests, are caused directly by the conduction of electric current, which encapsulates DC and skin effect. The expression for cables composed of multiple equivalent strands is:

$$R_{\text{cond}} = \frac{n_t}{n_s} \frac{l_{t,\text{mean}}}{S_s \sigma} \Phi_{\text{cond}}, \tag{2.10}$$

where n_t is the number of turns, n_s the number of strands, $l_{t,\text{mean}}$ is the mean winding turn length, S_s is the strand's section, σ is the cable material's conductivity and Φ_{cond} is a function that accounts for the AC dependence of the strand resistance (namely, the skin effect) and also depends on the strand's shape, size and material properties. In the case of circular windings $l_{t,\text{mean}} = \pi(r_{\text{w,ext}} + r_{\text{w,int}})$, where $r_{\text{w,ext}}$ and $r_{\text{w,int}}$ are the external and internal inductor radii respectively. Moreover, for circle-section strands, $S_s = \pi r_s^2$, where r_s is the strand radius, and Φ_{cond} can be expressed analytically in terms of r_s and δ, the skin depth. The parameter δ embodies the penetration depth of electromagnetic fields in a given material based on its conductivity, σ, magnetic permeability, μ, and the frequency, f, of the fields:

$$\delta = \sqrt{\frac{2}{\omega \mu \sigma}}, \tag{2.11}$$

where ω is the angular frequency, defined as $\omega = 2\pi f$. Most inductors are built with either copper or aluminum cable, whose σ with respect to temperature can be

expressed as:

$$\sigma_{\mathrm{Cu}}(T) = \frac{5.779 \cdot 10^7\,\mathrm{S\,m^{-1}}}{1 + 0.00398\,(T - 27\,^{\circ}\mathrm{C})\,\mathrm{K^{-1}}}, \tag{2.12}$$

$$\sigma_{\mathrm{Al}}(T) = \frac{3.77 \cdot 10^7\,\mathrm{S\,m^{-1}}}{1 + 0.00390\,(T - 20\,^{\circ}\mathrm{C})\,\mathrm{K^{-1}}}, \tag{2.13}$$

where T is the temperature. With these conditions, (2.10) can be rewritten as:

$$R_{\mathrm{cond}} = \frac{n_t}{n_s}\frac{\pi\left(r_{\mathrm{ext}} + r_{\mathrm{int}}\right)}{\pi r_s^2 \sigma}\Phi_{\mathrm{cond}}\left(r_s/\delta\right). \tag{2.14}$$

The analytical expression of Φ_{cond} for round strands is [21]:

$$\Phi_{\mathrm{cond}}(r_s/\delta) = \mathrm{real}\left(\frac{(-1+i)\frac{r_s}{\delta}J_0\left((-1+i)\frac{r_s}{\delta}\right)}{2J_1\left((-1+i)\frac{r_s}{\delta}\right)}\right) \tag{2.15}$$

where J_i is the Bessel function of the first kind and ith order.

Winding proximity losses, R_{prox}, are caused by the induced currents in each strand due to external magnetic fields. In applications with a single winding, the external field is generated by all inductor strands except the considered one. With a sufficient number of total strands, this condition can be relaxed, and the total field can be used assuming that the contribution of a single strand is not significant. The R_{prox} expression of a winding caused by the transversal magnetic field in the strand is:

$$R_{\mathrm{prox}} = n_t^3 n_s \frac{4\pi}{\sigma}\Phi_{\mathrm{prox}}\int\frac{\left|\mathbf{H}_{\mathrm{p.t.,p.A.}}\right|^2}{S_w}dV, \tag{2.16}$$

where Φ_{prox} is a series of Bessel functions that accounts for the AC effects of proximity losses according to strand shape, size and material, $\mathbf{H}_{\mathrm{p.t.,p.A.}}$ is the magnetic field generated by the winding per turn (p.t.) when driven by 1 A, (p.A.), which can be shortened to $\bar{\mathbf{H}}$, and S_w is the inductor's cross-section area, calculated as $S_w = n_t S_t$, where S_t is a single turn's cross-section. The expression of Φ_{prox} for round strands is [21]:

$$\Phi_{\mathrm{prox}}\left(r_s/\delta\right) = \mathrm{real}\left(\frac{r_s}{\delta}\frac{J_2\left((-1+j)\,\frac{r_s}{\delta}\right)}{J_0\left((-1+j)\,\frac{r_s}{\delta}\right)}\right), \tag{2.17}$$

The magnetic field integral can be simplified to an average calculation. In 2D geometries with axial symmetry:

$$R_{\mathrm{prox}} = n_t^3 n_s \frac{4\pi}{\sigma}\Phi_{\mathrm{prox}}\left(r_s/\delta\right)\left\langle 2\pi r\left|\bar{\mathbf{H}}\right|^2\right\rangle, \tag{2.18}$$

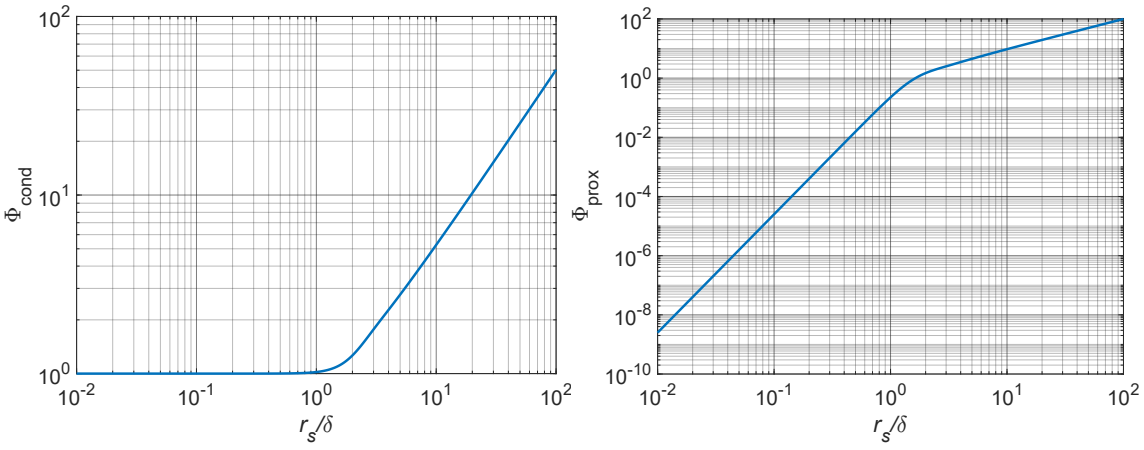

Figure 2.4: Dependence of the winding losses functions with r_s/δ. (a) Φ_{cond} (b) Φ_{prox}

The values of Φ_{cond} and Φ_{prox} as functions of r_s/δ, from (2.15) and (2.17) respectively, are shown in Fig. 2.4. The figure clearly shows that the smallest possible r_s will minimize AC losses. Moreover, losses are still very small when r_s is smaller than δ. Higher strand radii are strongly discouraged. However, the smallest r_s is not always the optimal choice for a litz wire. In addition to the cost, which increases as r_s decreases, another important limiting element is the packing factor, K_p, which is the ratio of real cable area, S_{cable}, to winding area, S_w:

$$K_p = S_{\text{cable}}/S_w. \tag{2.19}$$

As r_s decreases, the air gaps between strands and strand insulation become more relevant, reducing K_p. An expression can be found in [54], which expresses K_p in terms of a power law and parameters obtained from manufacturer data:

$$K_p = \left(\frac{r_s}{29.79\,\text{mm}}\right)^{0.1295} \tag{2.20}$$

The change of K_p with variation in r_s is represented in Fig. 2.5. For radii smaller than 100 µm, less than half of the available area can be used.

As it was mentioned previously, the simulations are carried out using an ideal disk, which actually corresponds to a single inductor turn, and using a single Ampere of current as a source. The impedance values can be generalized to n_t turns and n_s

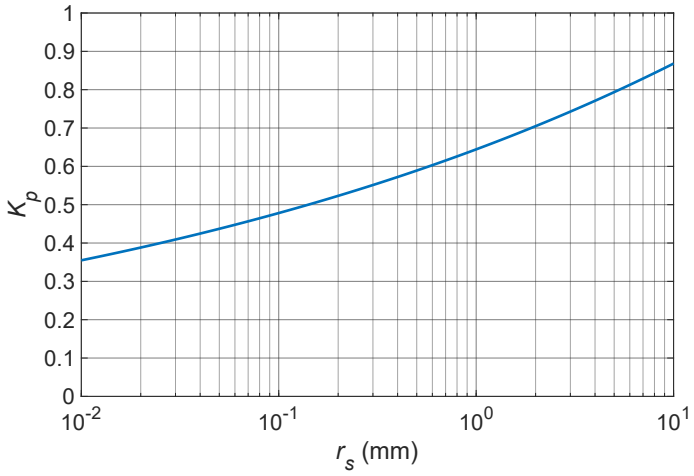

Figure 2.5: Dependence of K_p with r_s

strands (when applicable) with the following expressions:

$$\frac{R_{\text{ind}}}{R_{\text{ind,p.t.}}} = \frac{L_{\text{ind}}}{L_{\text{ind,p.t.}}} = n_t^2, \tag{2.21}$$

$$R_{\text{cond}} = \frac{n_t}{n_s} R_{\text{cond,p.t.,p.s.}}, \tag{2.22}$$

$$R_{\text{prox}} = n_t^3 n_s R_{\text{prox,p.t.,p.s.}}, \tag{2.23}$$

where $R_{\text{ind,p.t.}}$ is the single-turn ideal induction resistance, $L_{\text{ind,p.t.}}$ is the single-turn ideal induction inductance, $R_{\text{cond,p.t.,p.s.}}$ is the single-turn, single-strand conduction losses resistance and $R_{\text{prox,p.t.,p.s.}}$ is the single-turn, single-strand proximity losses resistance.

Considering the strong inductive component of the impedance, compensation capacitors are used to achieve resonance at the desired frequency. The equivalent impedance of the full IH system, Z_{eq}, can be defined as:

$$Z_{\text{eq}} = R_{\text{eq}} + j\omega L_{\text{eq}} + \frac{1}{j\omega C}, \tag{2.24}$$

where C is the capacitance of the resonant capacitor.

2.3 Design parameters

IH systems need to achieve several objectives in order to be functional and efficient. To gauge these objectives and assess the usability and quality of IH systems, relevant parameters can be defined and evaluated. These parameters can be used as scores to determine design suitability, particularly when they are at odds with one another. Chapter 4 will prominently use these scores.

2.3.1 Delivered power

The main objective of IH is, obviously, to deliver power. For any given system, there is a maximum power rating, $P_{\max}$, that should be achieved. Considering the voltage-fed system of Fig. 2.3, current and power can be obtained as:

$$I_{\text{rms}} = \frac{V_{\text{rms}}}{Z_{\text{eq}}}, \tag{2.25}$$

$$P = R_{\text{eq}} \left| I_{\text{rms}} \right|^2 = \frac{R_{\text{eq}} V_{\text{rms}}^2}{R_{\text{eq}}^2 + \left(\omega L_{\text{eq}} - \frac{1}{\omega C} \right)^2} \tag{2.26}$$

where V_{rms} is the input rms voltage. Depending on the inverter topology, the V_{rms} that is obtained from a given rms mains voltage, $V_{\text{mains,rms}}$, changes. Unless otherwise stated, this dissertation assumes that half-bridge inverters are used in conjunction with small DC bus capacitors, so their output voltage essentially modulates the rectified mains voltage [75]:

$$V_{\text{rms}} = \frac{\sqrt{2}}{\pi} V_{\text{mains,rms}}. \tag{2.27}$$

For monotonically increasing $R_{\text{eq}}(\omega)$ and monotonically decreasing $L_{\text{eq}}(\omega)$, maximum power is achieved at the resonant frequency, $\omega_{0,\text{res}}$, where inductive and capacitive reactance are cancelled:

$$\omega_{0,\text{eq}} = \frac{1}{\sqrt{L_{\text{eq}} C}}, \tag{2.28}$$

$$P_{\max} = P(\omega_{0,\text{eq}}) = \frac{V_{\text{rms}}^2}{R_{\text{eq}}}. \tag{2.29}$$

2.3.2 Power factor

The electrical power factor, PF, represents the ratio between the minimum current required to deliver the same power and the actual current. It also indicates indirectly the phase difference between voltage and current. With the sinusoidal regime, it is defined from the impedance as:

$$PF = \frac{\Re(Z_{\text{eq}})}{|Z_{\text{eq}}|} = \frac{R_{\text{eq}}}{\sqrt{R_{\text{eq}}^2 + \left(\omega L_{\text{eq}} - \frac{1}{\omega C} \right)^2}} \tag{2.30}$$

For IH applications in particular, it is interesting to consider the inductive power factor, PF_{ind}, which does not include the compensation capacitor:

$$PF_{\text{ind}} = \frac{R_{\text{eq}}}{\sqrt{R_{\text{eq}}^2 + \omega^2 L_{\text{eq}}^2}}. \tag{2.31}$$

Low values of PF_{ind} indicate much higher compensation capacitor voltage. PF_{ind} can also be put in terms of per turn impedance ignoring winding losses:

$$PF_{\text{ind}} \approx \frac{\cancel{n_t^2} R_{\text{ind,p.t.}}}{\cancel{n_t^2}\sqrt{R_{\text{ind,p.t.}}^2 + \omega^2 L_{\text{eq,p.t.}}^2}}. \tag{2.32}$$

Since PF_{ind} is not affected by n_t or C, it can only be modified by changing the system's geometry, the load's material or by the winding cable in a very small measure.

2.3.3 Inductor to load efficiency

The inverter output to load efficiency can be calculated from the resistances defined in the previous section:

$$\eta = \frac{R_{\text{load}}}{R_{\text{load}} + R_{\text{sh}} + R_{\text{cond}} + R_{\text{prox}}}. \tag{2.33}$$

The resistances can be put in terms of their per turn, per strand components:

$$\eta = \frac{n_t^2 R_{\text{load,p.t.}}}{n_t^2 R_{\text{load,p.t.}} + n_t^2 R_{\text{sh,p.t.}} + \dfrac{n_t}{n_s} R_{\text{cond,p.t.,p.s.}} + n_t^3 n_s R_{\text{prox,p.t.,p.s.}}}, \tag{2.34}$$

consequently:

$$\eta = \frac{R_{\text{load,p.t.}}}{R_{\text{load,p.t.}} + R_{\text{sh,p.t.}} + \dfrac{1}{n_t n_s} R_{\text{cond,p.t.,p.s.}} + n_t n_s R_{\text{prox,p.t.,p.s.}}}, \tag{2.35}$$

where the product $n_t n_s$ is the total number of strands in the winding, relevant in efficiency optimization.

2.3.4 Power distribution in the load

In general, IH does not generate heat evenly on the load surface. A measure of the quality of the distribution can be relevant to system design. An adequate measurement is the normalized standard deviation of Poynting's vector, called the power distribution for convenience, PD, which is defined as:

$$PD = \sqrt{\frac{\sum_{i=1}^{N} \left(\dfrac{S_{\text{load}_i}}{\overline{S}_{\text{load}}} - 1 \right)^2}{N-1}}, \tag{2.36}$$

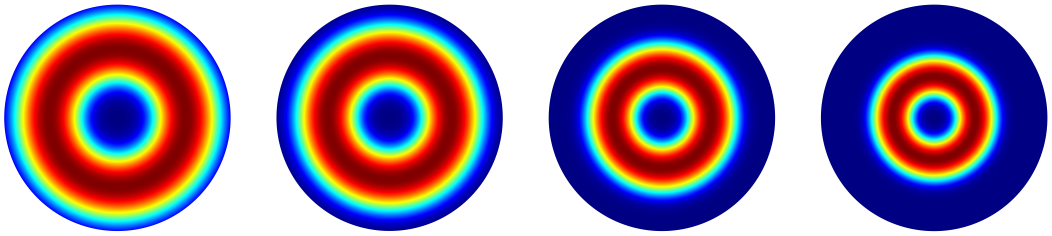

(a) 0.7198 (b) 0.7990 (c) 1.0171 (d) 1.1990

Figure 2.6: Poynting vector distribution and *PD* values of loads of different diameters, $\varnothing_{\text{load}}$, with an inductor of external diameter of $\varnothing_{w,\text{ext}} = 180\,\text{mm}$: (a) 180 mm, (b) 200 mm, (c) 250 mm, (d) 300 mm.

where S_{load_i} is the Poynting's vector component normal to the load, the index i refers to the uniformly distributed mesh points in the simulation, totalling N, and $\overline{S}_{\text{load}}$ is the mean value of S_{load_i} over all N points. As *PD* is a standard deviation, a lower value indicates more uniform distribution.

PD is entirely dependent on the system's geometry and materials, with no effect from compensation capacitors or number of inductor turns.

For reference, Fig. 2.6 shows distribution examples and their corresponding *PD* values, using an inductor of external diameter, $\varnothing_{w,\text{ext}} = 180\,\text{mm}$ and loads ranging from diameters, $\varnothing_{\text{load}}$, between 180 and 300 mm.

2.3.5 Emitted near field

Appliances are subject to regulations limiting their electromagnetic field emissions. IH cooktops in particular can have trouble complying with near magnetic field regulations. The most rigorous test involves measuring the induced voltage, V_{loop} in 3 orthogonal loops of $S_{\text{loop}} = 100\,\text{cm}^2$ area, 30 cm away from the appliance [89].

$$V_{\text{loop}} = \frac{\partial \int_S \mathbf{B}\hat{\mathbf{n}} dS}{\partial t}. \tag{2.37}$$

In the frequency domain, the time derivative can be substituted by $j\omega$:

$$V_{\text{loop}} = j\omega \int_S \mathbf{B}\hat{\mathbf{n}} dS. \tag{2.38}$$

The measuring device returns a mean value for the flux density, B_{meas}:

$$B_{\text{meas}} = \frac{V_{\text{loop}}}{j\omega S_{\text{loop}}}. \tag{2.39}$$

For easy comparison, the same mean value can be obtained in simulation:

$$B_{\text{sim}} = \frac{\int_S \mathbf{B}\hat{\mathbf{n}} dS}{S_{\text{loop}}} \tag{2.40}$$

Emitted field depends on the inductor number of turns and its current:

$$\mathbf{B}_{\text{rms}} = n_t I_{\text{rms}} \mathbf{B}_{\text{p.t.,p.A.}}, \tag{2.41}$$

where $\mathbf{B}_{\text{p.t.,p.A.}}$ is the magnetic flux generated per winding turn (p.t.) and per Ampere (p.A.), which is dependent on the system's geometry and materials. Following the measurement technique of the standard, the modulus of $\mathbf{B}$ is obtained as follows:

$$B_{\text{rms}} = |\mathbf{B}_{\text{rms}}| = \sqrt{B_{1,\text{rms}}^2 + B_{2,\text{rms}}^2 + B_{3,\text{rms}}^2}, \tag{2.42}$$

where the numbered subscripts denote the local probe cartesian coordinate system. The values obtained in simulation assume that the local system is aligned with the global one, allowing to use the x, y, z components directly. Accurate simulations should result in B_{rms} values close to B_{meas}.

2.4 General design process

Usually, the objectives of IH design are to reach a certain maximum power at a particular resonant frequency, aiming to maximize PF_{ind} and η and to minimize PD and emitted near field. IH system design involves chosing a geometry and materials to input to the FEA simulation. The results, with the power and frequency requirements, can be used to select n_t, n_s and C.

2.4.1 FEA simulations

As a rule of thumb, the inductor's external radius needs to be equal or smaller than the load radius in order to reach high η and PF. In contrast, according to Fig. 2.6, in order to maintain low PD, the inductor's external radius needs to be equal or larger than the intended load radius. Therefore, it is preferred when the inductor and the load have the same radius.

There is a wide variety of material properties in load materials, even when only considering ferromagnetic steel. In order to deliver the required power to most loads, the system is usually designed with the conductive material that provides the highest impedance, which is the one with the highest μ/σ ratio.

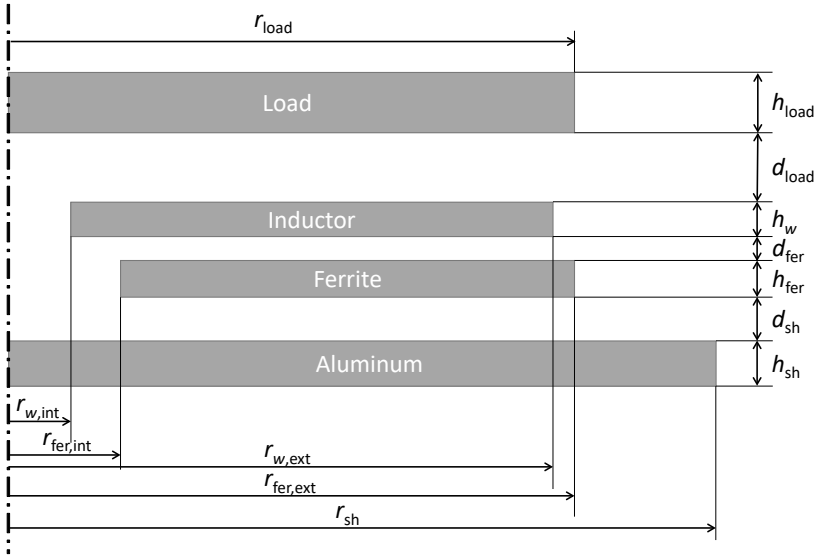

(a)

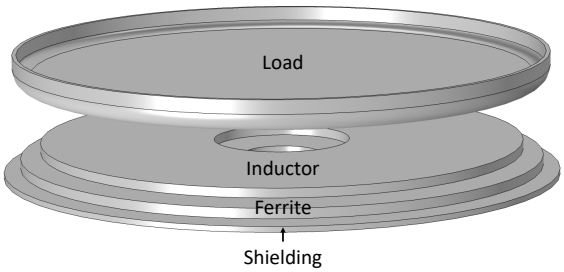

(b)

Figure 2.7: (a) 2D diagram of the simulated geometry. (b) 3D representation.

As mentioned previously, the simulations are carried out considering an annulus-shaped inductor turn and 1 A of input current. This results in per turn impedance and per Ampere-turn electromagnetic fields.

The geometry of the simulations is shown in Fig. 2.7. Fig. 2.7 (a) shows the 2D simplified geometry, where the rotational symmetry makes all elements either disks or annuli. Fig. 2.7 (a) shows the parameter names of radii, distances and thicknesses of all elements. All radii have corresponding diameters, such as $\varnothing_{w,\text{ext}} = 2r_{w,\text{ext}}$. Fig. 2.7 (b) shows the 3D equivalent, where a filleted section is added to the load, as can often be the case. This helps prevent discontinuity problems in the load's edge.

2.4.2 Selection of winding turns, resonant capacitor and cable

According to the maximum power requirement, $P_{\max}$, the required n_t can be obtained from (2.21) and (2.29), bearing in mind that $R_{\text{load,p.t.}}$ is frequency dependent:

$$n_t \leq \frac{V_{\text{rms}}}{\sqrt{R_{\text{load,p.t.}} P_{\max}}}. \tag{2.43}$$

Once n_t is chosen, L_{eq} is also fixed. C can be easily obtained from (2.28):

$$C = \frac{1}{\omega_{\text{res}}^2 L_{\text{eq}}}. \tag{2.44}$$

In regards to the efficiency, it can be expressed in terms of the total number of strands, $n_t n_s$ as it is shown in (2.35). Therefore, it can be optimized in terms of that product. As a continuous function, the derivative of η with respect to the product of $n_t n_s$ can be used to find the η maximum.

$$\frac{\partial \eta}{\partial \left(n_t n_s\right)} = 0 \rightarrow \left(n_t n_s\right)_{\text{opt}} = \sqrt{\frac{R_{\text{cond,p.t.,p.s.}}}{R_{\text{prox,p.t.,p.s.}}}}, \tag{2.45}$$

where $\left(n_t n_s\right)_{\text{opt}}$ is the optimum number of total strands that results in the maximum η, $\eta_{\max}$.

$$\eta_{\max} = \frac{R_{\text{load,p.t.}}}{R_{\text{load,p.t.}} + 2\sqrt{R_{\text{cond,p.t.,p.s.}} R_{\text{prox,p.t.,p.s.}}}} \tag{2.46}$$

For low and medium frequencies, maximum efficiency may not be realistically achievable due to space restrictions. Applying the definition of K_p from the previous section to round strands, the maximum number of total strands that can be fitted in the available winding volume are:

$$\left(n_t n_s\right)_{\max} = K_p \frac{S_w}{\pi r_s^2} \tag{2.47}$$

In addition to the efficiency, it is also relevant to consider the capacity of inductors to evacuate the heat they generate. Winding losses volume density, J_w, are defined as the ratio between the power losses, P_w, and the winding's volume, V_w:

$$J_w = \frac{P_w}{V_w} \tag{2.48}$$

Generally, inductors can evacuate from $4\,\text{W/cm}^3$ to $6\,\text{W/cm}^3$ unaided. If higher values are reached in simulation, the next iterated design should correct them.

2.5 Inductor to load distance analysis

This section analyzes the parameters defined in Section 2.3 for IH systems with different inductor and load diameter, $\varnothing_{w,\text{ext}}$ and $\varnothing_{\text{load}}$, respectively, and increasing distance, d_{load}.

2.5.1 Geometry and design

Table 2.1
$P_{\max}$ for each $r_{w,\text{ext}}$

$\varnothing_{w,\text{ext}}$(mm)	$P_{\max}$(W)
70	800
100	1400
120	1800
150	2400
180	3000
200	3300
250	3700
300	3700

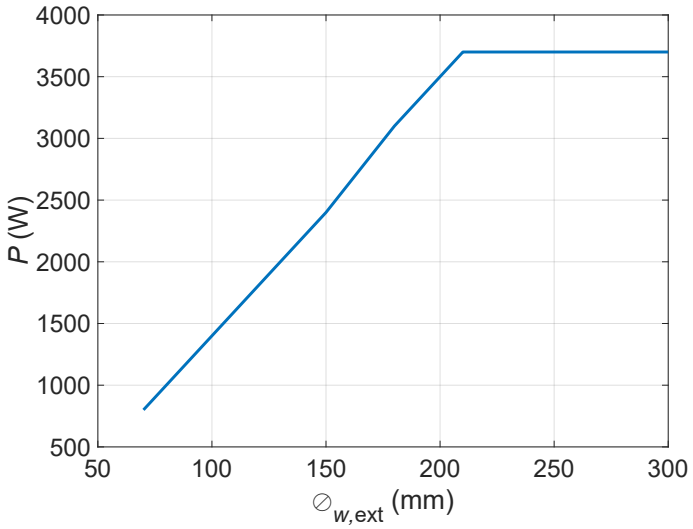

Figure 2.8: Maximum rated power depending on inductor diameter.

In this study, $r_{w,\text{ext}}$ and r_{load} will change together, the ferrite external radius, $r_{\text{fer,ext}}$, will be slightly larger than $r_{w,\text{ext}}$, r_{sh} will be larger still and $r_{w,\text{int}}$ and $r_{\text{fer,int}}$ will not change at all from their initial values between 20 and 25 mm. Inductor radius will range from 35 mm to 150 mm, while d_{load} will change from 5 mm to 60 mm. The required maximum power for each inductor diameter is listed in Table

2.1. Moreover, the rated power is interpolated linearly between each discrete value, as shown in Fig. 2.8.

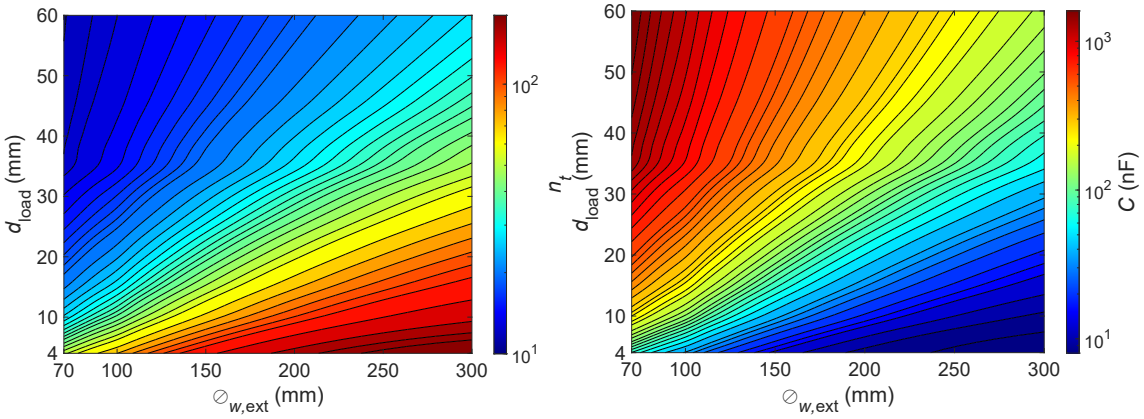

Figure 2.9: Calculated (a) n and (b) C to deliver maximum power at 30 kHz at each distance and inductor radius.

The values of n_t and C required to deliver the rated $P_{\max}$ at 30 kHz are obtained by means of the FEA simulations and are shown in Fig. 2.9.

2.5.2 Effects on the design parameters

2.5.2.1 Inductive power factor

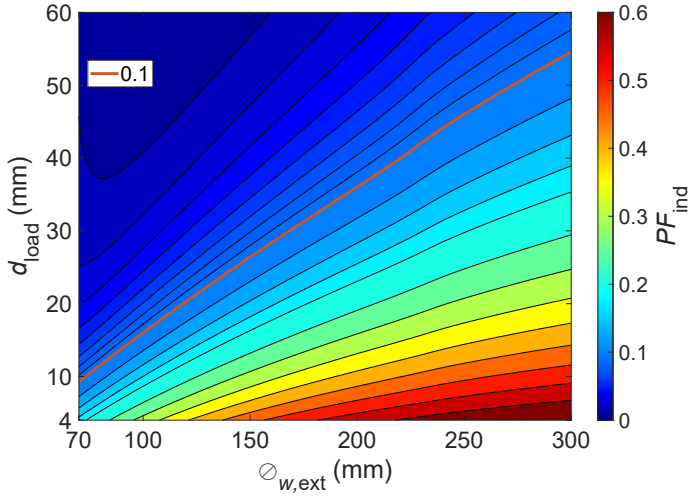

Figure 2.10: Simulated PF_{ind} for sweeping values of $\varnothing_{w,\text{ext}}$ and d_{load}.

Inductive power factor is only affected by geometry and materials. Fig. 2.10 shows the PF_{ind} distribution for different inductor-load diameter and distances. As d_{load} increases, PF_{ind} decreases, but, for higher $\varnothing_{w,\text{ext}}$, PF_{ind} decreases slower. Low PF_{ind} values indicate that in order to achieve the same R_{eq} at the same frequency, a

much higher L_{eq} is needed. To compensate the higher L_{eq}, a lower C is needed. For the same I_{rms} the reduced C causes more capacitor voltage. Therefore, low PF_{ind} causes high voltages, and values below 0.1, represented in Fig. 2.10, are usually avoided.

2.5.2.2 Efficiency and losses density

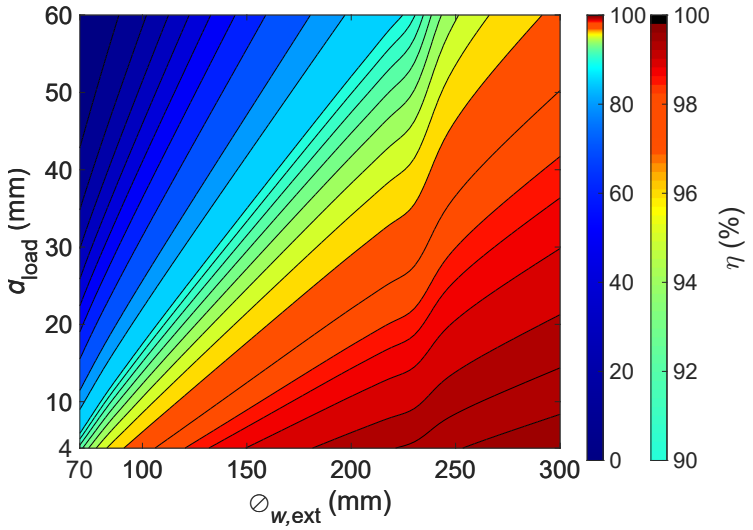

Figure 2.11: Simulated η for sweeping values of $\varnothing_{w,\text{ext}}$ and d_{load}.

The efficiency calculations have been carried out considering copper cable, with conductivity obtained from (2.12), $\sigma_{\text{Cu}}(T)$ at 100 °C. The litz cable has $\varnothing_s = 200\,\mu\text{m}$ using the minimum $n_t n_s$ between $(n_t n_s)_{\text{opt}}$ and $(n_t n_s)_{\text{max}}$. Fig. 2.11 shows the η distribution for different inductor-load diameter and distances. For any given distance, efficiency always improves for increasing $\varnothing_{w,\text{ext}}$ and $\varnothing_{\text{load}}$. Similarly, for any given diameter, efficiency always decreases for increasing d_{load}. Moreover, efficiency decrease with distance is much faster for smaller diameters. Consequently, the highest distances can only be reached efficiently with higher diameters.

Although low efficiency is not a hard restriction in IH, values below 90 % are usually avoided. Fig. 2.12 shows the same efficiency results cut off at the 90 % line. It highlights the maximum distance that each diameter can achieve and, conversely, the lowest diameter that should operate at each distance.

A more restrictive factor than η, also related to it is the winding losses volume density, J_w. As pointed out earlier, the heat that a given inductor can evacuate is limited, typically $J_{w,\text{limit}} = 5\,\text{W/cm}^3$ in normal operation conditions without ventilation. Fig. 2.13 shows the simulated values of J_w for the $\varnothing_{w,\text{ext}}$ and d_{load} sweep. As low $\varnothing_{w,\text{ext}}$ systems have lower efficiency and a smaller volume, their volumetric

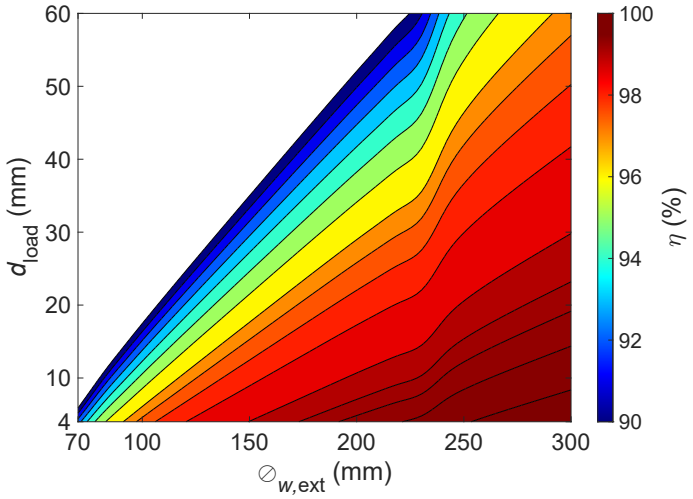

Figure 2.12: Simulated η with limit set at 90 %.

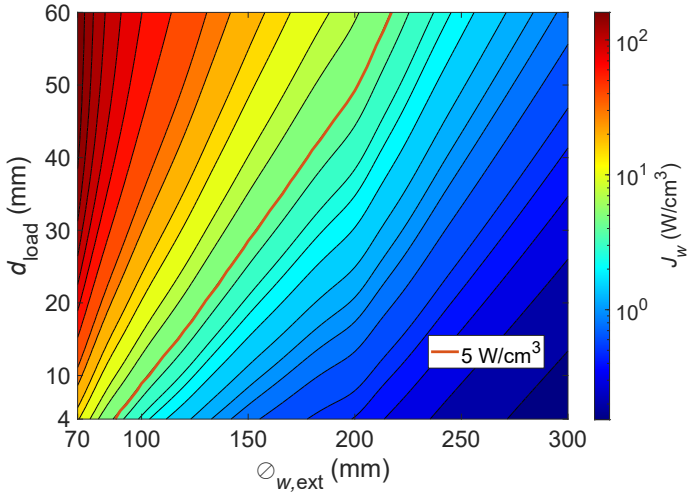

Figure 2.13: Simulated J_w with highlighted 5 W/cm^3 line.

losses can be several times greater than those of higher diameters. Comparing the limits set by $\eta = 95\,\%$ and $J_w = 5\,\mathrm{W/cm^3}$, the η one is slightly less restrictive, particularly at lower $\varnothing_{w,\mathrm{ext}}$.

2.5.2.3 Power distribution

PD calculations, as pointed out earlier, are independent from number of turns and compensation capacitors. Its calculations for the $\varnothing_{w,\mathrm{ext}}$ and d_{load} sweep is shown in Fig. 2.14. Generally, as distance increases, *PD* improves. For low $\varnothing_{w,\mathrm{ext}}$ and high d_{load} as well as for high $\varnothing_{w,\mathrm{ext}}$ and low d_{load}, *PD* worsens slightly with increasing d_{load}. Fig. 2.15 shows the power density distributions with highest and lowest *PD*, where both of them have $d_{\mathrm{load}} = 4\,\mathrm{mm}$, and the $\varnothing_{w,\mathrm{ext}}$ with the highest *PD* is 70 mm and the lowest is 300 mm. The images show that the hardest spots to heat are the center and the outermost perimeter. The area in between can be rather uniform

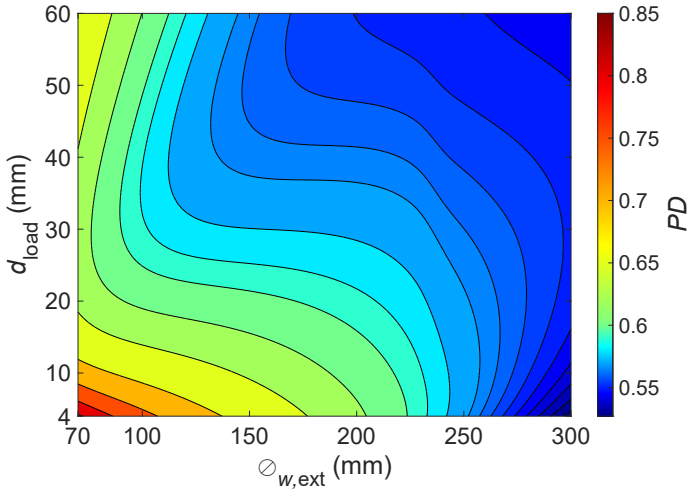

Figure 2.14: Simulated PD for sweeping values of $\varnothing_{w,\text{ext}}$ and d_{load}.

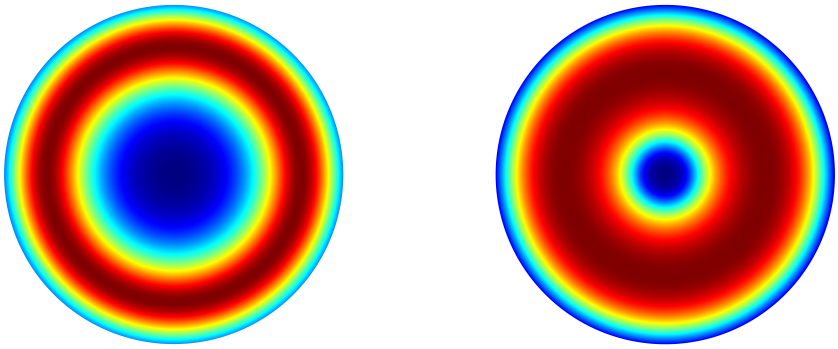

(a) $PD = 0.858$ (b) $PD = 0.527$

Figure 2.15: Poynting vector distribution in the worst and best cases (a) $\varnothing_{w,\text{ext}} = 70\,\text{mm}$, $d_{\text{load}} = 4\,\text{mm}$ and (b) $\varnothing_{w,\text{ext}} = 300\,\text{mm}$, $d_{\text{load}} = 4\,\text{mm}$ (not to scale).

with sufficiently large $\varnothing_{w,\text{ext}}$.

2.5.2.4 Emitted near field

Emitted magnetic field is extremely dependent on the geometry and materials, and linearly proportional to the inductor current and number of turns. As the simulated geometry is relatively simple, it is not fully representative of the emissions of complete appliances, which usually have asymmetric components. Nevertheless, it gives general trends of what can be expected in real systems.

Fig. 2.16 shows the per turn, per Ampere emitted field and Fig. 2.17 shows the simulated values of B_{rms} for the $\varnothing_{w,\text{ext}}$ and d_{load} sweep. The limit set by norm at the frequency range used by IH appliances is $6.25\,\mu\text{T}$ [89], which is marked in the figure. B_{rms} steadily increases with distance for all the considered $\varnothing_{w,\text{ext}}$ range. For the lowest $\varnothing_{w,\text{ext}}$ values, B_{rms} increases more slowly, though *a priori* it is hard to

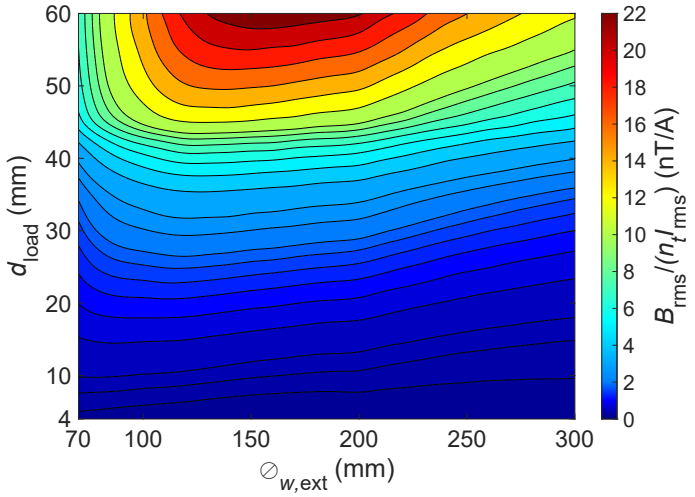

Figure 2.16: Simulated $\frac{B_{\mathrm{rms}}}{n_t I_{\mathrm{rms}}}$ for sweeping values of $\varnothing_{w,\mathrm{ext}}$ and d_{load}.

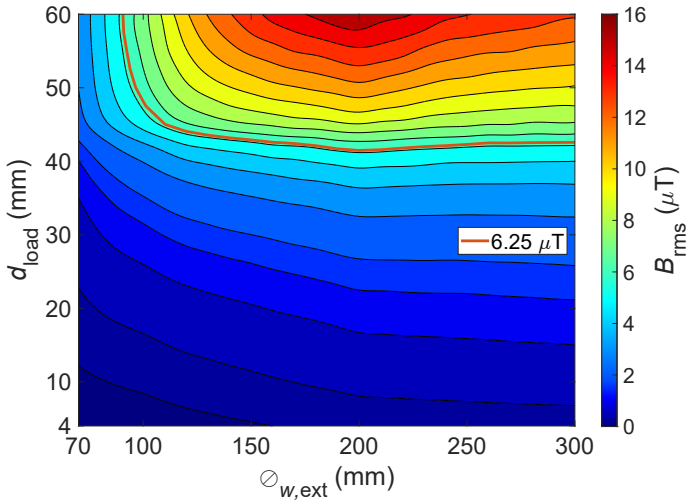

Figure 2.17: Simulated B_{rms} for sweeping values of $\varnothing_{w,\mathrm{ext}}$ and d_{load}.

tell whether it is because of the geometry or the low inductor current.

At medium and high d_{load}, the emitted field increases sharply and then decreases slowly as $\varnothing_{w,\mathrm{ext}}$ increases. As power increases almost linearly with $\varnothing_{w,\mathrm{ext}}$, current increases as a square root function. The small current increase and small per turn, per Ampere emission reduction cancel each other at the norm limit in Fig. 2.17.

2.5.3 Safe zone of operation

The combination of all the limits observed in the previous subsections provide a zone of operation where IH can operate efficiently and safely. Fig. 2.18 shows the zone of operation in green and a yellow zone where the emission limit is exceeded but it is posible to improve the design.

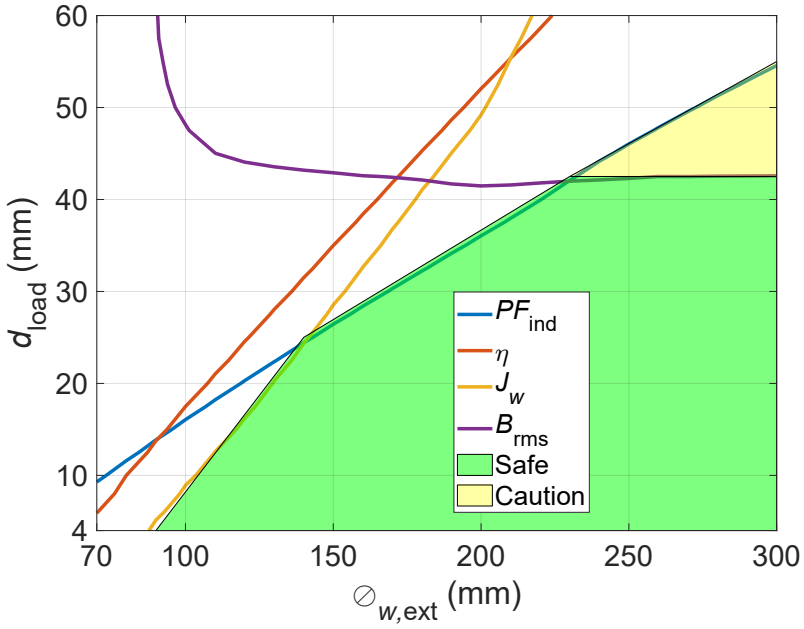

Figure 2.18: Operation limits for sweeping values of $\varnothing_{w,\text{ext}}$ and d_{load}.

2.6 Ferrite volume analysis

It is important to remember that all previous results, including Fig. 2.18 have been obtained with a 2D geometry. However, in real applications the ferrite is not a continuous medium, and there are air gaps between bars. Therefore, a relevant aspect of IH geometry is the ferrite coverage of the inductor. After particular $\varnothing_{w,\text{ext}}$ and d_{load} values are chosen to create a design, it is important to consider the volume of ferrite that will be used.

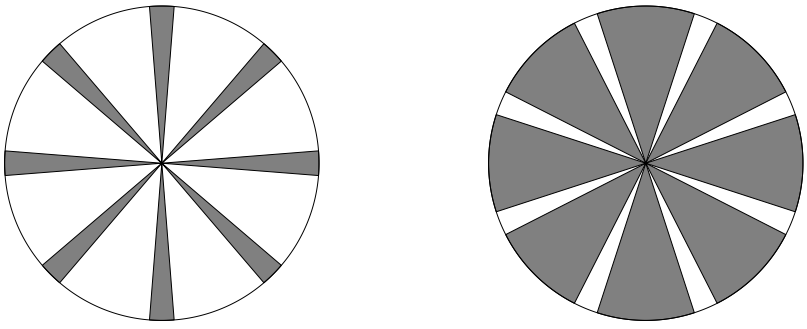

(a) (b)

Figure 2.19: Ferrite coverage, c_{fer}, examples of (a) 20 % and (b) 80 %.

A simulation of different ferrite coverage, c_{fer} has been carried out. Eight circle sectors of varying angle are used as the ferrite geometry. Fig. 2.19 represents the cases of 20 % and 80 % as examples. Moreover, different ferrite to shielding distances, d_{sh}, have also been simulated to determine its effects in the relevant parameters.

For a geometry with $\varnothing_{w,\mathrm{ext}} = 210\,\mathrm{mm}$ and $d_{\mathrm{load}} = 34\,\mathrm{mm}$, c_{fer} is swept from 10 % to 100 % and d_{sh} is swept from 200 µm to 25 mm. The same parameters from the previous section are represented for this simulation.

2.6.1 Impact on the relevant parameters

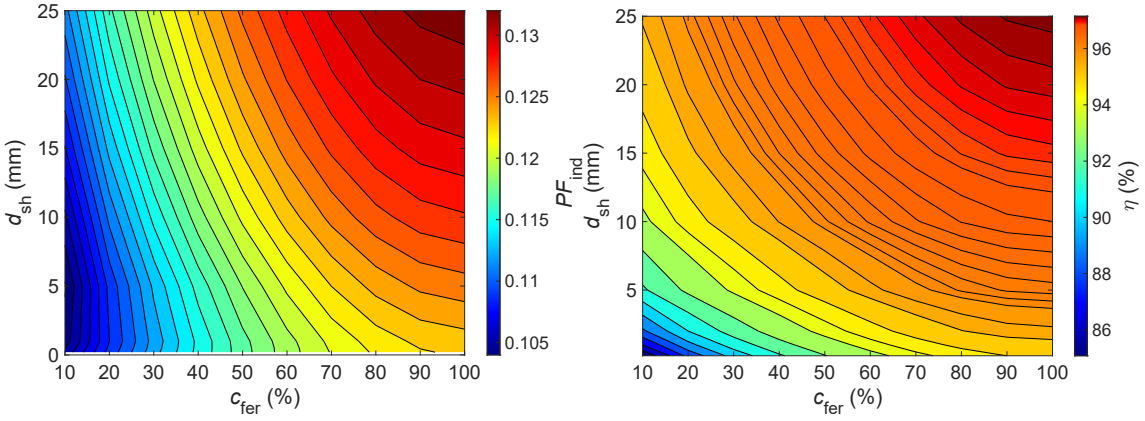

(a) (b)

Figure 2.20: Simulated (a) PF_{ind} and (b) η for sweeping values of c_{fer} and d_{sh}.

Fig. 2.20 (a) shows the simulated PF_{ind} values for sweeping values of c_{fer} and d_{sh}. As c_{fer} increases, so does PF_{ind}. Similarly, PF_{ind} increases slowly with d_{sh}, which means that R_{ind} decreases slower than L_{ind}. In this case, the difference between the upper and lower values is small.

Fig. 2.20 (b) shows the simulated η values for sweeping values of c_{fer} and d_{sh}. The efficiency increases with both c_{fer} and d_{sh}.

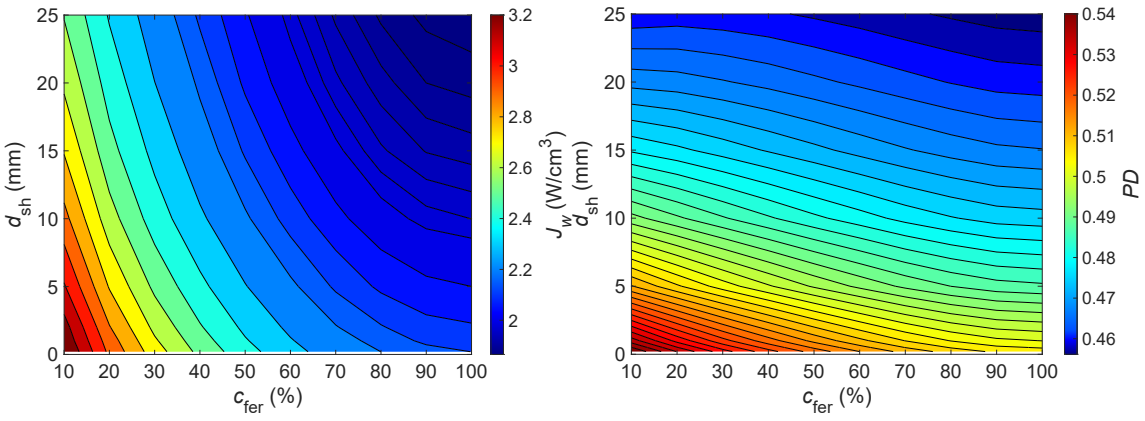

(a) (b)

Figure 2.21: Simulated (a) J_w and (b) PD for sweeping values of c_{fer} and d_{sh}.

Fig. 2.21 (a) shows the simulated J_w values for sweeping values of c_{fer} and d_{sh}

at $P = 3000\,\mathrm{W}$. As c_{fer} increases, J_w decreases, and as d_{sh} increases, J_w decreases more slowly.

Fig. 2.21 (b) shows the simulated PD values for sweeping values of c_{fer} and d_{sh}. PD decreases slowly as c_{fer} increases and it decreases faster with increasing d_{sh}. The difference between the upper and lower limits are small.

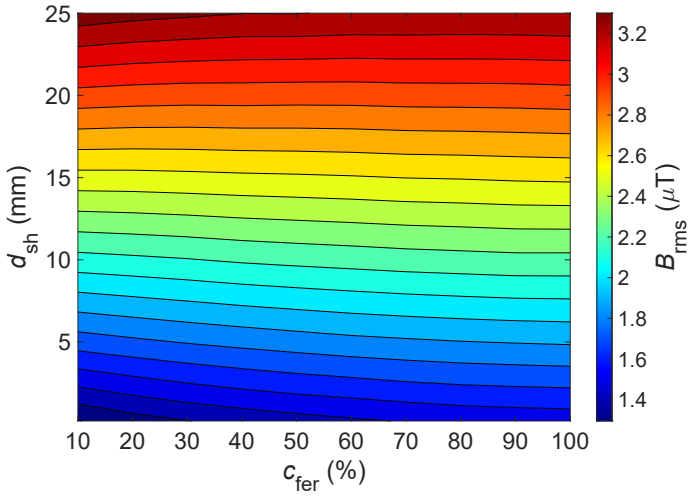

Figure 2.22: Simulated B_{rms} for sweeping values of c_{fer} and d_{sh}.

Fig. 2.22 shows the simulated B_{rms} values for sweeping values of c_{fer} and d_{sh}. B_{rms} increases rapidly with d_{sh} increases. B_{rms} barely changes with c_{fer} increments.

2.6.2 Pareto representation

From these figures, it can be seen that c_{fer} and d_{sh} mostly affect η, and by extension J_w, as well as B_{rms}. Therefore, in order to select the most appropriate geometry, the design should focus on efficiency and emitted field.

Fig. 2.23 is a Pareto representation of the simulated B_{rms} and η. The color of the circles represents the different d_{sh} and the tone of the grey lines represent the c_{fer} values. The objective is to minimize both J_w and B_{rms} and the Pareto front is formed by the $200\,\mu\mathrm{m}$ d_{sh} line and the $100\,\%$ c_{fer} line. The most Pareto-efficient point has $d_{\mathrm{sh}} = 200\,\mu\mathrm{m}$ and $c_{\mathrm{fer}} = 100\,\%$, as can be expected.

2.7 Prototypes and experimental measurements

2.7.1 Prototype description

Several inductor have been designed to prototype and operate within the safe zone of operation. Two of them have $\varnothing_{w,\mathrm{ext}} = 180\,\mathrm{mm}$ with different c_{fer} to operate

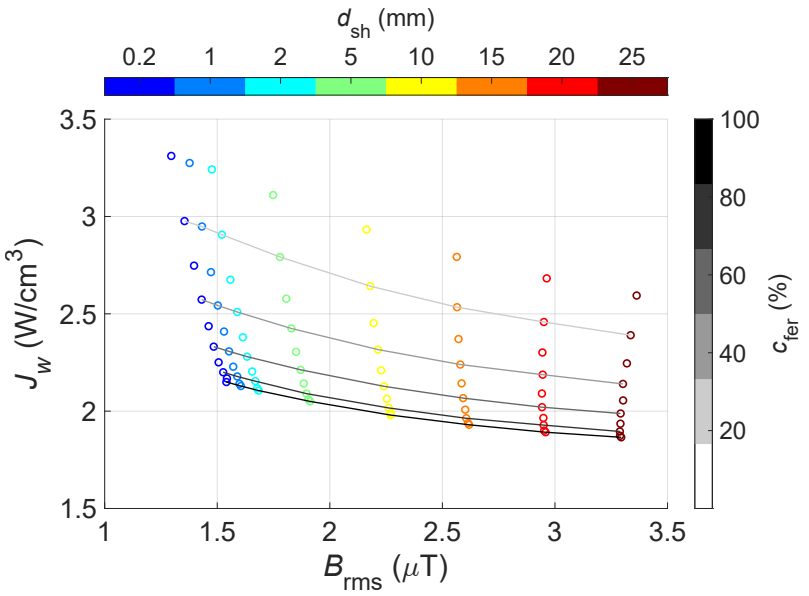

Figure 2.23: Pareto representation of simulated J_w and B_{rms} for sweeping values of c_{fer} and d_{sh} at $P = 3000\,\text{W}$.

at $d_{\text{load}} = 20\,\text{mm}$ and deliver 3100 W. Another has $\varnothing_{w,\text{ext}} = 210\,\text{mm}$ with almost $c_{\text{fer}} = 100\,\%$ to operate at $d_{\text{load}} = 34\,\text{mm}$ and deliver 3700 W.

One inductor of $\varnothing_{w,\text{ext}} = 180\,\text{mm}$ inductor has five 71 mm long, 23.5 mm wide ferrite bars, resulting in $c_{\text{fer}} = 32.47\,\%$. The other $\varnothing_{w,\text{ext}} = 180\,\text{mm}$ inductor has seven bevelled 74.2 mm long, 29.5 mm wide ferrite bars, resulting in $c_{\text{fer}} = 57.78\,\%$.

In order to maximize efficiency, copper litz cable is used with $r_s = 100\,\mu\text{m}$ and the maximum number of total strands, $(n_t n_s)_{\text{max}}$. For the 180 mm $\varnothing$ inductors, $(n_t n_s)_{\text{max}} = 3400$. In order to maximize efficiency for a limited $(n_t n_s)_{\text{max}}$, $(n_t n_s)_{\text{opt}}$ has to be as close as possible. As frequency increases, $(n_t n_s)_{\text{opt}}$ decreases, and near 60 kHz both values match. As very high frequencies are detrimental to the switching devices, a compromise $f_{\text{res}} = 40\,\text{kHz}$ is chosen to minimize electronics stress, resulting in $n_t = 19$ and therefore maximum n_s is around 180. For the 210 mm $\varnothing$ inductor, $(n_t n_s)_{\text{max}} = 4200$, and η is less of a concern. Therefore, a value of $n_t = 29$ achieves $f_{\text{res}} = 20\,\text{kHz}$ and limits n_s at around 144.

Fig. 2.24 shows the inductor prototypes of $\varnothing_{w,\text{ext}} = 180\,\text{mm}$ with 5 and 7 ferrite bars respectively, and the 210 mm $\varnothing$ prototype without its ferrite plane.

The circuit diagram, including inverter, inductors and loads is shown in Fig. 2.25. The main differences with Fig. 2.3 are the voltage input to the system, the bus and snubber capacitors, and the bifurcation of C. The mains voltage is rectified in a full diode bridge, it is filtered by 3.3 µF capacitor and it is inverted

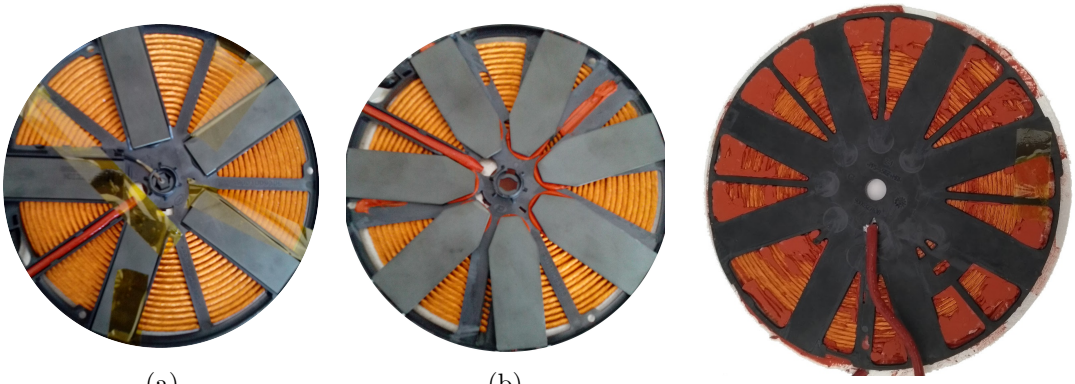

(a) (b) (c)

Figure 2.24: Inductor prototypes captured from below: (a) 180 mm ⌀, 5 ferrites, $c_{\text{fer}} = 32.47\,\%$, (b) 180 mm ⌀, 7 ferrites, $c_{\text{fer}} = 57.78\,\%$, (c) 210 mm ⌀, $c_{\text{fer}} = 100\,\%$.

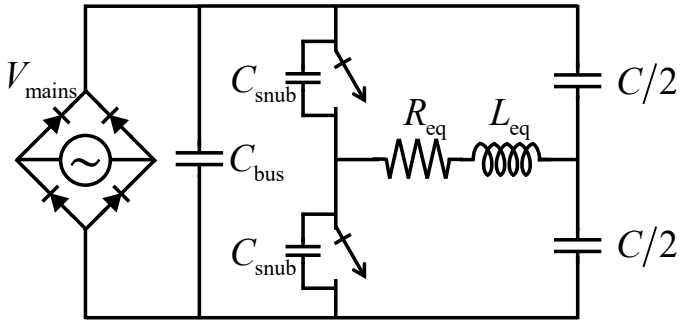

Figure 2.25: IH prototype circuit diagram.

by a IGBT half-bridge inverter. The transistors use 15 nF snubber capacitors to minimize turn-off losses. The C capacitor is split to ensure zero DC voltage and eliminate all even harmonics. The inverter uses frequency control to deliver power.

2.7.2 Measurements

The inductors have been measured in the low signal regime to validate the impedance simulations. The frequency sweeps have been carried out with a Keysight E4980AL LCR meter, whose low signal regime operates at a lower work point in the $B - H$ curve of materials. Afterward, measurements in the full power regime are used to validate P, I, PF_{ind} and B_{rms} simulations.

2.7.2.1 Low signal regime

The five ferrite 180 mm ⌀ inductor and the 210 mm ⌀ inductor are measured without load. Fig. 2.26 shows the measured R and L compared to the simulations. The resistance increase with frequency is due to the conduction and proximity AC effects,

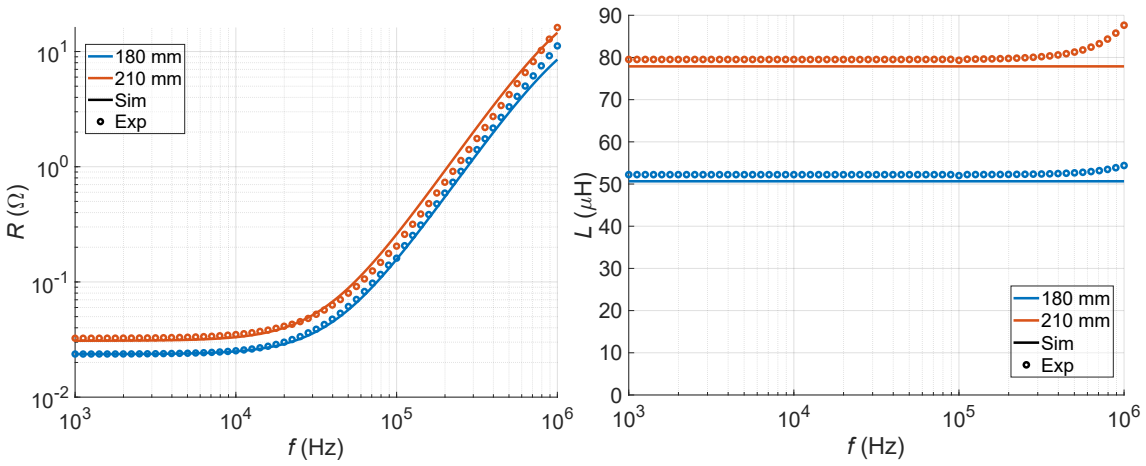

(a) (b)

Figure 2.26: LCR measurements of the 5 ferrite $\varnothing_{w,\text{ext}} = 180\,\text{mm}$ inductor and the $\varnothing_{w,\text{ext}} = 210\,\text{mm}$ inductor: (a) R, (b) L.

considered in the model, whereas the inductance increase at high frequencies is due to parasitic capacitance effects not considered in the model. The measurements and simulations are in very good agreement, verifying the simulation geometry and the copper losses calculations.

2.7.2.2 Full power regime

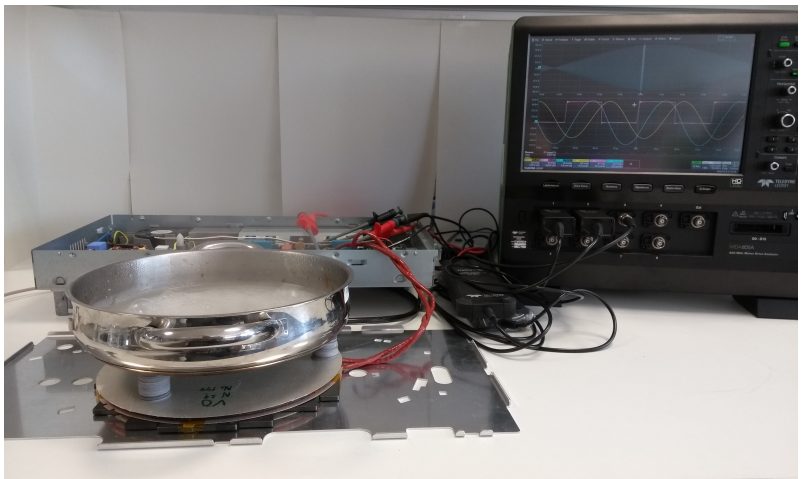

Figure 2.27: Full power experimental setup with the 210 mm ∅ inductor.

All three inductors have been tested delivering power to ferromagnetic loads of $\mu = 400 - 175j$, $\sigma = 2 \times 10^6\,\text{S/m}$ [143], with $\varnothing_{\text{load}} \approx \varnothing_{w,\text{ext}}$, and $d_{\text{load}} = 20\,\text{mm}$. Fig. 2.27 shows the full power experimental setup with the 210 mm ∅ inductor and the mica pieces to used to separate the inductor and the load.

Fig. 2.28 shows the comparison between the simulated and experimental results

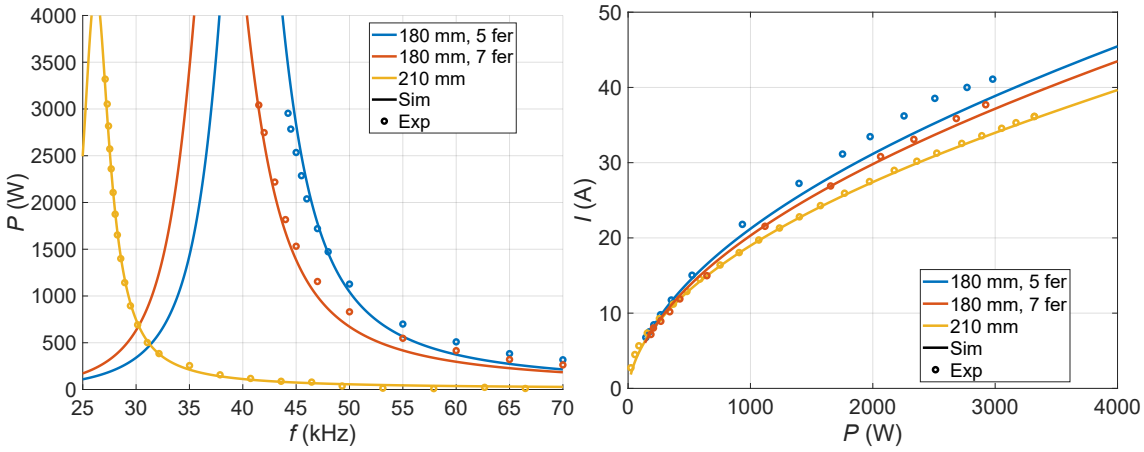

(a) (b)

Figure 2.28: Experimental measurements of all three inductors: (a) P, (b) I.

of P and I of all three inductors. Increasing the distance complicates the frequency control of P due to the PF_{ind} decrease. The simulated values and experimental results match very well, validating the system.

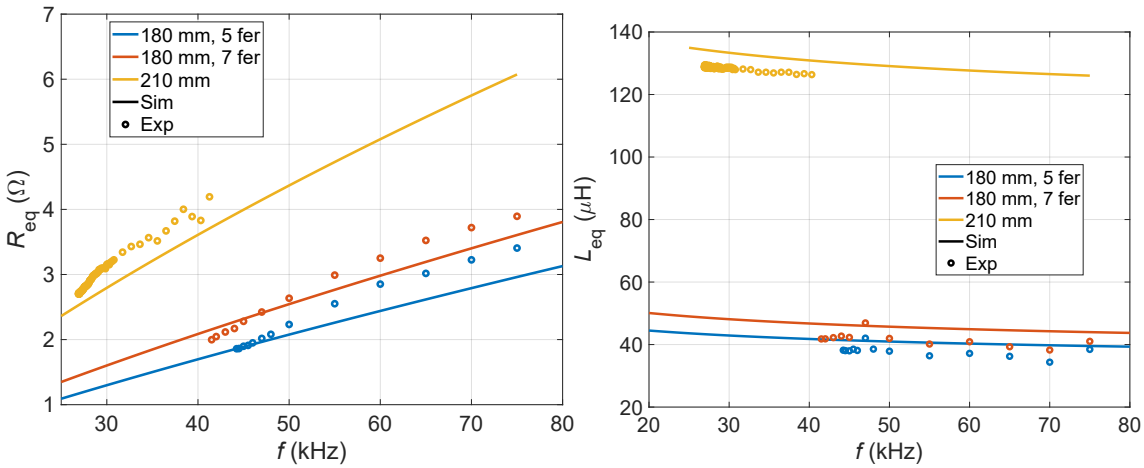

(a) (b)

Figure 2.29: Impedance experimental measurements of all three inductors: (a) R_{eq}, (b) L_{eq}.

Fig. 2.29 shows the impedance measurements, obtained through inductor voltage, V_{ind}, and current, I, oscilloscope measurements and the process defined in Appendix C, and the FEA simulated values. Inductance values generally agree and resistances start losing accuracy as frequency increases.

Fig. 2.30 shows simulated values and experimental measurements of B_{rms} at several distances for the 5 ferrite $\varnothing_{w,\text{ext}} = 180\,\text{mm}$. As distance increases, so does the simulation's accuracy. The measurements at the norm's distance [89] are validated.

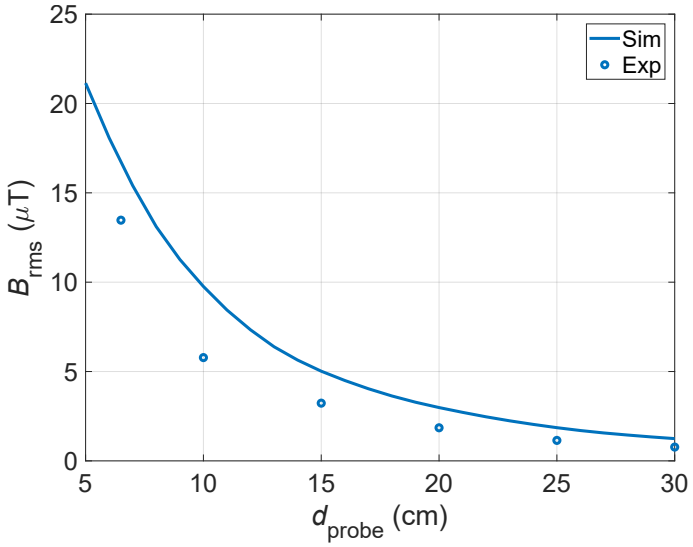

Figure 2.30: B_{rms} measurements at several distances from the 180 mm ∅, 7 ferrite inductor.

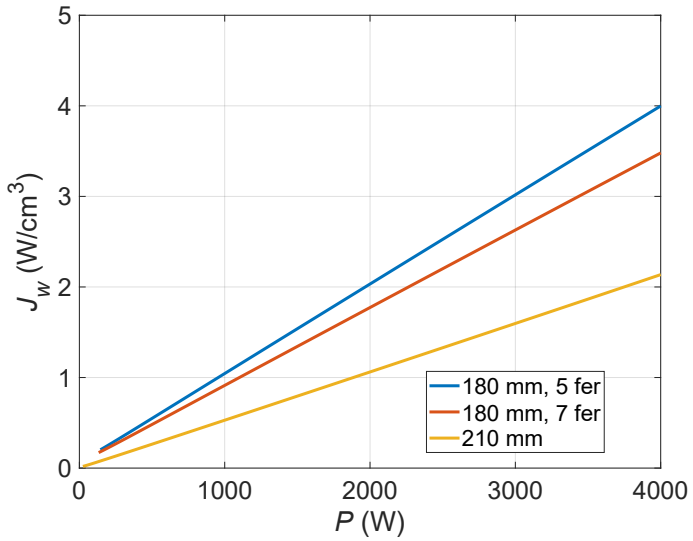

Figure 2.31: Simulated J_w of all three inductors.

Fig. 2.31 represents the simulated J_w for the three inductors, showing that they will not overheat. As expected, the inductors with fewer ferrite volume have more shielding losses, and therefore more volumetric losses.

Appendix D compiles a list of the most relevant experimental results of the dissertation.

2.8 Conclusion

Induction heating (IH) systems can be stretched to bigger heights than usual, with compromises in efficiency, power factor and emitted magnetic flux. Simulations and experimental results agree, validating the assumptions.

To enable high-distance IH, no expense may be spared. To prevent efficiency loss, inductors must be wound without gaps between turns to maximize the number of strands. The strands themselves have to be of sufficiently small diameter, to minimize conduction and proximity losses. Additionally, ferrite preferably ought to cover the entire area between winding and aluminum shielding to minimize shielding losses and to boost ideal induction impedance. Moreover, the relatively low power factors cause capacitor voltage to increase significantly, so the designer must be vigilant to select the components with the most appropriate rms voltage limit. These guidelines enable windings bigger than 130 mm to reach 20 mm distances and 220 mm windings and above to reach 40 mm.

As the simulations and experimental results show, IH systems can be pushed to their limits and operate at much higher distances than is conventional. However, small inductor diameters and very high distances are not feasible with the current technology. A single inductor is not effective enough in these situations.

WPT systems offer a potential solution: power transfer between inductors. Using a secondary inductor as an energy bridge between the cooktop inductor and the ferromagnetic load can potentially improve power factor, efficiency, power distribution and emitted near field. The next chapter will explore this idea and analyze its implications in detail.

Chapter 3

Inductively Coupled Heating

This chapter develops the inductors-load system of the ICH concept, which is an extension of single inductor systems. A parametric analysis is used to determine the values that produce optimal results in the systems. Electromagnetic simulations are used to determine the feasibility of the optimum design parameters. The design guidelines extracted from the analysis and simulations will be applied to design systems with different inductor configurations. Some of these designs are prototyped and experimentally tested.

Table of contents

3.1 Introduction . . . 93
3.2 Modelling . . . 93
3.2.1 Total impedance and induction impedance . . . 94
3.2.2 Load impedance through Poynting's vector . . . 95
3.2.3 Winding losses . . . 96
3.2.4 Matrix representation . . . 98
3.3 Two-inductor ICH system . . . 99
3.4 Design parameters . . . 101
3.4.1 Geometry . . . 101
3.4.2 Goal parameters . . . 101
3.4.3 Dimensionless design parameters . . . 103
3.5 ICH system design process . . . 104
3.5.1 Resonant frequencies . . . 104
3.5.2 Selection of winding cable . . . 105
3.5.3 Impedance simulations . . . 108
3.6 Same-diameter prototype . . . 111
3.6.1 Low signal regime . . . 111
3.6.1.1 Prototype description . . . 111
3.6.1.2 Measurements . . . 111
3.6.2 Full signal regime . . . 113
3.6.2.1 Design and prototype . . . 113
3.6.2.2 Measurements . . . 114
3.7 Conclusion . . . 115

3.1 Introduction

The previous chapter proves that IH can be used at higher distances and enable IuW. However, the inductor diameters and inductor-load distances are constrained to a fairly small safe zone of operation. High losses and small power factor are the most limiting parameters for small diameters, while emitted magnetic flux can be more restricting at higher diameters. The addition of a passive inductor can act as an energy bridge between the cooktop's primary inductor and the ferromagnetic load. This passive inductor enables impedance tuning, which can improve the power factor, distribute the losses to reduce winding heating and potentially reducing emitted field. Essentially, the relevant parameters outside the IH safe zone can be improved in a new ICH safe zone.

(a) (b)

Figure 3.1: IuW implementations with (a) single inductor, (b) ICH.

The new configuration uses a coupled inductor in conjunction with the primary inductor for the original purpose of induction heating. The name inductively coupled heating (ICH) aims to encapsulate the new configuration and the same goal in a short abbreviation. Fig. 3.1 shows a possible implementation of ICH under worktop where the passive inductor is attached to the load in comparison with single inductor IuW.

3.2 Modelling

The addition of multiple inductors does not change the fundamental physics, nor does it invalidate previous assumptions and simplifications. First order harmonic, ideal coil model, symmetry and IBC replacing dissipative media still apply as described in the previous chapter. With multiple inductors, electromagnetic field linearity is applied to the simulations with multiple magnetic field sources.

Total magnetic field, $\mathbf{H}$, magnetic flux, $\mathbf{B}$ and electric field $\mathbf{E}$ are simply the sum of the fields generated by each inductor. For a general n number of inductors:

$$\mathbf{H} = \sum_{i=1}^{n} \mathbf{H}_i, \tag{3.1}$$

where the subscript i denotes the field generated by the ith inductor. Moreover, as the field generated by each inductor is also linearly dependent with number of turns, n_t and current, I, total field can be expressed as:

$$\mathbf{E} = \sum_{i=1}^{n} n_{t,i} I_i \mathbf{E}_{i,\text{p.t.,p.A.}}. \tag{3.2}$$

Therefore, to fully characterize a system with n_t inductors, n_t simulations need to be carried out where each single-turn inductor is fed unitary current and generates its own magnetic field.

3.2.1 Total impedance and induction impedance

With multiple inductors, instead of a single impedance element, there are n_t by n_t matrices with ij subscripts, where the ith inductor generates the field, and the impedance is measured in the jth inductor. Similar to single-inductor systems, the following relations are established:

$$L_{ij} = L_{\text{ind},ij}, \tag{3.3}$$

$$R_{ij} = R_{\text{ind},ij} + R_{w,ij}, \tag{3.4}$$

$$R_{\text{ind},ij} = R_{\text{load},ij} + R_{\text{sh},ij}, \tag{3.5}$$

$$R_{w,ij} = R_{\text{cond},ij} + R_{\text{prox},ij}. \tag{3.6}$$

The relation between the per-turn impedance and total impedance for induction impedance are:

$$\frac{L_{\text{ind},ij}}{L_{\text{ind},ij,\text{p.t.}}} = \frac{R_{\text{load},ij}}{R_{\text{load},ij,\text{p.t.}}} = \frac{R_{\text{sh},ij}}{R_{\text{sh},ij,\text{p.t.}}} = n_{t_i} n_{t_j}. \tag{3.7}$$

With multiple inductors, the field generated by the current of the ith winding, I_i, induces voltages in each of the inductors, $V_{\text{ind},ij}$:

$$V_{\text{ind},ij} = -\oint E_{i,\phi} dl_j, \forall i, j \subset \{1, 2, ..., n\}, \tag{3.8}$$

where dl_j is the longitudinal differential of inductor j, where $V_{\text{ind},ij}$ is induced. Self and mutual impedance are defined by the division of $V_{\text{ind},ij}$ with respect to I_i:

$$Z_{\text{ind},ij} = \frac{V_{\text{ind},ij}}{I_i}, \forall i, j \subset \{1, 2, ..., n\}. \tag{3.9}$$

Self and mutual induction impedances are complex, and therefore they have resistive and inductive components:

$$Z_{\text{ind},ij} = R_{\text{ind},ij} + j\omega L_{\text{ind},ij}. \tag{3.10}$$

For simple geometries, the reciprocity theorem can be proven analytically, meaning that $R_{\text{ind},ij} = R_{\text{ind},ji}$ and $L_{\text{ind},ij} = L_{\text{ind},ji}$ [150, 151].

3.2.2 Load impedance through Poynting's vector

Resistances $R_{\text{load},ij}$ and $R_{\text{sh},ij}$ are still obtained from Poynting's vector, but the expressions becomes more complicated. Field linearity (3.1) applied to Poynting's vector definition results in:

$$\mathbf{S} = \left(\sum_{i=1}^{n} \mathbf{E}_i\right) \times \left(\sum_{j=1}^{n} \mathbf{H}_j^*\right), \tag{3.11}$$

which can be expanded to:

$$\mathbf{S} = \sum_{i=1}^{n}\sum_{j=1}^{n} \mathbf{E}_i \mathbf{H}_j^* = \sum_{i=1}^{n}\sum_{j=1}^{n} \mathbf{S}_{ij}, \tag{3.12}$$

where $\mathbf{S}_{ij}$ is the mutual power density generated by inductors i and j, associated with the load resistance, $R_{\text{load},ij}$, by:

$$R_{\text{load},ij} = \frac{\Re\left(\int_{S_{\text{load}}} \mathbf{S}_{ij}\hat{\mathbf{n}} dS_{\text{load}}\right)}{I_i I_j^*}, \tag{3.13}$$

where $\Re$ denotes the real component of a complex number and $\mathbf{S}_{ij}\hat{\mathbf{n}}$ corresponds to the normal component of $\mathbf{S}_{ij}$ on the surface S_{load}, and it is usually shortened to S_{ij}. The calculation of shielding resistance, $R_{\text{sh},ij}$, is analogous.

The symmetry of resistances calculated from Poynting's vector, that is, the relation $R_{\text{load},ij} = R_{\text{load},ji}$ and $R_{\text{sh},ij} = R_{\text{sh},ji}$ can be demonstrated in surfaces where the impedance boundary condition (IBC) is fulfilled. In IBC surfaces, $\mathbf{H}$ can be obtained from $\mathbf{E}$ using this expression [143]:

$$\sqrt{j\omega\frac{\mu}{\sigma}}\hat{\mathbf{n}} \times \mathbf{H} = \hat{\mathbf{n}} \times (\hat{\mathbf{n}} \times \mathbf{E}). \tag{3.14}$$

Applying (3.14) to S_{ij}:

$$S_{ij} = \sqrt{j\frac{\sigma}{\omega\mu^*}}\,(\hat{\mathbf{n}} \times \mathbf{E}_i) \cdot \left(\hat{\mathbf{n}} \times \mathbf{E}_j^*\right). \tag{3.15}$$

For any $\hat{\mathbf{n}}$ belonging to an orthonormal coordinate system of basis $\{\hat{\mathbf{e}}_1, \hat{\mathbf{e}}_2, \hat{\mathbf{e}}_3\}$:

$$\hat{\mathbf{n}}\times\mathbf{E}_i = \begin{vmatrix} \hat{\mathbf{e}}_1 & \hat{\mathbf{e}}_2 & \hat{\mathbf{e}}_3 \\ n_1 & n_2 & n_3 \\ E_{i1} & E_{i2} & E_{i3} \end{vmatrix} = (n_2E_{i3} - n_3E_{i2})\,\hat{\mathbf{e}}_1 + (n_3E_{i1} - n_1E_{i3})\,\hat{\mathbf{e}}_2 + (n_1E_{i2} - n_2E_{i1})\,\hat{\mathbf{e}}_3, \tag{3.16}$$

$$\begin{aligned}(\hat{\mathbf{n}} \times \mathbf{E}_i)\cdot\left(\hat{\mathbf{n}} \times \mathbf{E}_j^*\right) = {} & n_2^2(E_{i3}E_{j3}^* + E_{i1}E_{j1}^*) - n_2n_3(E_{i3}E_{j2}^* + E_{i2}E_{j3}^*) + n_3^2(E_{i2}E_{j2}^* + E_{i1}E_{j1}^*) - \\ & - n_1n_3(E_{i1}E_{j3}^* + E_{i3}E_{j1}^*) + n_1^2(E_{i3}E_{j3}^* + E_{i2}E_{j2}^*) - n_1n_2(E_{i2}E_{j1}^* + E_{i1}E_{j2}^*).\end{aligned} \tag{3.17}$$

Despite the long equation, its terms can be classified into two kinds of expressions according to the product of the inductors' number of turns. Using $k \subset \{1, 2, 3\}$, with $3 + 1$ oveflowing to 1:

$$n_k^2\left(E_{ik+1}E_{jk+1}^* + E_{ik+2}E_{jk+2}^*\right) = n_k^2\left(E_{jk+1}E_{ik+1}^* + E_{jk+2}E_{ik+2}^*\right)^*, \tag{3.18}$$

$$n_kn_{k+1}\left(E_{ik}E_{jk+1}^* + E_{ik+1}E_{jk}^*\right) = n_kn_{k+1}\left(E_{jk}E_{ik+1}^* + E_{jk+1}E_{ik}^*\right)^*. \tag{3.19}$$

Therefore, S_{ij} is by definition hermitian or self-adjoint:

$$(\hat{\mathbf{n}} \times \mathbf{E}_i) \cdot \left(\hat{\mathbf{n}} \times \mathbf{E}_j^*\right) = \left((\hat{\mathbf{n}} \times \mathbf{E}_j) \cdot (\hat{\mathbf{n}} \times \mathbf{E}_i^*)\right)^*, \tag{3.20}$$

and consequently:

$$S_{ij} = S_{ji}^*. \tag{3.21}$$

Although $S_{ij} \neq S_{ji}$, overall S is the sum of all elements (3.12). Considering that $S_{ij} + S_{ji} = 2\Re(S_{ij})$, the imaginary part disappears, and consequently $R_{\text{load},ij} = R_{\text{load},ji}$, $R_{\text{sh},ij} = R_{\text{sh},ji}$.

3.2.3 Winding losses

Multiple inductors do not affect the conduction losses of each winding, but they do increase the proximity effects components due to the field generation and losses dissipation location.

Conduction losses only affect the current-carrying winding, therefore:

$$R_{\text{cond},ij} = 0 \;\forall\; i \neq j. \tag{3.22}$$

Moreover, the relation between per-turn, per-strand conduction resistance, $R_{\text{cond},ii,\text{p.t.},\text{p.s.}}$, and $R_{\text{cond},ii}$ is still:

$$R_{\text{cond},ii} = \frac{n_{t,i}}{n_{s,i}} R_{\text{cond},ii,\text{p.t.},\text{p.s.}}, \tag{3.23}$$

where the per-turn, per-strand subscript can be shortened to s for convenience:

$$R_{\text{cond},ii,\text{p.t.},\text{p.s.}} = R_{\text{cond},ii,s} \tag{3.24}$$

Proximity losses with multiple windings involve more dimensions [152]. Specifically, they involve the product of the full field with its conjugate and the winding they affect, resulting in three dimensions. With respect to the **H** field, proximity losses are calculated from the square of the absolute norm:

$$\mathbf{H} = \sum_{i=1}^{n} \mathbf{H}_i, \tag{3.25}$$

$$|\mathbf{H}|^2 = \left(\sum_{i=1}^{n} \mathbf{H}_i\right) \cdot \left(\sum_{j=1}^{n} \mathbf{H}_j^*\right). \tag{3.26}$$

Similarly to the previous subsection, $|H_{ij}|^2$ can be defined as:

$$|H_{ij}|^2 = \mathbf{H}_i \mathbf{H}_j^* = (\mathbf{H}_j \mathbf{H}_i^*)^* = \left(|H_{ji}|^2\right)^*. \tag{3.27}$$

It is proven that $|H_{ij}|^2$ is also hermitian. Each inductor, with the k subscript, is affected by the $|H_{ij}|^2$ field, producing proximity losses according to (2.16) and (2.18), due to the perpendicular field, $R_{\text{prox},ijk}$:

$$R_{\text{prox},ijk,s} = \frac{4\pi}{\sigma} \Phi_{\text{prox}} \int_{V_k} \frac{\left|\bar{\mathbf{H}}_{ij}\right|^2}{S_{w,k}} dV_k, \tag{3.28}$$

$$R_{\text{prox},ijk} = n_{t,i} n_{t,j} n_{t,k} n_{s,k} R_{\text{prox},ijk,s}, \tag{3.29}$$

where $R_{\text{prox},ijk,s}$, is the per-turn, per-strand proximity resistance of element ijk. The self-adjoint nature of $\mathbf{H}_{ij,\text{p.t.},\text{p.A.}}$ produces symmetry along the $i = j$ plane, that is: $R_{\text{prox},ijk} = R_{\text{prox},jik}$.

Curiously, despite affecting each k inductor, the resistance is measured in inductors i, j as self-resistance if $i = j$ and mutual resistance if $i \neq j$ due to the fact that proximity losses are induction losses. Total proximity resistance measured in each ij element is defined as:

$$R_{\text{prox},ij} = \sum_{k=1}^{n} R_{\text{prox},ijk}. \tag{3.30}$$

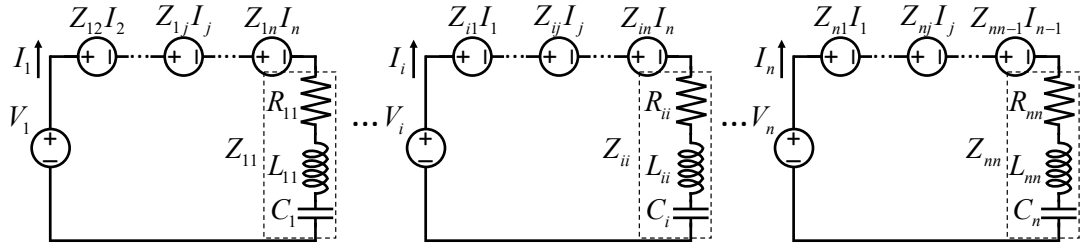

Figure 3.2: Circuit of multiple coupled inductors fed individually.

3.2.4 Matrix representation

Total self and mutual impedance elements, including compensation capacitors, C_i, can be defined as:

$$Z_{ij} = \begin{cases} R_{ij} + j\omega L_{ij} + \dfrac{1}{j\omega C_i}, \ \forall\, i = j \\ R_{ij} + j\omega L_{ij}, \ \forall\, i \neq j \end{cases} . \tag{3.31}$$

The subscripts i and j range from 1 to the number of inductors, n. All Z_{ij} elements can be represented in a bidimensional matrix:

$$\mathbf{Z} = \begin{pmatrix} Z_{11} & Z_{12} & \cdots & Z_{1j} & \cdots & Z_{1n} \\ Z_{21} & Z_{22} & \cdots & Z_{2j} & \cdots & Z_{2n} \\ \vdots & \vdots & \ddots & \vdots & & \vdots \\ Z_{i1} & Z_{i2} & \cdots & Z_{ij} & \cdots & Z_{in} \\ \vdots & \vdots & & \vdots & \ddots & \vdots \\ Z_{n1} & Z_{n2} & \cdots & Z_{nj} & \cdots & Z_{nn} \end{pmatrix}, \tag{3.32}$$

where $\mathbf{Z}$ is symmetric meaning that $Z_{ij} = Z_{ji}$. In a system where each inductor has an independent supply voltage, V_i, and they are not interconnected, the circuit is represented in Fig. 3.2, and its system of equations to solve for inductor current, I_i, can be expressed in matrix form:

$$\mathbf{V} = \begin{pmatrix} V_1 & V_2 & \cdots & V_i & \cdots & V_n \end{pmatrix}^{\mathrm{T}}, \tag{3.33}$$

$$\mathbf{I} = \begin{pmatrix} I_1 & I_2 & \cdots & I_i & \cdots & I_n \end{pmatrix}^{\mathrm{T}}, \tag{3.34}$$

$$\mathbf{ZI} = \mathbf{V}, \tag{3.35}$$

$$\mathbf{I} = \mathbf{Z}^{-1}\mathbf{V}. \tag{3.36}$$

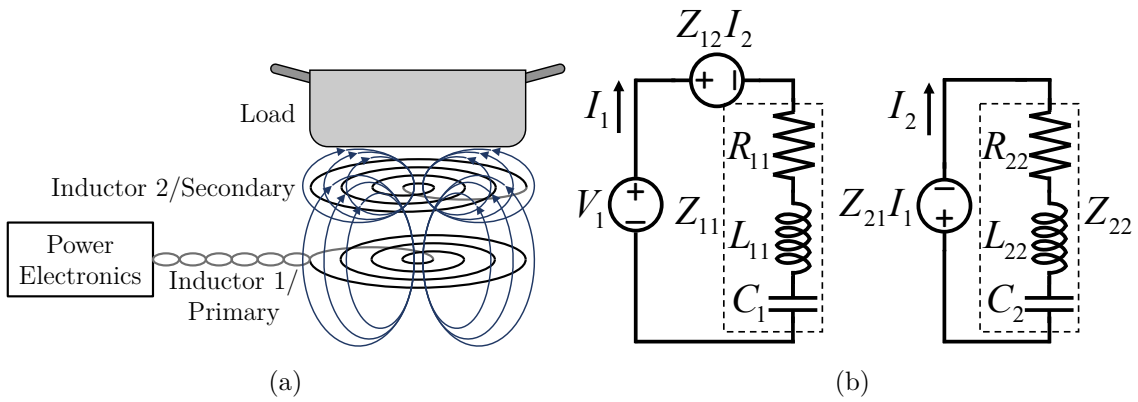

Figure 3.3: Two-inductor ICH: (a) schematic representation, (b) circuit with passive secondary.

3.3 Two-inductor ICH system

ICH uses an externally-fed primary inductor and a passive secondary inductor. The resulting system is represented in Fig. 3.3 (a), and its circuit is represented in Fig. 3.3 (b). The system of equations of (3.35) becomes:

$$\begin{pmatrix} Z_{11} & Z_{12} \\ Z_{21} & Z_{22} \end{pmatrix} \begin{pmatrix} I_1 \\ I_2 \end{pmatrix} = \begin{pmatrix} V_1 \\ 0 \end{pmatrix}, \tag{3.37}$$

where $V_2 = 0$ since the secondary inductor is not fed externally. The equivalent impedance of the full system from the point of view of the inverter, Z_{eq}, can be defined as:

$$Z_{\text{eq}} = \frac{V_1}{I_1} = Z_{11} - \frac{Z_{12}^2}{Z_{22}}, \tag{3.38}$$

where the $Z_{12} = Z_{21}$ relation is applied. Z_{eq} can be divided into resistive and inductive components, as well as the primary resonant capacitor:

$$Z_{\text{eq}} = R_{\text{eq}} + j\omega L_{\text{eq}} + \frac{1}{j\omega C_1}, \tag{3.39}$$

where:

$$R_{\text{eq}} = R_{11} + \frac{2R_{12}\omega L_{12}\left(\omega L_{22} - \dfrac{1}{\omega C_2}\right) - \left(R_{12}^2 - \omega^2 L_{12}^2\right) R_{22}}{R_{22}^2 + \left(\omega L_{22} - \dfrac{1}{\omega C_2}\right)^2}, \tag{3.40}$$

$$L_{\text{eq}} = L_{11} + \frac{2R_{12}\omega L_{12}R_{22} - \left(R_{12}^2 - \omega^2 L_{12}^2\right)\left(\omega L_{22} - \dfrac{1}{\omega C_2}\right)}{\omega\left(R_{22}^2 + \left(\omega L_{22} - \dfrac{1}{\omega C_2}\right)^2\right)}. \tag{3.41}$$

R_{eq} and L_{eq} in ICH systems are extremely dependant on ω, C_2 and Z_{12}. In conventional IH systems, R and L are frequency dependent to a lesser degree, as are R_{ij} and L_{ij}.

Despite the sizeable number of elements, the relation with per-turn impedance can be put in simple terms considering (3.7), with a small sleight of hand and ignoring losses:

$$R_{\text{eq}} = n_{t,1}^2 R_{\text{eq,p.t.}}, \tag{3.42}$$

$$L_{\text{eq}} = n_{t,1}^2 L_{\text{eq,p.t.}}, \tag{3.43}$$

$$R_{\text{eq,p.t.}} = R_{11,\text{p.t.}} + \frac{2R_{12,\text{p.t.}}\omega L_{12,\text{p.t.}}\left(\omega L_{22,\text{p.t.}} - \frac{1}{\omega C_{2,\text{p.t.}}}\right) - \left(R_{12,\text{p.t.}}^2 - \omega^2 L_{12,\text{p.t.}}^2\right) R_{22,\text{p.t.}}}{R_{22,\text{p.t.}}^2 + \left(\omega L_{22,\text{p.t.}} - \frac{1}{\omega C_{2,\text{p.t.}}}\right)^2}, \tag{3.44}$$

$$L_{\text{eq,p.t.}} = L_{11,\text{p.t.}} + \frac{2R_{12,\text{p.t.}}\omega L_{12,\text{p.t.}} R_{22,\text{p.t.}} - \left(R_{12,\text{p.t.}}^2 - \omega^2 L_{12,\text{p.t.}}^2\right)\left(\omega L_{22,\text{p.t.}} - \frac{1}{\omega C_{2,\text{p.t.}}}\right)}{\omega\left(R_{22,\text{p.t.}}^2 + \left(\omega L_{22,\text{p.t.}} - \frac{1}{\omega C_{2,\text{p.t.}}}\right)^2\right)}, \tag{3.45}$$

$$Z_{\text{eq,p.t.}} = R_{\text{eq,p.t.}} + j\omega L_{\text{eq,p.t.}} + \frac{1}{j\omega C_{1,\text{p.t.}}}, \tag{3.46}$$

where $C_{1,\text{p.t.}}$ and $C_{2,\text{p.t.}}$ are mathematical *per-turn* capacitors that enable the relation:

$$X_{ii} = n_{t,i}^2\left(\omega L_{ii,\text{p.t.}} - \frac{1}{\omega C_{i,\text{p.t.}}}\right) = n_{t,i}^2 X_{ii,\text{p.t.}}, \tag{3.47}$$

where X_{ii} is the reactance of Z_{ii} and $X_{ii,\text{p.t.}}$ the single-turn reactance.

As observed in (3.42) and (3.43), total equivalent impedance only depends on $n_{t,1}$, whereas $n_{t,2}$, the number of turns of the passive inductor, is not relevant. This does not mean, however, that n_2 is meaningless, as it is a determining factor for I_2 and inductor/capacitor voltage, $V_{\text{ind},2} = -V_{C,2}$. Therefore, according to (3.37) and (3.7):

$$I_2 = -\frac{n_{t,1}}{n_{t,2}}\frac{Z_{12,\text{p.t.}}}{Z_{22,\text{p.t.}}} I_1, \tag{3.48}$$

$$V_{C,2} = \frac{I_2}{j\omega C_2} = j n_{t,1} n_{t,2} \frac{Z_{12,\text{p.t.}}}{\omega C_{2,\text{p.t.}} Z_{22,\text{p.t.}}} I_1. \tag{3.49}$$

Therefore, for a fixed value of $n_{t,1}$, I_2 is inversely proportional to $n_{t,2}$ and $V_{\text{ind},2}$, $V_{C,2}$ are proportional to $n_{t,2}$.

The presence of multiple resonant tanks causes multiple resonant frequencies to

exist:

$$\omega_{0,1} = \frac{1}{\sqrt{L_{11}C_1}}, \tag{3.50}$$

$$\omega_{0,2} = \frac{1}{\sqrt{L_{22}C_2}}, \tag{3.51}$$

$$\omega_{0,\mathrm{eq}} = \frac{1}{\sqrt{L_{\mathrm{eq}}C_1}}, \tag{3.52}$$

where $\omega_{0,1}$, $\omega_{0,2}$ and $\omega_{0,\mathrm{eq}}$ are the angular resonant frequencies for the primary inductor, secondary inductor and full equivalent system respectively.

3.4 Design parameters

3.4.1 Geometry

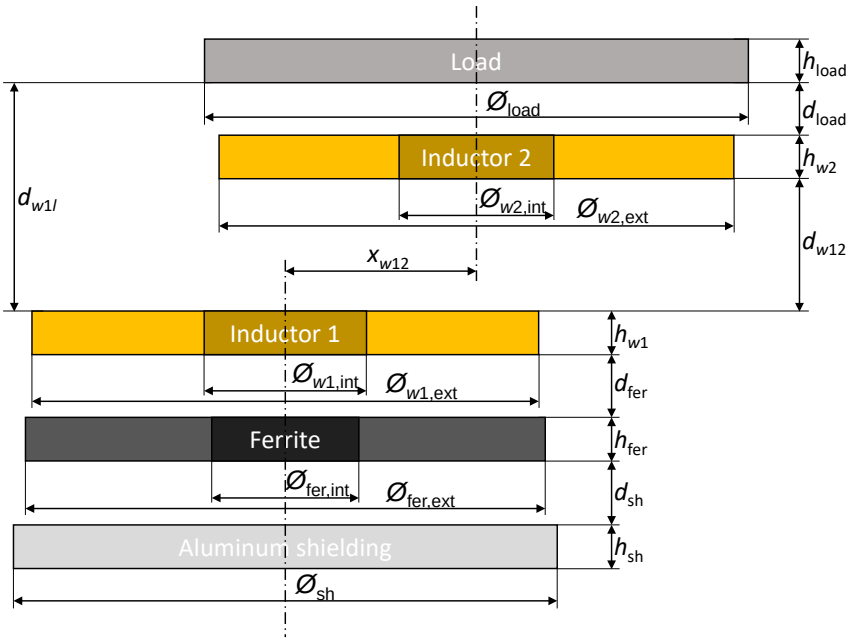

Figure 3.4: ICH geometry diagram.

ICH geometry elements and their parameters are inherited from IH geometry, with distinctions between inductors and the distances between them, represented in Fig. 3.4. The figure shows the general grouping of elements. The primary inductor, ferrite bars and aluminum shielding are concentric, and they may be horizontally offset from the secondary inductor and load, which are also concentric.

3.4.2 Goal parameters

The same parameters defined in the previous chapter can be used to determine system suitability in ICH. Their definitions change slightly to adapt to multiple

inductors.

Delivered power, P and power factor, PF, use global equivalent resistance, R_{eq}, and inductance, L_{eq}, in their multiple-inductor definitions, with near-identical nomenclature:

$$I_{1,\text{rms}} = \frac{V_{1,\text{rms}}}{Z_{\text{eq}}}, \tag{3.53}$$

$$P = R_{\text{eq}} \left| I_{1,\text{rms}} \right|^2 = \frac{R_{\text{eq}} V_{1,\text{rms}}^2}{R_{\text{eq}}^2 + \left(\omega L_{\text{eq}} - \dfrac{1}{\omega C_1} \right)^2}. \tag{3.54}$$

$$PF = \frac{\Re(Z_{\text{eq}})}{|Z_{\text{eq}}|} = \frac{R_{\text{eq}}}{\sqrt{R_{\text{eq}}^2 + \left(\omega L_{\text{eq}} - \dfrac{1}{\omega C_1} \right)^2}}, \tag{3.55}$$

$$PF_{\text{ind}} = \frac{R_{\text{eq,p.t.}}}{\sqrt{R_{\text{eq,p.t.}}^2 + \omega^2 L_{\text{eq,p.t.}}^2}}, \tag{3.56}$$

where $R_{\text{eq,p.t.}}$ and $L_{\text{eq,p.t.}}$ are obtained in (3.44) and (3.45) respectively.

Efficiency calculations for multiple-inductor systems can be expressed in terms of power:

$$\eta = \frac{P_{\text{load}}}{P_{\text{load}} + P_{\text{sh}} + P_{\text{cond}} + P_{\text{prox}}}, \tag{3.57}$$

$$P_{\text{load}} = \sum_{i=1}^{n} \sum_{j=1}^{n} n_{t,i} n_{t,j} I_i I_j^* R_{\text{load},ij,\text{p.t.}}, \tag{3.58}$$

$$P_{\text{sh}} = \sum_{i=1}^{n} \sum_{j=1}^{n} n_{t,i} n_{t,j} I_i I_j^* R_{\text{sh},ij,\text{p.t.}}, \tag{3.59}$$

$$P_{\text{cond}} = \sum_{i=1}^{n} \frac{n_{t,i}}{n_{s,i}} I_i I_i^* R_{\text{cond},ii,s}, \tag{3.60}$$

$$P_{\text{prox}} = \sum_{i=1}^{n} \sum_{j=1}^{n} \sum_{k=1}^{n} n_{t,i} n_{t,j} n_{t,k} n_{s,k} I_i I_j^* R_{\text{prox},ijk,s}. \tag{3.61}$$

Despite ICH and WPT being similar systems, induction heating η can not be measured directly. Since $R_{\text{load},ij}$ are part of R_{ij}, and there are no effective ways to measure induced voltage and currents in the ferromagnetic load, there is no accesible terminal to measure P_{load}, either directly or indirectly [153].

Power distribution, PD is calculated from the total S_{load} generated by the sum each inductor element, $S_{\text{load},ij}$ (3.12):

$$PD = \sqrt{\frac{\sum_{l=1}^{N} \left(\dfrac{\sum_{i=1}^{n} \sum_{j=1}^{n} S_{\text{load},ijl}}{\sum_{i=1}^{n} \sum_{j=1}^{n} S_{\text{load},ij}} - 1 \right)^2}{N-1}}, \tag{3.62}$$

where subscript l represents each uniformly distributed load mesh point.

Emitted magnetic field is simply the sum of the field generated by all inductors. Considering an orthonormal coordinate system of basis $\{\hat{\mathbf{e}}_1, \hat{\mathbf{e}}_2, \hat{\mathbf{e}}_3\}$, rms field probe measurement can be calculated as:

$$|\mathbf{B}_{\text{rms}}| = \sqrt{\sum_{j=1}^{3} \left| \sum_{i=1}^{n} n_{t,i} I_{i,\text{rms}} \frac{\int_S \mathbf{B}_i \hat{\mathbf{e}}_j dS}{S_{\text{loop}}} \right|^2} \tag{3.63}$$

3.4.3 Dimensionless design parameters

Some dimensionless factors are very useful in understanding and designing multiple-inductor systems. Inductor quality factor, Q_{ij}, describes the resonant characteristics of the winding, as it relates its reactance to its resistance, similar to PF_{ind}:

$$Q_{ij} = \frac{\omega L_{ij}}{R_{ij}}. \tag{3.64}$$

In WPT, it is beneficial for Q_{ij} to be as high as possible, as all R_{ij} represents losses. In IH and ICH, low Q_{ij} represents high power transfer per circulating energy. Although Q_{ij} can be calculated for both self and mutual impedance elements, mutual elements are usually disregarded in WPT due to small inductive losses. Values of Q_{ii} from 0 to 0.5 indicate that the inductor is unable to resonate. The range from 0.5 to 5 is typically found in conventional IH systems. The range between 5 and 30 is not used in either conventional IH or WPT but it is potentially beneficial for ICH. Low efficiency or strong coupling WPT systems have Q_{ii} up to 100, typical values for weak coupling are in the several hundreds [154], and recent research has been able to achieve 1300 [155].

Resistive and inductive coupling factors, $k_{R,ij}$ and $k_{L,ij}$, respectively, can be defined between mutual impedance and its respective self-impedance elements:

$$k_{R,ij} = \frac{R_{ij}}{\sqrt{R_{ii} R_{jj}}}, \tag{3.65}$$

$$k_{L,ij} = \frac{L_{ij}}{\sqrt{L_{ii} R_{jj}}}. \tag{3.66}$$

The inductive coupling factor, $k_{L,ij}$, corresponds to the proportion of magnetic flux that is generated from inductor i that reaches inductor j and as such, it ranges from 0 to 1. $k_{R,ij}$ also ranges from 0 to 1, but its meaning is less obvious. Phase

angle between inductor currents shifts as $k_{R,ij}$ changes, as well as the phase between the magnetic fields they generate.

Mutual quality factor (3.67) can be written in terms of coupling and self quality factors:

$$Q_{ij} = \frac{k_{L,12}}{k_{R,12}}\sqrt{Q_{11}Q_{22}}. \tag{3.67}$$

Most of the global equivalent impedance can be rewritten in terms of quality and coupling factors:

$$R_{\text{eq,p.t.}} = R_{11,\text{p.t.}}\left(1 + k_{R,12}^2\frac{2Q_{12}\left(Q_{22} - \dfrac{1}{\omega C_{2,\text{p.t.}}R_{22,\text{p.t.}}}\right) + Q_{12}^2 - 1}{1 + \left(Q_{22} - \dfrac{1}{\omega C_{2,\text{p.t.}}R_{22,\text{p.t.}}}\right)^2}\right), \tag{3.68}$$

$$L_{\text{eq,p.t.}} = \frac{R_{11,\text{p.t.}}}{\omega}\left(Q_{11} + k_{R,12}^2\frac{2Q_{12} + (Q_{12}^2 - 1)\left(Q_{22} - \dfrac{1}{\omega C_{2,p.t.}R_{22,\text{p.t.}}}\right)}{1 + \left(Q_{22} - \dfrac{1}{\omega C_{2,\text{p.t.}}R_{22,\text{p.t.}}}\right)^2}\right). \tag{3.69}$$

3.5 ICH system design process

Aside from geometry considerations, the passive inductor in ICH adds a degree of freedom to the design of the overall system. From (3.44) and (3.45) it can be seen that the only new element that can be tuned is C_2, as $n_{t,2}$ only has a local effect. The singular new degree of freedom may appear limiting, but its effects fundamentally change how system design is undertaken.

3.5.1 Resonant frequencies

Instinctively, it may appear that setting $\omega_{0,1} = \omega_{0,2}$ would yield the most optimal design. In fact, WPT systems, applying the correct assumption that $R_{12} \simeq 0$, operate under that design rule in most circumstances. In that particular case:

$$Z_{\text{eq}}(\omega_{0,2}) = R_{11} + \frac{\omega_{0,2}^2 L_{12}^2}{R_{22}}. \tag{3.70}$$

However, $R_{12} \neq 0$ in ICH, therefore:

$$Z_{\text{eq}}(\omega_{0,2}) = R_{11} - \frac{R_{12}^2 - \omega_{0,2}^2 L_{12}^2 + j2\omega_{0,2}R_{12}L_{12}}{R_{22}}. \tag{3.71}$$

The cancellation of self-inductance does not eliminate all reactance because of the non-zero R_{12}. In other words the relation $\omega_{0,1} = \omega_{0,2} = \omega_{0,\text{eq}}$ can not be satisfied.

In this case, $C_{1,\text{p.t.}}$ and $C_{2,\text{p.t.}}$ are determined from a choice of $\omega_{0,2}$ and $\omega_{0,\text{eq}}$:

$$C_{2,\text{p.t.}} = \frac{1}{\omega_{0,2}^2 L_{22,\text{p.t.}}}, \tag{3.72}$$

$$C_{1,\text{p.t.}} = \frac{1}{\omega_{0,\text{eq}}^2 L_{\text{eq,p.t.}}}, \tag{3.73}$$

where $L_{\text{eq,p.t.}}$ is calculated from (3.45), substituting $C_{2,\text{p.t.}}$ from (3.72).

3.5.2 Selection of winding cable

Cable selection is based on the optimization of the efficiency,considering its expression (3.57). For ICH in particular, where I_2 is entirely dependant on I_1 as seen in (3.48), I_2 can be substituted in the power expressions:

$$K_Z = \frac{Z_{12,\text{p.t.}}}{Z_{22,\text{p.t.}}}, \tag{3.74}$$

$$I_2 = -\frac{n_{t,1}}{n_{t,2}} K_Z I_1. \tag{3.75}$$

In the case of P_{load}, substituting in (3.58):

$$\begin{aligned} P_{\text{load}} = {} & n_{t,1}^2 I_1 I_1^* R_{\text{load},11,\text{p.t.}} - n_{t,1} n_{t,2} I_1 \frac{n_{t,1}}{n_{t,2}} K_Z^* I_1^* R_{\text{load},12,\text{p.t.}} \\ & - n_{t,2} n_{t,1} \frac{n_{t,1}}{n_{t,2}} K_Z I_1 I_1^* R_{\text{load},21,\text{p.t.}} + n_{t,2}^2 \left(\frac{n_{t,1}}{n_{t,2}}\right)^2 K_Z I_1 K_Z^* I_1^* R_{\text{load},22,\text{p.t.}}. \end{aligned} \tag{3.76}$$

Considering that for any complex number a, $aa^* = |a|^2$ and $a + a^* = 2\Re(a)$:

$$P_{\text{load}} = n_{t,1}^2 |I_1|^2 \left(R_{\text{load},11,\text{p.t.}} - 2\Re(K_Z) R_{\text{load},12,\text{p.t.}} + |K_Z|^2 R_{\text{load},22,\text{p.t.}}\right). \tag{3.77}$$

The same process can be applied to the other power contributions involved in η:

$$P_{\text{sh}} = n_{t,1}^2 |I_1|^2 \left(R_{\text{sh},11,\text{p.t.}} - 2\Re(K_Z) R_{\text{sh},12,\text{p.t.}} + |K_Z|^2 R_{\text{sh},22,\text{p.t.}}\right), \tag{3.78}$$

$$P_{\text{cond}} = n_{t,1}^2 |I_1|^2 \left(\frac{1}{n_{t,1} n_{s,1}} R_{\text{cond},11,s} + \frac{1}{n_{t,2} n_{s,2}} |K_Z|^2 R_{\text{cond},22,s}\right), \tag{3.79}$$

$$\begin{aligned} P_{\text{prox}} = {} & n_{t,1}^2 |I_1|^2 \left(n_{t,1} n_{s,1} R_{\text{prox},111,s} + n_{t,2} n_{s,2} R_{\text{prox},112,s}\right. \\ & -2 n_{t,1} n_{s,1} \Re(K_Z) R_{\text{prox},121,s} - 2 n_{t,2} n_{s,2} \Re(K_Z) R_{\text{prox},122,s} \\ & \left. + n_{t,1} n_{s,1} |K_Z|^2 R_{\text{prox},221,s} + n_{t,2} n_{s,2} |K_Z|^2 2 R_{\text{prox},222,s}\right). \end{aligned} \tag{3.80}$$

As $n_{t,1}$ and $|I_1|^2$ are common factors in all of them, currents can be removed from (3.57) entirely, and $n_{t,1}^2$ can be simplified from numerator and denominator,

assuming that losses have little effect on K_Z, due to the resistive components of $Z_{12,\text{p.t.}}$ and $Z_{22,\text{p.t.}}$. The only elements with numbers of turns and strands are P_{cond} and P_{prox}. The terms $(n_{t,1}n_{s,1})$ and $(n_{t,2}n_{s,2})$ are linearly independent in the previous expressions. Partial derivatives of η with respect to $(n_{t,1}n_{s,1})$ and $(n_{t,2}n_{s,2})$ yield the optimum number of total strands for either inductor, $(n_{t,i}n_{s,i})$,:

$$\frac{\partial \eta}{\partial \left(n_{t,1}n_{s,1}\right)} = 0 \rightarrow \left(n_{t,1}n_{s,1}\right)_{\text{opt}} = \sqrt{\frac{R_{\text{cond},11,s}}{R_{\text{prox},111,s} - 2\Re(K_Z)R_{\text{prox},121,s} + |K_Z|^2 R_{\text{prox},221,s}}}, \tag{3.81}$$

$$\frac{\partial \eta}{\partial \left(n_{t,2}n_{s,2}\right)} = 0 \rightarrow \left(n_{t,2}n_{s,2}\right)_{\text{opt}} = \sqrt{\frac{|K_Z|^2 R_{\text{cond},22,s}}{R_{\text{prox},112,s} - 2\Re(K_Z)R_{\text{prox},122,s} + |K_Z|^2 R_{\text{prox},222,s}}}. \tag{3.82}$$

These expressions are very similar to the single inductor case (2.45), with the addition of K_Z. In the case that losses resistances are high enough to change K_Z substantially, these expressions can be used iteratively to eventually arrive at the optimum values. For example, losses can be disregarded to calculate an initial value of K_Z. (3.81) and (3.82) are used to calculate an iteration of $(n_{t,i}n_{s,i})$. The $(n_{t,i}n_{s,i})$ value is used to calculate a better approximation of K_Z and the process is repeated until $(n_{t,i}n_{s,i})$ barely changes. The process generally requires only two iterations to reach asymptotic values in $(n_{t,1}n_{s,1})$ and $(n_{t,2}n_{s,2})$.

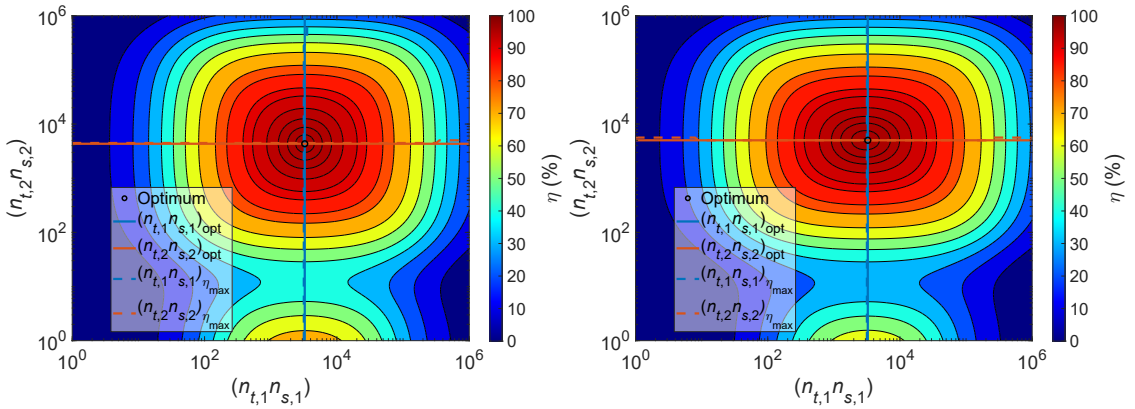

(a) (b)

Figure 3.5: Efficiency variation due to different $(n_{t,1}n_{s,1})$ and $(n_{t,2}n_{s,2})$ with inductors separated (a) $d_{w12} = 32\,\text{mm}$ and (b) $d_{w12} = 40\,\text{mm}$.

Figure 3.5 shows the efficiency variation due to total number of $\varnothing_s = 200\,\mu\text{m}$ strands of each inductor in a ICH system with a $\varnothing_{w,\text{ext}} = 180\,\text{mm}$ primary and secondary inductors separated $d_{w12} = 32\,\text{mm}$ and $40\,\text{mm}$. The optimum $(n_{t,1}n_{s,1})$

Table 3.1
Optimum $n_{t,i}n_{s,i}$ values in Fig. 3.5.

d_{w12}	$(n_{t,1}n_{s,1})$	$(n_{t,2}n_{s,2})$
32 mm	3268	4325
40 mm	3261	5010

and $(n_{t,2}n_{s,2})$ in these cases using (3.81) and (3.82) respectively are shown as continuous lines and represented in Table 3.1. The change in geometry causes $(n_{t,1}n_{s,1})_{\text{opt}}$ to decrease very slightly and $(n_{t,2}n_{s,2})_{\text{opt}}$ to increase moderately.

In either case, when η is high and K_Z is independent from $(n_{t,i}n_{s,i})$, it is proven that for any given $(n_{t,1}n_{s,1})$ value, the $(n_{t,2}n_{s,2})$ that gives maximum efficiency is the same, and the reverse also holds true. This is clearly represented in Fig. 3.5, where the dashed blue lines are the $n_{t,1}n_{s,1}$ values that maximizes η at each $n_{t,2}n_{s,2}$ point, $(n_{t,1}n_{s,1})_{\eta\text{max}}$, and the red dashed lines show the opposite, $(n_{t,2}n_{s,2})_{\eta\text{max}}$. When $\eta \geq 70\,\%$, the continuous and dashed lines overlap, and even below this threshold the lines barely change.

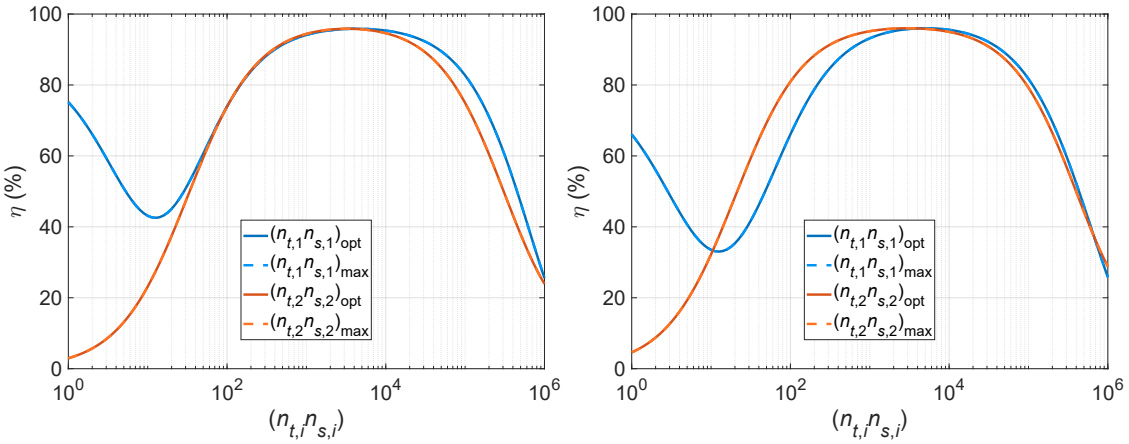

Figure 3.6: η variation with $(n_{t,i}n_{s,i})$ at $(n_{t,j}n_{s,j})_{\text{opt}}$ $(\forall i \neq j)$ for (a) $d_{w12} = 32\,\text{mm}$ (b) $d_{w12} = 40\,\text{mm}$.

Fig. 3.6 shows η variation with $(n_{t,2}n_{s,2})$ at $(n_{t,1}n_{s,1})_{\text{opt}}$ and $(n_{t,1}n_{s,1})_{\eta\text{max}}$ and vice-versa for the same cases as Fig. 3.5. It is clear that η hardly changes between considering $(n_{t,i}n_{s,i})_{\text{opt}}$ or $(n_{t,i}n_{s,i})_{\eta\text{max}}$. The local minimum at $(n_tn_s)_2 = 10$ and local maximum at $(n_tn_s)_2 = 1$ exist due to the great effect of losses on K_Z. As $(n_tn_s)_2$ increases, K_Z becomes independent from losses. This dependence is disregarded in (3.74), and the local minima does not appear in (3.82).

3.5.3 Impedance simulations

Equations (3.46), (3.68) and (3.69) show that the parameters that affect equivalent system impedance are $R_{11,\text{p.t.}}$, $n_{t,1}$, Q_{11}, Q_{12}, Q_{22}, $k_{R,12}$, $C_{1,\text{p.t.}}$, $C_{2,\text{p.t.}}$ and ω, with non-linear dependencies. Of these, only $n_{t,1}$, $C_{1,\text{p.t.}}$, $C_{2,\text{p.t.}}$ and ω are independent from the geometry and materials and are fully in control of the designer. In order to determine the effect of each of them on the system, several parametric sweeps are carried out.

As a starting point, a finite element simulation is used to obtain reasonable values of $R_{11,\text{p.t.}}$, Q_{11}, Q_{12}, Q_{22} and $k_{R,12}$. The simulated system represented in Fig. 3.4 includes two $\varnothing_{w,\text{ext}} = 180\,\text{mm}$ inductors separated $d_{w12} = 42\,\text{mm}$, with the ferromagnetic load 50 mm away from the primary inductor. Parameters $n_{t,1}$, $C_{1,\text{p.t.}}$ are calculated to ensure $P_{\max} = 3700\,\text{W}$ at $f_{0,\text{eq}} = 25\,\text{kHz}$:

$$C_{1,\text{p.t.}} = \frac{1}{\omega_{0,eq}^2 L_{\text{eq,p.t.}}}, \tag{3.83}$$

$$n_{t,1} = \frac{V_{\text{rms}}}{\sqrt{P_{\max} R_{\text{eq,p.t.}}}}, \tag{3.84}$$

where V_{rms} is the rms input voltage.

For $C_{2,\text{p.t.}}$, it is more beneficial to put it in terms of $f_{0,2}$:

$$C_{2,\text{p.t.}} = \frac{1}{(2\pi f_{0,2})^2 L_{22,\text{p.t.}}}. \tag{3.85}$$

According to (3.67), Q_{12} can be expressed as:

$$Q_{12} = \frac{k_{L,12}}{k_{R,12}} \sqrt{Q_{11} Q_{22}}. \tag{3.86}$$

Then, Q_{11}, Q_{22}, $k_{R,12}$, $k_{L,12}$ and $f_{0,2}$ are swept one by one, leaving the rest constant, and the resulting P and PF_{ind} are plotted. Fig. 3.7 shows the parameter and frequency sweeps with P as a continuous line and PF_{ind} with a discontinuous line.

Fig. 3.7 (a) shows the effects of increasing Q_{11}, which is equivalent to moving away the load from the primary inductor. PF_{ind} decreases, the P curve's slope increases and a second peak in the power appears near $f_{0,2}$.

Fig. 3.7 (b) shows the effects of increasing Q_{22}, which equates to moving away the secondary inductor from the load. PF_{ind} increases near $f_{0,2}$, the P curve's slope increases to a lesser degree, and the second power peak is less pronounced.

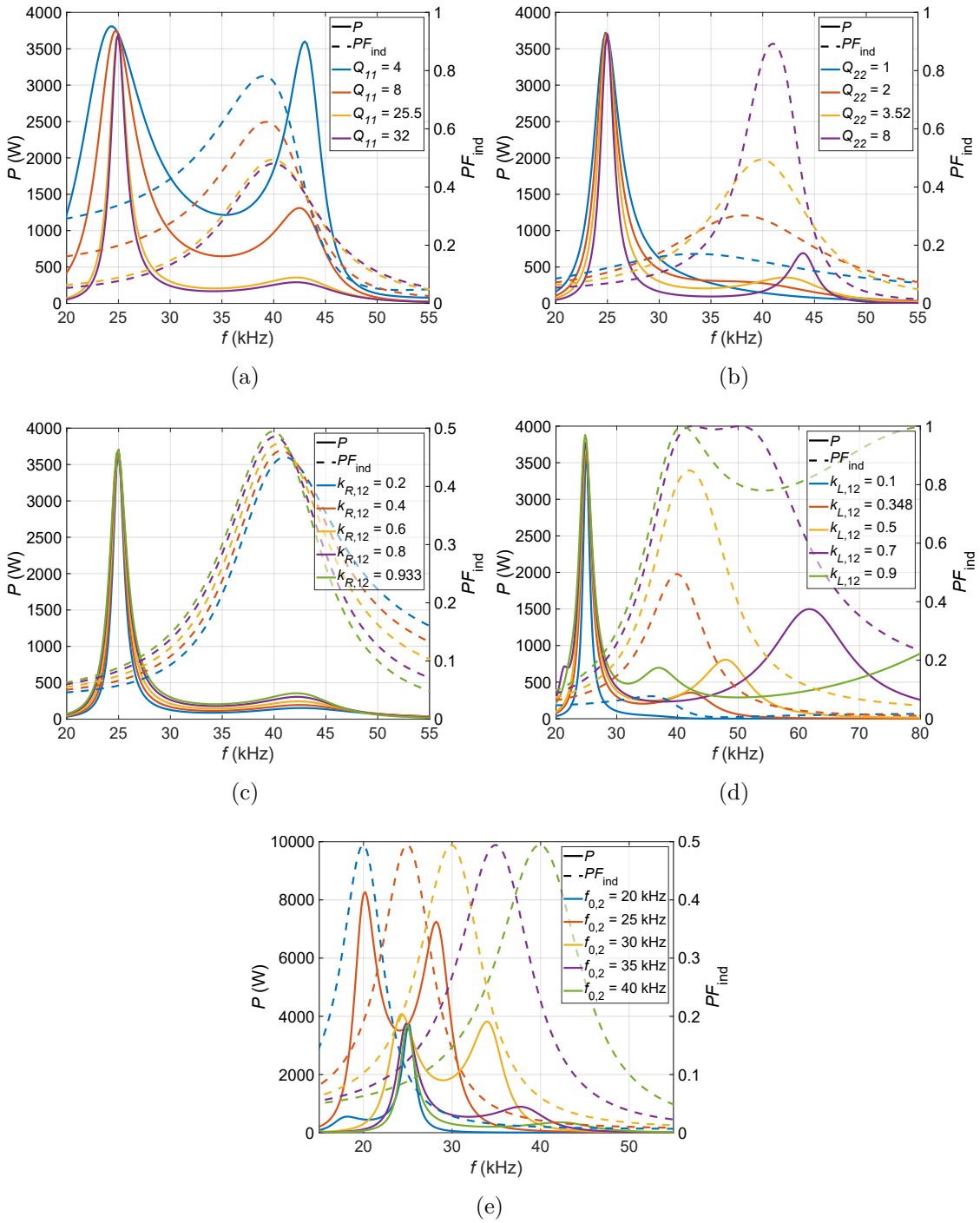

Figure 3.7: Simulated P and PF_{ind} sweeping (a) Q_{11}, (b) Q_{22}, (c) $k_{R,12}$, (d) $k_{L,12}$ and (e) $f_{0,2}$.

Fig. 3.7 (c) shows the effects of increasing $k_{R,12}$, which is the same as bringing the inductors and the load closer together. PF_{ind} increases at and below $f_{0,2}$ and decreases above $f_{0,2}$, P increases slightly, decreasing its slope slightly near $f_{0,\text{eq}}$.

Fig. 3.7 (d) shows the effects of increasing $k_{L,12}$, which is also equivalent to bringing the inductors together. PF_{ind} increases significantly near $f_{0,2}$, and the second P peak increases and moves to higher frequencies.

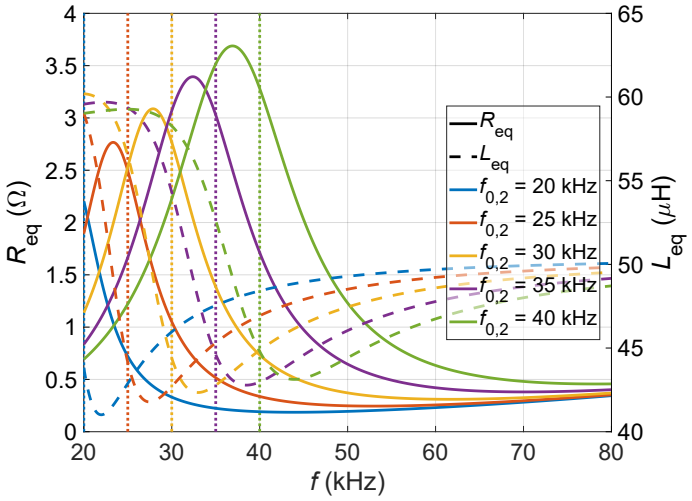

Figure 3.8: R_{eq} and L_{eq} evolution with f for different $f_{0,2}$.

Fig. 3.7 (e) shows the effects of increasing $f_{0,2}$ while maintaining $f_{0,\text{eq}}$ fixed at 25 kHz, which is achieved by adjusting C_2. The PF_{ind} peak follows $f_{0,2}$, and the second P peak becomes more prominent as $f_{0,2}$ and $f_{0,\text{eq}}$ come close together.

The characteristic second power peak observed in the simulations appears due to a rapid change in R_{eq} and L_{eq} at $f_{0,2}$, as depicted in Fig. 3.8. It is a phenomenon which has already been extensively observed in WPT, called pole-splitting or bifurcation [125, 156, 157]. The condition for pole-splitting to occur in WPT, with the parameters translated to those of ICH is:

$$k_{L,12} > \frac{R_{22}}{\omega L_{22}} = \frac{1}{Q_{22}}, \tag{3.87}$$

where R_{22} substitutes the load resistance of WPT systems. The previous observations agree with (3.87) to reduce pole splitting: reduce $k_{L,12}$ (increase distance between inductors) and reduce Q_{22} (bring secondary inductor and load closer together).

As shown in Fig. 3.7, most parameters offer a choice between low PF_{ind} with a simple P curve, or high PF_{ind} with a complex P curve that has local maxima and minima. This has releveant consequences for inductor and inverter design. On one hand, the conventional frequency control of P forces to search for a compromise between adequate PF_{ind} and simple P control. On the other hand, in cases where power control is carried out by modifying the voltage of the resonant inverter, the design can optimize for maximum PF_{ind} and work at constant frequency. The first option is chosen for this ICH system, and all subsequent systems presented throughout the dissertation.

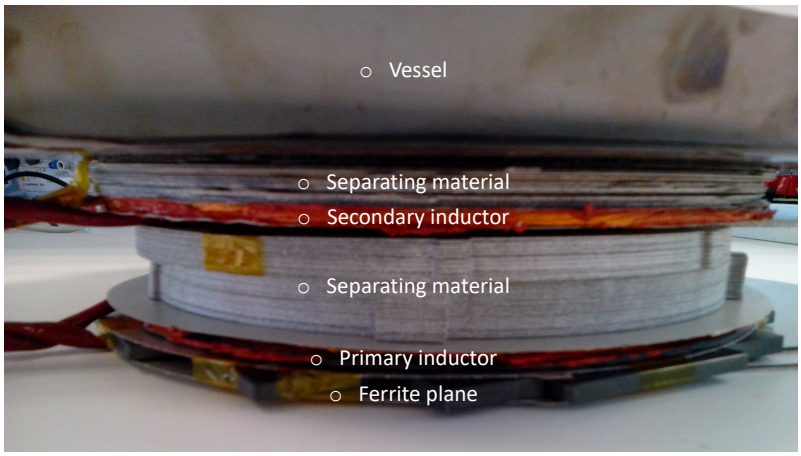

Figure 3.9: ICH LCR setup.

3.6 Same-diameter prototype

In order to verify the FEA simulations, low signal and full power measurements have been carried out.

3.6.1 Low signal regime

3.6.1.1 Prototype description

The low signal regime is used to determine the validity of the impedance FEA simulations, with a particular interest in the mutual component. Two $\varnothing_{w,\text{ext}} = 210\,\text{mm}$ inductors with $n_t = 29$, $n_s = 144$, a ferrite plane at the bottom and the ferromagnetic load at the top, shown in Fig. 3.9, are measured with a LCR meter. The sizeable diameter and winding construction reduces parasitic capacitance to enable better simulation accuracy. Measurements are taken at four d_{w1l} values, keeping the secondary inductor at a relative distance of 80 % between them. Self impedances are measured directly, while mutual impedances are obtained indirectly from in-phase and opposite-phase measurements of both inductors, in such a way that they induce a direct connection voltage, V_D and an inverse voltage V_I:

$$V_D = (Z_{11} + 2Z_{12} + Z_{22})\, I_1, \tag{3.88}$$

$$V_I = (Z_{11} - 2Z_{12} + Z_{22})\, I_1, \tag{3.89}$$

$$Z_{12} = \frac{V_D - V_I}{4I_1}. \tag{3.90}$$

3.6.1.2 Measurements

Fig. 3.10 shows the simulated values in continuous lines and the measured LCR values in circles. As the secondary inductor and load are separated from the primary

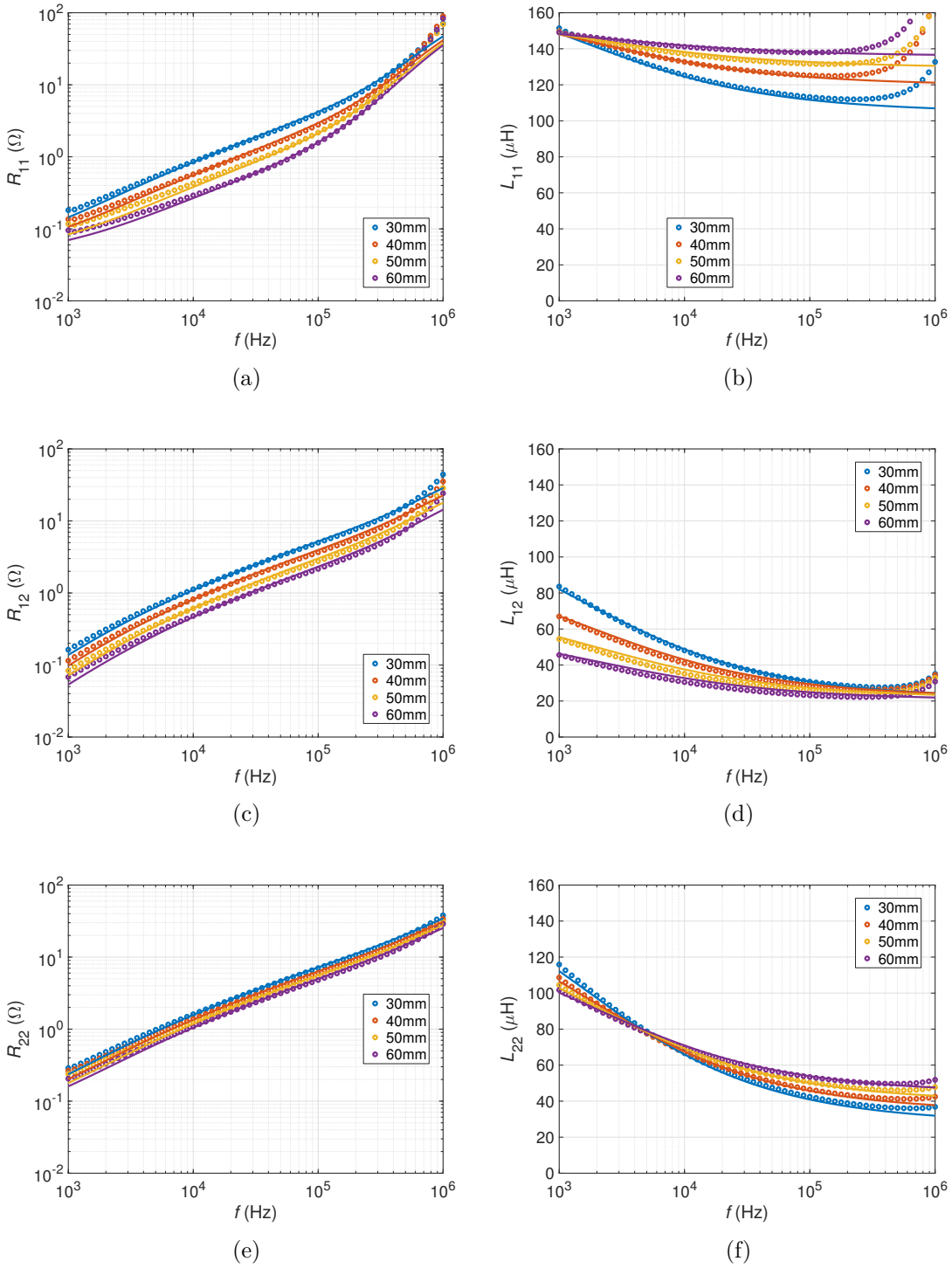

Figure 3.10: Measurements of R_{ij} in the first column, L_{ij} in the second column, with 11 elements in the first row, 12 in the second row and 22 in the third row for different d_{w12} values.

inductor, R_{11}, R_{12}, L_{12} and R_{22} decreases, L_{11} increases and L_{22} decreases at low f and increases at high f. The values are in good agreement in the 10 kHz to 200 kHz range, validating the impedance simulations. The discrepancies above 200 kHz for the inductance and 500 kHz are due to capacitive effects that are not modelled.

Table 3.2
Parameter comparison between equivalent IH and ICH systems with $\varnothing_{w,\text{ext}} = 180\,\text{mm}$, $d_{\text{load}} = 42\,\text{mm}$ and a ferrite plane.

System	PF_{ind}	η	J_w
IH	0.059	91.6 %	5.25 W/cm^3
ICH	0.25	96.7 %	1.56 W/cm^3

3.6.2 Full signal regime

3.6.2.1 Design and prototype

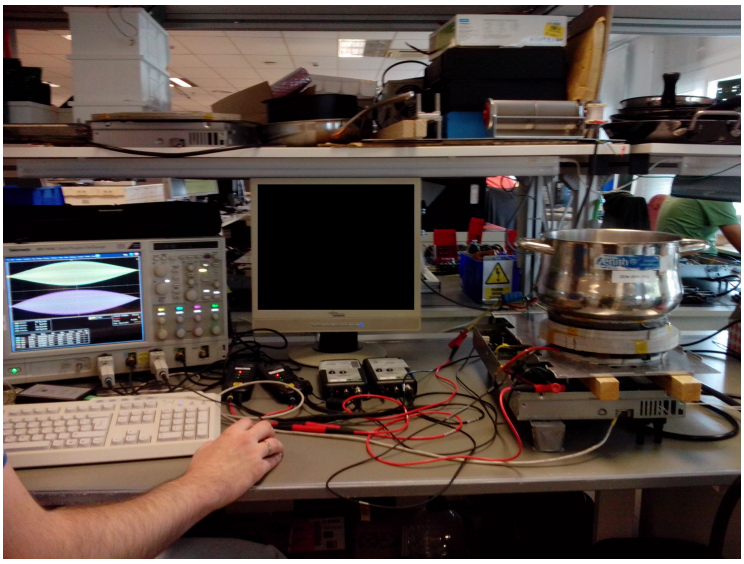

Figure 3.11: Experimental setup

For the full signal regime, the system shown in Fig. 3.11 uses two identical $\varnothing_{wi,\text{ext}} = 180\,\text{mm}$ inductors with $n_t = 19$ turns of $\varnothing_s = 200\,\mu\text{m}$, $n_{si} = 180$ strands litz wire. Fig. 3.12 (a) shows the η variation with $(n_{t,1}n_{s,1})$ and $(n_{t,2}n_{s,2})$, marking the optimum point and the selected values for the prototype. For the given inductor geometry, the maximum number of strands, $(n_{t,i}n_{s,i})_{\max} = 19 \cdot 180$, which in this case is slightly above $(n_{t,1}n_{s,1})_{\text{opt}} = 3347$, but below $(n_{t,2}n_{s,2})_{\text{opt}} = 4850$.

The primary inductor has a ferrite plane attached beneath, and the aluminum shielding is placed just beneath the ferrite plane. The inductors are separated $d_{w12} = 42\,\text{mm}$, and the load is $d_{\text{load}} = 5\,\text{mm}$ away from the secondary inductor, with a total distance between primary inductor and load of $d_{w1l} = 50\,\text{mm}$.

Fig. 3.12 (b) represents the simulated $J_{w,1}$, $J_{w,2}$ and η, showing that η can reach 97 %, a common value in conventional IH applications, and that the inductors run fairly cool below 2.5 W/cm^3. This stands in contrast with Table 3.2, whose

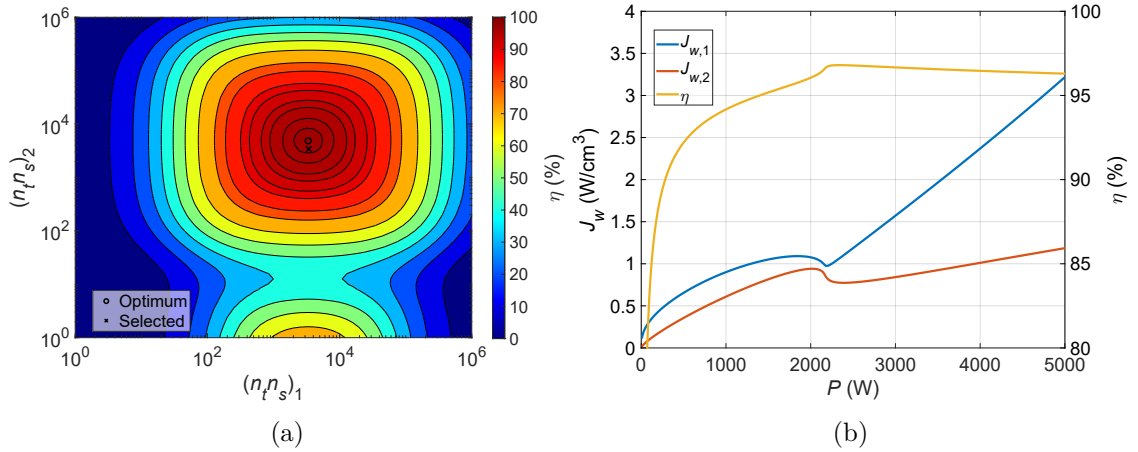

(a) (b)

Figure 3.12: (a) Prototype $n_{t,i}n_{s,i}$ selection. (b) Simulated $J_{w,1}$, $J_{w,2}$ and η of the prototype ICH system.

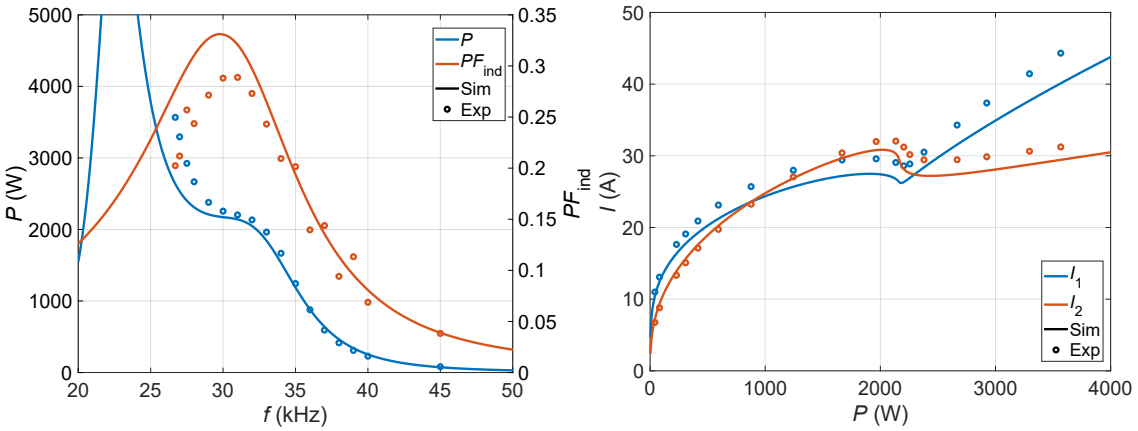

(a) (b)

Figure 3.13: Simulated and experimental values of (a) P and PF_{ind}, (b) I_1 and I_2.

equivalent IH point would be limited by copper losses and be much worse off in efficiency and PF_{ind}.

3.6.2.2 Measurements

A half-bridge inverter is used to feed the system, using frequency control and maintaining symmetrical duty cycle. As a result, maximum PF_{ind} is not maintained for all P range. 800 nF capacitor tanks were selected for both primary and secondary tanks, resulting in $f_{0,2} \simeq 30\,\text{kHz}$ and $f_{0,\text{eq}} = 23\,\text{kHz}$. In simulation, maximum PF_{ind} is achieved at 2200 W, and the mild pole-splitting causes a "plateau" to appear at 30 kHz, instead of a second peak. The pole-splitting is not strong due to the separation between $f_{0,\text{eq}}$ and $f_{0,2}$, and $k_{L,12}$ only being 20 % higher than $1/Q_{22}$ (3.87).

Fig. 3.13 shows the experimental results compared with the simulations. They

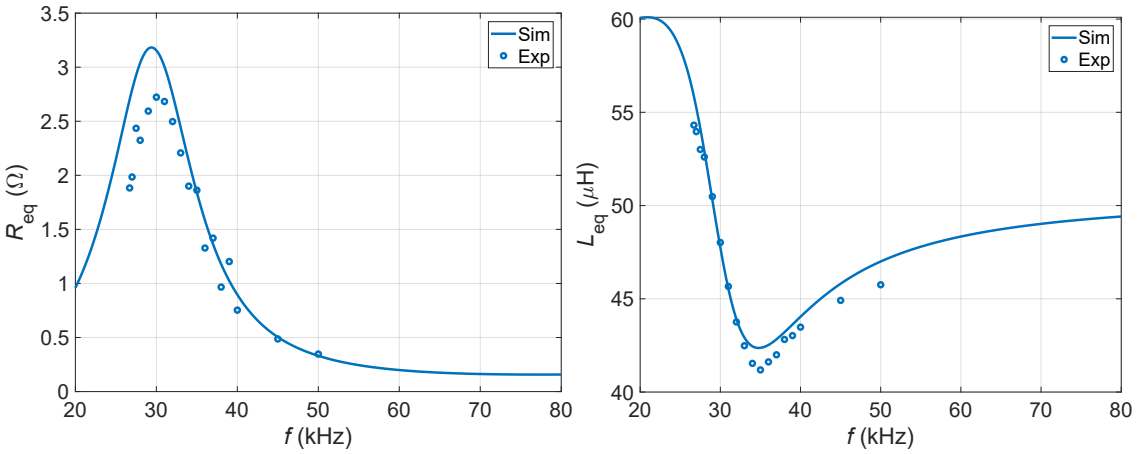

(a) (b)

Figure 3.14: Impedance simulated and experimental values, (a) R_{eq}, (b) L_{eq} zoom

are in good agreement, except for the slight overestimation of PF_{ind} near $f_{0,2}$. The tested ICH system is comfortably above the PF_{ind} limit of 0.1. If the system was voltage-controlled at a fixed frequency, maximum PF_{ind} could be maintained for all the power range.

Fig. 3.14 shows the comparison between simulated impedance and experimental measurements. The slight errors in impedance at low frequencies are responsible for the inaccuracies in Fig. 3.13. The effect of $f_{res,2} \approx 32\,\text{kHz}$ can be seen in the R_{eq} maximum and L_{eq} minimum, which in turn causes the pole-splitting plateau in P and the PF_{ind} peak.

Appendix D compiles a list of the most relevant experimental results of the dissertation.

3.7 Conclusion

The simulations and experimental measurements verify the feasibility of ICH systems. The tested prototype is able to maintain high PF_{ind} 10 mm higher than the IH limit, while improving η and $J_{w,i}$.

There are many geometrical degrees of freedom that influence system impedance. External and internal inductor diameter can be used to fine-tune coupling between windings. Moreover, effective designs can be achieved with very different winding external diameters, allowing for the adaptation of many load sizes. It is more advantageous to have the secondary inductor closer to the ferromagnetic load, which significantly helps with system construction and implementation. The distance

between the secondary winding and load can also be used to alter impedance. Pole-splitting can become a controllability or functionality concern, but it can be mitigated by the system design.

These results are very encouraging to continue exploring what ICH systems can accomplish, and each following chapter focuses on a particular topic. The next chapter analyzes the combination of a relatively small primary inductor with a larger secondary inductor and load, with particular focus on power distribution.

Chapter 4

Large diameter load adaptation to a smaller primary inductor

This chapter develops the design process of ICH systems to adapt large loads and secondary inductors to smaller primary inductors. In this case, the design efforts are focused on the power distribution, and a scoring system is used to achieve optimal solutions, including delivered power, electronics' stress and efficiency. A near optimal design is chosen to develop as a prototype, which is tested under working conditions up to 3680 W *at several distances.*

Table of contents

4.1 Introduction 119
4.2 System simulation and design 120
4.2.1 Score definition 123
4.2.2 Simulation results. 124
4.3 Viability of the design and comparison with IH 128
4.3.1 Distance comparison with IH 128
4.3.2 Lateral misalignment 132
4.4 Experimental measurements 135
4.5 Conclusion. 139

Figure 4.1: Proposed system geometry with appliance and primary inductor beneath the kitchen surface and load with attached secondary inductor above.

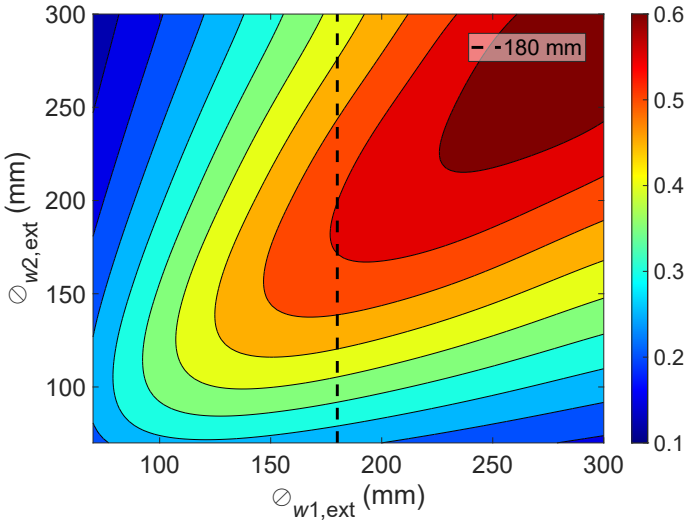

Figure 4.2: Inductive coupling, k_L, at 30 kHz for sweeping $\varnothing_{w1,\text{ext}}$ and $\varnothing_{w1,\text{ext}}$ values.

4.1 Introduction

Adaptation of different sizes of vessels to the same primary inductor is an interesting ICH application. In contrast with current cooktop layouts of different burner sizes, ICH allows layouts with identical primary inductors, and each load to have appropriate secondary inductors attached. This way cooktops acquire a certain degree of flexibility, as each load can be place on top of any primary inductor, with relatively small added cost.

Fig. 4.1 shows a possible implementation with a $\varnothing_{w1,\text{ext}} = 180\,\text{mm}$ primary inductor, a $\varnothing_{w2,\text{ext}} = 290\,\text{mm}$ secondary inductor and $\varnothing_{\text{load}} = 290\,\text{mm}$ cooking vessel and a kitchen surface of 20 mm thickness. The $\varnothing_{w1,\text{ext}} = 180\,\text{mm}$ primary inductor is able to achieve adequate coupling with secondary inductors ranging from 90 mm $\varnothing$ to 300 mm, as depicted in Fig. 4.2, making its size the most versatile for the

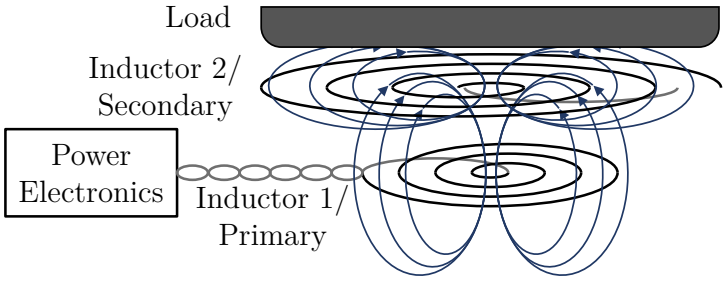

(a)

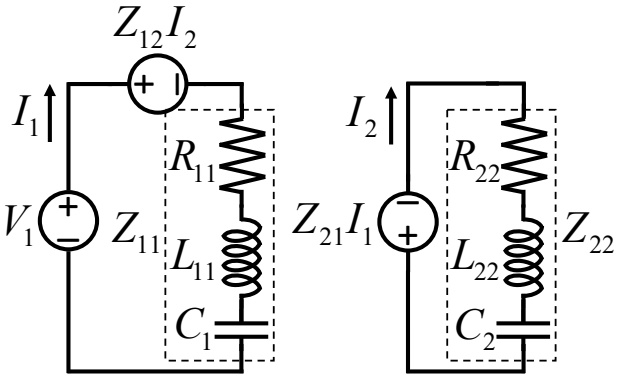

(b)

Figure 4.3: ICH system: (a) schematic representation, (b) circuit

primary inductor role.

4.2 System simulation and design

The change between the ICH system of the previous chapter and the one proposed here is simply the matching size of the secondary inductor and ferromagnetic load, as represented schematically in Fig. 4.3 (a). Therefore, the system circuit, shown in Fig. 4.3 (b), and system of equations are still the same:

$$\begin{pmatrix} Z_{11} & Z_{12} \\ Z_{21} & Z_{22} \end{pmatrix} \begin{pmatrix} I_1 \\ I_2 \end{pmatrix} = \begin{pmatrix} V_1 \\ 0 \end{pmatrix}. \tag{4.1}$$

As each inductor has different $\varnothing_{w,\text{ext}}$, the Poynting's vector they generate roughly reach their respective outer diameters. Both phase and amplitude of I_2 with respect to I_1 are dependent on K_Z, $n_{t,1}$ and $n_{t,2}$.

To improve PD, S_{22} (or $R_{\text{load},22}$ in resistance terms) should be maximized with respect to S_{11}, and their phase difference should be moderately destructive to avoid excess heating in the center. To exemplify this, Fig. 4.4 shows the Poynting's vector distribution on the bottom surface of the load for different conditions. In (a) and

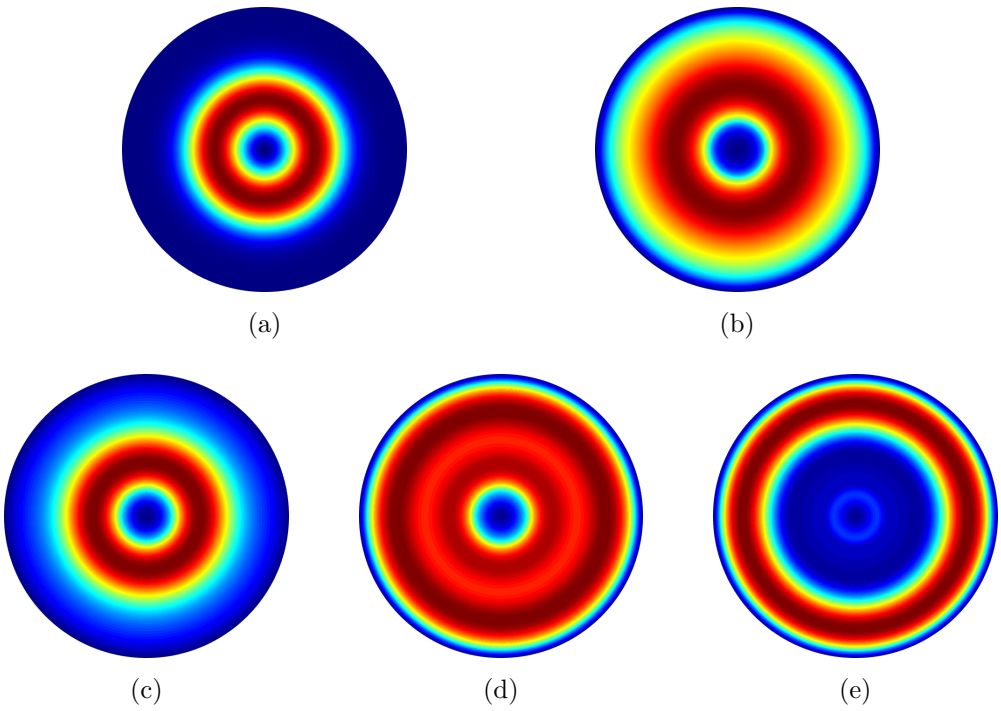

Figure 4.4: Power distribution of (a) active primary only, (b) active secondary only, and both due to current phase differences of: (c) 0°, (d), 135°, (e) 180°.

(b), only one of the inductors is active, the primary and secondary respectively. In (c), (d) and (e), both inductors have the same rms current running through them, with changing phase differences. All subfigures have relative color scales, so their maximum values are different.

When the currents are in phase, the center of the load has the most power density, while it decreases sharply at higher diameters. When they are in opposite phase, S_{11} generated by the primary inductor is completely cancelled, and the highest power density is found in outer diameters. For an intermediate obtuse angle, the primary's power contribution is reduced enough to have a nearly uniform power distribution across the entire surface. The optimum phase angle is entirely dependant on the magnetic field distribution, and consequently, on the system's geometry and materials, as well as the currents' frequency and amplitude. Considering the expressions derived in the previous chapter:

$$K_Z = \frac{Z_{12,\text{p.t.}}}{Z_{22,\text{p.t.}}}, \tag{4.2}$$

$$I_2 = -\frac{n_{t,1}}{n_{t,2}} K_Z I_1, \tag{4.3}$$

$$P_{\text{load}} = n_{t,1}^2 \left|I_1\right|^2 \left(R_{\text{load},11,\text{p.t.}} - 2\Re(K_Z) R_{\text{load},12,\text{p.t.}} + \left|K_Z\right|^2 R_{\text{load},22,\text{p.t.}}\right). \tag{4.4}$$

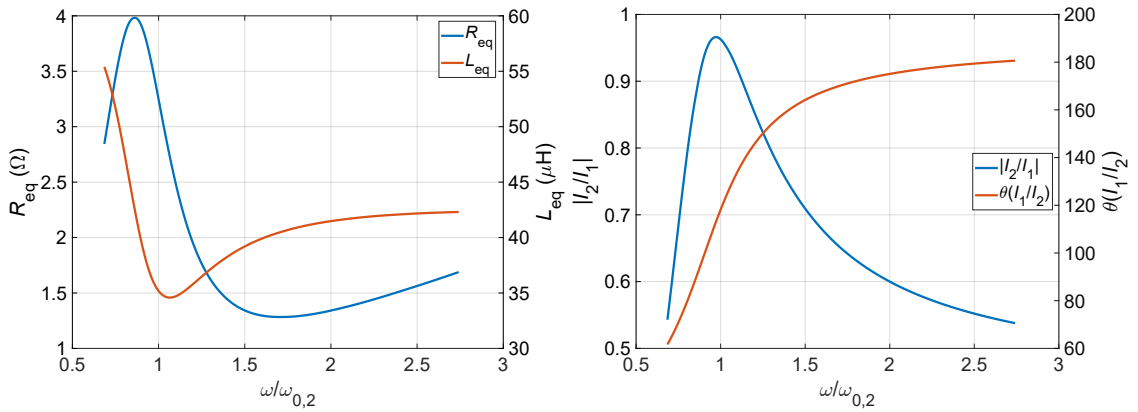

(a) (b)

Figure 4.5: Variation with relative frequency of (a) R_{eq} and L_{eq}, (b) Currents ratio and phase difference.

Both phase and amplitude of I_2 with respect to I_1 are dependent on K_Z, which can be modified through the secondary capacitor, C_2. Fig. 4.5 shows the variation of R_{eq}, L_{eq}, $|I_2/I_1| = n_{t,1}/n_{t,2}\,|K_Z|$ and $\angle(I_1/I_2) = \angle(K_Z)$ with respect to relative frequency, $\omega/\omega_{0,2} = f/f_{0,2}$. As the currents can not be controlled independently, the optimum phase angle has to be achieved with the selection of $f_{0,2}$. This limitation prevents the design process to decouple the optimal power distribution from other relevant parameters, making power distribution an important part of the optimization process. Moreover, the previous chapter showed that maximum PF_{ind} is achieved at f below $f_{0,2}$, whereas Fig. 4.5 (b) shows that, according to the phase angle, optimum PD is found above $f_{0,2}$. Therefore, a compromise must be reached to satisfy the following conditions:

- Deliver P_{max} up to 3680 W (230 V × 16 A mains input) using frequency control only.
- Achieve optimal PD at a medium power rating and avoid bad distributions in other cases.
- Minimize system reactance in order to reduce inductor current and capacitor voltage for all power ratings, especially at high power.
- Minimize pole splitting to prevent losing zero voltage switching (ZVS) and facilitate power control.
- Achieve good efficiency.
- Maintain previous design goals for distances between primary and secondary

inductors from 6 mm to 50 mm.

4.2.1 Score definition

In contrast to previous chapters, not all design parameters are aligned. The main challenge to overcome in this ICH system is the harmonization of several design goals that are partially opposed. The clearest example was shown with PF_{ind} and PD, where the most advantageous frequencies for PD are above $f_{0,2}$, while the most advantageous ones for PF_{ind} are below $f_{0,2}$. The interaction between power reach and PF_{ind} depends on the R_{eq} peak. PF_{ind} will improve with higher resistances, but since this is a voltage-fed system, P will decrease. Emitted magnetic flux is not a concern in this case due to the large load. As a result, it is not considered in the optimization process.

If there were only two optimization parameters, Pareto representations could have been used. Four, however, are very unwieldy for such methods. In order to assign a quantitative value to the compliance of each design with these goals, a score system is introduced to assess them:

- Ability to reach 3680 W.
- Uniformity of power distribution.
- System's reactance.
- Efficiency.

Most of the following scores have been defined previously, so a brief reminder will suffice for them.

The power reach score, PR, is defined as the ratio between $\max(P)$ and the desired $P_{\max}$, which is 3680 W in this case:

$$PR = \frac{\max(P)}{P_{\max}}. \tag{4.5}$$

The power distribution score, PD, is the relative standard deviation of Poynting's vector, $\mathbf{S}$, where low values are desired:

$$PD = \sqrt{\frac{\sum_{l=1}^{N} \left(\frac{\sum_{i=1}^{2} \sum_{j=1}^{2} S_{\text{load},ijl}}{\overline{\sum_{i=1}^{2} \sum_{j=1}^{2} S_{\text{load},ij}}} - 1 \right)^2}{N-1}}. \tag{4.6}$$

For visual reference, PD for the cases presented in Fig. 4.4 are (c) 0.767, (d) 0.468 and (e) 1.067.

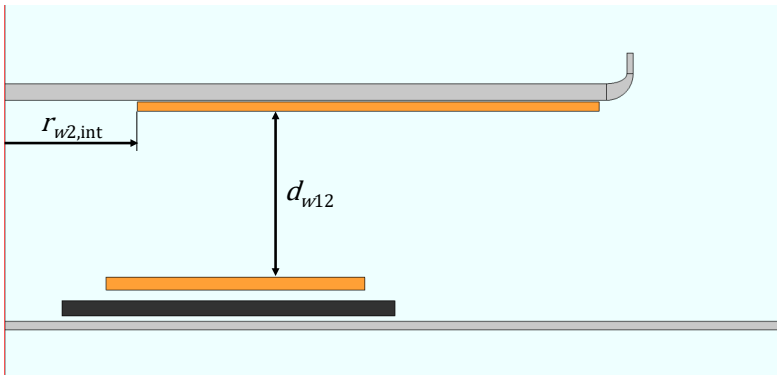

Figure 4.6: 2D simulation geometry showing the swept parameters

The system's reactance is measured with the electrical power factor, PF, defined as:

$$PF = \frac{R_{\text{eq}}}{|Z_{\text{eq}}|}, \tag{4.7}$$

where Z_{eq} includes the resonant capacitors. Even though PF and PF_{ind} are related, PF is a better indicator for excess current and PF_{ind} is better for excess capacitor voltage and P curve slope.

Efficiency, η, is defined as total useful power divided by total power delivered to the system:

$$\eta = \frac{P_{\text{load}}}{P_{\text{load}} + P_{\text{sh}} + P_{\text{cond}} + P_{\text{prox}}}. \tag{4.8}$$

The previous chapter presented a more detailed breakdown of the winding losses.

Though no explicit score is used to account for pole splitting, the optimization with the previous scores ensures that $f_{0,2} < f_{0,\text{eq}}$, avoiding operating in the valley between power peaks.

The impedance values obtained in the next subsection will be used to design a prototype with these goals in mind, choosing values for $\varnothing_{w,\text{int},2}$ and C_2.

4.2.2 Simulation results

FEA simulations are carried out with a primary inductor of $\varnothing_{w1,\text{ext}} = 180\,\text{mm}$ with a ferrite plane, and a secondary inductor of $\varnothing_{w2,\text{ext}} = 290\,\text{mm}$ because of the high k_L achieved with the primary inductor, as shown in Fig. 4.2. Moreover, the simulation sweeps the distance between inductors, d_{w12}, and $\varnothing_{w2,\text{int}}$ values, as depicted in Fig. 4.6. Additionally, C_2 is swept with fixed $C_1 = 800\,\text{nF}$, $n_{t,1} = 19$ turns and $n_{t,2} = 20$ turns to calculate scores for each design using $V_{\text{rms}} = 230\,\text{V}$. The primary inductor parameters are fixed due to the maximum copper volume available in the previous

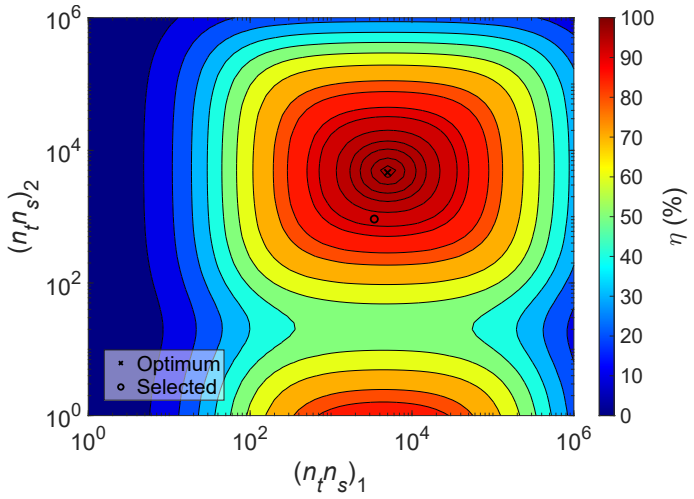

Figure 4.7: Simulated η depending on $(n_{t,1}n_{s,1})$ and $(n_{t,2}n_{s,2})$ and selected values.

ICH application. The effects of parameters $n_{t,2}$ and C_2 are intertwined in $C_{2,s.t.}$, so only one of the needs to be swept.

To calculate efficiency, the primary inductor uses $n_{s,1} = 180$, $\varnothing_s = 200\,\mu m$ copper strands, fixed by the previous ICH application, and the secondary inductor uses $n_{s,2} = 48$, $\varnothing_s = 300\,\mu m$ aluminum strands to reduce weight and cost, with a small penalty to η. Fig. 4.7 shows the variation of η depending on $(n_{t,1}n_{s,1})$ and $(n_{t,2}n_{s,2})$, with optimum values and the selected values. A slightly sub-optimum cable is chosen for the secondary inductor to reduce winding weight and cost while maintaining adequate efficiency.

Fig. 4.8 shows the scores from the simulated cases when two of the input parameters are fixed and the other is modified. When they are fixed, the values are $d_{w12} = 20\,mm$, $C_2 = 800\,nF$ and $\varnothing_{w2,int} = 30\,mm$. From the second row onwards, P is used in the horizontal axis, while the first row uses frequency.

As can be appreciated, there are instances where the same values of power can be reached for different frequencies due to pole-splitting, so when power is used as the horizontal axis, there will be instances of the same power having different PF, PD or η, because of the different f. To avoid operating in the pole-splitting range, the frequency ranges to the left of the power peaks are not used.

The effects of each input parameter and frequency on each output score can be appreciated in each subfigure. In (a), PR first decreases, then increases with climbing distance. In (b), PR first decreases and then increases with bigger capacitances. In (c), PR increases with longer internal radius. In (d), PF decreases with climbing distance. In (e), PF's maximum value increases with bigger capacitances, as well

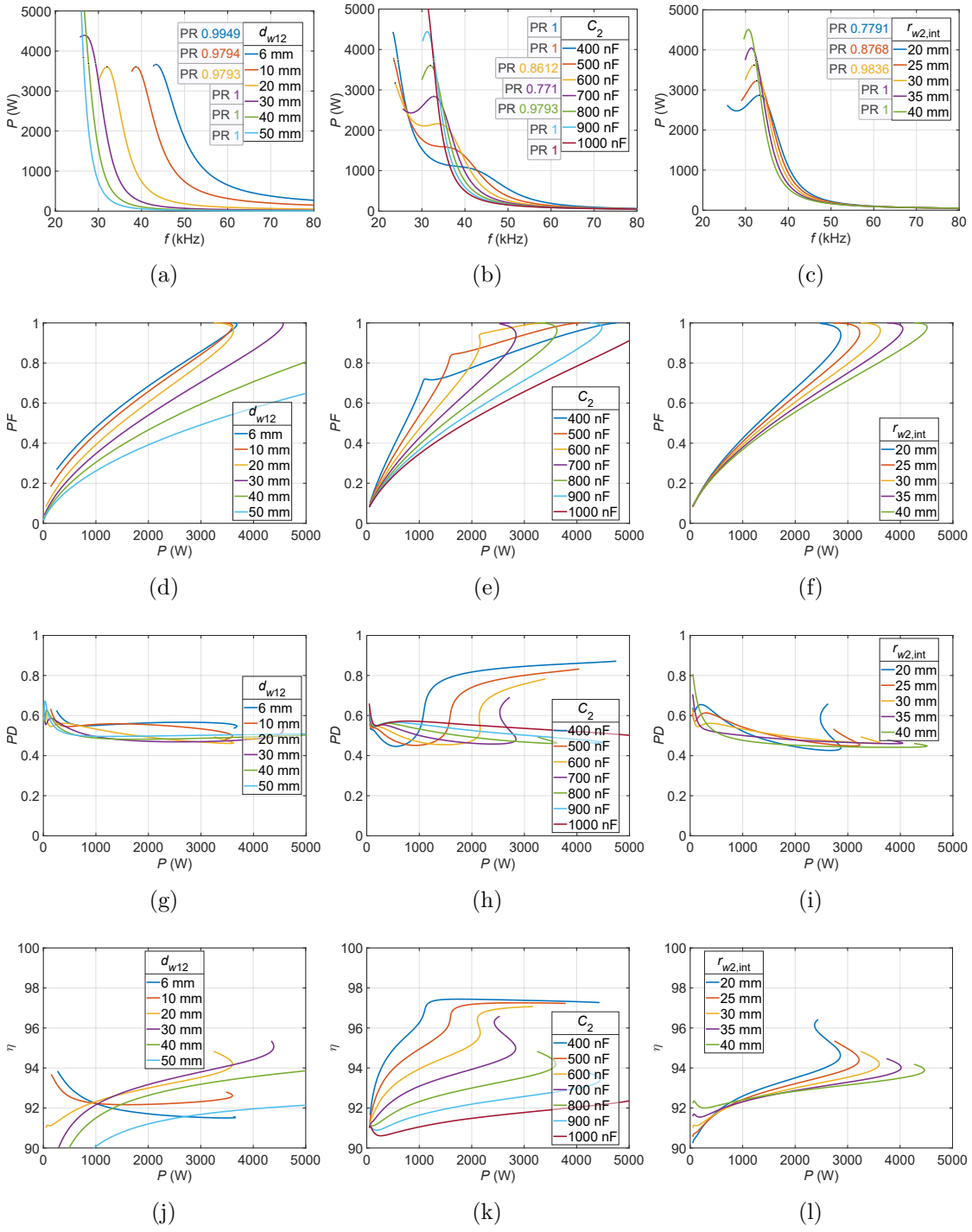

Figure 4.8: Simulation results: P (first row), PF (second row), PD (third row), η (fourth row) considering variations of d_{w12} (first column), C_2 (second column) and $\varnothing_{w2,\text{int}}$ (third column). The fixed values are $d_{w12} = 20\,\text{mm}$, $C_2 = 800\,\text{nF}$ and $\varnothing_{w2,\text{int}} = 30\,\text{mm}$.

as displacing said maximum to higher P points. In (f), PF's maximum is displaced to higher P points with longer internal radius. In (g), PD decreases sligthly with climbing distance. In (h), PD's minimum is displaced to higher P points with bigger C_2. In (i), PD becomes more uniform with longer $r_{w2,\text{int}}$. In (j), η first increases,

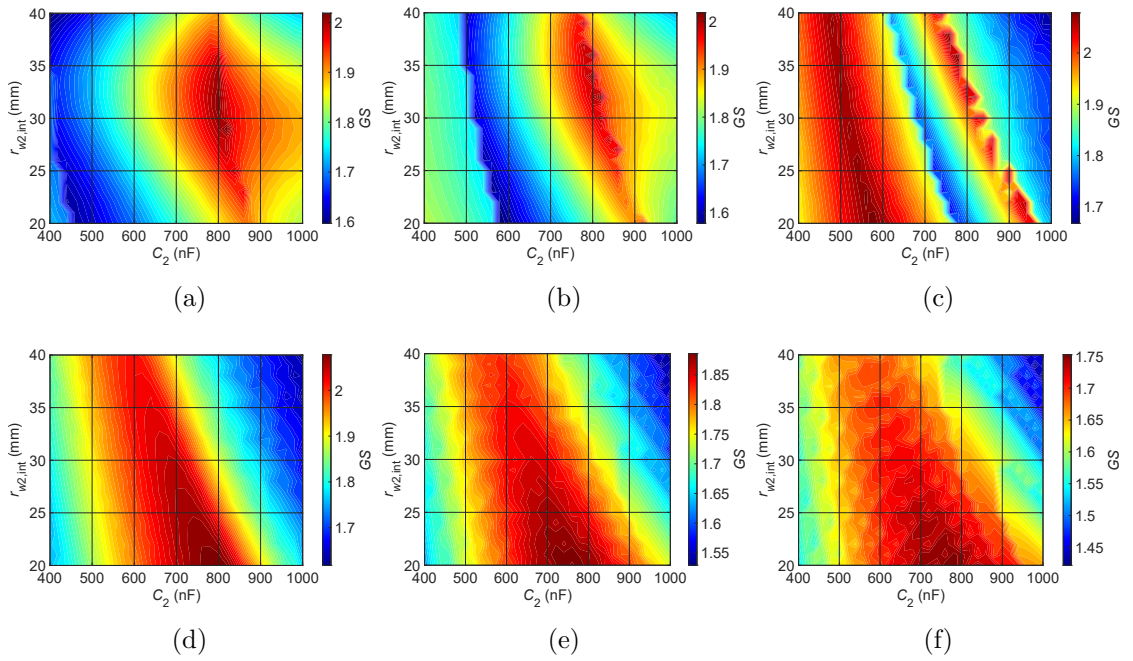

Figure 4.9: *GS* distribution at all simulation distances: (a) 6 mm, (b) 10 mm, (c) 20 mm, (d) 30 mm, (e) 40 mm, (f) 50 mm.

then decreases with distance, due to the induced currents in the secondary, which has higher losses because of its aluminum wire. In (k), η decreases with C_2 increments. Finally, in (l), η decreases with $r_{w2,\text{int}}$ increments.

The partial incompatibility between PF and PD can be appreciated in Fig. 4.8, (e) and (h) for most C_2 values, where $f_{0,2}$ can be detected by a slope change in (e) and a minimum value in (h). As C_2 increases, PF increases more slowly with P, but PD stays low for bigger P ratings. For changes in $r_{w2,\text{int}}$, in Fig. 4.8 (c), (f), and (i), higher values allow for better PR, but PF increases more slowly, and the PD curve changes somewhat.

As can be seen from Fig. 4.8, PF, PD, and η are frequency dependent, whereas a single score value for each simulation case would be preferable. Therefore, a weighted mean is calculated for each case to obtain averaged $\overline{PF}$, $\overline{PD}$, $\overline{\eta}$ where the weights are the delivered P for each point in the figure. This way, more relevance is given to the more important high power cases, without completely ignoring low power cases.

In order to condense these results and make them more approachable, a global score, GS, is created to combine all four:

$$GS = PR + \overline{PF} - \overline{PD} + \overline{\eta}. \tag{4.9}$$

Weights could have been applied to prioritize scores over the others, but all are

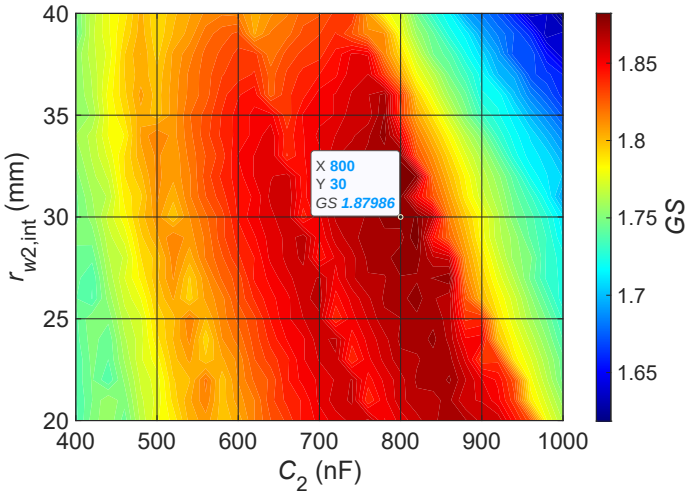

Figure 4.10: Average GS distribution for all distances.

considered equally important for this optimization. Each combination of C_2 and $r_{w2,\text{int}}$ is assigned a GS value, so the optimum for each inductor to inductor distance can be easily determined from the representations in Fig. 4.9. At smaller d_{w12}, the absolute maximum is located in high values of C_2 and middle values of $r_{w2,\text{int}}$, while at higher d_{w12} a new maximum appears for low C_2 and low $r_{w2,\text{int}}$, moving steadily towards bigger C_2.

Finally, in order to choose the best design for all distances, GS can be averaged, as is shown in Fig. 4.10. The optimum design according to these criteria has $r_{w2,\text{int}} = 30\,\text{mm}$ and uses a $C_2 = 800\,\text{nF}$, though the built prototype has $r_{w2,\text{int}} = 32\,\text{mm}$ and maintains $C_2 = 800\,\text{nF}$.

4.3 Viability of the design and comparison with IH

4.3.1 Distance comparison with IH

As was mentioned earlier, considering the size of the secondary inductor and the simulated η, instead of winding it with contiguous turns of coper wire, aluminum wire of $n_{s,2} = 48$ strands of $\varnothing_s = 300\,\mu\text{m}$ was used to wind the $n_{t,2} = 20$ turns. The primary inductor has $n_{t,1} = 19$ contiguous turns of copper wire of $n_{s,1} = 180$ strands of $\varnothing_s = 200\,\mu\text{m}$, the maximum number that can fit in the available space, with a ferrite plane below. The reuse of the same primary inductor for all sizes and the cable choice of the secondary inductor helps with cost reduction in commercial applications as well as their manufacturing process. Conversely, each vessel needs

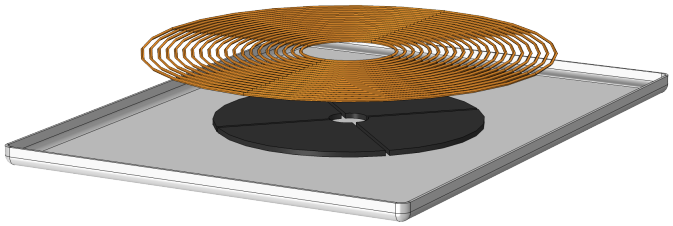

Figure 4.11: Detailed elements in the 3D simulation differing from the 2D simulated system.

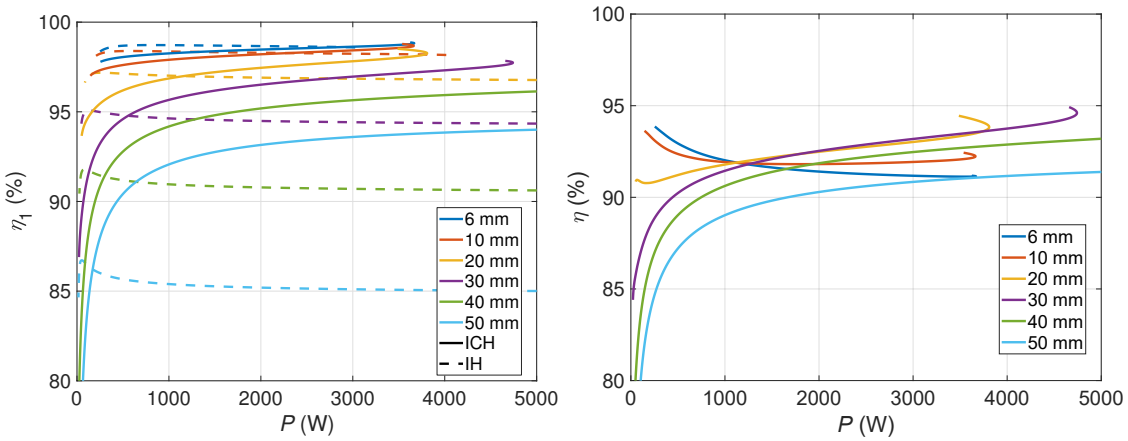

Figure 4.12: Simulated efficiency for different distances of (a) primary inductor in the full ICH system and heating the same load on its own, and (b) full ICH system.

to be attached to a secondary winding.

Fig. 4.11 represents the changes made when transitioning from a 2D geometry to 3D to obtain more accurate FEA impedances. The most important is the division of the secondary inductor into individual turns, followed by the ferrite plane divided into four circle sectors.

The efficiency of the primary inductor in the ICH system, η_1, is defined as:

$$\eta_1 = \frac{P_{\text{load}}}{P_{\text{load}} + P_{\text{sh},11} + P_{\text{sh},21} + P_{w,\text{cond},11} + P_{w,\text{prox},111} + 2P_{w,\text{prox},121} + P_{w,\text{prox},221}}, \tag{4.10}$$

where only the power losses that affect the primary inductor are included.

Fig. 4.12 compares η_1 and the efficiency of a conventional IH inductor in Fig. 4.12 (a) with the overall ICH η in Fig. 4.12 (b). The dashed line data represents simulations where the ICH primary inductor works on its own and the full line represents the simulated data where it is a part of the ICH system. The IH configuration does not use a secondary inductor, so to make the comparison fair, d_{load} is considered in the IH case, while d_{w1l} is considered in the ICH case, as the

Table 4.1
Global score comparison between 2D and 3D simulations

Distance (mm)	6	10	20	30	40	50
2D *GS*	2.010	1.967	1.972	1.894	1.781	1.655
3D *GS*	2.061	2.051	2.031	1.958	1.911	1.830

virtual kitchen surface thickness in both cases.

Fig. 4.12 shows that transitioning from IH to ICH, the primary inductor increases η_1 at $d_{w12} > 10\,\text{mm}$. Overall η of the full ICH system surpasses that of the IH system after 30 mm. At first, IH η is higher than ICH η because having two inductors involves two sources of losses, not to mention that the overall magnetic field is increased, increasing proximity and shielding losses further. As d_{w12} increases, R_{load} decreases in IH and losses increase faster, while the ICH system is able to maintain $R_{\text{load},ij}$ at higher distances, and losses increase more slowly. As the secondary inductor is wound with a sub-optimal aluminum wire in order to reduce cost and weight, η of the overall system catches up with the IH system at a higher distance than it would have if the secondary inductor used the same cable as the primary winding. Nevertheless, it is also important to bear in mind that even in the situations where total η is lower, the losses are divided between both inductors, resulting in smaller inductor losses density, $J_{w,i}$. As shown in Fig. 4.12, the primary inductor of the ICH system will endure less losses than the inductor in the conventional IH system.

GS has been calculated from the 3D FEA results, and represented in Table 4.1. The small differences are due to a beneficial effect on *PD* being narrowly bigger than the negative effect on *PF* and η on smaller distances, and more significant in higher distances. Overall, the differences are small enough to make the 2D optimum design valid for the actual 3D geometry.

To determine the differences between the ICH design and a conventional IH system, a $\varnothing_{w,\text{ext}} = 290\,\text{mm}$ inductor has been designed to deliver 3680 W at a 20 mm distance between inductor and load at the same $f_{0,1}$. For a fair comparison, the IH inductor uses the same cable than the primary inductor of the ICH system and the same amount of ferrite. Since the $\varnothing_{w1,\text{ext}} = 290\,\text{mm}$ IH inductor needs $n_t = 19$ turns, 530 g of copper are used in the winding's construction. The primary ICH inductor uses 336 g of copper and the secondary inductor uses 101 g of aluminum. Though the IH inductor uses more material, the ICH system requires more manufacturing,

Table 4.2
Score comparison between IH and ICH designs

Distance (mm)		6	10	20	30	40	50
PR	IH 180	0.810	**1.000**	**1.000**	**1.000**	**1.000**	**1.000**
	IH 290	0.470	0.616	**1.000**	**1.000**	**1.000**	**1.000**
	ICH	**1.000**	**1.000**	**1.000**	**1.000**	**1.000**	**1.000**
PF	IH 180	0.706	0.621	0.408	0.283	0.212	0.170
	IH 290	**0.812**	**0.754**	**0.656**	**0.479**	**0.371**	0.306
	ICH	0.654	0.606	0.517	0.433	**0.371**	**0.313**
PD	IH 180	1.427	1.388	1.286	1.174	1.063	0.952
	IH 290	0.599	0.601	0.582	0.550	0.516	0.482
	ICH	**0.509**	**0.472**	**0.405**	**0.368**	**0.356**	**0.355**
η_{total}	IH 180	**0.987**	**0.983**	**0.970**	0.947	0.911	0.856
	IH 290	**0.987**	**0.984**	**0.972**	**0.955**	**0.931**	**0.894**
	ICH	0.919	0.922	0.922	0.912	0.897	0.872
GS	IH 180	1.075	1.215	1.088	1.004	0.994	1.050
	IH 290	1.671	1.752	**2.046**	1.884	1.774	1.719
	ICH	**2.061**	**2.051**	2.031	**1.958**	**1.911**	**1.830**

making their cost roughly equivalent for this comparison.

Table 4.2 shows the scores of the primary inductor of the ICH system at each simulated distance, bearing in mind that the load is slightly closer in the IH case due to the lack of a secondary inductor. Bold font is used to mark the higher scores for easier reading. For *PR*, in IH, R_{load} decreases with distance, preventing the $\varnothing_{w,\text{ext}} = 290\,\text{mm}$ design at 20 mm to deliver full power at closer distances, and the IH $\varnothing_{w,\text{ext}} = 180\,\text{mm}$ design at $d_{\text{load}} = 6\,\text{mm}$. Considering *PF*, the IH inductor of $\varnothing_{w,\text{ext}} = 180\,\text{mm}$ deteriorates quickly, but the one with $\varnothing_{w,\text{ext}} = 290\,\text{mm}$ is able to maintain better performance up to a rather high distance. Bearing in mid *PD*, the secondary inductor in the ICH system causes a lower standard deviation of S_{load} in the ICH case for all considered distances. For η, the large diameter of the $\varnothing_{w,\text{ext}} = 290\,\text{mm}$ IH inductor, and the use of a suboptimum material in the secondary ICH inductor causes a higher η of the $\varnothing_{w,\text{ext}} = 290\,\text{mm}$ IH system for all simulated d_{w12}, while the smaller IH system worsens faster. As *GS* is currently defined, the inability to reach full power at the lower d_{w12} due to the high R_{load}, and the overall worse *PD* makes the $\varnothing_{w,\text{ext}} = 290\,\text{mm}$ IH design slightly worse in most

situations except the one it was specifically designed for.

It is relevant to consider that in IH systems of smaller $\varnothing_{w,\text{ext}}$, such as the one shown in the Table, the penalties applied to PF and η due to the higher d_{w12} are more pronounced. ICH becomes more appealing in this situation because it overcomes the high d_{w12} problems of small and big $\varnothing_{\text{load}}$ using a single primary inductor type compatible with all secondary sizes.

Moreover, though this was not a critical concern in this comparison, reactance compensation becomes a problem in IH with smaller $\varnothing_{w,\text{ext}}$ and higher d_{load} due to the lower PF_{ind}, as seen in previous chapters. In order to deliver the same amount of P, and thus achieve the same R_{eq}, the ICH system entails a much lower L_{eq} than that of a IH system. In the 20 mm case of the comparison, the ICH system has $L_{\text{eq}} = 35\,\mu\text{H}$ and the $\varnothing_{w,\text{ext}} = 290\,\text{mm}$ IH system at the same distance has $L_{\text{eq}} = 53\,\mu\text{H}$ despite the better PF in the IH system. To achieve the same $f_{0,\text{eq}}$, a lower C is needed in the IH case, which will result in higher V_C for the same I.

4.3.2 Lateral misalignment

The effects of lateral misalignment, x_{w12}, are very important in WPT applications, particularly when precise positioning is not achievable, such as in electric vehicle charging, [158, 159]. In the case of the proposed ICH system, significant misalignments should be easily detected and corrected by attentive users, but their effects must still be determined in order to know whether preventive or corrective actions are needed. Therefore, simulations at $d_{w12} = 20\,\text{mm}$ have been carried out, where the load and its attached secondary inductor are misaligned up to $x_{w12} = 70\,\text{mm}$, almost half their $r_{w2,\text{ext}}$. Additionally, lateral misalignments with only the $\varnothing_{w1,\text{ext}} = 180\,\text{mm}$ primary inductor and the $\varnothing_{w,\text{ext}} = 290\,\text{mm}$ IH inductor described in the previous section have also been simulated for further comparison.

Table 4.3 shows the score results for both IH and ICH systems. In both IH simulations, all parameters except PR slowly and steadily worsen with x_{w12}. In the particular case of the $\varnothing_{w,\text{ext}} = 180\,\text{mm}$ inductor, the variations are very small because the $\varnothing_{\text{load}} = 290\,\text{mm}$ load never stops covering the inductor. In the ICH case, PR is not affected, PF first increases and then decreases, PD worsens significantly, and η improves slightly. As the inductors are misaligned, coupling is reduced and the secondary inductor receives less and less P, worsening distribution and reducing secondary losses. At first, $k_{L,12}$ reduction also results in better impedance matching

Table 4.3

Scores when load is misaligned at a 20 mm distance

Misalignment (mm)		0	10	30	50	70
PR	IH 180	**1.000**	**1.000**	**1.000**	**1.000**	**1.000**
	IH 290	**1.000**	**1.000**	**1.000**	**1.000**	**1.000**
	ICH	**1.000**	**1.000**	**1.000**	**1.000**	**1.000**
PF	IH 180	0.409	0.409	0.408	0.406	0.398
	IH 290	**0.657**	**0.647**	**0.627**	**0.592**	**0.544**
	ICH	0.517	0.626	0.591	0.546	0.463
PD	IH 180	1.322	1.320	1.312	1.319	1.396
	IH 290	0.531	0.543	0.629	0.757	**0.896**
	ICH	**0.405**	**0.395**	**0.516**	**0.745**	1.066
η_{total}	IH 180	0.970	0.970	0.970	**0.970**	**0.968**
	IH 290	**0.972**	**0.972**	**0.971**	0.968	0.963
	ICH	0.922	0.928	0.939	0.951	0.959
GS	IH 180	1.054	1.056	1.064	1.056	0.971
	IH 290	**2.098**	2.075	1.969	**1.804**	**1.611**
	ICH	2.031	**2.156**	**1.996**	1.749	1.353

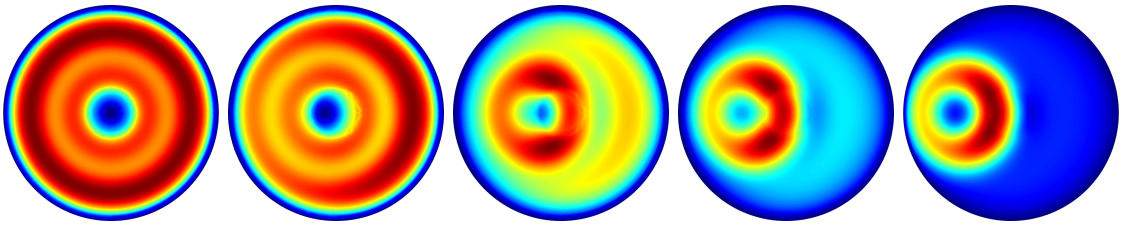

(a) (b) (c) (d) (e)

Figure 4.13: Power distribution of load misalignment at 20 mm distance and 3680 W for the ICH system: (a) 0 mm, (b) 10 mm, (c) 30 mm, (d) 50 mm, (e) 70 mm.

for this distance, but *PF* eventually worsens as well.

Overall, the system can function with the simulated misalignments without adverse effects to the electronics, but the heating performance is strongly penalized. In comparison, the ICH system is slightly better for small misalignments and the $\varnothing_{w,\text{ext}} = 290$ mm IH system is narrowly more robust to high x_{w12}.

The simulated distributions at $P_{\max} \simeq 3680$ W are shown in Fig. 4.13. Although the most problematic misalignments should be easy to spot for most people, the

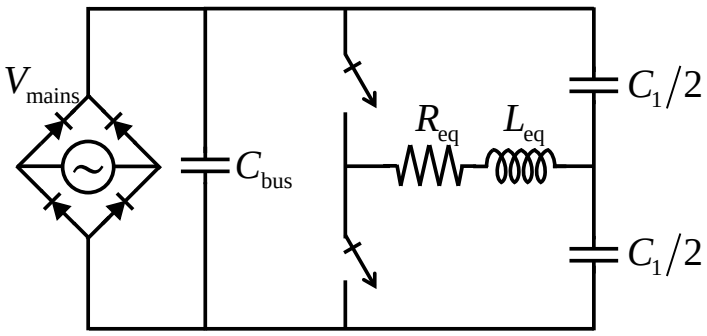

Figure 4.14: Setup topology.

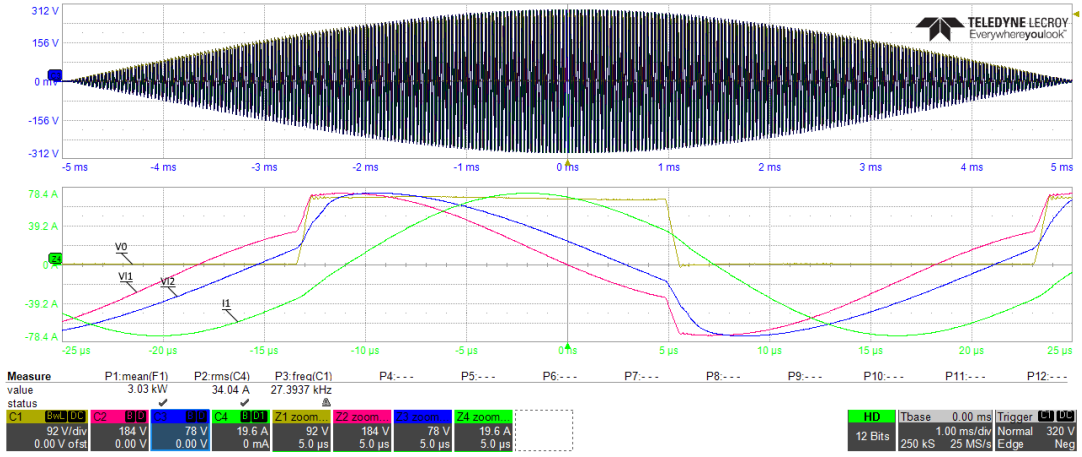

Figure 4.15: Oscilloscope capture of the system with the secondary in open circuit at 10 mm delivering 3000 W.

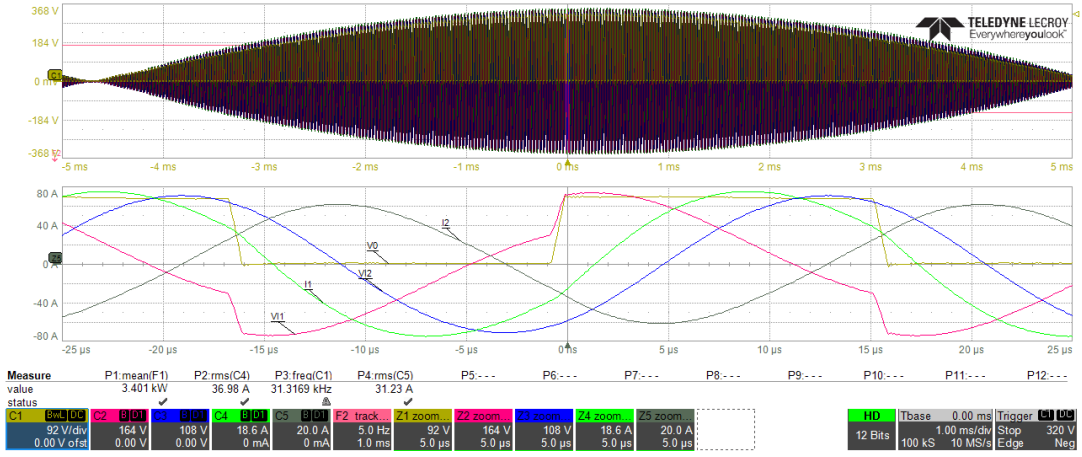

Figure 4.16: Oscilloscope capture of the full system at 20 mm delivering 3400 W.

ICH system would probably benefit from a guiding system of some kind, which at least should be able to detect whether the load is centered or not.

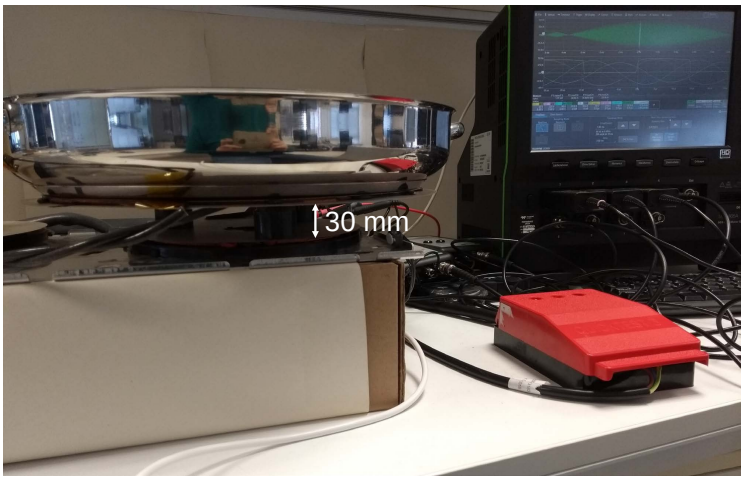

Figure 4.17: Experimental setup.

4.4 Experimental measurements

The designed ICH system is fed with the half-bridge inverter shown in Fig. 4.14 with symmetrical duty cycle, using only f to control P. Voltage and current probes are used to measure inverter voltage, V_o, primary inductor current and voltage, I_1, $V_{\text{ind},1}$, and secondary inductor current and voltage, I_2, $V_{\text{ind},2}$. Sample captures are shown on Figs. 4.15 and 4.16, where C1 is V_o, C2 is $V_{\text{ind},1}$, C3 is $V_{\text{ind},2}$, C4 is I_1 and C5 is I_2.

The experimental setup is shown in Fig. 4.17. The ICH system is on the left of the Figure, as close as possible to the 3D simulated geometry, using polyphenylene sulfide (PPS) separators between inductors to achieve the simulated distances. On the right, the oscilloscope employed is shown. The electronics converter was repurposed from a commercially available IH appliance.

In order to evidence the improvement from a single inductor to the full ICH system and verify the impedance matrix, measurements with the secondary inductor in open circuit are taken first for the smaller d_{w12}, as shown on Fig. 4.18. Due to limitations of the power stage, not all simulated frequencies can be reached with the prototypes. In general, there is good agreement between simulations and measurements. The measured L_{11} and L_{12} values on Fig. 4.18 (f) and (d) at low f peel away from the simulated predictions. The most likely causes are the geometric tolerances and the saturation of the vessel material at high magnetic field strength, both of which explain why the effect is lessened at farther distances between inductors.

Further measurements of the full system were taken for most simulated distances,

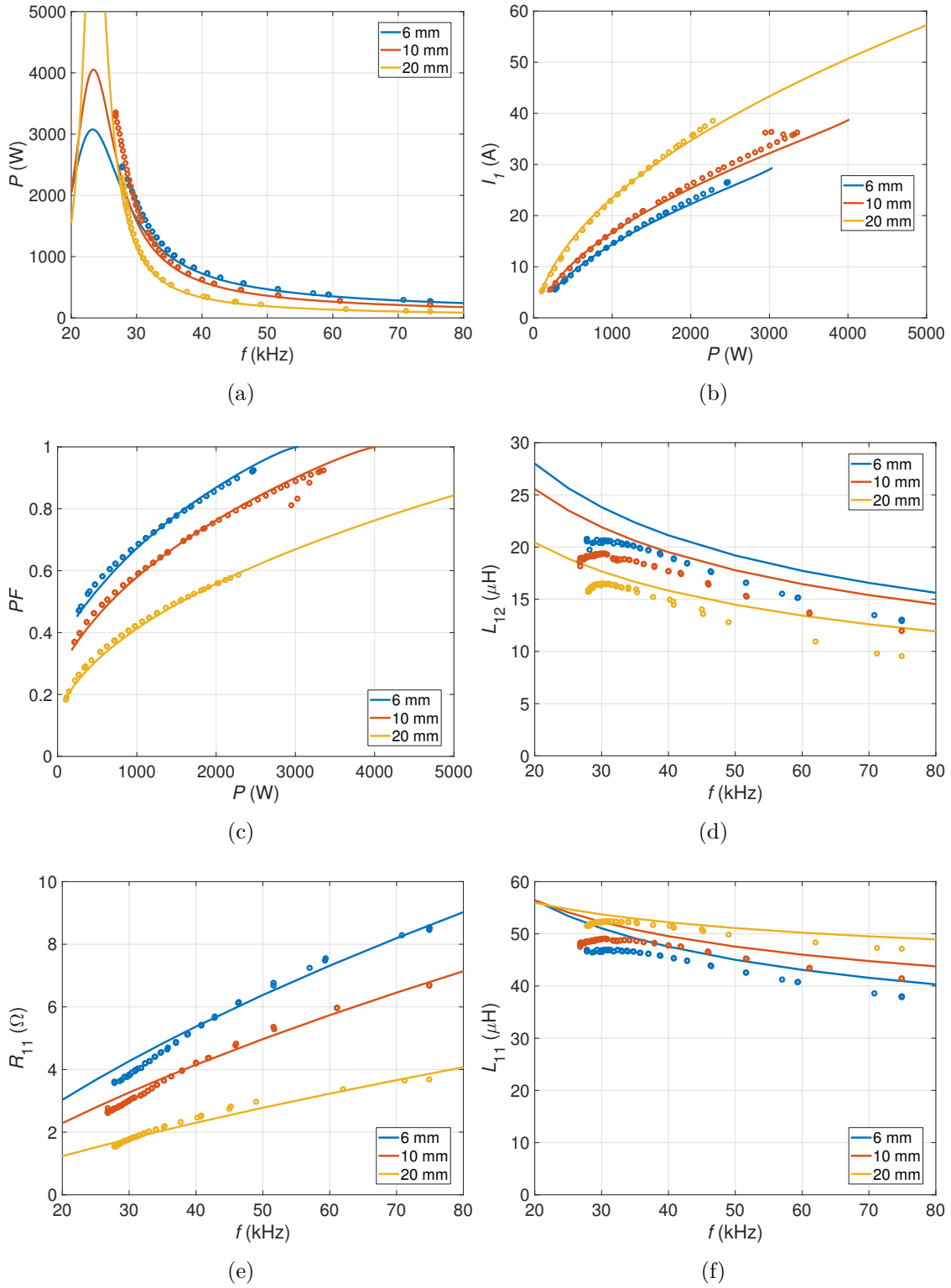

Figure 4.18: Open secondary experimental results: (a) P, (b) I_1, (c) PF, (d) L_{12}, (e)R_{11} and (f) L_{11}.

whose results are shown on Fig. 4.19. The experimental measurements confirm the simulated results in most cases, and the comparison with the open secondary results shows the significant improvement in PF and I_1 from the single $\varnothing_{w,\text{ext}} = 180\,\text{mm}$ IH

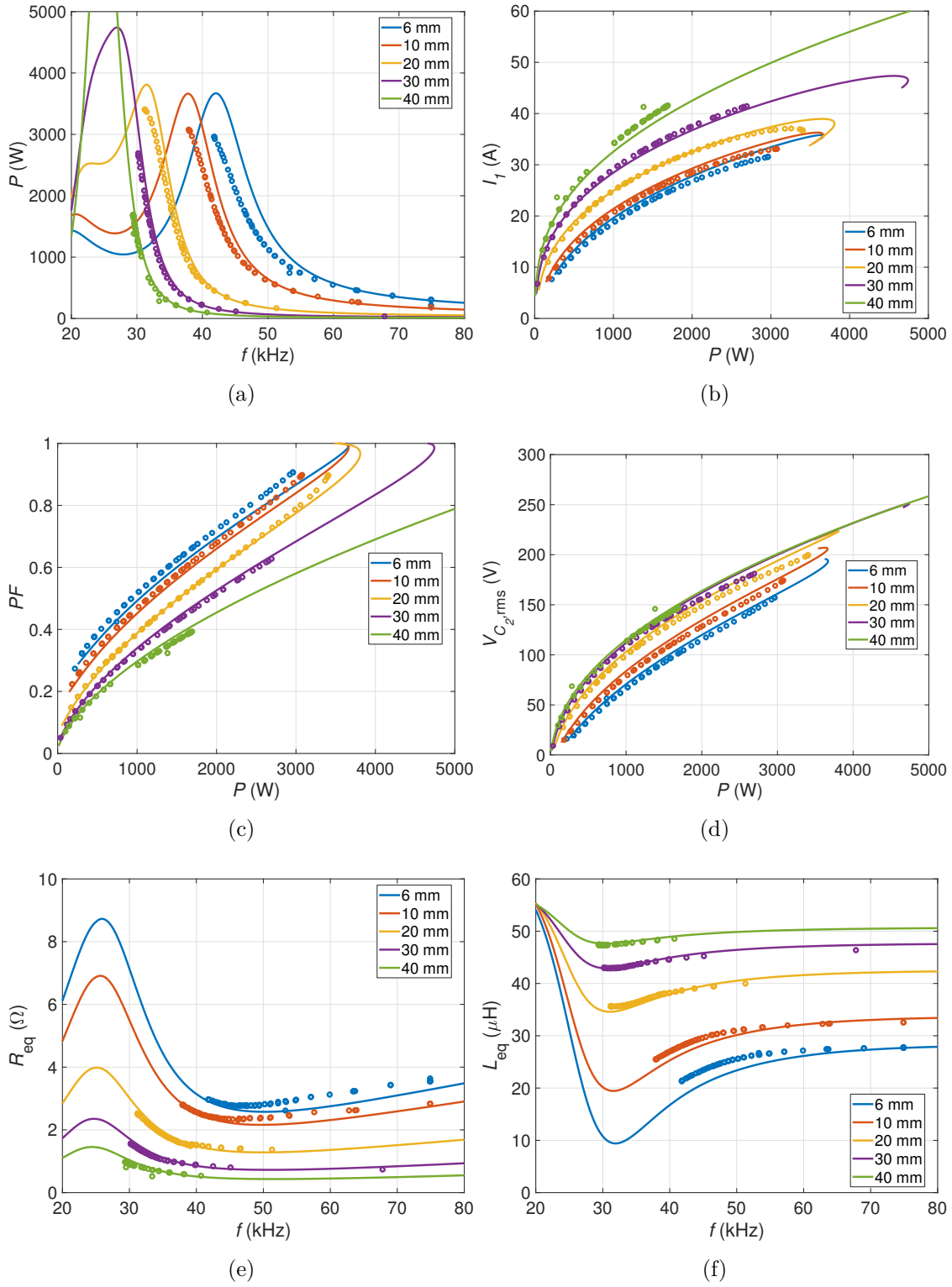

Figure 4.19: Full ICH system experimental results: (a) P, (b) I_1, (c) PF, (d) $V_{C_2,\text{rms}}$, (e) R_{eq} (f) L_{eq}.

system to the full ICH system. As can be seen in Fig. 4.19 (a), there is discrepancy in the P versus f measurement for the smaller d_{w12}. As confirmed by Fig. 4.19 (f), the inductance errors from the impedance matrix directly affect L_{eq}.

(a) (b)

Figure 4.20: Water boiling at high power with secondary inductor (a) off and (b) on.

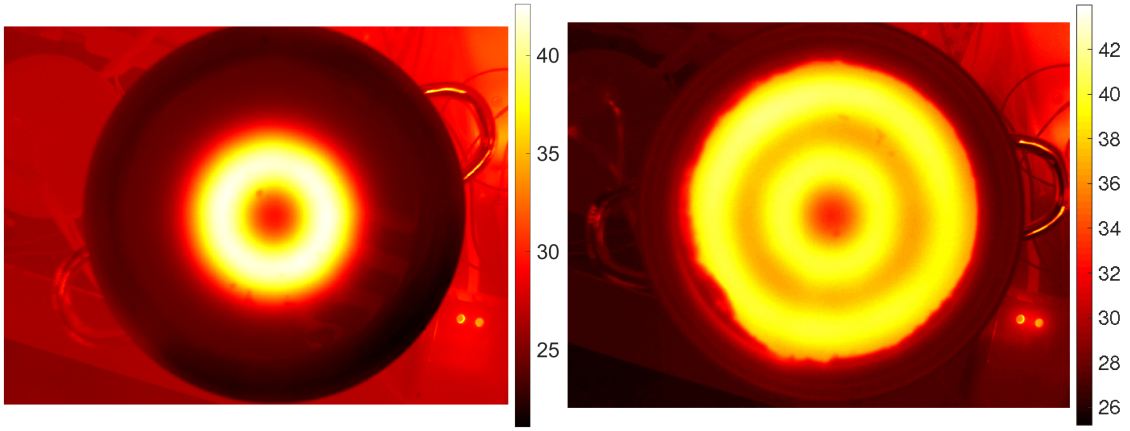

(a) (b)

Figure 4.21: Thermographic images with (a) only the primary inductor and (b) the full system.

In order to qualitatively determine the uniformity of the power distribution, pictures were taken boiling water at $d_{w12} = 10\,\text{mm}$ and $P = 3000\,\text{W}$, shown in Fig. 4.20. Additionally, thermographic images without water were taken for more quantitative results, shown in Fig 4.21. These images were taken when a sudden $P = 3000\,\text{W}$ was applied to the room temperature vessel. The intent was to obtain a temperature distribution as close as possible to the power distribution by minimizing the time in which the heat transfer mechanisms could act. Mean temperature and standard deviation on the vessel's surface are 28.8 °C and 6.3 °C respectively in Fig. 4.21 (a) and 37.8 °C and 2.7 °C in Fig. 4.21 (b). Both figures confirm that the system design provides good *PD*, as expected from the simulations.

Appendix D compiles a list of the most relevant experimental results of the dissertation.

4.5 Conclusion

The simulations and experimental results demonstrate that ICH can indeed be used to adapt a small primary inductor to a relatively big vessel, highlighting the improvement of the ICH system over the traditional IH system. The defined scores allowed an easier optimization complying with the design goals of power delivery, power distribution, electronics stress and efficiency. The simulations were verified with experimental results in terms of system impedance and electrical parameters, as well as the power distribution.

The results also prove that this ICH system can be used effectively at distances higher than 10 mm while achieving the design goals. Therefore, it is suitable to implement the IuW concept without the disadvantages of losing kitchen surface thickness or the disadvantages of increased distance in conventional IH applications. The use of the most common inverter and control methods also ensures a smoother transition from a conventional IH appliance to an ICH appliance.

Lateral misalignment does not negatively affect the electronics, but it penalizes power distribution significantly. Guiding systems should be explored to implement the system into a finished, commercial product. The guidance could rely on mutual impedance measurements, voltage measurements in an array of small inductors, or similar techniques.

Although the prototype is not optimal for each individual goal and inductor distance, it is the most versatile for the distance range presented. On the one hand, if the final application had a fixed distance, the design could be optimized for that situation only. On the other hand, if optimum performance was desired in all cases, a further improvement could be the ability for the secondary capacitor to switch values to best suit each situation.

Chapter 5

Multiple loads with a single transmitter

This chapter develops the design process of ICH systems to heat two magnetically independent loads on different horizontal planes simultaneously, creating a small oven. A single primary inductor acts as transmitter to transfer power to a secondary inductor attached to the bottom load, which is connected electrically with a third inductor that heats the top load. The power ratio is critical for cooking results, so its relation with the system impedance is established. It is intended to deliver more power to the top load with respect to the bottom load. A prototype was built to validate the impedance results in the small signal regime first and then the full power regime was used to verify power and current simulations.

Table of contents

5.1 Introduction 143
5.2 System model and design 144
5.2.1 ICH system model 144
5.2.2 System design and relevant parameters 150
5.3 Experimental measurements 156
5.3.1 Small signal regime 156
5.3.2 Full power regime 158
5.4 Conclusion 164

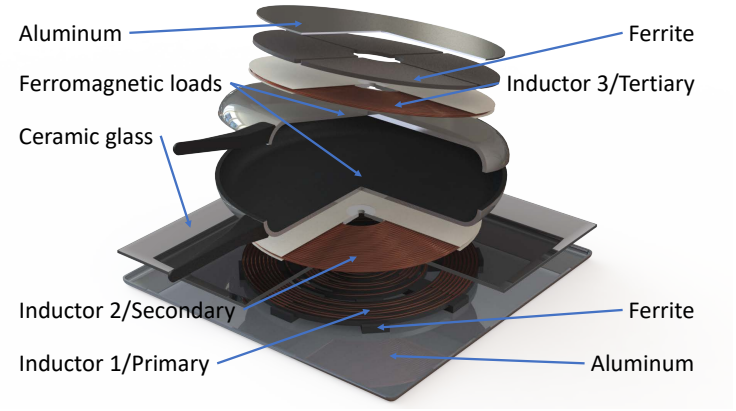

(a)

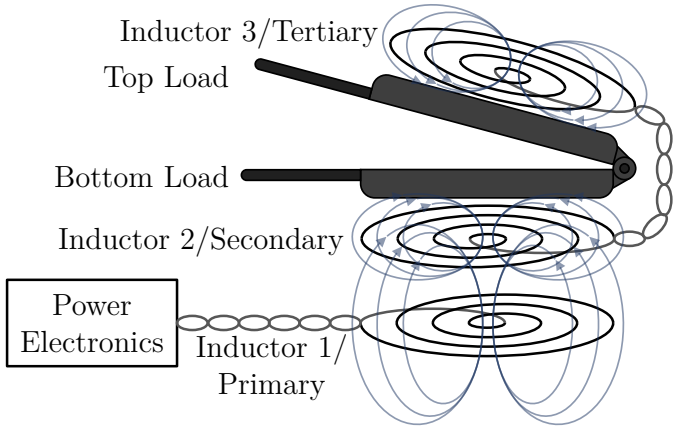

(b)

Figure 5.1: (a) Exploded system geometry and (b) inductor connections diagram.

5.1 Introduction

Currently, there is an increasing demand for small appliances that use WPT technology, and many of them require heating. Moreover, some of these appliances require heating areas independent from its bottom surface, unreachable by IH alone or other conventional cooking technologies, such as gas or electrical glass-ceramic.

An ICH system with a third inductor connected in series with the secondary inductor can be used to create cordless portable ovens and double-sided pans where both upper and lower baking sheets are heated simultaneously, as shown in Fig. 5.1. The main advantages of this kind of cooking appliance are their enclosed space to prevent heat loss, like an oven, and their small volume to reduce energy requirements. Instead of flipping manually to keep both sides heated, the proposed system will heat both sides simultaneously, with a single correct "upright" position.

A single inductor is fed by a power electronics inverter, which heats the bottom

load and transmits power to a secondary inductor which in turn is electrically connected to a third coil to heat an independent, top load. Consequently, a single primary cooktop inductor is able to deliver power to two different loads simultaneously, which can be placed in different planes, preventing their coupling. In the case of Fig. 5.1 (a), the uncoupled heating zone is the top cover of a small, slim oven. In its current form, the first and second inductors need to be aligned, and the bottom cooking zone should be placed just above the secondary inductor. Nevertheless, the third inductor and top cooking zone or vessel can be placed anywhere, requiring only an electrical connection to the secondary coil as depicted in the diagram in Fig. 5.1 (b).

The objective of this chapter is to design and test a $\varnothing_{w1,\text{ext}} = 210\,\text{mm}$ ICH system capable to deliver $P = 3000\,\text{W}$ to two ferromagnetic loads, where at least 50 % of power is transferred to the top load. This requirement ensures that the system can give more heat to the top load, in order to cook meals that need higher temperature on the top, and to correct imbalances in processes that require homogeneous temperature. The position of the loads prevents coupling between their corresponding inductors and thus requires an electrical connection. The system must also work in conjunction with a conventional IH cooktop to reduce cost, and so that the secondary inductor itself does not need a cord to connect to the mains, an inverter topology or bulky filters.

The power flow in the system goes as follows: the induction heating cooktop feeds the primary inductor, which simultaneously heats the bottom load and transfers power to the second inductor. The second inductor contributes to heating the bottom load and is electrically connected to the third inductor. The third inductor's sole purpose is to heat the top load.

The power ratio objective is achieved with impedance tuning only, without additional active components.

5.2 System model and design

5.2.1 ICH system model

The modelled system depicted in Fig. 5.1 (a) consists of a $\varnothing_{w1,\text{ext}} = 210\,\text{mm}$ primary inductor with ferrite bars and an aluminum shielding tray, a $\varnothing_{w2,\text{ext}} = 210\,\text{mm}$ attached to the bottom ferromagnetic load and a third inductor of the same size attached to the top ferromagnetic load. The first and second inductors are separated

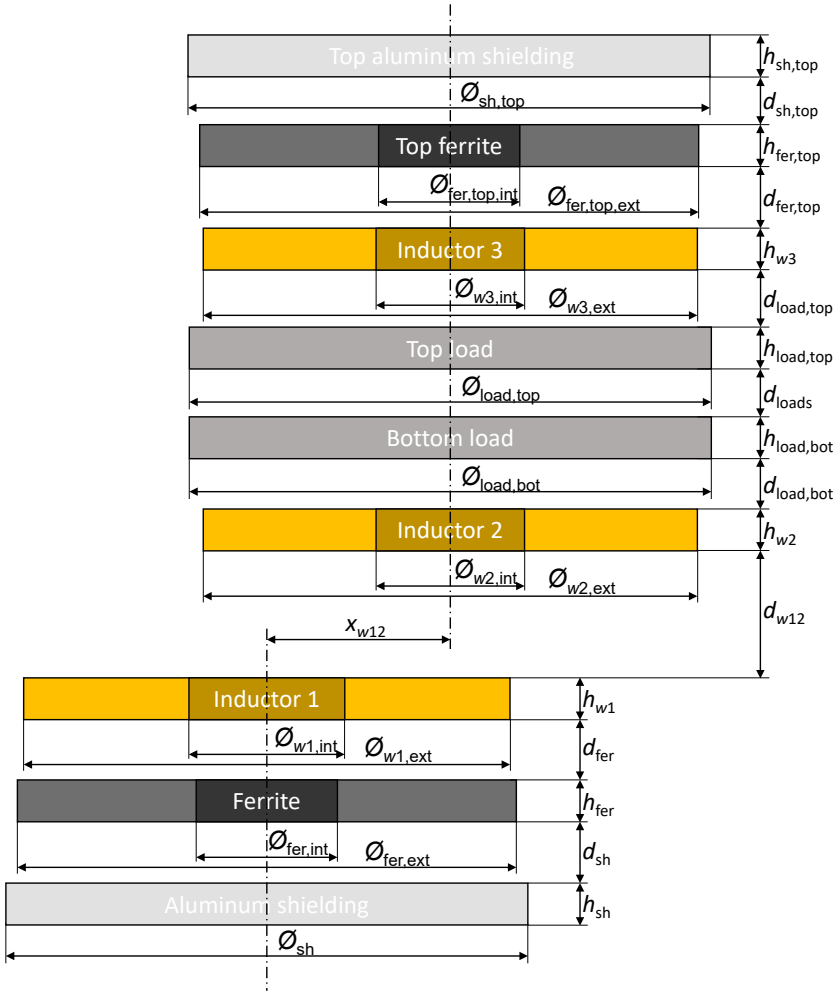

Figure 5.2: System geometry parameters

by ceramic glass and are magnetically coupled. The third inductor has a ferrite plane and a second aluminum tray above it for magnetic shielding. It is not magnetically coupled with the others, but it is electrically connected to the second inductor. Fig 5.2 shows a diagram with the geometry parameters.

The circuit diagram of a generic three inductor system is shown in Fig. 5.3 (a). As described in previous chapters, this circuit can be expressed in the form of a matrix equation:

$$\begin{pmatrix} Z_{11} & Z_{12} & Z_{13} \\ Z_{21} & Z_{22} & Z_{23} \\ Z_{31} & Z_{32} & Z_{33} \end{pmatrix} \begin{pmatrix} I_1 \\ I_2 \\ I_3 \end{pmatrix} = \begin{pmatrix} V_1 \\ V_2 \\ V_3 \end{pmatrix}, \tag{5.1}$$

where I_i is the current of the ith inductor, V_i is its external voltage and Z_{ij} the elements of the impedance matrix, including capacitor reactance.

In this case, the second and third inductors are connected in series. Therefore, only two resonant capacitors are needed, one for the primary inductor and another

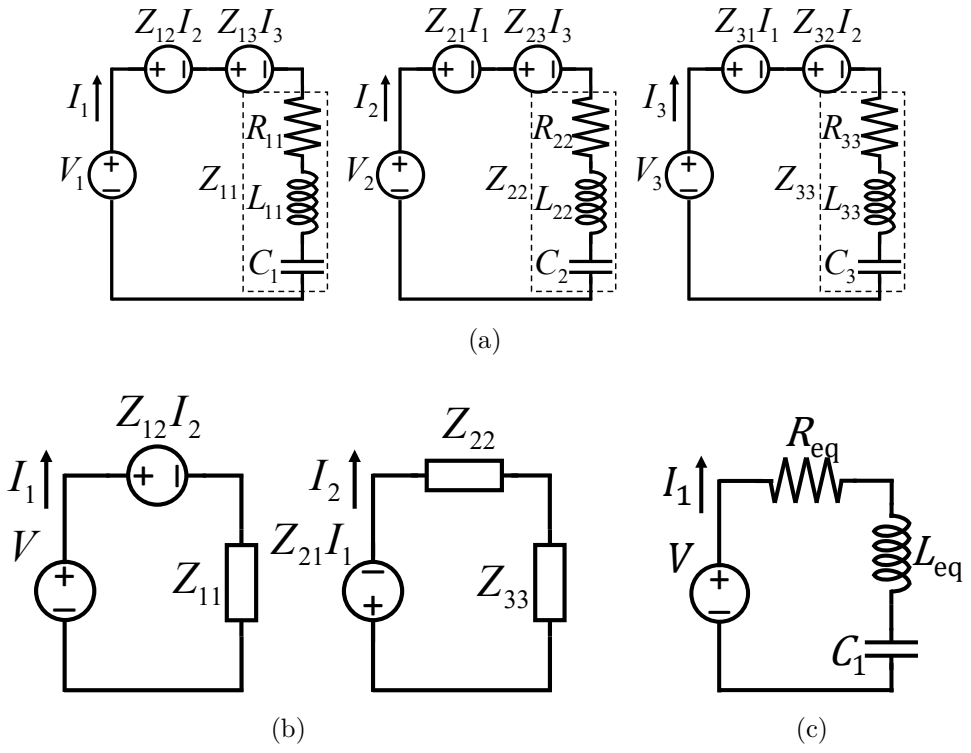

Figure 5.3: Circuit diagrams: (a) generic three-inductor (b) proposed system's simplified circuit (c) inverter equivalent impedance circuit.

for the receiver side, that is, the series connected second and third inductors. The equations can then be simplified, as the current running through both inductors is the same and the voltage sum is zero, since there is no external voltage source:

$$I_2 = I_3, \tag{5.2}$$

$$V_2 + V_3 = 0. \tag{5.3}$$

Therefore, the reduced order equation system is:

$$\begin{pmatrix} Z_{11} & Z_{12} + Z_{13} \\ Z_{21} + Z_{31} & Z_{22} + 2Z_{23} + Z_{33} \end{pmatrix} \begin{pmatrix} I_1 \\ I_2 \end{pmatrix} = \begin{pmatrix} V_1 \\ 0 \end{pmatrix}. \tag{5.4}$$

In this system, the third inductor will heat a load inaccessible to the first two, as both loads are magnetically independent. Consequently, the terms Z_{13} and Z_{23} are considered negligible, which will be verified in the simulations. Therefore the equations can then be simplified to:

$$\begin{pmatrix} Z_{11} & Z_{12} \\ Z_{21} & Z_{22} + Z_{33} \end{pmatrix} \begin{pmatrix} I_1 \\ I_2 \end{pmatrix} = \begin{pmatrix} V_1 \\ 0 \end{pmatrix}, \tag{5.5}$$

and the resulting simplified circuit is shown in Fig. 5.3 (b). Moreover, the magnetic independence of the top load and third inductor makes Z_{33} the only impedance

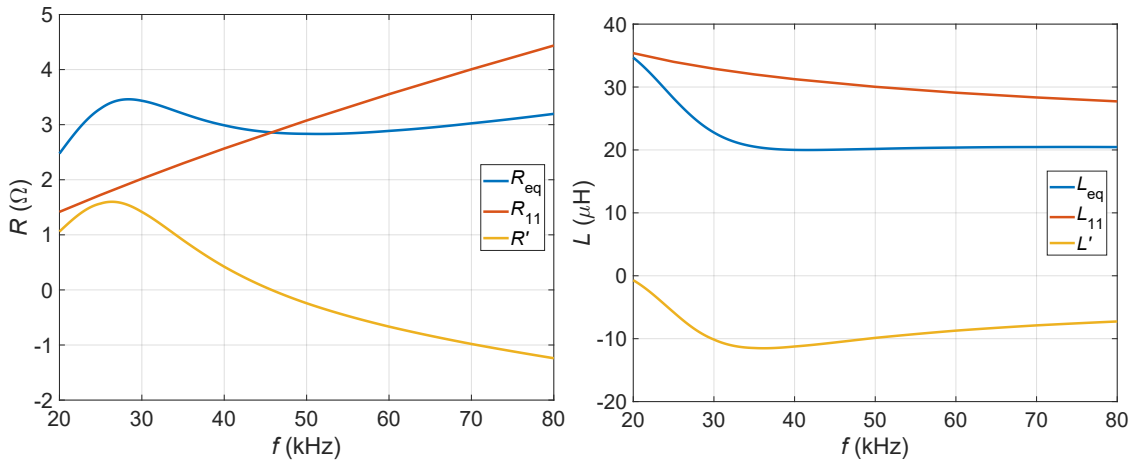

(a) (b)

Figure 5.4: Equivalent resistance (a) and inductance (b) breakdown according to (5.9) and (5.10).

matrix element related to the top load. Z_{11}, Z_{12} and Z_{22} all relate to the bottom load.

As the primary inductor is the only one with a voltage source, the system can be reduced to a single equivalent impedance, Z_{eq}, from the inverter's point of view. The circuit of Fig. 5.3 (b) can therefore be simplified to that of Fig. 5.3 (c). Moreover, the equivalent impedance is defined as:

$$Z_{\text{eq}} = \frac{V_1}{I_1} = Z_{11} - \frac{Z_{12}^2}{Z_{22} + Z_{33}}, \tag{5.6}$$

where the receiver side impedance can be expressed together for simplicity:

$$R_{\text{rec}} = R_{22} + R_{33}, \tag{5.7}$$

$$L_{\text{rec}} = L_{22} + L_{33}. \tag{5.8}$$

Equivalent resistance, R_{eq}, and inductance, L_{eq}, can be defined as:

$$R_{\text{eq}} = R_{11} + \underbrace{\frac{2R_{12}\omega L_{12}\left(\omega L_{\text{rec}} - \frac{1}{\omega C_2}\right) - \left(R_{12}^2 - \omega^2 L_{12}^2\right) R_{\text{rec}}}{R_{\text{rec}}^2 + \left(\omega L_{\text{rec}} - \frac{1}{\omega C_2}\right)^2}}_{R'}, \tag{5.9}$$

$$L_{\text{eq}} = L_{11} + \underbrace{\frac{2R_{12}\omega L_{12}R_{\text{rec}} - \left(R_{12}^2 - \omega^2 L_{12}^2\right)\left(\omega L_{\text{rec}} - \frac{1}{\omega C_2}\right)}{\omega\left(R_{\text{rec}}^2 + \left(\omega L_{\text{rec}} - \frac{1}{\omega C_2}\right)^2\right)}}_{L'}, \tag{5.10}$$

where R', L' are the resistance and inductance reflected to the primary side. Equations (5.9) and (5.10) have the same structure as (3.40) and (3.41) respectively.

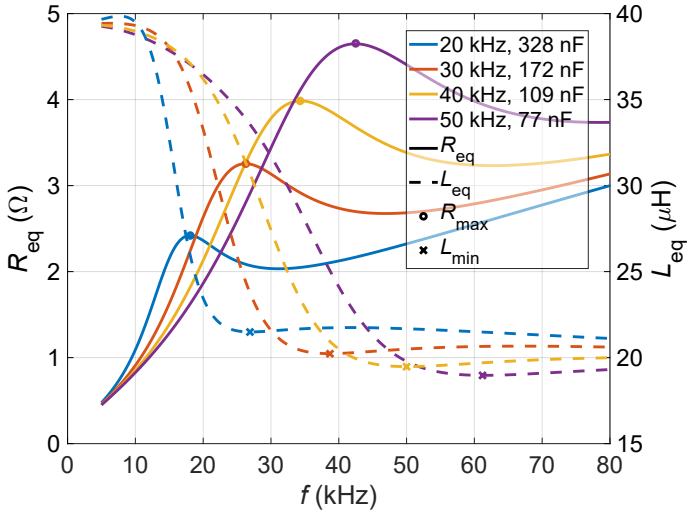

Figure 5.5: Simulated equivalent resistance and inductance versus frequency for different $\omega_{0,\text{rec}}$, with specific C_2 values.

For visual reference, the contributions of the elements R_{11}, R', and L_{11}, L' to R_{eq} and L_{eq} respectively are represented in Fig. 5.4 for ferromagnetic loads. R' increases R_{eq} at the low frequency range, with a maximum peak, and decreases it in others. L' only decreases L_{eq} at the considered frequency range, with a minimum valley close to the R_{eq} peak. In this case, the resonant frequency of individual inductors, $\omega_{0,i}$ is not useful to determine the behaviour of the entire receiver, composed of the second and third inductors in series. Moreover, receiver side resonant frequency, $\omega_{0,\text{rec}}$ can be defined as:

$$\omega_{0,\text{rec}} = \frac{1}{\sqrt{(L_{22} + L_{33})C_2}}, \tag{5.11}$$

which has the same relevance as $\omega_{0,2}$ did in previous chapters. Fig. 5.5 shows simulated impedance values for the proposed system, changing C_2 and keeping the values of $n_{t,i} = 19$ and $C_1 = 800\,\text{nF}$ constant. The values of C_2 are determined using (5.11) to achieve the stated $\omega_{0,\text{rec}}$ for each color. As shown, the impedance can be in the same order of magnitude than the values of a typical domestic IH application which means that it could be compatible with current cooktops. Moreover, both R_{eq} and L_{eq} are strongly dependent with f, with maximum and minimum values marked with circles and crosses respectively. Maximum R_{eq} values are found slightly to the left of $\omega_{0,\text{rec}}$ while minimum L_{eq} values are found slightly to the right.

These extreme values of impedance close together in f also affect other derived values, such as the power ratio, PR_{top}, between the top ferromagnetic load power,

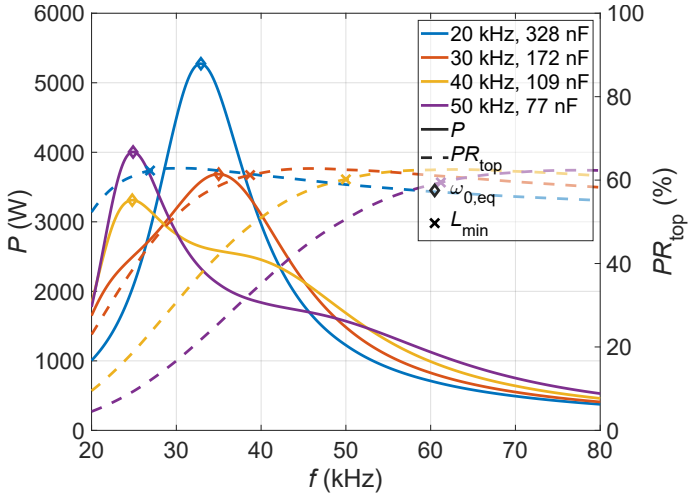

Figure 5.6: Simulated total power and percentage of power delivered to the top load versus frequency for different $\omega_{0,\mathrm{rec}}$.

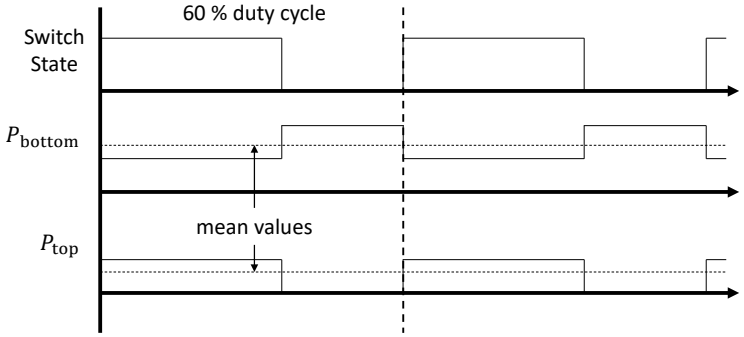

Figure 5.7: Power split diagram depending on receiver connection state.

$P_{\mathrm{load,top}}$ and total transferred power, P, defined as:

$$P = P_{\mathrm{load,bottom}} + P_{\mathrm{load,top}}, \tag{5.12}$$

$$PR_{\mathrm{top}} = \frac{P_{\mathrm{load,top}}}{P} = \frac{R_{33}\left|I_3\right|^2}{R_{\mathrm{eq}}\left|I_1\right|^2} = \frac{R_{33}\left|Z_{12}\right|^2}{R_{\mathrm{eq}}\left|Z_{22}+Z_{33}\right|^2}, \tag{5.13}$$

where $P_{\mathrm{load,bottom}}$ is the power delivered to the bottom load. PR_{top} has a maximum value at f close to the inductance minimums, as shown in Fig. 5.6 for the same parameters of Fig. 5.5. The shift of $\omega_{0,\mathrm{rec}}$ causes a change in L_{eq}, as explained previously, which in turn causes a change in $\omega_{0,\mathrm{eq}}$ from 35 kHz to 25 kHz.

In Fig. 5.6 it can also be seen that for most of the P curve in the 20 and 30 kHz cases, the ratio of the power delivered to the top load is almost constant at 60 %. Consequently, this design is most suitable for applications where PR_{top} needs to remain nearly constant for all delivered P values.

A degree of independent $P_{\mathrm{load,top}}$ control can be achieved using a switch on the receiver side. The switch would enable alternating the power split between

Table 5.1
Per-turn resistance values of the impedance matrix at 30 kHz

i \ j	$R_{i1,\text{p.t.}}(\text{m}\Omega)$	$R_{i2,\text{p.t.}}(\text{m}\Omega)$	$R_{i3,\text{p.t.}}(\text{m}\Omega)$
$R_{1j,\text{p.t.}}$	6.72	8.59	0.00202
$R_{2j,\text{p.t.}}$	8.59	11.1	0.00187
$R_{3j,\text{p.t.}}$	0.00202	0.00187	18.8

Table 5.2
Per-turn inductance values of the impedance matrix at 30 kHz

i \ j	$L_{i1,\text{p.t.}}(\text{nH})$	$L_{i2,\text{p.t.}}(\text{nH})$	$L_{i3,\text{p.t.}}(\text{nH})$
$L_{1j,\text{p.t.}}$	114	76.2	0.00671
$L_{2j,\text{p.t.}}$	76.2	97.4	0.00891
$L_{3j,\text{p.t.}}$	0.00671	0.00891	110

100 %–0 %, opening the receiver circuit, and 40 %–60 %, connecting the receiver circuit. Time averages can be used to interpolate intermediate ratios, as depicted in Fig. 5.7. Higher PR_{top} would enable a wider range of power splits. However, the capability to independently select the power for each load is not implemented in this first approach.

5.2.2 System design and relevant parameters

In order to obtain the impedance matrix, the system was simulated in 3D in COMSOL Multiphysics. 2D simulations are discouraged because the system uses ferrite bars in its primary inductor, breaking full axial symmetry.

Impedance results at 30 kHz are shown in Tables 5.1 and 5.2, where the simplification made in (5.5) is justified. The coupling factors for the table values are $k_{L,12} = 0.7231$ and $k_{R,12} = 0.9946$. As expected, the symmetry in the impedance matrix, that is, the relation $Z_{ij} = Z_{ji}$, is also verified.

The emitted magnetic flux needs to be analyzed in this application due to several inductors operating simultaneously. Fig. 5.8 represents the simulated magnetic field generated, $|\mathbf{B}|$, first by only the first inductor, $|\mathbf{B}_1|$, in a IH configuration, and then by the full ICH system when delivering 3000 W. The field levels are similar in both cases, with more magnitude in the IH case in the radial direction and more magnitude in the ICH system in the vertical direction.

Fig. 5.9 represents the simulated Poynting's vector, S, in the loads, first in the

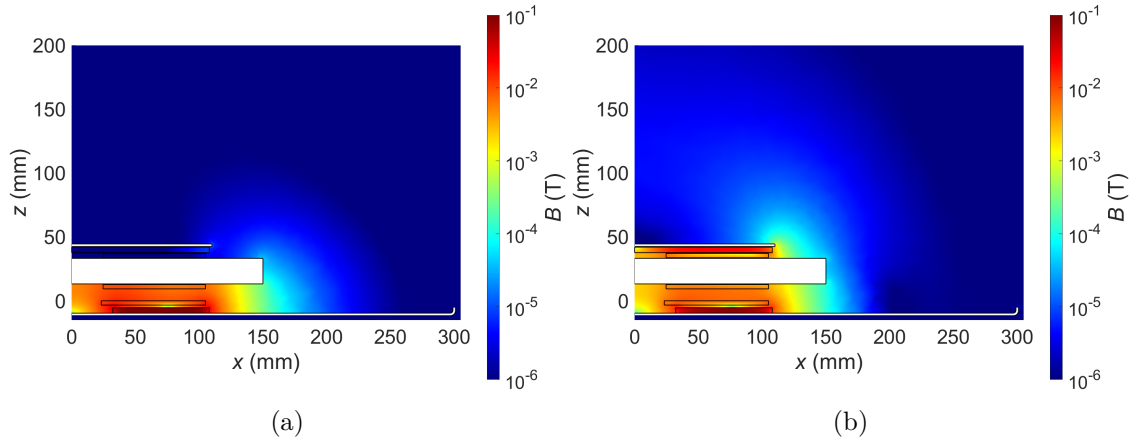

Figure 5.8: Simulated magnetic field to deliver 3000 W (a) First inductor only (b) Full ICH system.

IH case and then by the full ICH system when delivering 3000 W. Considering the external diameters of the inductors compared to the loads, the power distribution is as even as it can possibly be. Therefore, no further action needs to be taken to improve it.

The finite element simulation has provided the per-turn inductor elements of the impedance matrix represented in Table 5.1 and Table 5.2. Now it remains to select the number of turns, $n_{t,i}$, of each inductor and the capacitor values, C_i. As part of a commercial half-bridge IH appliance, P is frequency controlled. Consequently, the ICH system needs to have a monotonic relation between f and P, from 0 W to 3000 W.

As the system must be compatible with an existing IH cooktop, C_1 and $n_{t,1}$ are predetermined. In this study, the values that can be changed by design are $n_{t,2}$ and $n_{t,3}$, as well as C_2.

In order to operate at a relatively constant PR_{top}, the working frequencies have to be greater than those of the maximum R_{eq} and minimum L_{eq}, as seen in Figs. 5.5 and 5.6. These extreme values are related to the resonance of the receiver side, $\omega_{0,\text{rec}}$.

In most cases maximum power is obtained at the equivalent system's resonance, $\omega_{0,\text{eq}}$. PR_{top} is desired to remain constant up to maximum P, so $\omega_{0,\text{eq}}$ has to be set at a slightly higher frequency than $\omega_{0,\text{rec}}$, which can be seen in Fig. 5.6. When $\omega_{0,\text{rec}}$ is set at 20 and 30 kHz, $\omega_{0,\text{eq}}$ is above 30 kHz and PR_{top} ranges between 10 % and 60 %. Fig. 5.5 also shows that $\omega_{0,\text{rec}}$ causes an inflection point in the P curve due the impedance extreme values, both R_{eq} and L_{eq}.

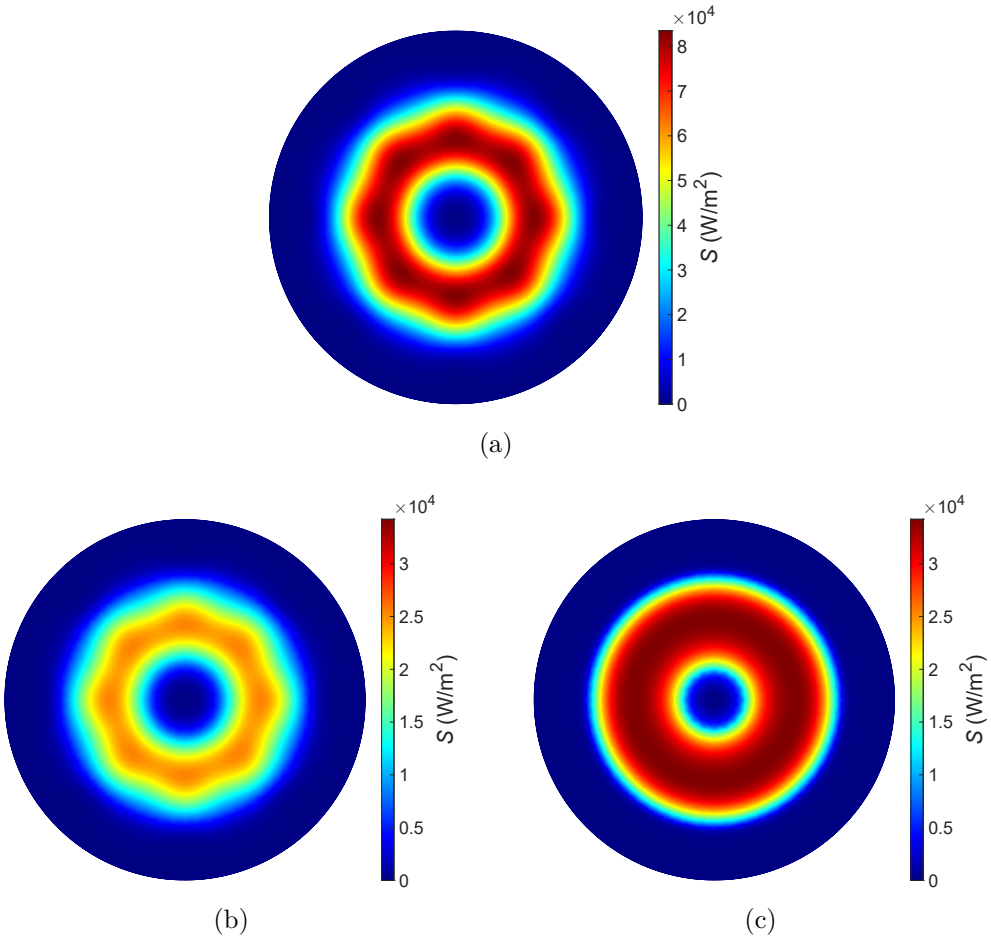

Figure 5.9: Simulated power density to deliver 3000 W (a) First inductor only (b) Full ICH system bottom (c) Full ICH system top.

Writing (5.6) in terms of single-turn impedance elements:

$$Z_{\text{eq}} = n_{t,1}^2 \left(Z_{11,\text{p.t.}} - \frac{Z_{12,\text{p.t.}}^2}{Z_{22,\text{p.t.}} + \dfrac{n_{t,3}^2}{n_{t,2}^2} Z_{33,\text{p.t.}}} \right). \tag{5.14}$$

This expression shows that $n_{t,2}$ and $n_{t,3}$ only affect Z_{eq} by their relative values to each other. Moreover, for each fixed value of $n_{t,3}/n_{t,2}$, the impedance only depends on $n_{t,1}$.

Bearing these considerations in mind, the design process goes as follows. In order to be able to deliver 3000 W with near constant PR_{top}, the system must have a $\omega_{0,\text{eq}}$ at higher ω than $\omega_{0,\text{rec}}$, and R_{eq} needs to satisfy:

$$\frac{V_{o,\text{rms}}^2}{R_{\text{eq}}} > 3000\,\text{W} \,@\, \omega_{0,\text{eq}}, \tag{5.15}$$

where $V_{o,\text{rms}}$ is the inverter output rms voltage. The half-bridge inverter uses a small DC bus capacitor, so its output voltage essentially modulates the rectified

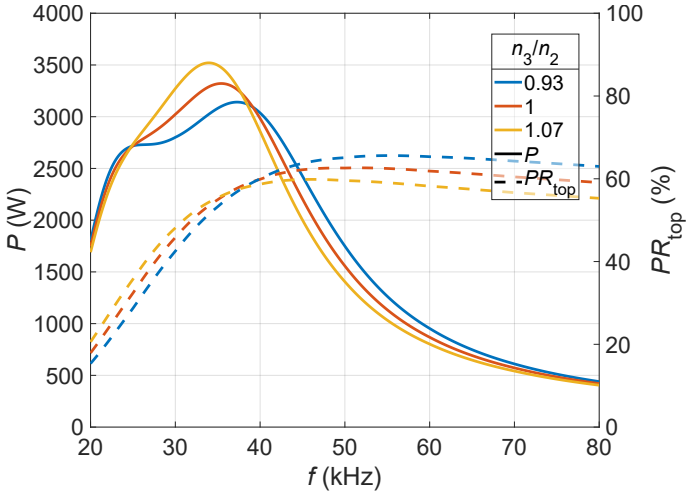

Figure 5.10: Simulated P and PR_{top} variation with n_3/n_2.

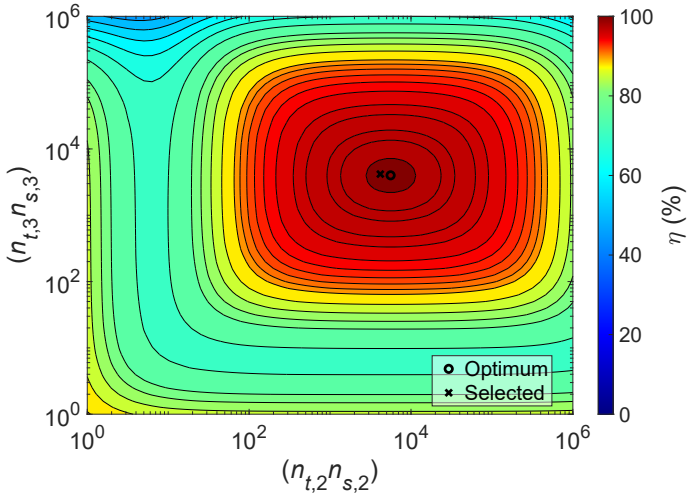

Figure 5.11: System η with sweeping $(n_{t,2}n_{s,2})$ and $(n_{t,3}n_{s,3})$.

mains voltage:

$$V_{\text{rms}}^2 = \frac{\sqrt{2}}{\pi} V_{\text{mains,rms}}. \tag{5.16}$$

In terms of number of turns and capacitor values, $C_{2,\text{p.t.}}$ can be selected to fix $\omega_{0,\text{rec}}$ at the desired value:

$$C_{2,\text{p.t.}} = \frac{1}{\omega_{0,\text{rec}}^2 \left(L_{22,\text{p.t.}} + \dfrac{n_{t,3}^2}{n_{t,2}^2} L_{33,\text{p.t.}} \right)}. \tag{5.17}$$

After selecting a potential $\omega_{0,\text{rec}}$, the designer must ensure that the 3000 W maximum power condition is met, as well as verify that $\omega_{0,\text{rec}} < \omega_{0,\text{eq}}$.

Since only the relative value of $n_{t,2}$ with $n_{t,3}$ affects global impedance, their absolute values can be used to freely select the ratio of $V_{\text{ind},2}$ and I_2 when delivering

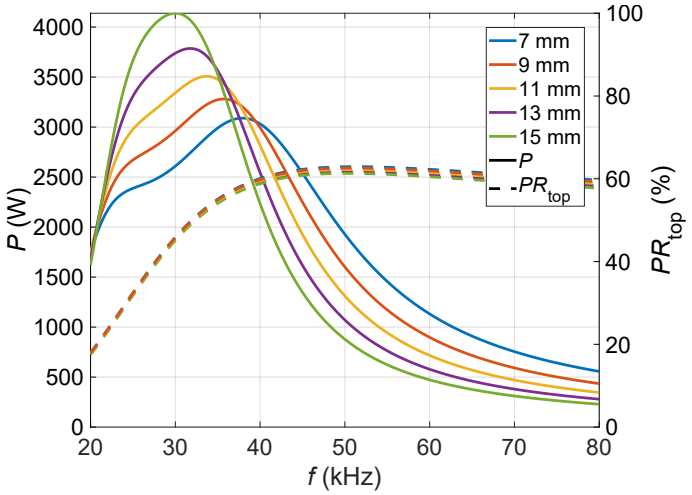

Figure 5.12: Simulated power and power ratio variation with inductor distance.

the same P. The effects of the $n_{t,3}/n_{t,2}$ ratio on P and PR_{top} are shown in Fig. 5.10. An increase of the ratio increases maximum P and PR_{top} and reduces $\omega_{0,\text{eq}}$. In this case, $n_{t,2} = n_{t,3}$ has been chosen for simplicity, as it fulfills the PR_{top} requirement using identical coils, simplifying the manufacturing process. Additionally, if the shielding of the third inductor was not required, the equal n_t would enable a symmetrical design, without distinguishable top or bottom loads. PR_{top} would be maintained, whichever side ended up on top.

System efficiency includes losses elements from all three inductors. As the primary inductor is fixed due to the commercial cooktop, $n_{t,1} = 17$, $n_{s,1} = 180$ and $\varnothing_{s,1} = 200\,\mu\text{m}$ are already set. Fig. 5.11 shows the simulated η for sweeping values of $(n_{t,2}n_{s,2})$ and $(n_{t,3}n_{s,3})$, with highlighted optimum and selected values. The difference between optimum and selected values are due to cable construction limitations. The optimum value of 97.4 % is similar to those of conventional IH systems.

The system is intended to work with an IH cooktop, which has a 4-5 mm thick ceramic glass. Additionally, depending on the final design, the housing of the proposed system would add an additional 4-5 mm too the distance between primary and secondary inductors. The FEA simulations have assumed a total 9 mm distance between inductors. Fig. 5.12 shows the effects of increasing inductor distance on P and PR_{top}. Separating the receiver increases maximum P and reduces $\omega_{0,\text{eq}}$, but it barely has an effect on PR_{top}. As a result, PR_{top} is slightly reduced at maximum P.

Usually, small adjustments need to be made in order to end up with an integer n_t and available C values. The prototype in this chapter has a predetermined $n_{t,1}$

Table 5.3
Experimental system design parameters

Inductor	$n_{t,i}$	$n_{s,i}$	C_i (nF)
1, primary	17	180	1080
2, secondary	29	144	150
3, tertiary	29	144	–

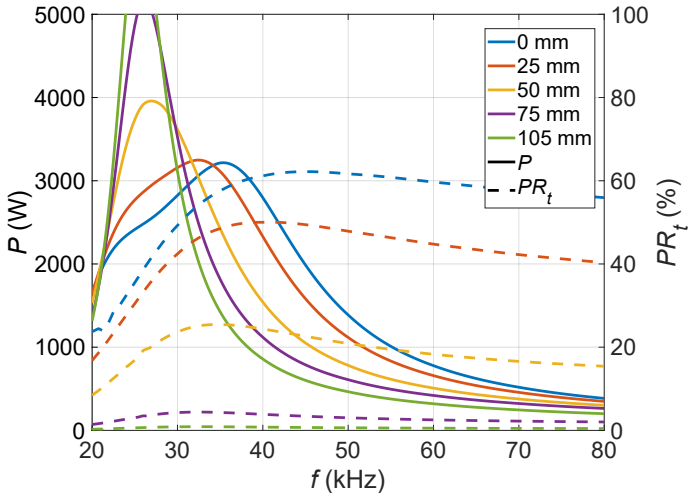

Figure 5.13: P and PR_t variation with radial load misalignment.

and C_1 for the primary inductor defined by the commercial cooktop, 17 turns and 1080 nF, the selected $n_{t,2}$ and $n_{t,3}$ are 29 turns, the chosen $n_{s,2} = n_{s,3} = 144$ and the selected C_2 has 150 nF. This results in a $\omega_{0,\text{eq}}$ of 35 kHz and $\omega_{0,\text{rec}}$ of 30 kHz. The system parameters are listed in Table 5.3 for convenience.

A high n_t was chosen for the second and third inductors to show that their absolute value would only affect the current and voltage ratio in the receiver side, and that Z_{eq} would remain constant as long as the value of $C_{2,\text{p.t.}}$ was maintained by changing C_2 accordingly. Copper cable is used for all inductors due to efficiency requirements and relatively small inductor volume.

As any IH application, the system could be subjected to rapid movements by the user. Fig. 5.13 shows how P and PR_{top} changes with horizontal inductor distance, $x_{w,12}$, illustrating that for any misalignment, the system will immediately reduce its P and PR_{top} if the frequency is not changed. Moreover, the P and PR_{top} changes are significant even for $x_{w,12}$ smaller than 25 mm. The simulated η does not decrease considerably with $x_{w,12}$, as shown in Fig. 5.14, where the minimum value remains above 93 %. Due to how the system works inherently, it does not need complex

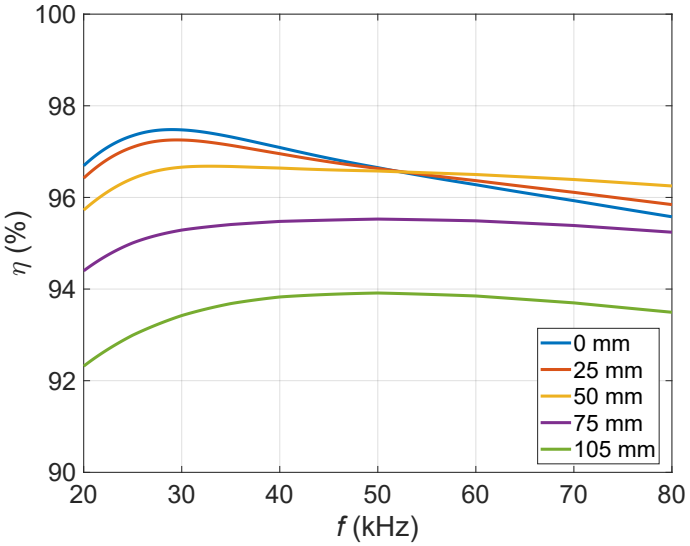

Figure 5.14: Efficiency variation with load misalignment.

Figure 5.15: LCR setup measuring inductors one and two.

control to operate safely, and it is easy to detect misalignment and warn the user to correct it and maximize PR_{top} again.

5.3 Experimental measurements

First, in order to verify the impedance simulation results, measurements of the impedance matrix have been taken in a small signal regime at several frequencies. Then, the system has been tested delivering full power to two ferromagnetic loads to validate the proposed design.

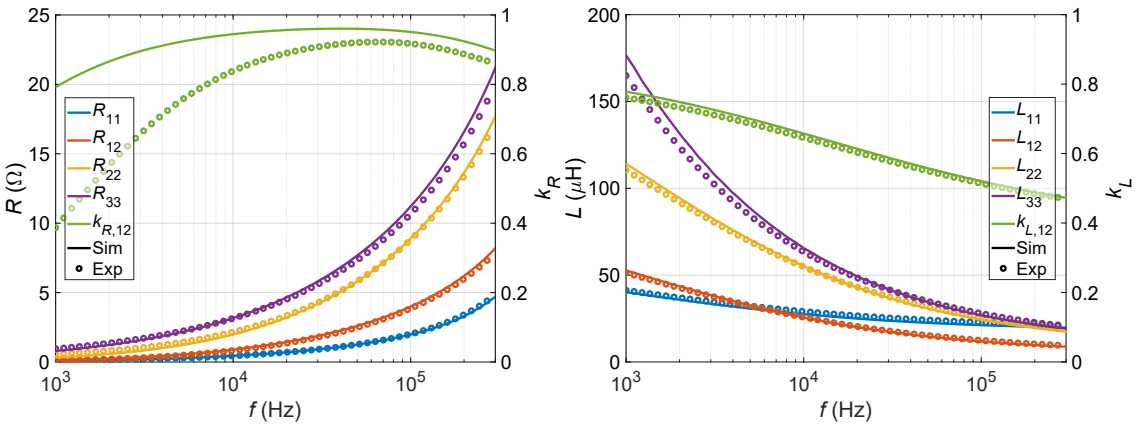

(a) (b)

Figure 5.16: Resistance (a) and inductance (b) of the impedance matrix elements measured by LCR.

5.3.1 Small signal regime

A LCR meter has been used to measure self impedance of inductors one, two and three as well as the mutual impedance between one and two. Given that the third inductor is decoupled from the rest, as verified by the simulations, mutual impedances with the third inductor have not been considered. Fig. 5.15 shows the small signal setup with the first two inductors. The third one is measured on its own.

While self impedances were measured directly, the mutual impedance was calculated from two indirect measurements. The difference between in-phase and opposite-phase measurements of the series connected inductors cancels out the self impedance contribution.

Fig. 5.16 shows simulated values with continuous lines and experimental values in dots. Most impedance curves show very good agreement, with a maximum error of 7 %. The coupling factors, as indirect measurements, are more divergent.

Overall, these measurements verify the simulation accuracy for the given geometry and f, with material properties congruent with small signal analysis. The results are encouraging to go ahead to the following full power test.

5.3.2 Full power regime

As mentioned in section 5.2.2, the system is fed by a half-bridge inverter, which modulates the rectified mains voltage. The relevant parts of the simulated geometry

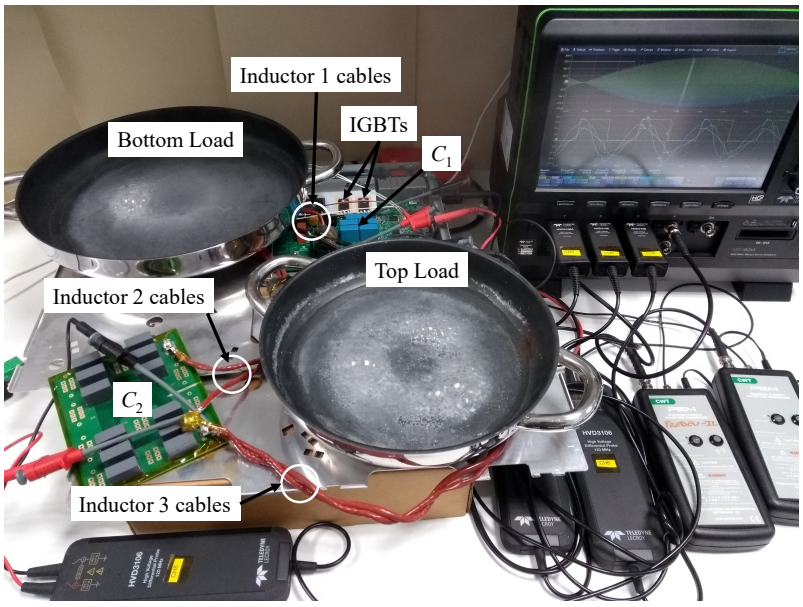

Figure 5.17: Experimental setup with both bottom and top loads boiling water.

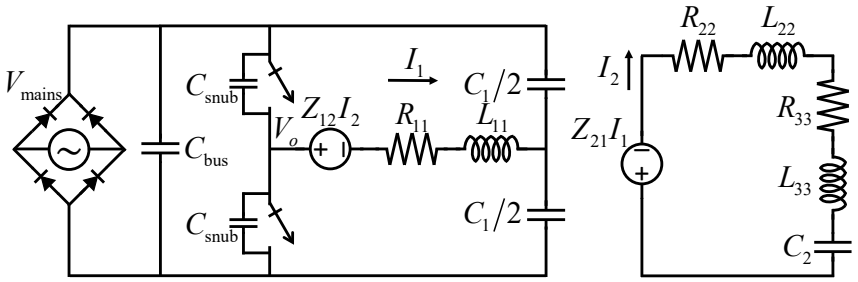

Figure 5.18: Prototype's circuit diagram.

stay the same, such as $d_{\text{load,bot}}$, $d_{\text{load,top}}$ and all the diameters. However, in order to help heat dissipation in the relatively lengthy experimental measurements and maintain ferromagnetic material properties with constant temperature, the independent load is a second water filled pan as seen in Fig. 5.17. This situation is equivalent to flipping the top half of the small oven while maintaining the electrical connection between secondary and tertiary inductors. This partition of the geometry is valid as long as each half maintains their relative geometry and materials of the original, and the inductors are kept far enough away to avoid coupling.

In the experimental setup, the first inductor is connected to the IH appliance's inverter and placed beneath the bottom load. The second inductor is placed above the first inductor and beneath the bottom load and connected to the C_2 capacitor board and to the third inductor. The third inductor is likewise connected to the second inductor and the C_2 board, and it is placed beneath the top load.

The circuit diagram, including inverter, inductors and loads is shown in Fig.

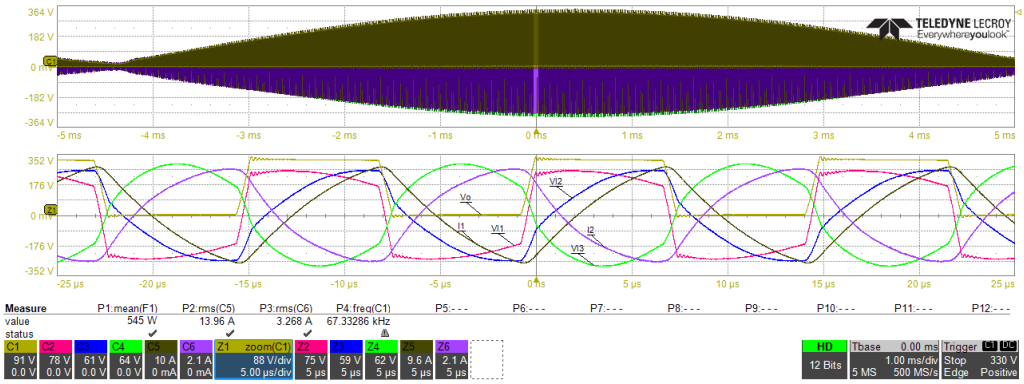

(a)

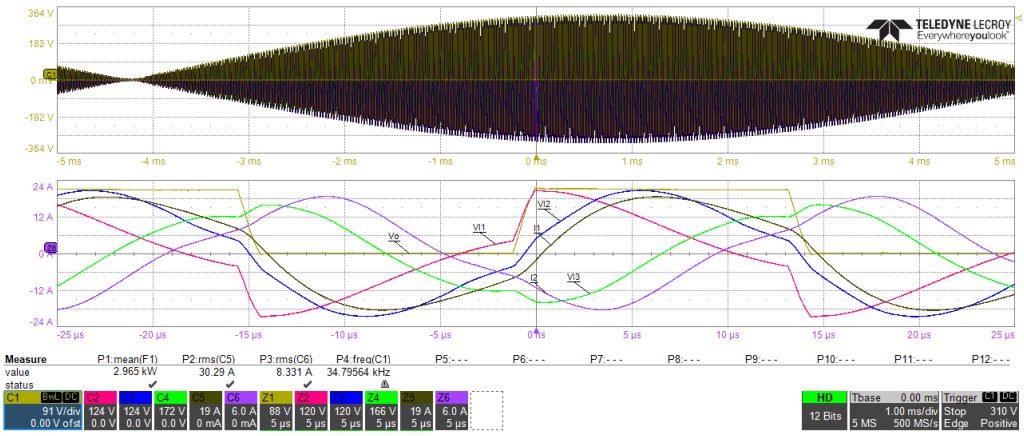

(b)

Figure 5.19: Oscilloscope captures (a) 500 W, (b) 3000 W.

5.18.

Waveforms have been captured with an oscilloscope of inverter output voltage, V_o, primary inductor voltage, V_{L1}, second inductor voltage, V_{L2}, third inductor voltage, V_{L3}, primary inductor current, I_1, and secondary inductor current, I_2. Sample captures when delivering 500 W and 3000 W are shown in Fig. 5.19. At low P, in Fig. 5.19 (a), the waveforms have almost triangular and exponential shapes, while at high P, in 5.19 (b) the waveforms are more sinusoidal.

In addition to the experimental setup to take measurements, a functional prototype has also been built and shown in Fig. 5.20. The compartmentalization of the electronics and their position near the hinge, away from the loads, are enough to prevent the high temperatures from reaching the ceramic capacitors.

Calculations up to now have assumed the first order harmonic for its frequency calculations. In order to better determine the accuracy of the FEA simulations, the half-bridge inverter has been simulated in LTspice in order to obtain waveforms and

(a)

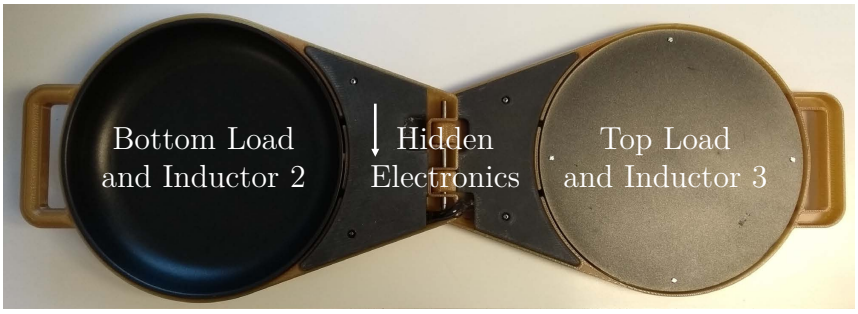

(b)

Figure 5.20: Functional prototype: (a) closed lid (b) fully open.

electrical parameters.

The simulated circuit is that of Fig. 5.18 with small modifications. A Matlab script was used to change impedance values for each frequency, run all simulations and store results.

Fourier transformations were used to calculate the experimental impedance values from inductor voltage, $V_{\text{ind},i}$, and current, I_i, waveforms:

$$Z_{\text{eq}} = \frac{V_{\text{ind},1}}{I_1}, \tag{5.18}$$

$$Z_{33} = \frac{V_{\text{ind},3}}{I_3}. \tag{5.19}$$

Z_{11} and Z_{12} can be obtained from measurements with the receiver in open circuit, if $I_2 = 0$:

$$Z_{11} = \frac{V_{\text{ind},1}}{I_1}, \tag{5.20}$$

$$Z_{12} = \frac{V_{\text{ind},2}}{I_1}. \tag{5.21}$$

Knowing all other terms, Z_{22} can be extracted from (5.6):

$$Z_{22} = \frac{Z_{12}^2}{Z_{11} - Z_{\text{eq}}} - Z_{33}. \tag{5.22}$$

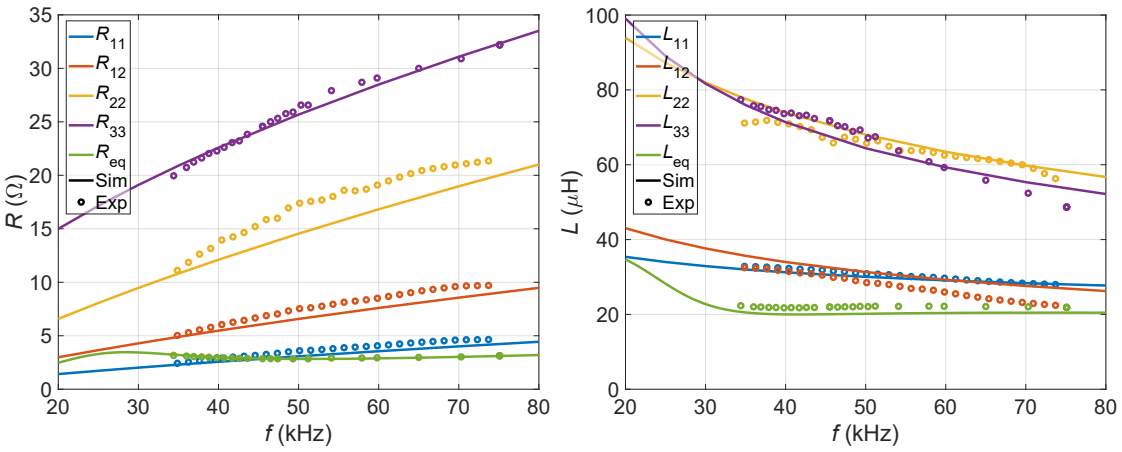

(a) (b)

Figure 5.21: Comparison between simulated and experimental impedance: (a) R and (b) L.

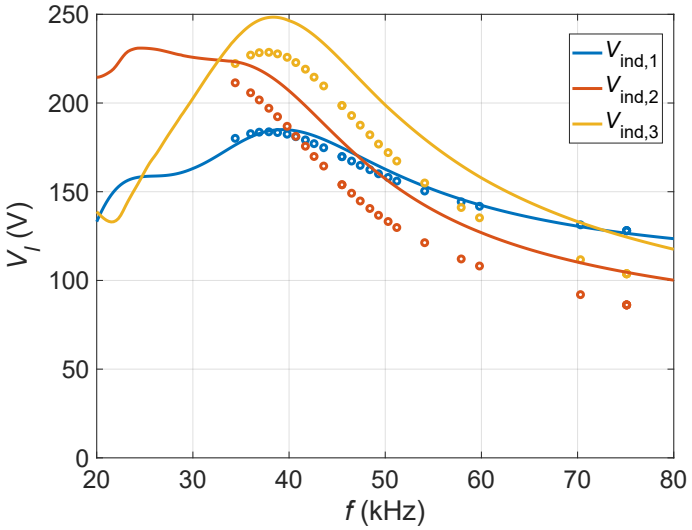

Figure 5.22: Inductor voltages, both simulated and measured.

The results are shown in Fig. 5.21, where the measured values are predicted for the most part by the FEA simulations.

Fig. 5.22 represents the simulated and measured inductor voltages. Fig. 5.23 represents the comparison between the simulated and measured values of P, PR_{top} and I when the receiver side is either disconnected: (a) and (b), or connected: (c) and (d). Fig. 5.23 (a) shows that the P peak at $\omega_{0,\text{eq}}$ is much higher than the desired P_{max}, 3000 W. Consequently, the equivalent impedance is more inductive at 3000 W and more current is required to deliver the same amount of power than the full system, as shown by comparing Fig. 5.23 (b) and (d). Therefore, reduction of time-average PR_{top} can be achieved by disconnecting the receiver, bearing in mind that high P could be too stressful to the electronics. In Fig. 5.23 (c), the small

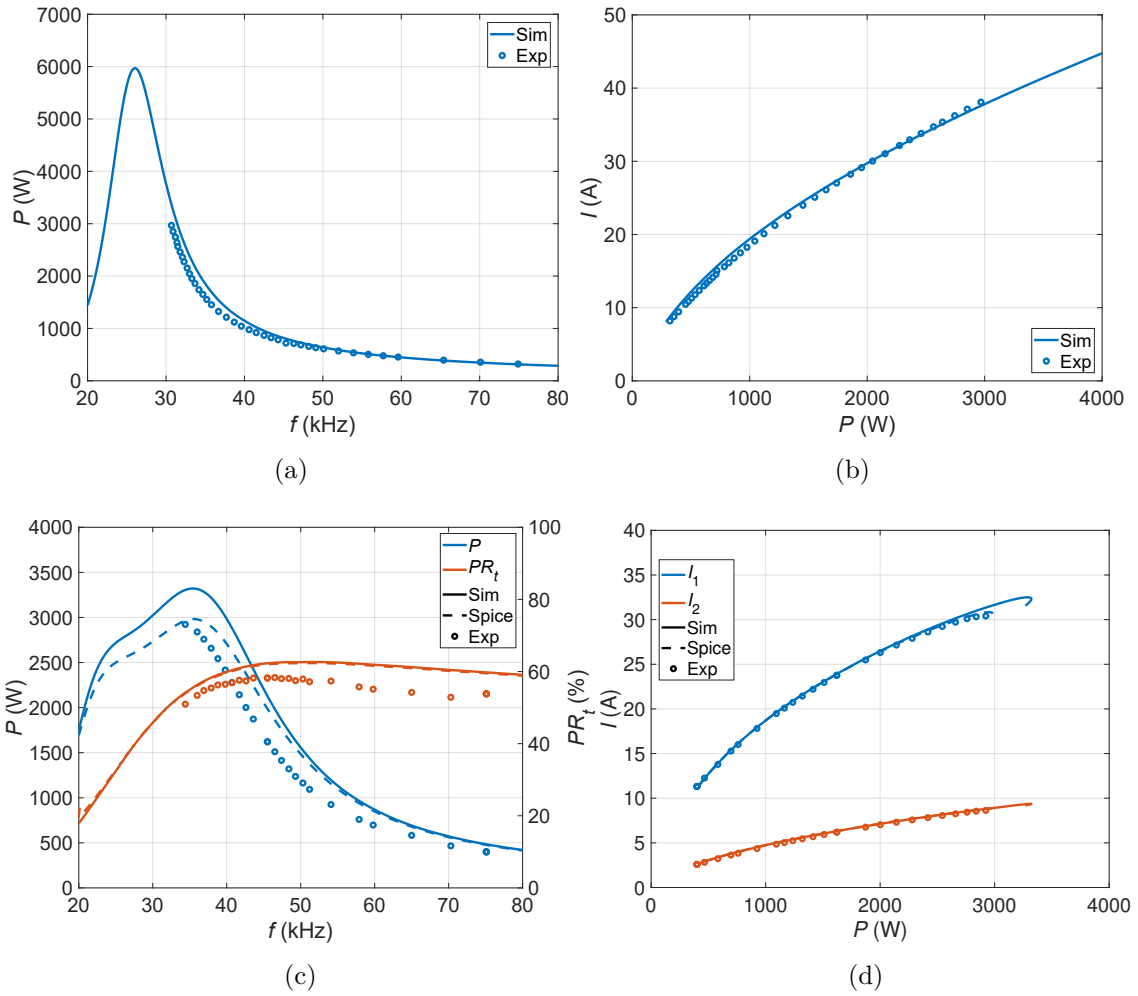

Figure 5.23: Power measurements with a disconnected receiver: (a) P (b) I. Measurements with connected receiver: (c) P and PR_{top} and (d) I_1 and I_3.

error in L_{eq} causes a shift of $\omega_{0,\text{eq}}$ and a slight reduction of PR_{top}, but otherwise simulations were able to predict the experimental results, confirming the validity of the calculation and design method.

As a result of a PR_{top} higher than 50 %, more than half of the total power goes to the top load, which is qualitatively shown in Fig. 5.17 with the bubble density of the boiling water. For further confirmation, Fig. 5.24 shows the temperature distribution with a thermographic camera when $P = 3000\,\text{W}$ is applied to the system with empty vessels until 100 °C are reached.

Fig. 5.25 shows experimental measurements of P and PR_{top} with radial misalignment. The measurements reinforce the validity of the simulations.

Appendix D compiles a list of the most relevant experimental results of the dissertation.

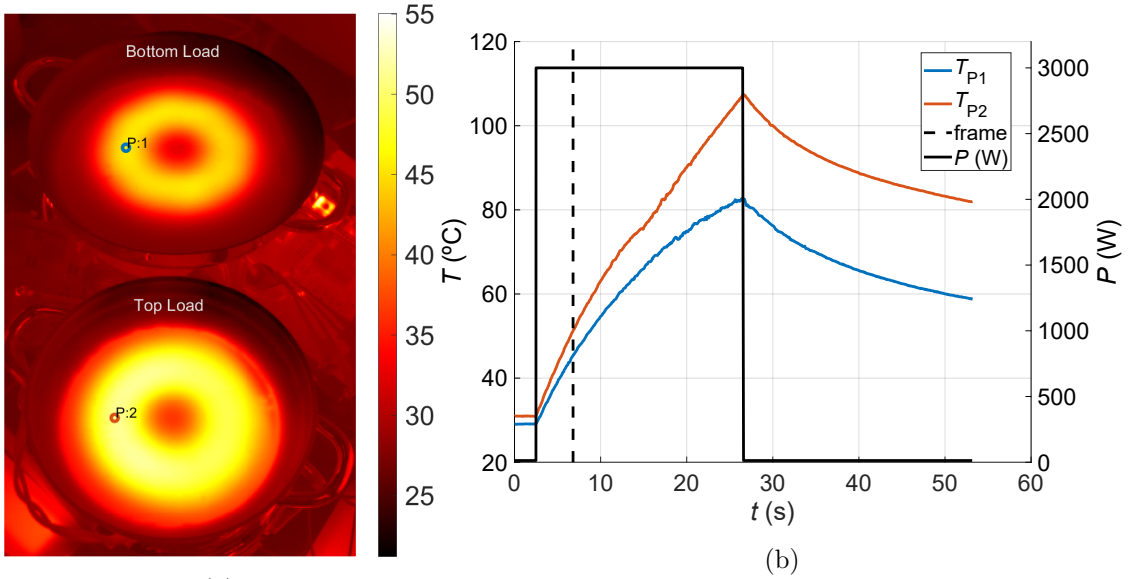

(a) (b)

Figure 5.24: Thermographic camera measurements with 3000 W. (a) Frame at 6.8 s. (b) Temperature evolution of indicated points.

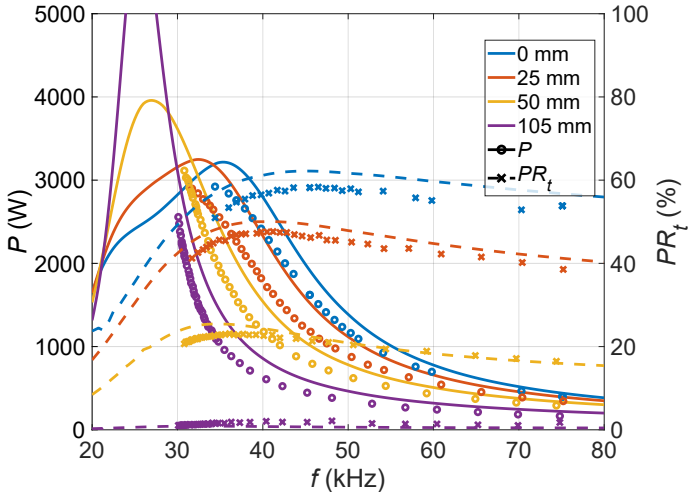

Figure 5.25: Measured P and PR_t variation with radial load misalignment.

5.4 Conclusion

The analysis and simulations presented in this chapter show that IH and inductive coupling can be used in conjunction to deliver power to multiple ferromagnetic loads with a single source in an new ICH application. A single cooktop inductor can be used to heat two loads in different planes with adequate power ratio. This allows heating uncoupled elements that are not directly placed on top of the cooktop or extending the heating zone for long vessels, such as rectangular grills.

The experimental verification affirms the accuracy of the simulated impedance

matrix. In order to maintain a consistent power ratio, global system resonant frequency must be higher than the receiver side resonant frequency. The ratio between turns of the second and third inductors can be used to modify the power ratio, though their absolute value does not affect equivalent impedance. This degree of freedom can be used to select the relative voltage and current in the receiver side. Full power delivery measurements clearly verify the simulations, with only a small shift in resonant frequency and a small reduction in calculated power ratio.

Considering that the power ratio between both loads is currently fixed by geometry and design, further steps should be taken to be able to control the amount of power delivered to each load. For example, a switch in the receiver side could be used to change between operating in a conventional IH configuration with the primary inductor only and the full ICH configuration. The addition of independent power control could also lead to food temperature control inside the oven with additional sensors and electronics.

System misalignment reduces power delivery to the top load, but the system can still operate safely and efficiently. Therefore, the misalignment can be detected and communicated to the user, so that they may correct it. Future work could investigate the compatibility of this kind of system with total active surface cooktops to completely mitigate the misalignment problem.

Overall, this kind of system is technically viable when all due precautions are taken.

Chapter 6

Small receiver ICH system

This chapter focuses on the design of an ICH system with an extended range of distances and a small receiver. The most important challenges are the small power factor associated with small diameters, and the placement of secondary side capacitors. Feeding small loads is part of the required flexibility of IH systems, and it is the toughest in normal situations and more so in high distance systems.

Table of contents

6.1 Introduction 167
6.2 System analysis and design 168
6.2.1 Inductor-load system 168
6.2.2 Capacitor location and orientation. 171
6.2.3 Induced voltage and track twinning 173
6.2.4 Individual track routing 174
6.3 Experimental results 176
6.3.1 Electrical measurements 176
6.3.2 Thermal measurements. 180
6.4 Conclusion 182

Figure 6.1: Representation of the proposed glassless induction concept

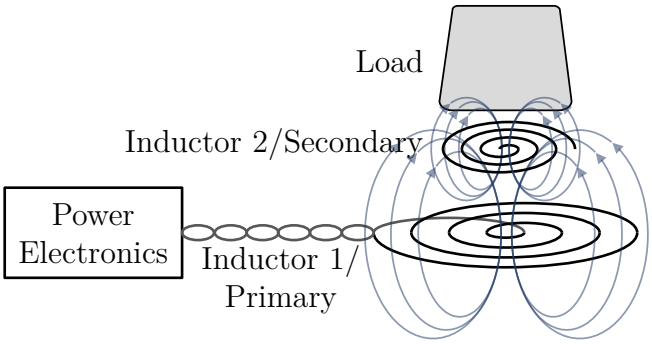

Figure 6.2: Representation of the proposed glassless induction concept

6.1 Introduction

IH appliances must be able to heat vessels of small size. Traditionally, specific inductors are designed for this purpose. However, the distance increase between inductor and load necessary in IuW implementation significantly damages the performance of small inductors, as proven in Chapter 2. This can be solved by means of ICH technology.

The implementation of the IuW concept with a small receiver ICH system is depicted in Fig. 6.1. The primary inductor has $\varnothing_{w1,\text{ext}} = 180\,\text{mm}$ in order to be compatible with the rest of the ICH systems presented in this thesis. The primary inductor with ferrites and shielding are placed beneath the kitchen worktop, while the $\varnothing_{\text{load,ext}} = 90\,\text{mm}$ load, represented as a moka pot, secondary inductor and compensation capacitors are placed above. The system is intended to work for a range of distances d_{w12} between 6 and 30 mm. The secondary inductors and capacitors are housed together beneath the ferromagnetic load. A diagram of the

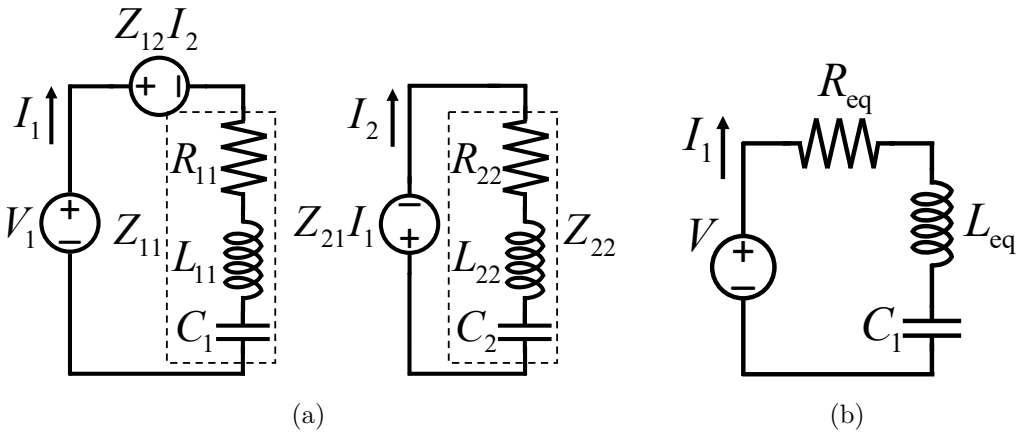

Figure 6.3: System circuits: (a) Full system (b) Equivalent impedance

system is depicted in Fig. 6.2. The system circuit shown in Fig. 6.3 (a) is the same as those of ICH systems with a single transmitter and receiver, which can be also be expressed by the system of equations:

$$\begin{pmatrix} Z_{11} & Z_{12} \\ Z_{21} & Z_{22} \end{pmatrix} \begin{pmatrix} I_1 \\ I_2 \end{pmatrix} = \begin{pmatrix} V \\ 0 \end{pmatrix}, \tag{6.1}$$

where the diagonal elements include capacitors.

The geometry is simulated with COMSOL Multiphysics considering a single turn for each winding, as usual. Parameters $n_{t,1}$ and C_1 are 19 turns and 800 nF respectively from the previous ICH systems, and $n_{t,2}$ and C_2 have to be chosen. Similar to previous chapters, equivalent impedance, Z_{eq}, is defined as:

$$Z_{\text{eq}} = \frac{V}{I_1} = Z_{11} - \frac{Z_{12}^2}{Z_{22}}. \tag{6.2}$$

The equivalent circuit is represented in Fig. 6.3 (b). To ensure low stress in the electronics and minimize power losses, the currents should be kept low, particularly at higher P demands, with 1500 W maximum power. This can be achieved by a careful selection of C_2, to generate a maximum in R_{eq} and a minimum in L_{eq} near $\omega_{0,2}$, as depicted in Fig. 6.4. For each $f_{0,2}$, the R_{eq} peak occurs slightly below $f_{0,2}$, and the L_{eq} valley is placed slightly above $f_{0,2}$.

6.2 System analysis and design

6.2.1 Inductor-load system

The simulated d_{w12} distances range from 6 to 40 mm, so that the system could be used in IH applications with ceramic glass as well as in the IuW concept with a thick

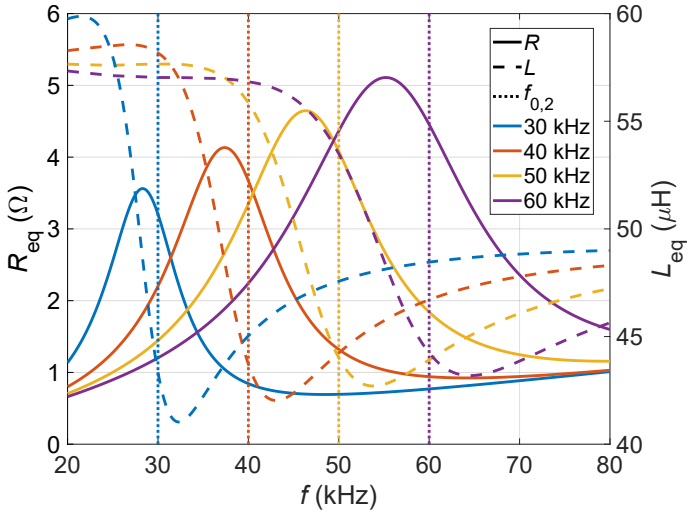

Figure 6.4: Impedance extrema with changing secondary resonant frequency.

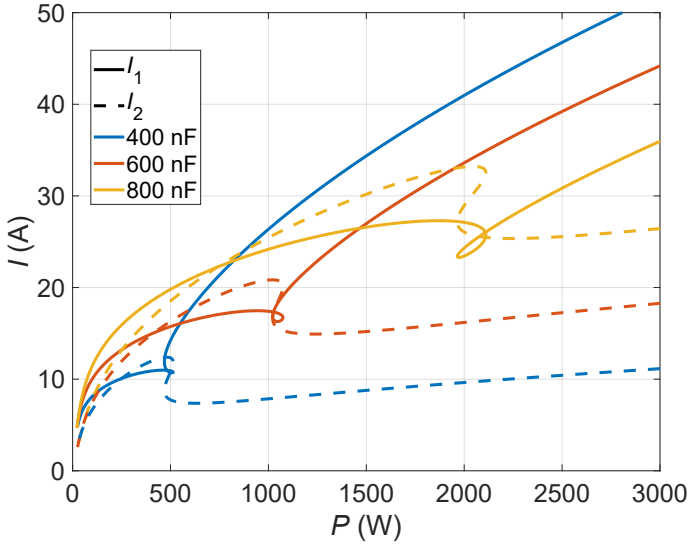

Figure 6.5: Current variation with secondary capacitor.

worktop. With such a small diameter, power distribution barely changes with the design parameters. Therefore, a detailed score analysis is not necessary to arrive at optimal designs. Actions that benefit PF, η and J_w are aligned.

Fig. 6.5 depicts the dependence of I_1 and I_2 with C_2, and consequently $f_{0,2}$, for the $d_{w12} = 20\,\text{mm}$ case where P is frequency controlled. The same comparison has been carried out for all distances, and the 750 nF option in conjunction with $n_{t,2} = 22$ is the most beneficial secondary capacitor to minimize current in all of the considered situations.

Fig. 6.6 shows simulated η with sweeping values of $(n_{t,1}n_{s,1})$ and $(n_{t,2}n_{s,2})$ and highlighted optimum and selected values. The primary inductor maintains the $n_{s,1} = 180$ from previous chapters, and is slightly above its optimum. The secondary

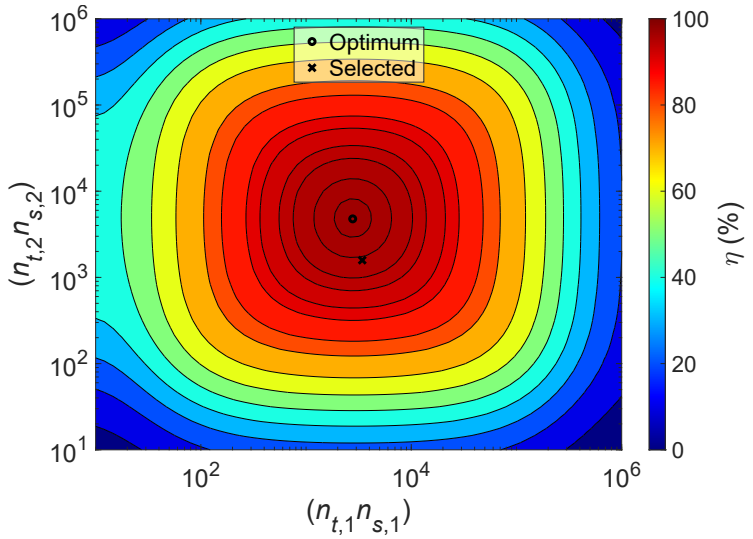

Figure 6.6: Efficiency variation due to different $(n_{t,1}n_{s,1})$ and $(n_{t,2}n_{s,2})$ at $d_{w12} = 20\,\text{mm}$ at $d_{w12} = 20\,\text{mm}$.

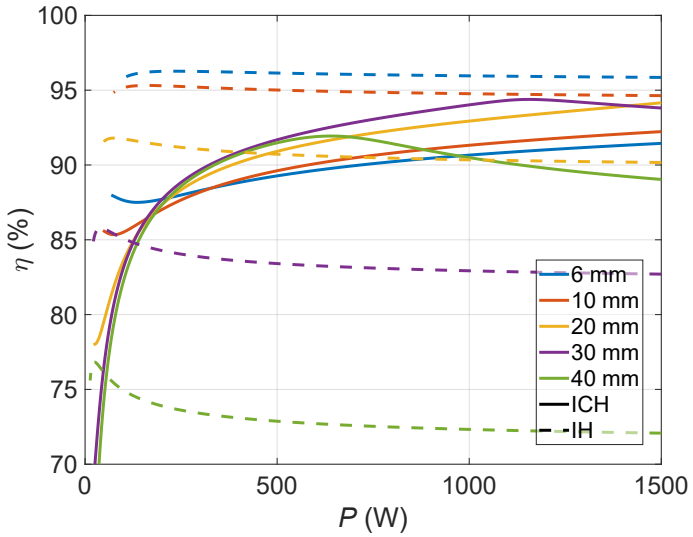

Figure 6.7: Simulated efficiency of the full ICH system and primary only (IH).

inductor, due to volume restrictions, can only house $n_{s,2} = 72$ strands out of the optimum 217.

The simulated η of the chosen design are plotted in Fig. 6.7, comparing the IH situation where only the primary inductor is active and the full ICH system. The addition of the secondary inductor decreases overall η at low d_{w12} due to the additional passive components, but clearly improves η above 10 mm distances, where conventional IH η drops quickly.

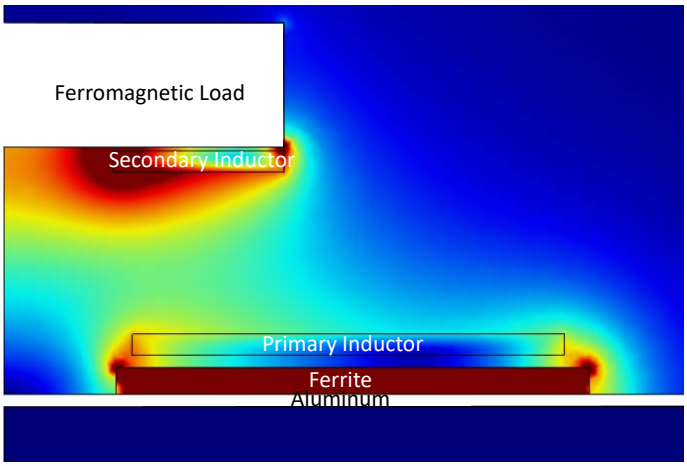

(a)

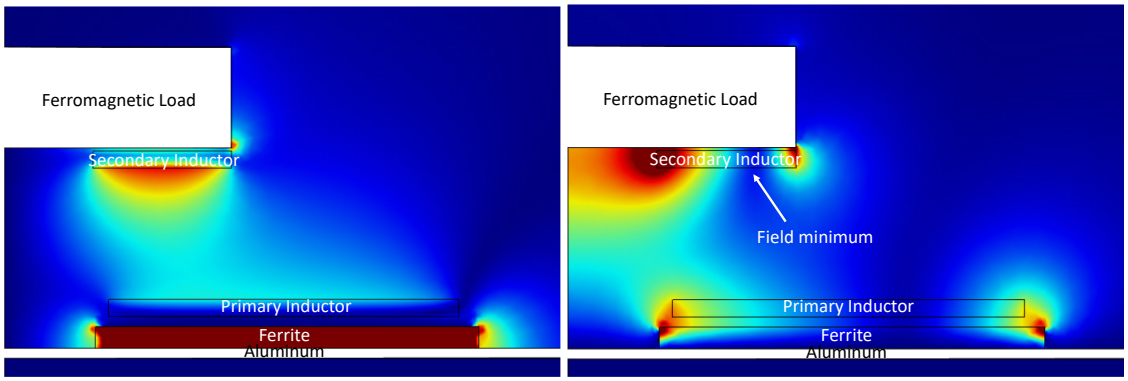

(b) (c)

Figure 6.8: 2D axyssimmetric simulation of **B** field: (a) $|\mathbf{B}|$, (b) $|B_r|$, (c) $|B_z|$.

6.2.2 Capacitor location and orientation

There is not much space to integrate the compensation capacitors with moka pots. It is preferable to include all electronics in the same compartment and prevent multiple interconnected pieces that attach to the load. WPT applications have the possibility of shielding the magnetic field above the receiver inductor, and place the electronics on top of the shielding. In ICH, the magnetic field must reach the ferromagnetic load, and shielding is not an option.

FEA simulations show that $|\mathbf{B}|$ is strong near the secondary inductor, represented in Fig. 6.8 (a). However, its distribution is not uniform along the three spatial directions. Magnetic flux in the azimuthal direction, B_φ, is zero due to the axial symmetry, the flux modulus in the radial direction, $|B_r|$, is represented in Fig. 6.8 (b), and the flux modulus in the vertical direction, $|B_z|$, is represented in Fig. 6.8 (c).

There is a space at $\frac{3}{4}r_{w2,\text{ext}}$ where B_z is low, while B_r is quite strong and stable,

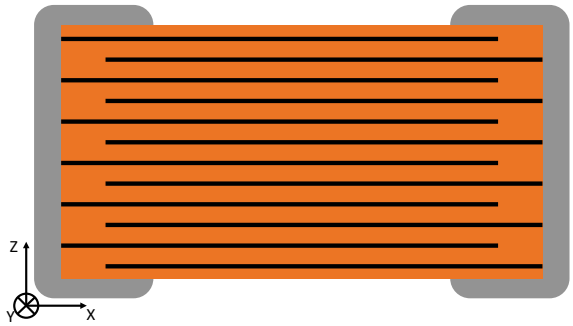

Figure 6.9: Multilayer ceramic capacitor diagram

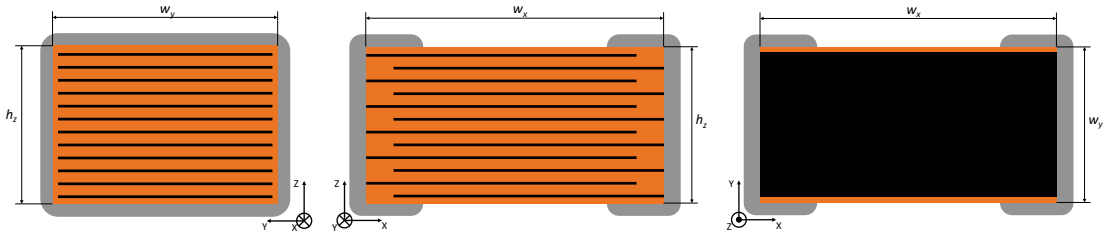

(a) (b) (c)

Figure 6.10: MLCC cross-sections: (a) X direction, (b) Y direction, (c) Z direction

and B_φ is negligible. In that position, the effects of B_z are minimal and so it becomes the optimal position to place components. Moreover, objects that have a low profile along one direction can be aligned with the radial direction to minimize induced voltage in said direction, while the field strength in the other directions is not strong enough to cause significant effects.

Surface mounted devices and electronic boards can benefit the most from this kind of magnetic field distribution, since these devices are generally quite thin, as are the copper tracks of the boards they are mounted on.

In the case of multi-layer ceramic capacitors (MLCCs), whose diagram is shown in Fig. 6.9, they have the biggest metallic surface in the Z direction. Due to the electrodes, they have some surface area in the X direction. They project the least surface in the Y direction, because of the thinner part of the terminals, and the thin cross section of the electrodes.

The three cross-sections of a MLCC according to the axes depicted in Fig. 6.9 are represented in Fig. 6.10. Proximity losses generated in the capacitors increase considerably with the metallic cross-section facing the magnetic field. As the biggest cross-section, the Z plane must be placed in a low flux direction. Therefore, the surface mounted capacitors align their local Z direction with the B_z field, in the

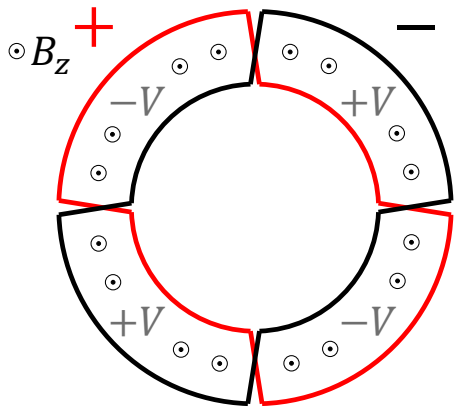

Figure 6.11: Voltage induction in twinned tracks.

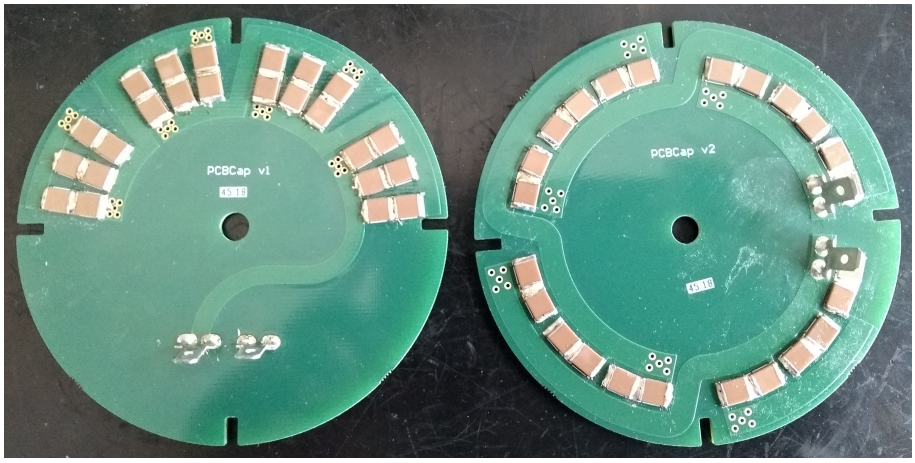

Figure 6.12: PCB prototypes. PCBCap v1, shown on the left, applies the suboptimum capacitor orientation, whereas PCBCap v2, on the right, does use the optimum capacitor orientation.

location where the vertical flux is minimal. Additionally, it is preferable to orient the local Y direction with the B_r direction, combining the minimum cross-section with the maximum field and avoid more losses.

6.2.3 Induced voltage and track twinning

To fully cancel the effect of B_z, the cables or PCB tracks carrying different voltages can be twinned to simultaneously balance currents, reduce the intersecting area and invert the polarity of each successive loop, minimizing induced voltage in most cases and completely cancelling it in geometries with axial symmetry, as shown in Fig. 6.11.

An application example of these guidelines can be seen in Fig. 6.12, where both prototypes have the capacitors placed near the external radius, minimizing the effect of B_z. Both prototypes also have an even number of twinned track sections. Prototype PCBCap v1 uses the suboptimum capacitor orientation, but occupies less

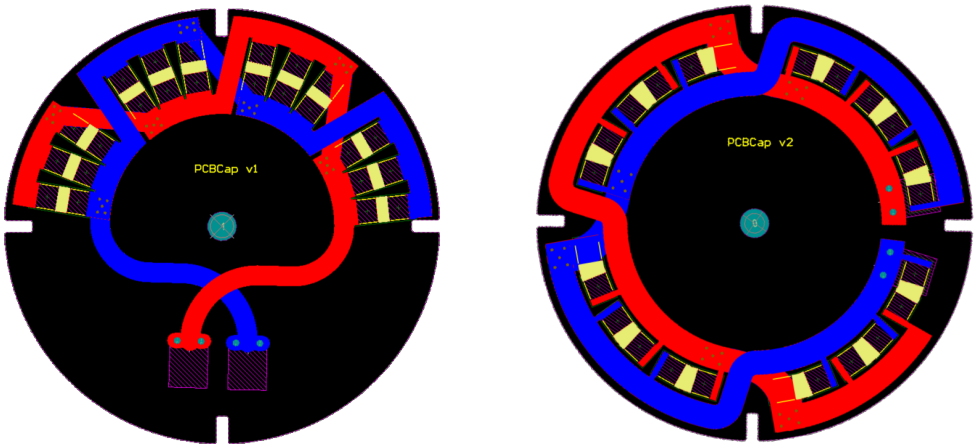

(a) (b)

Figure 6.13: PCB schematics of prototypes: (a) PCBCap v1 and (b) PCBCap v2.

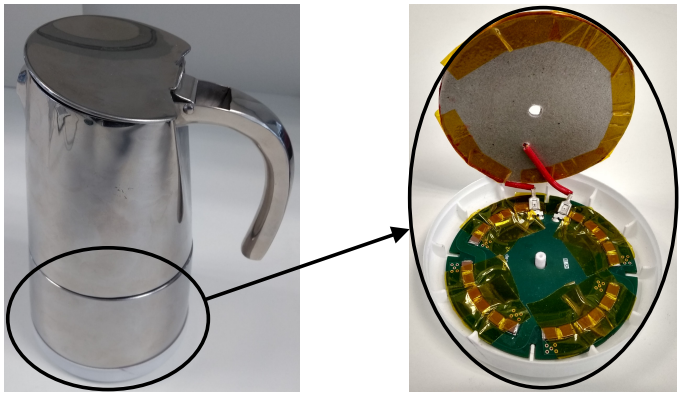

Figure 6.14: Moka pot with housing attached on the left and open housing with capacitor PCB and secondary winding on the right.

area, while PCBCap v2 does use the optimum orientation while occupying more surface area. Both orientations can work at the rated power. To better show the tracks, the PCB schematic is represented in Fig. 6.13, with positive voltage in red, negative in blue, and capacitor midpoints in yellow.

These PCB prototypes were implemented in a small housing with the secondary inductor, as shown in Fig. 6.14 on the right, and then fitted to the moka pot shown on the left, highlighting the ICH prototype's small size and unobtrusive look.

6.2.4 Individual track routing

Since the PCB tracks may be the most affected part of the system, a reduction in proximity losses can also significantly reduce the temperature increment in the tracks. A possible solution is the separation of the main PCB track into individual

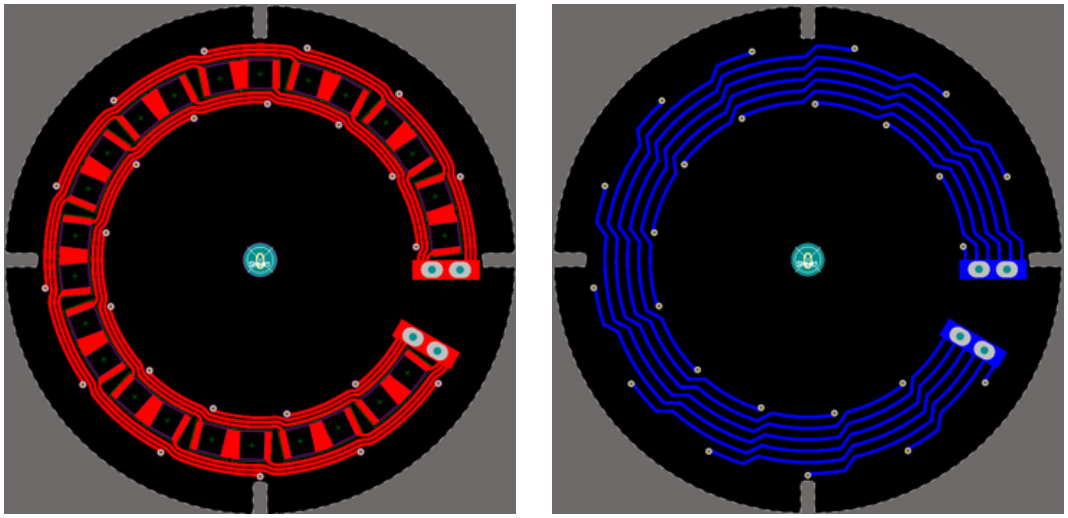

(a) (b)

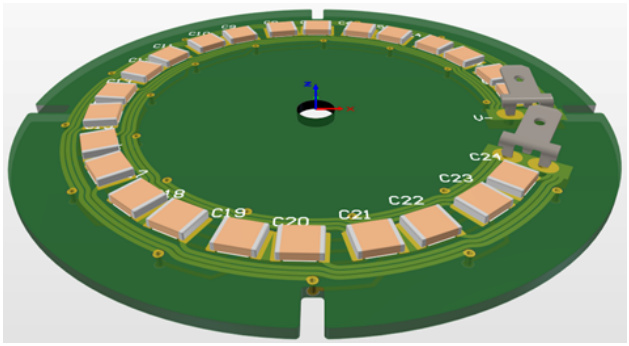

(c)

Figure 6.15: Individual PCB track routing: (a) top layer, (b) bottom layer, (c) PCB perspective.

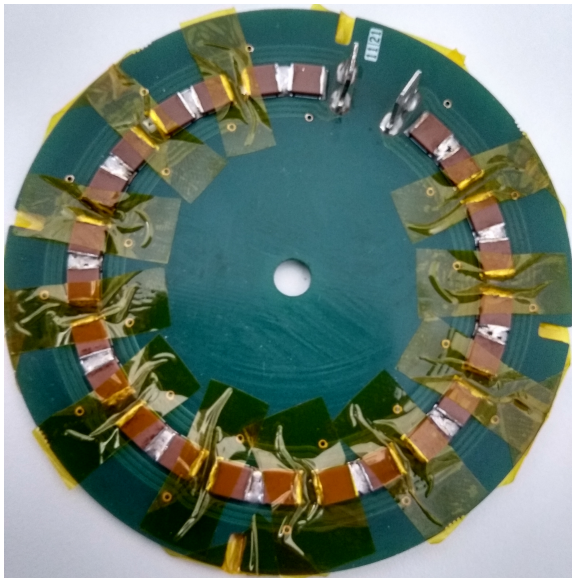

Figure 6.16: PCB individual track prototype (PCBLitz).

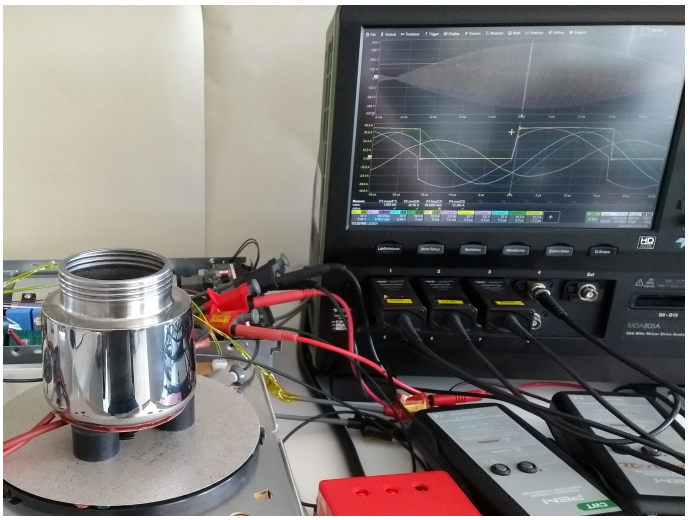

Figure 6.17: Experimental setup.

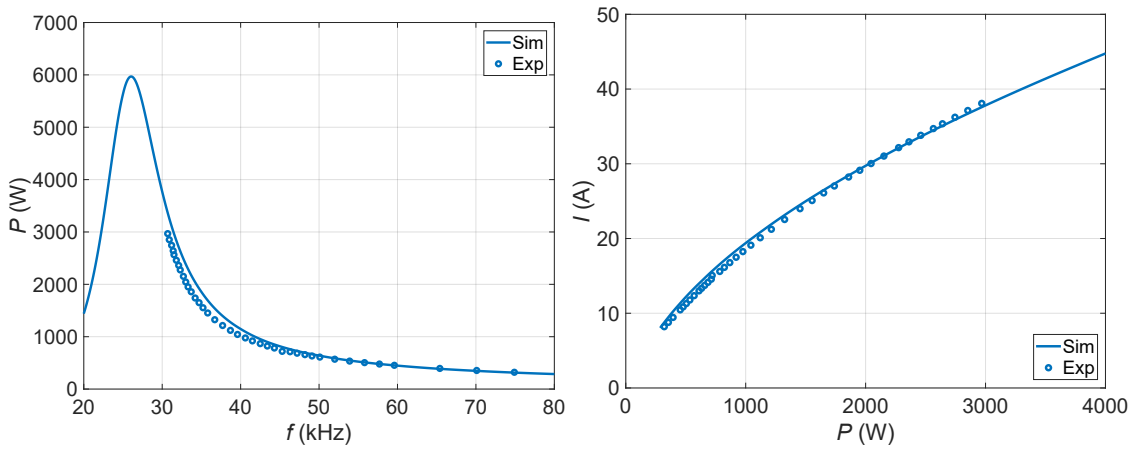

Figure 6.18: Primary inductor only (IH) measurements at $d_{\text{load}} = 20\,\text{mm}$ of (a) P and (b) I.

thinner tracks for each of the 12 parallel capacitors [160], as shown in Fig. 6.15.

Fig. 6.16 shows a prototype of the individual track PCB, shortened for convenience as PCBLitz. It will undergo the same thermal measurements than the previous prototypes.

6.3 Experimental results

6.3.1 Electrical measurements

The full system has been tested delivering P up to 1500 W at the simulated distances with frequency control and a $\varnothing_{w1,\text{ext}} = 180\,\text{mm}$ commercial cooktop inductor. It is worth pointing out that 1500 W on a $\varnothing_{\text{load}} = 90\,\text{mm}$ load entails a $23.6\,\text{W/cm}^2$

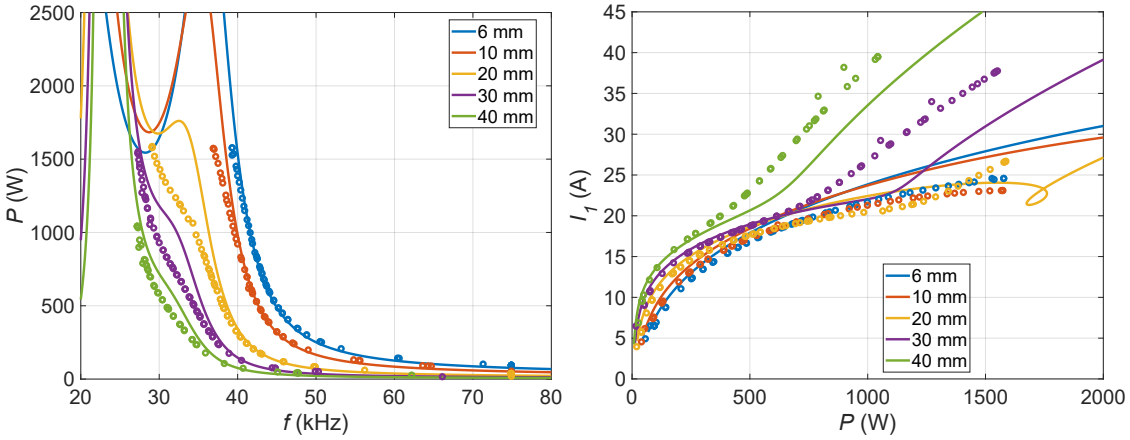

(a) (b)

Figure 6.19: Full system (ICH) measurements of (a) P and (b) I.

Table 6.1
Parameter comparison between IH with the primary inductor only and the full ICH system (simulations)

	Primary only			Full ICH system		
Distance (mm)	P_{max} (W) @ < 40 A	I (A) @ < 1500 W	η (%) @ < 1500 W	P_{max} (W) @ < 40 A	I_1 (A) @ < 1500 W	η (%) @ < 1500 W
6 mm	2840	28	95.8	3400	28	91.4
10 mm	2250	32	94.6	3900	27	92.2
20 mm	1240	44	90.1	3200	24	94.2
30 mm	730	59	82.7	2080	31	93.8
40 mm	460	74	72.0	1250	45	89.0

power density, whereas the typical 3700 W applied to a standard $\varnothing_{load} = 210$ mm load results in 10.7 W/cm^2.

Wave measurements of inverter voltage, inductor voltages and currents have been taken with an oscilloscope. Measurements with the secondary inductor in open circuit have also been taken to compare results between the IH system with the primary inductor only and the full ICH system. The additional measurements are also used to calculate the elements of the impedance matrix.

Fig. 6.17 shows the experimental setup, where the primary and secondary inductors have been separated $d_{w12} = 20$ mm with measured disks of PPS. Simulated and measured values of P and I_1 for the IH primary inductor only case in Fig. 6.18 and for the full ICH system in Fig. 6.19. The measured values generally agree with the simulations, and the system behaves as expected. The figures and Table

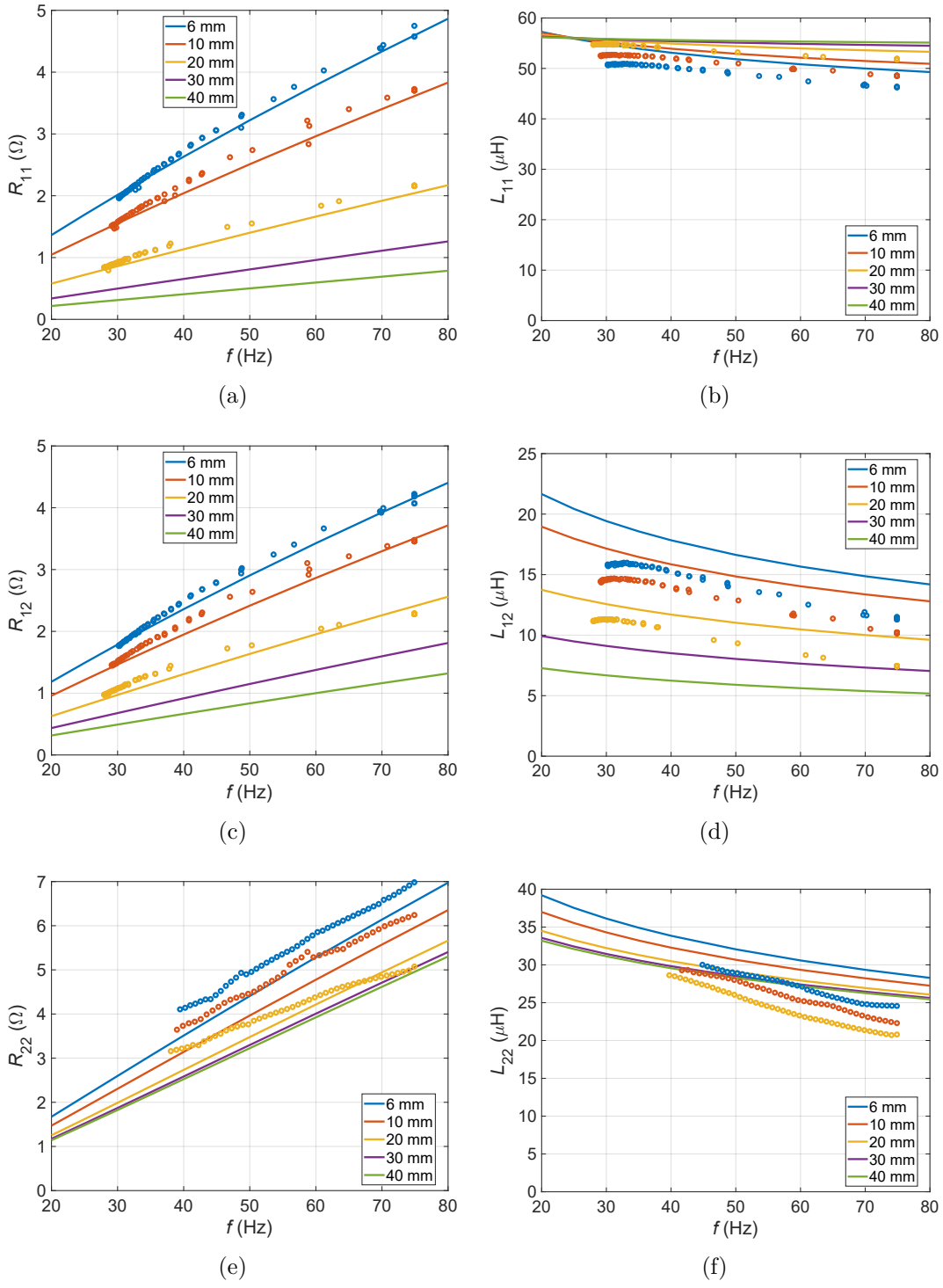

Figure 6.20: Simulated and calculated winding impedance: (a) R_{11} (b) L_{11} (c) R_{12} (d) L_{12} (e) R_{22} (f) L_{22}

6.1 confirm that the active secondary inductor manages to reduce I_1 for all cases, except low P at low d_{w12}.

Furthermore, the system's impedance has been calculated from the measurements of both the IH and the ICH case. The impedances that are calculated

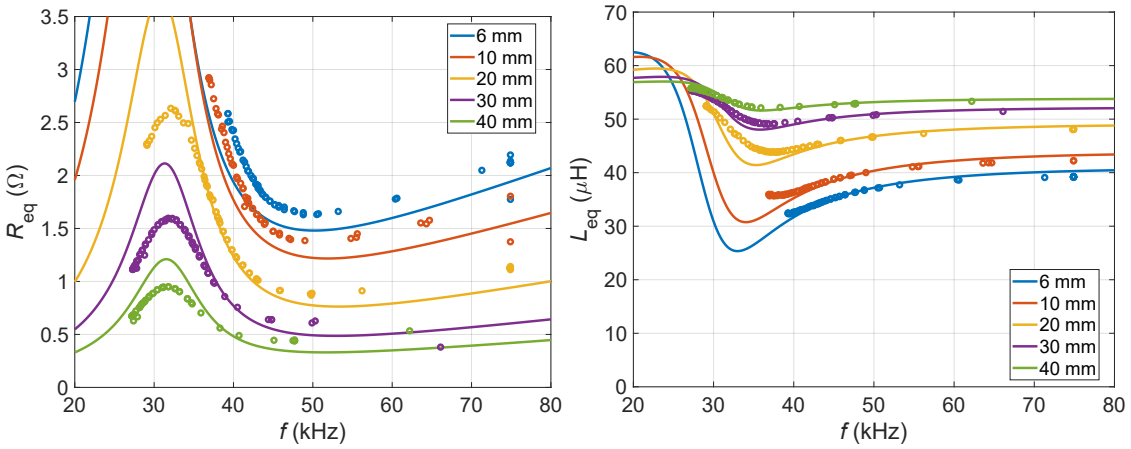

(a) (b)

Figure 6.21: Simulated and calculated impedance: (a) R_{eq} (b) L_{eq}

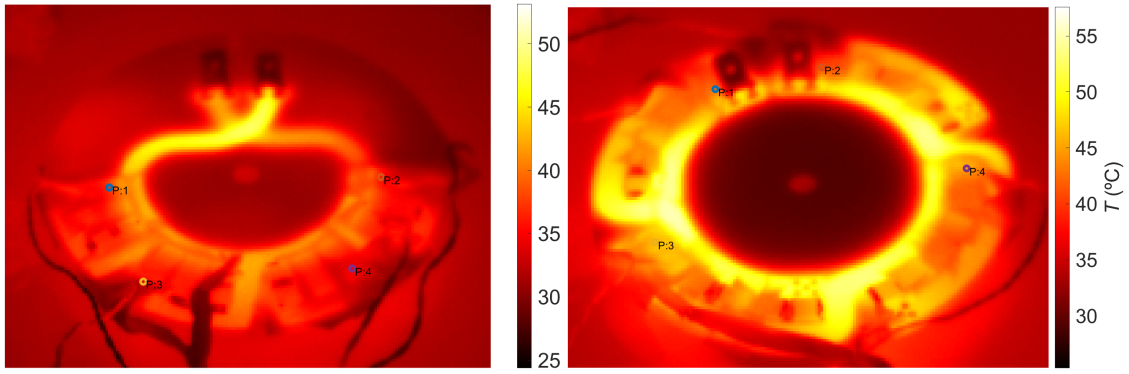

(a) (b)

Figure 6.22: Temperature distribution due to strong magnetic field: (a) PCBCap v1 and (b) PCBCap v2.

directly from the measured waveforms are Z_{eq} from the full ICH system, Z_{11} and Z_{12} from the IH system with the primary inductor only. Z_{22} is calculated indirectly as:

$$Z_{22} = \frac{Z_{12}^2}{Z_{11} - Z_{eq}}. \tag{6.3}$$

The individual winding impedances are shown in Fig. 6.20, where primary impedance and R_{12} matches very well, L_{12} and secondary impedance are slightly off. As R_{22} and L_{22} are obtained indirectly, the result is satisfactory. The equivalent impedance is shown in Fig. 6.21, where both R_{eq} and L_{eq} match fairly well except at the R_{eq} peak and the L_{eq} valley, due to the overestimation in the L_{12} simulation.

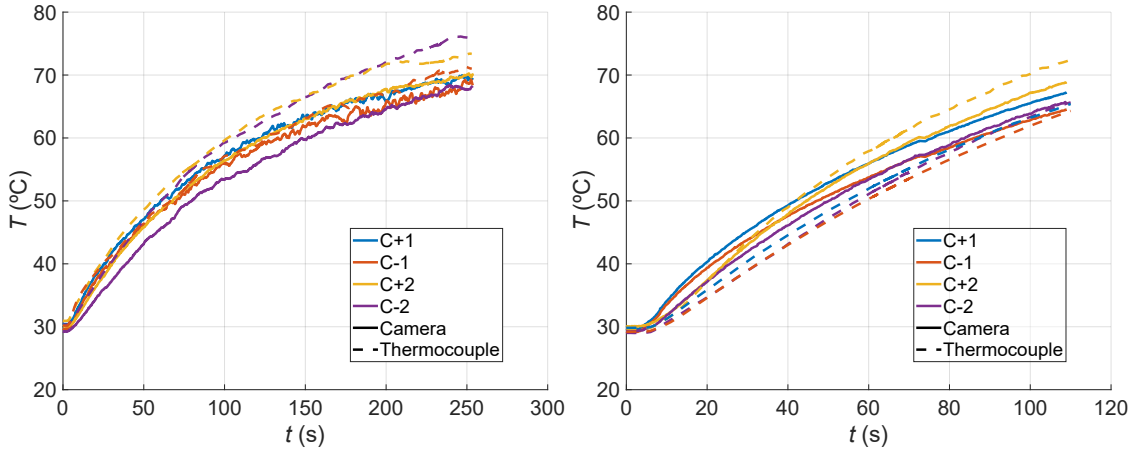

(a) (b)

Figure 6.23: Temperature increment due to strong magnetic field: (a) PCBCap v1 and (b) PCBCap v2.

6.3.2 Thermal measurements

Temperature measurements were taken with a thermographic camera and thermocouples with both prototypes in several configurations. Fig. 6.22 shows the temperature distribution in the PCBs when a strong magnetic field is applied without the ferromagnetic load on top. Fig. 6.23 shows the measured capacitor temperatures at the points marked in Fig. 6.22. It can be seen from Fig. 6.22 that most heat is generated in the PCB tracks and not in the capacitors.

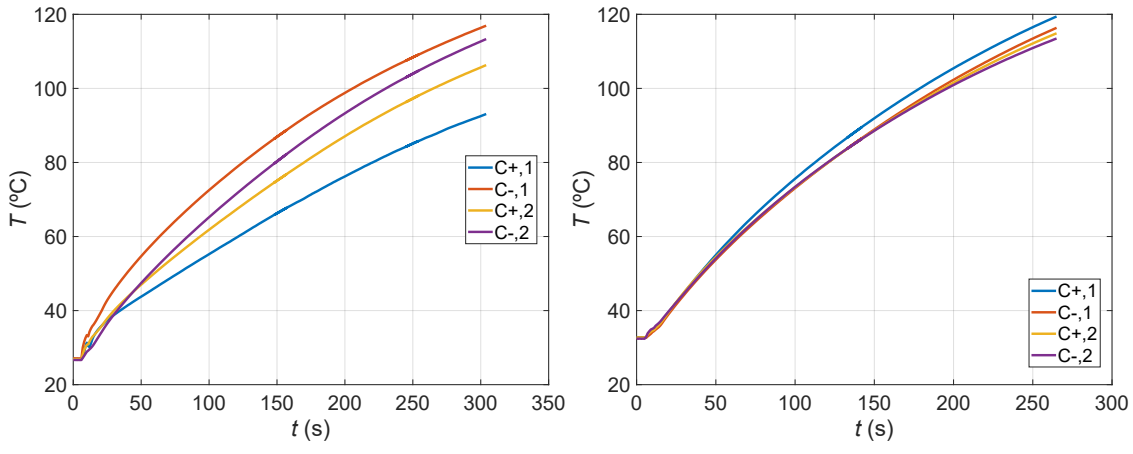

(a) (b)

Figure 6.24: Temperature increment due to strong magnetic field, circulating current, thermal insulation and load proximity: (a) PCBCap v1 and (b) PCBCap v2.

Fig. 6.24 shows the temperature increment with the full system depicted in Fig. 6.14, operating at 500 W. The effects of circulating current and close proximity with

the moka pot are a temperature increment of 50 °C while that of the magnetic field is around 40 °C.

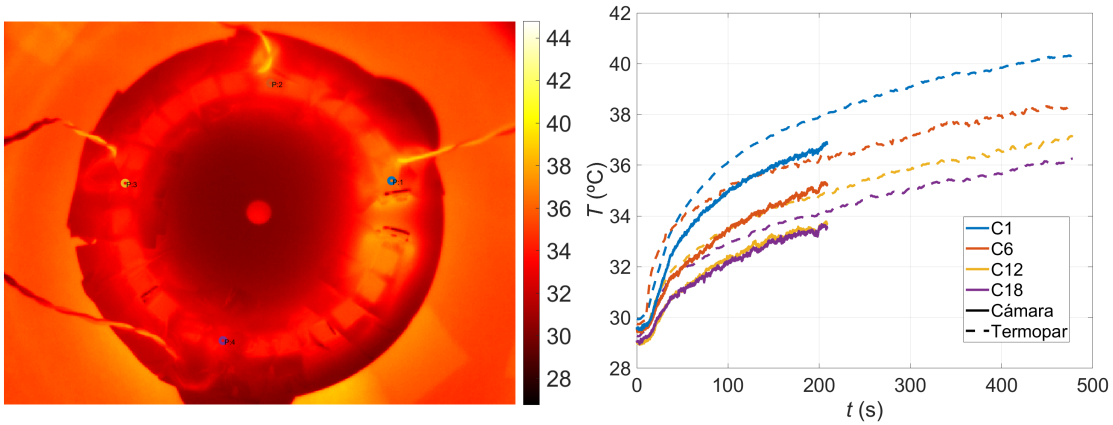

(a) (b)

Figure 6.25: PCBLitz under magnetic field: (a) thermographic image and (b) temperature increment.

Fig. 6.25 shows a thermal image of the PCBLitz prototype and the measured temperatures with the camera and thermocouples of the marked capacitors when a strong magnetic field is applied. In this case, the temperature increment is 10 °C at most.

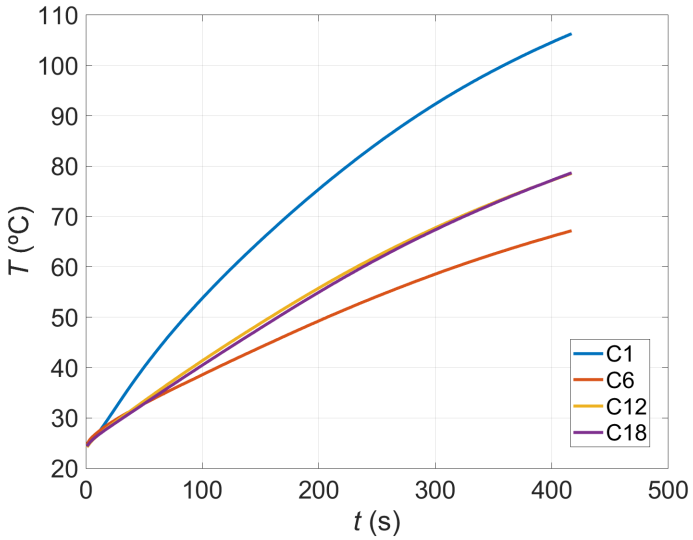

Figure 6.26: Temperature increment in PCBLitz due to strong magnetic field, circulating current and thermal insulation.

Fig. 6.26 shows the PCBLitz temperature increment with the full system depicted in Fig. 6.14 operating at 500 W. Temperature increase is slowed significantly in the worst-case capacitor, the one closest to the connector, and the rest

have much lower temperature. The measurements show that the PCBLitz prototype could withstand the temperatures caused by normal operation with minimal changes in PCB connectors.

Appendix D compiles a list of the most relevant experimental results of the dissertation.

6.4 Conclusion

Conventional IH systems have trouble with detection and heating of really small loads. The simulations and experimental results show that small loads can be adapted successfully with ICH systems, delivering much more power than conventional systems with adequate power factor and efficiency. Additionally, the resonant capacitors can be housed under the load without adverse effects from the magnetic fields, as confirmed by the thermal measurements.

The actions to prevent damage and interference to the capacitors, ordered from more to less effective are:

- *Individual PCB track routing:* minimizes proximity losses in capacitor tracks.
- *Orientation of biggest capacitor metallic surface area with small magnetic flux:* significantly decreases heating in the capacitors.
- *Twinning tracks:* Reduces induced voltage in the resonant tank.
- *Orientation of the second biggest capacitor metallic surface area with small magnetic flux:* decreases heating in the capacitors.

Thermal and electric measurements show that with a few improvements, the secondary winding and resonant capacitors can be housed together and be attached beneath the ferromagnetic load.

Chapter 7

EMI reduction of ICH systems

This chapter investigates the emitted magnetic flux differences between conventional IH systems and ICH systems. Magnetic flux emissions of both kinds of systems are simulated, and their dependence with coil current and turn number is outlined. Designs of both kind of systems with similar geometries are developed, prototyped and measured. The measurements show that well designed ICH systems reduce magnetic flux emissions with respect to IH systems with high inductor-load distance.

Table of contents

7.1 Introduction 185
7.2 Measuring procedures and methods 185
7.3 EMI FEA simulations 186
7.3.1 Conventional IH systems 186
7.3.2 ICH systems 187
7.4 Experimental results 191
7.5 Conclusion 195

7.1 Introduction

Conventional IH systems usually comply with EMC regulations. However, large air-gap systems, like IuW, emit much more flux, and can potentially violate the restrictions. Therefore, this chapter aims to analyze the electromagnetic emissions of IuW IH systems and compare them with ICH systems.

The electromagnetic emissions of induction cookers are limited by EMC regulation, which concerns two documents. First, the International Commission on Non-Ionizing Radiation Protection (ICNIRP) [85] proposed recommendations about user exposure to time-varying electromagnetic fields. Second, measurement methods for electromagnetic fields of household appliances with regard to human exposure were regulated by the International Electrotechnical Commission (IEC) [89]. This chapter fits within the frame established in both documents.

7.2 Measuring procedures and methods

Proper estimation of appliances' field emissions must be in accordance with the standards. Near field emission measurement procedures and methods for magnetic fields are specified in the IEC 62233:2005 standard [89]. This standard sets that the magnetic field should be measured at a horizontal distance from the appliance to the probe, d_{probe}, of 30 cm from each side of the device along a vertical line, and it should be averaged over an area of 100 cm^2 in order to avoid inhomogeneities. The test vessel must have the same diameter of the inductor or slightly bigger, $\varnothing_{w,\text{ext}} \leq \varnothing_{\text{load}}$. Moreover, the limit recommended by the 1998 ICNIRP guidelines is 6.25 µT rms for the range comprised from 800 Hz to 150 kHz for the general public [85]. The frequencies used in IH cooktops fall in this range. Newer ICNIRP recommendations [87] have increased the general public exposure limit in the range between 3 kHz and 10 MHz to 27 µT, but they have yet to be included in newer home appliance standards and regulations.

According to the standard, near field commercial probes consist of three perpendicular and circular loops of area $S_{\text{loop}} = 100\,\text{cm}^2$. Considering that the loop surfaces are aligned with the three directions of an arbitrary orthonormal coordinate system $(\hat{\mathbf{e}}_\mathbf{1}, \hat{\mathbf{e}}_\mathbf{2}, \hat{\mathbf{e}}_\mathbf{3})$, the flux emitted by a single inductor is:

$$\mathbf{B} = B_{e_1}\hat{\mathbf{e}}_\mathbf{1} + B_{e_2}\hat{\mathbf{e}}_\mathbf{2} + B_{e_3}\hat{\mathbf{e}}_\mathbf{3}. \tag{7.1}$$

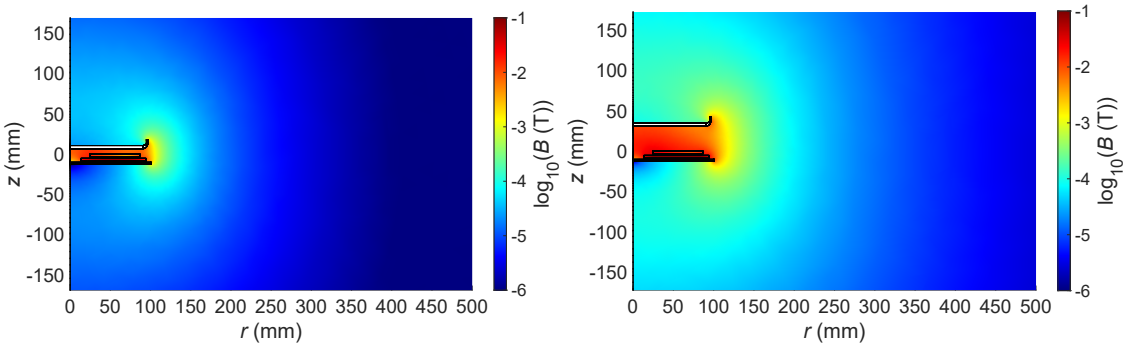

Figure 7.1: Decimal logarithm of magnetic flux produced to deliver 3000 W to the load at 30 kHz and d_{load} of (a) 6 mm, (b) 30 mm.

For multiple inductors:

$$\mathbf{B} = \left(\sum_{i=1}^{n} B_{i,e_1}\right)\hat{\mathbf{e}}_\mathbf{1} + \left(\sum_{i=1}^{n} B_{i,e_2}\right)\hat{\mathbf{e}}_\mathbf{2} + \left(\sum_{i=1}^{n} B_{i,e_3}\right)\hat{\mathbf{e}}_\mathbf{3}. \tag{7.2}$$

Applying (2.40) and (2.41), the magnitude specified in the IEC 62233:2005 standard and measured by the commercial probe, considering inductors' $n_{t,i}$ and I_i:

$$B_{\text{rms}} = \sqrt{\sum_{j=1}^{3}\left|\sum_{i=1}^{n} n_{t,i} I_{i,\text{rms}} \frac{\int_{S_{e_j}} \overline{B_{i,e_j}}\, dS_{e_j}}{S_{\text{loop},e_j}}\right|^2}, \tag{7.3}$$

where $\overline{B_{i,e_j}} = B_{i,e_j,\text{p.t.,p.A.}}$.

To meet the standard, the condition $B_{\text{rms}} < 6.25\,\mu\text{T}$ must be kept for any point with a horizontal $d_{\text{probe}} = 30\,\text{cm}$ from the edge of the cooktop.

7.3 EMI FEA simulations

7.3.1 Conventional IH systems

The simulated IH system has $\varnothing_{w,\text{ext}} = 180\,\text{mm}$ with small increments in other diameters to reach $\varnothing_{w,\text{ext}} < \varnothing_{\text{load}} < \varnothing_{\text{fer,ext}} < \varnothing_{\text{sh}}$. d_{load} ranges from 6 to 30 mm and Fig. 7.1 shows simulated magnetic flux for the lowest and highest d_{load} delivering 3000 W. As it can be observed, the higher the distance is, the higher is the magnitude of the magnetic field in the surrounding area of the cooktop. Generally speaking, the magnetic field is partially shielded by the load, and the shielding is less effective with increasing d_{load}.

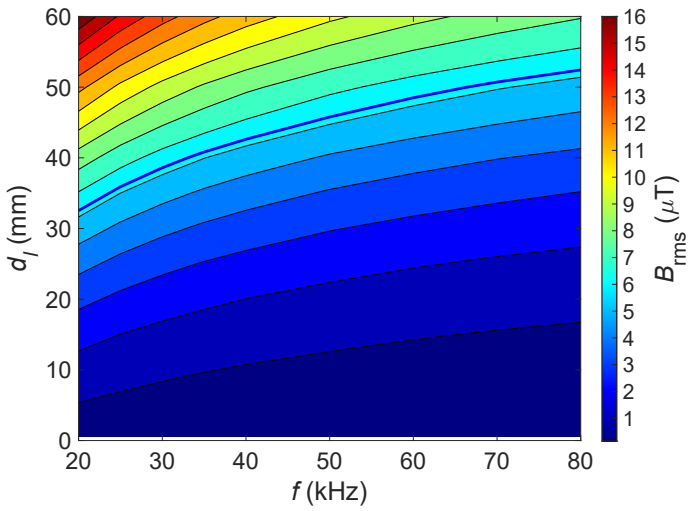

Figure 7.2: Magnetic flux measured by simulated probe when delivering 3000 W to the load for different frequencies and distances. The IEC 62233 [89] limit is highlighted in a thicker blue line.

For the same reason, when the frequency of the excitation increases, the level of B_{rms} decreases. The dependency of B_{rms} with d_{load} and f is shown in Fig. 7.2, where the limit of the current standard is also represented. Considering that the rated P is usually supplied at f below 40 kHz, for the depicted inductor of $\varnothing_{w,\mathrm{ext}} = 180$ mm, the maximum allowable distance would be less than 40 mm, which is similar to the thickness of regular worktops. Therefore, commercial solutions of under-worktop IH arrangements could compromise the fulfilment of current regulations. Therefore, ICH is explored as an alternative solution to decrease emitted magnetic flux.

7.3.2 ICH systems

Considering an ICH system of two windings, from (7.3) it can be determined that emitted and measured magnetic flux are very dependent on winding current, I_i, including their absolute value, $|I_i|$ and phase angle, φ_i, and more specifically, the phase difference between 1 and 2, φ:

$$I_i = |I_i|\, e^{j\omega t+\varphi_i}, \tag{7.4}$$

$$\varphi = \varphi_2 - \varphi_1. \tag{7.5}$$

The **B** field is dependent on both φ_1 and φ_2, but B_{rms}, as the vector's norm, is only dependent on φ.

The simulated ICH geometry is very similar to the previous IH system. $\varnothing_{w,\mathrm{ext,IH}} = \varnothing_{w1,\mathrm{ext}} = \varnothing_{w2,\mathrm{ext}}$ and $\varnothing_{\mathrm{load}}$, $\varnothing_{\mathrm{fer,ext}}$, $\varnothing_{\mathrm{sh}}$ also remain the same. In this case, d_{load} remains constant and small, while d_{w12} is swept from 6 to 30 mm.

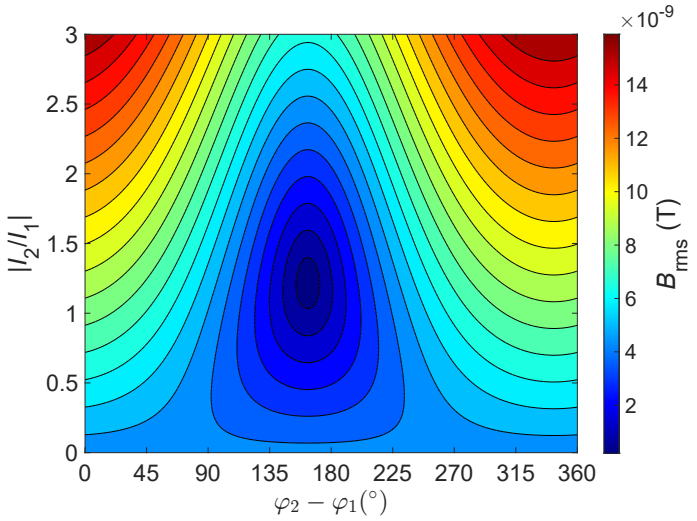

Figure 7.3: Magnetic flux generated by the ICH system with 1 Ampere-turn in the primary inductor at 30 mm and 30 kHz for different current ratios and phase angles.

For a fixed I_1, with $n_{t,1} = n_{t,2} = 1$, the magnetic flux generated by the system freely changing $|I_2|$ and φ in simulation is shown in Fig. 7.3. When the currents are in phase, the fields have a constructive effect that increases the total radiated field when I_2 increases, as could be expected. When the currents are in near opposite phase, there is a current ratio that minimizes the radiated field.

Phase and amplitude differences between inductor currents also determine the delivered P on the vessel's bottom surface [143]. Therefore, the effect of φ on P is also relevant. The calculation of P_{load}, specifically, can be retrieved from Chapter 3:

$$P_{\text{load}} = n_{t,1}^2 \left|I_1\right|^2 R_{\text{load,11,p.t.}} + 2n_{t,1}n_{t,2}\Re\left(I_1 I_2^*\right) R_{\text{load,12,p.t.}} + n_{t,2}^2 \left|I_2\right|^2 R_{\text{load,22,p.t.}}. \quad (7.6)$$

For fixed $n_{t,1} = n_{t,2} = 1$ and $|I_1| = 1\,\text{A}$, $|I_2|$ affects the last term of the sum directly and $\Re\left(I_1 I_2^*\right)$ and φ only affects $\Re\left(I_1 I_2^*\right)$.

Fig. 7.4 shows P delivered by the ICH system in simulation with fixed $n_{t,1} = n_{t,2} = 1$, $|I_1| = 1\,\text{A}$ and variable $|I_2|$ and φ with full freedom. It can be seen that an increase in $|I_2|$ increases P, and a phase difference between currents reduces P notably.

In order to minimize B_{rms} while maximizing P, the ratio P/B_{rms} is represented in Fig. 7.5. This Figure shows that the optimum operation point is very near the flux minimum observed in Fig. 7.3, where P is also smaller, but to a much lesser degree, as seen in Fig. 7.4. Unfortunately, the current ratio and phase difference can not be selected freely because only the primary inductor is fed directly, so the only way to change them is via the compensation capacitors. The orange line in

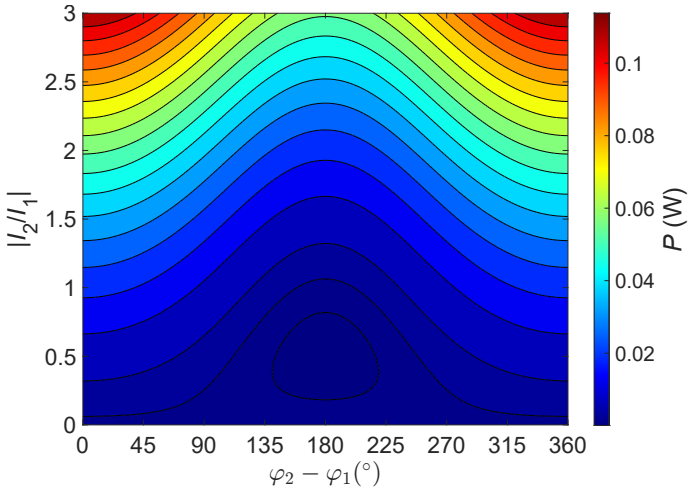

Figure 7.4: Power delivered by the ICH system with 1 Ampere-turn in the primary inductor at 30 mm and 30 kHz for different current ratios and phase angles.

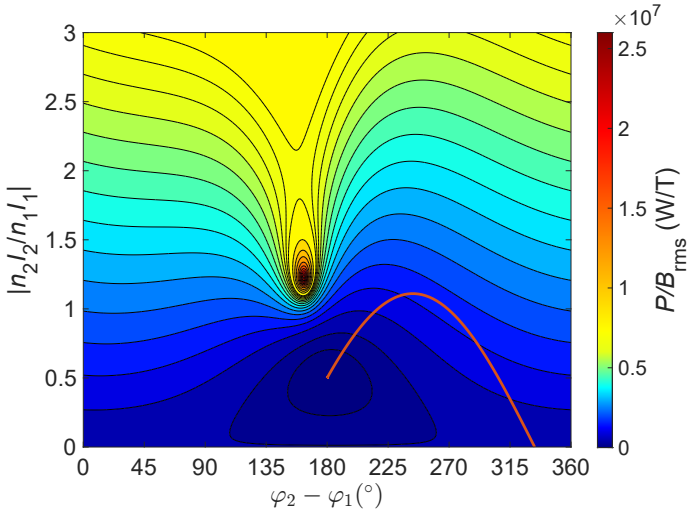

Figure 7.5: Power delivered by the ICH system per emitted magnetic field with 1 Ampere-turn in the primary inductor at 30 mm and 30 kHz for different current ratios and phase angles. The orange line represents the values that can be achieved with the system

Fig. 7.5 represents the ratios and phase differences that can be reached by design, changing $C_{2,\text{p.t.}}$.

Fig. 7.6 shows the magnetic flux generated by the ICH system at d_{w12} of 6 mm and 30 mm delivering 3000 W at 30 kHz. A qualitative comparison with Fig. 7.1 shows that the ICH system emits less magnetic field for the same f and P.

Ideal designs for the IH and ICH systems have been developed with the objective of reaching 3000 W at 30 kHz for different d_{load}. Fig. 7.7 shows P for the IH and ICH system, and Fig. 7.8 shows B_{rms} for both systems calculated at a d_{probe} of 30 cm. The Figure shows that at low d_{load}, for equal f and P, the ICH system

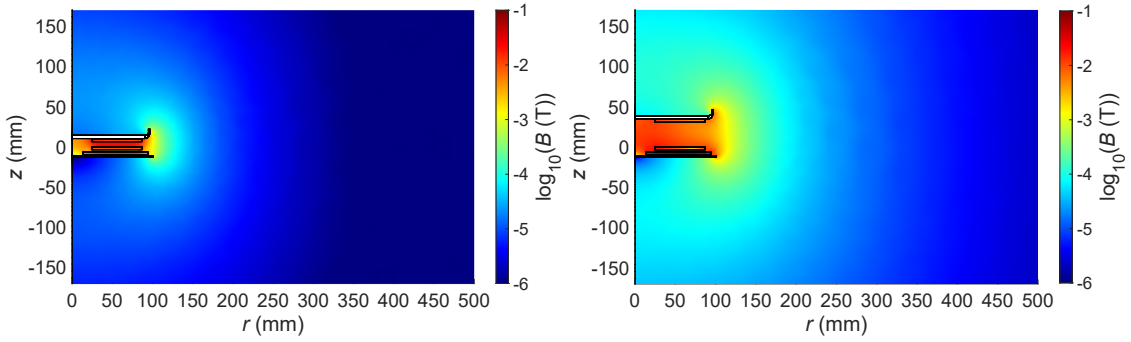

Figure 7.6: Decimal logarithm of magnetic flux produced by the ICH system to deliver 3000 W to the load at 30 kHz and d_l of (a) 6 mm, (b) 30 mm.

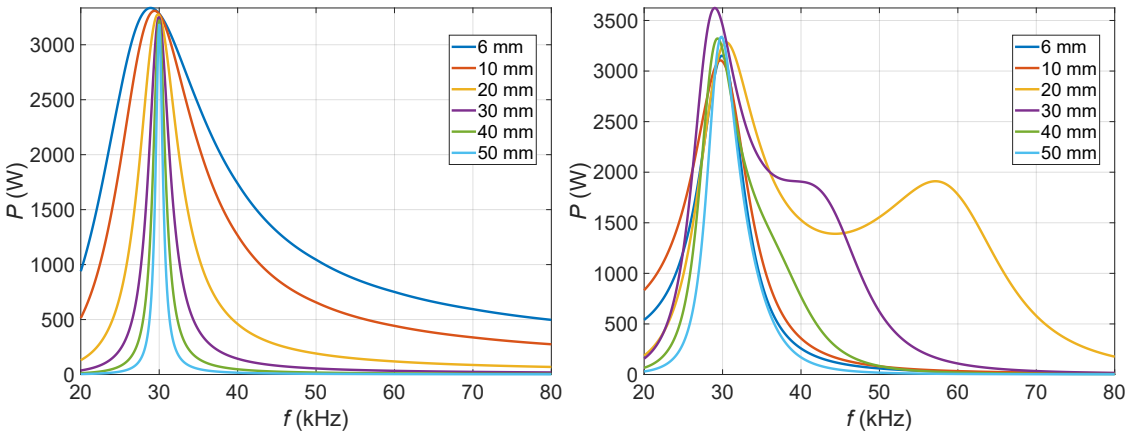

Figure 7.7: Output power for the (a) IH system (b) ICH system.

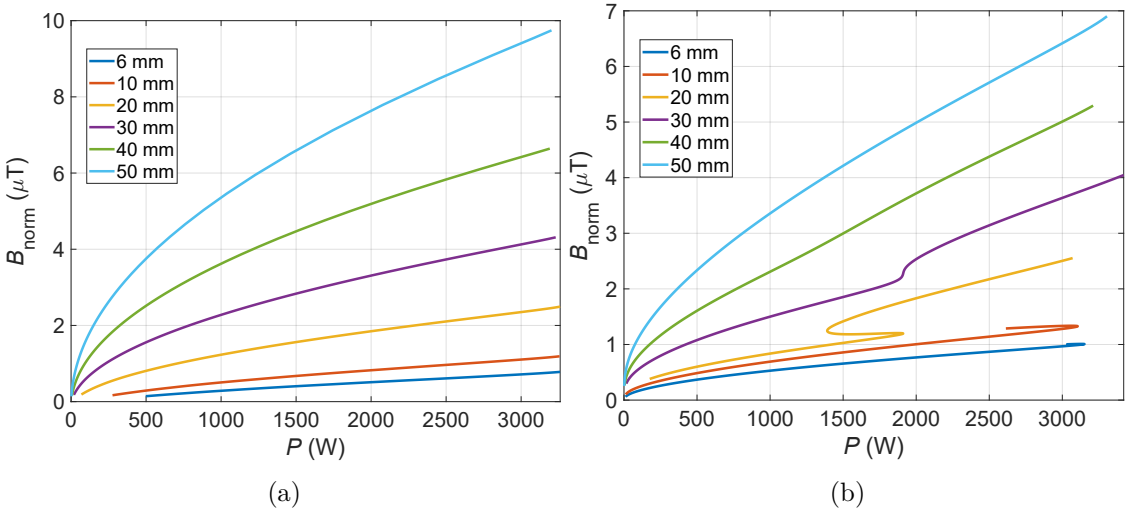

Figure 7.8: Probe calculated magnetic flux for the (a) IH system (b) ICH system.

Table 7.1
Prototype parameters

System	n_1	n_2	C_1	C_2	η
IH	32	–	200 nF	–	92.19
ICH 400 nF	19	19	480 nF	400 nF	96.45
ICH 800 nF	19	19	480 nF	800 nF	96.20

Figure 7.9: Experimental setup.

emits more magnetic flux than the conventional IH system. As distance increases, emitted flux increases faster for the IH system that the ICH system, surpassing it at 20 mm. Multiple inductors generate magnetic fields that can have constructive or destructive interference. At low d_{load} and high k_L, the system design with better performance produces constructive interference, while at higher distances the interference becomes destructive.

7.4 Experimental results

The experimental measurements focus on the 30 mm distance. To achieve similar power and frequency, three 180 mm ∅ windings are prototyped. Two of them have 19 turns, and the third has 32.

With these inductors and different compensation capacitor combinations, adequate designs for the IH and ICH systems for 30 mm can be achieved. Table 7.1 groups the relevant parameters for each prototype, where the estimated efficiency is also included. Two very similar ICH prototypes are selected to accentuate the relevance of C_2 selection in terms of emitted magnetic field.

Fig. 7.9 shows the experimental setup. It maintains the axial symmetry of the 2D

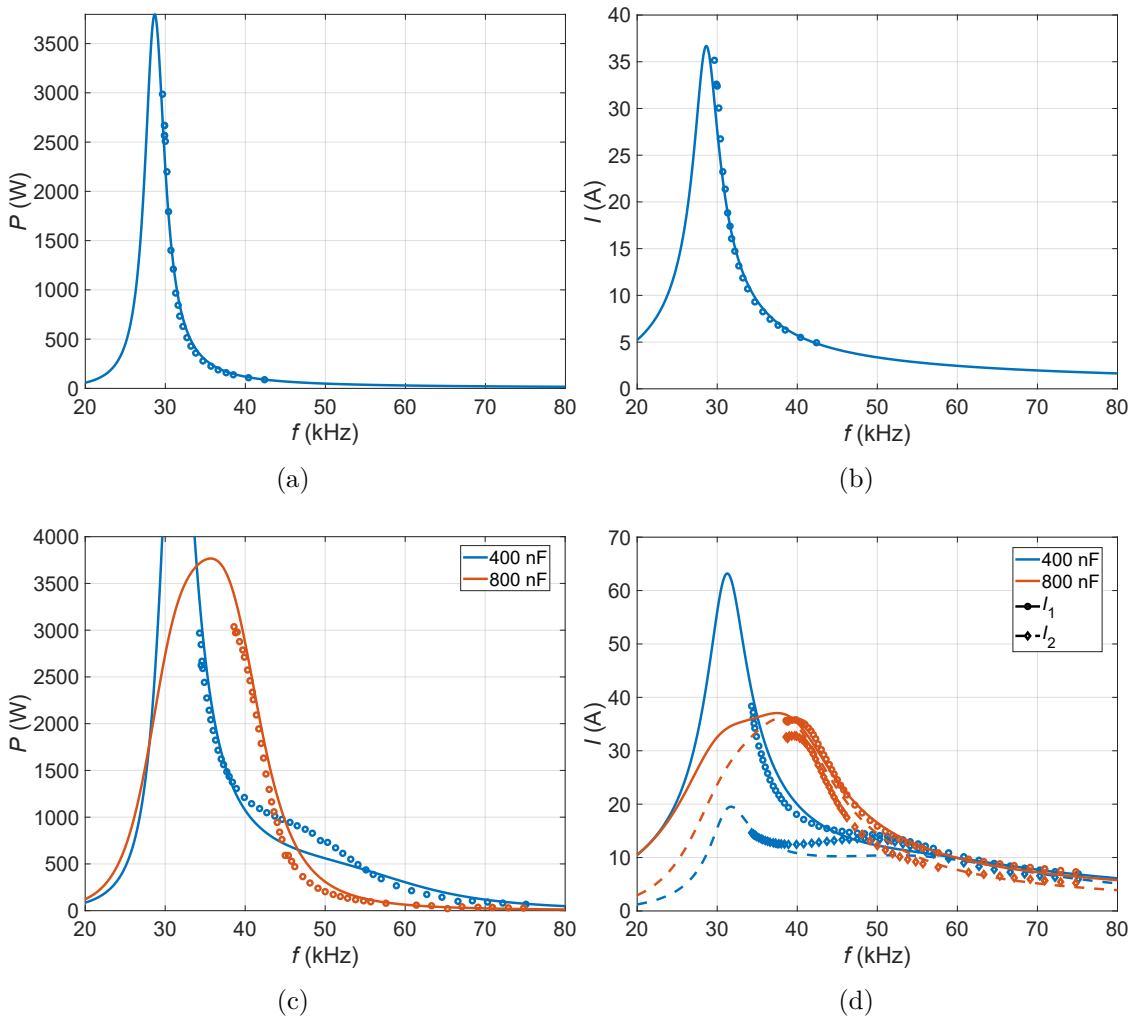

Figure 7.10: Simulated and experimental values of P and I of the 2D IH and ICH designs with sweeping frequency. (a) IH P, (b) IH I, (c) ICH P, (d) ICH I.

simulation with the aluminum shielding disk, the ferrite plane composed of four 90º circle sectors and a flat ferromagnetic load with the same diameter as the inductors, complying with the norm's size restrictions. The oscilloscope is used to measure voltage and currents in the system. Voltage probes are attached to the inverter output and both inductors, and current probes are attached to the inductors. The field probe is used to take measurements from $d_{\text{probe}} = 0\,\text{cm}$ up to the 30 cm of the IEC 62233:2005 standard [89] in 5 cm increments.

The measured P and I_1, I_2 are shown in Fig. 7.10. The measurements of the IH system match the simulations perfectly. The simulated and experimental values of the 400 nF ICH system are close, with small discrepancies at higher f. The experimental values of the 800 nF ICH system fit the simulated ones very well. The congruent P and I measurements validate the impedance calculations of the FEA

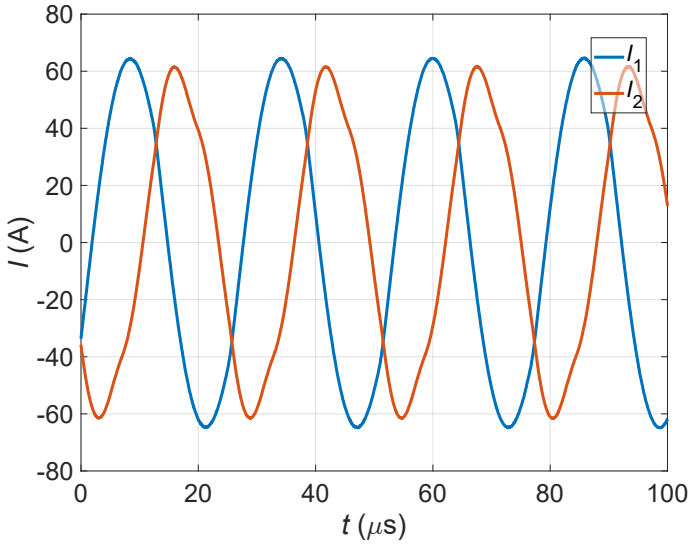

Figure 7.11: Current waveforms in the 800 nF ICH system.

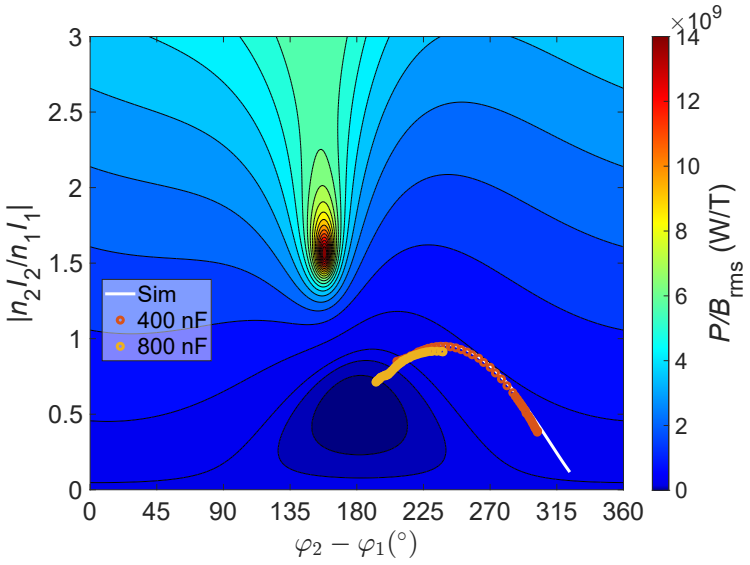

Figure 7.12: Simulated P/B_{rms} ratio for the prototyped 2D ICH cases, with simulated and experimental current ratios and phase differences.

simulations, and therefore, the next step is the magnetic field measurements. Fig. 7.11 shows the measured current waveforms for the 800 nF ICH system, where their phase difference can be observed.

Fig. 7.12 shows the simulated P/B_{rms} ratio for the measured 2D ICH cases and the simulated and measured current ratios and phase differences. While both the 400 nF and 800 nF cases operate along the white line, the point at which the system reaches 3000 W, the rightmost one in both cases, is different. From Fig. 7.12 it can be inferred that the 800 nF design will emit less magnetic field.

Fig. 7.13 shows the measured and simulated B_{rms} for the IH and ICH cases for

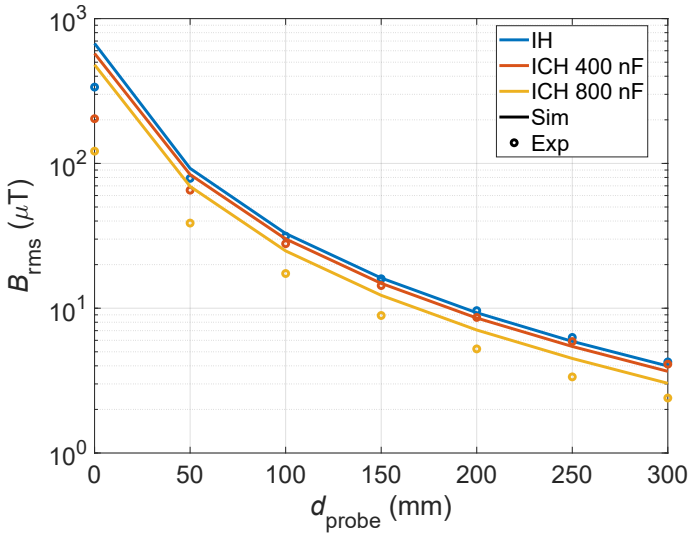

Figure 7.13: Simulated and measured B_{rms} at different d_{probe} for the 2D IH and ICH systems.

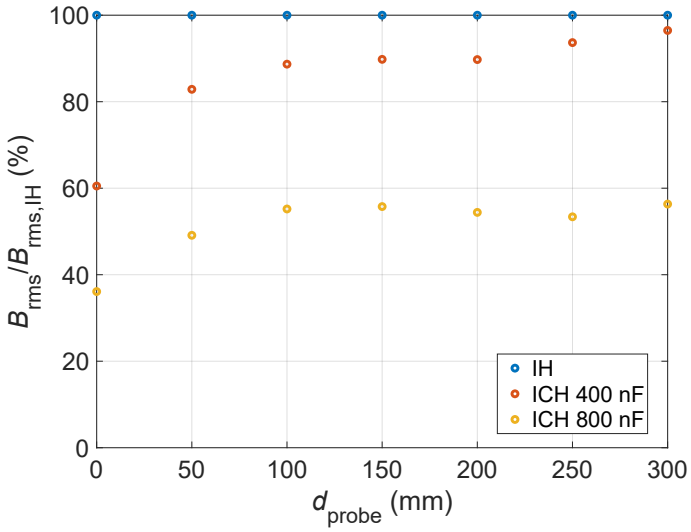

Figure 7.14: Ratio between the measured B_{rms} in all systems with respect to the IH system's.

the d_{probe} range mentioned previously. In all cases, the experimental and simulated values are closest at the farthest d_{probe} and they diverge as they get closer to the system. This is likely due to minor geometry elements in the experimental setup that deviate from the simulated 2D axial symmetry, which are accentuated the closer the probe comes to the systems.

Fig. 7.14 represents the ratio between the measured B_{rms} of all prototypes with respect to the IH system's. From the IH to the 400 nF ICH system, the emitted field decreases 3.5 % at 30 cm and a median of 10.3 % for all considered d_{probe}. From the IH to the 800 nF ICH system, the field decreases 43.7 % at 30 cm and a median of 45.6 %, more than was expected from the simulations.

For ease of comparison, the simulated and experimental probe values at $d_{\text{probe}} =$

Table 7.2
Measured and simulated f, P, I and B_{rms} values at 3000 W

System	f (kHz)		P (W)		I_1 (A)		I_2 (A)		B_{rms} (µT)		B_{rms} reduction (%)	
	Sim	Exp	Sim	Exp	Sim	Exp	Sim	Exp	Sim	Exp	@ 30 cm	median
IH	29.5	29.6	2967	2986	32.07	35.15	–	–	3.988	4.257	–	–
ICH 400 nF	34.6	34.3	3030	2969	39.05	38.36	15.03	14.63	3.665	4.107	3.5	10.3
ICH 800 nF	39.7	39.0	2988	2980	35.66	35.79	34.97	32.78	3.029	2.398	43.7	45.6

30 cm are shown in Table 7.2, along with f, P and I.

7.5 Conclusion

In this chapter, it has been proven that ICH systems emit the same amount or less magnetic flux than IH systems of similar geometry and characteristics. Furthermore, a good ICH design focused on electromagnetic interference (EMI) can significantly reduce emitted field.

Magnetic field emissions in multiple inductor systems depend on the current ratio and current phase difference, with optimal power to flux points of operation. For ICH in particular, the absolute optimal point can not be reached, but local optimums can be selected through careful design.

Active elements in the receiver side, such as a DC/DC stage, can add degrees of freedom to reach more favourable power to magnetic flux emission ratios. Though more costly, those new elements could reduce emissions or increase power for the same magnetic flux.

Chapter 8

Conclusion

This last chapter concludes the dissertation. It summarizes the main research contributions, it lists the main conclusions that can be extracted from the work, and it highlights possible lines of future research.

Table of contents

8.1 Summary 199
8.2 Conclusion 201
8.3 Future research 202

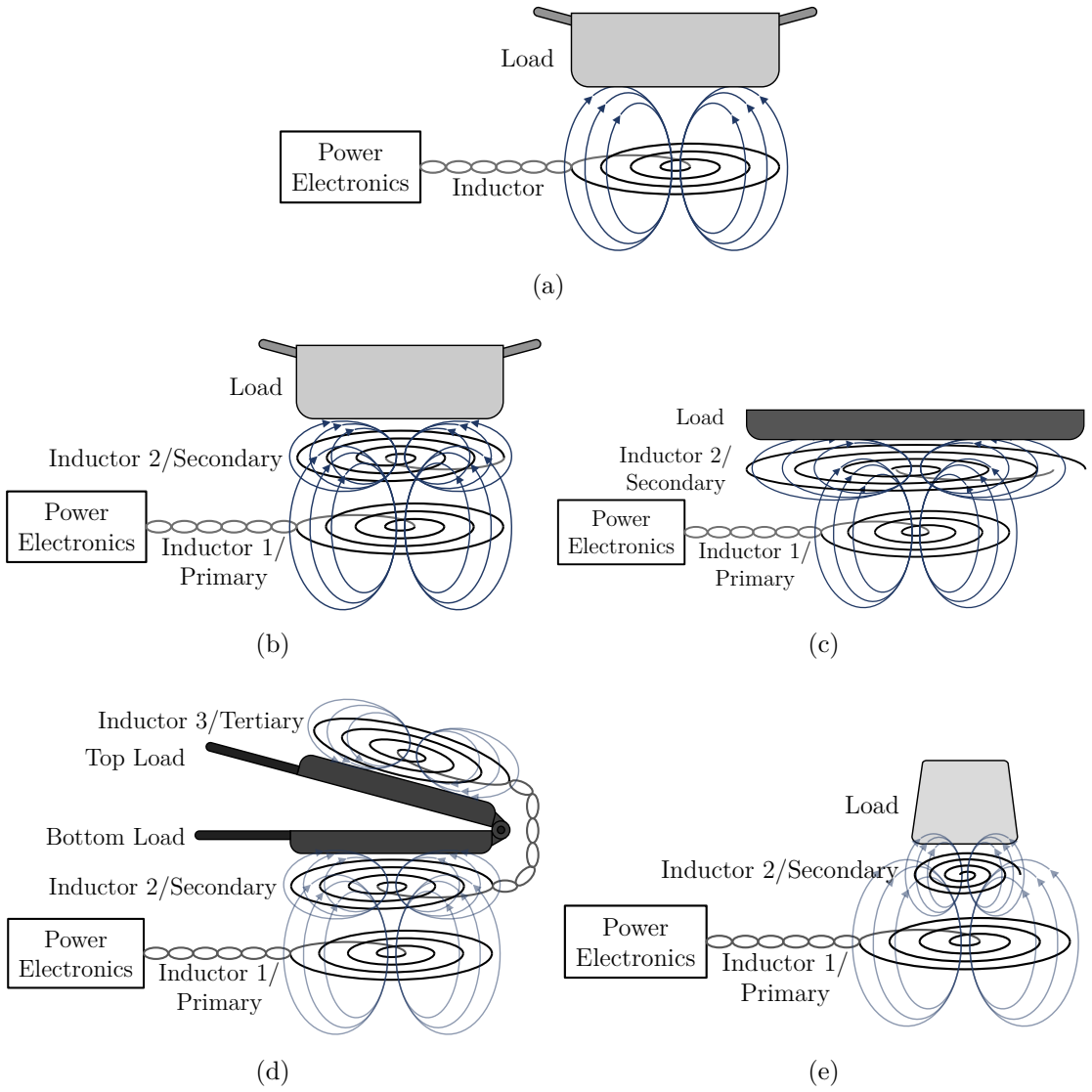

Figure 8.1: Diagram representation of the systems developed in each chapter: (a) IuW, (b) same-diameter ICH, (c) big secondary ICH, (d) two-load, single-transmitter ICH, (e) small secondary ICH.

8.1 Summary

The dissertation's goal is to find solutions for the inductor-load distance problem in IuW technology from the perspective of the inductor-load system design. Single inductor systems are suitable as long as the ratio between inductor-load distance and diameter is relatively small, favoring the form factor and shape of large inductors. Fig. 8.1 represents the diagrams of all types of system developed throughout the dissertation as a visual summary. In this dissertation, the following developments have been carried out:

1. Simulation and design of single inductor IH systems of different diameters at

increasing worktop thickness. Determination of the distance limit for each diameter according to efficiency, coupling between inductor and load, ability to deliver sufficient power, heat distribution in the load and magnetic flux emissions.

2. Exploration of the possibility of adding a second inductor attached to the load, acting as an energy bridge between the primary inductor and the vessel, which is called inductively coupled heating (ICH) in this dissertation.

3. Simulation and design of ICH systems, attempting to make them adapt to the most diverse situations possible. Ideally, a fixed design of primary inductor and resonant capacitor should be able to deliver power to secondary inductors and loads of different sizes at any distance and horizontal offset. These designs are also evaluated according to efficiency, electronic components' stress, their ability to reach the desired power and its distribution.

4. Prototyping and building the most promising IH and ICH designs. Testing these prototypes in low signal conditions for impedance measurement, and in high signal conditions for full power delivery measurements. The results are compared with the corresponding simulations, determining their validity and accuracy.

The activities of this list have been presented in the different dissertation chapters and contributions to the state-of-the-art as follows:

Chapter 2 models conventional IH systems. System are simulated with different inductor-load distance and inductor diameter. Contributions [161] and [162] presents the limitations of these systems, calculated in terms of figures of merit such as power factor, efficiency, winding volumetric losses and emitted magnetic flux. Several prototypes are designed, realized and experimentally verified.

Chapter 3 introduces the modelling and design of ICH systems. Contribution [163] shows that ICH systems outperform conventional IH systems as distances increase. A prototype is designed and tested to validate the ICH concept and the simulations.

Each of the following chapters focuses on one individual strength of ICH systems to test it and highlight it.

Chapter 4 aims to adapt a large secondary inductor and vessel combination to a smaller primary inductor. Contribution [164] introduces a scoring system based on

figures of merit and applies it to determine overall performance, and a near-optimal design is chosen for prototyping. A prototype is tested for its impedance and heating distribution, both of which are verified.

Chapter 5 presents a hybrid ICH and WPT system which uses part of the energy transferred to the secondary inductor to feed a third inductor and heat an additional load. Contributions [165, 166] give design steps to maximize the power ratio that is delivered to the additional load and develops a prototype. The impedance and thermal measurements confirm the simulations. Patents [167–170] further describes system construction and added functionality.

Chapter 6 develops an ICH system to adapt a very small load to a medium-sized primary inductor. Contribution [171] analyzes the positioning and orientation of secondary capacitors within the magnetic field, minimizing its heating effect, and the PCB layout to minimize proximity losses. Power and thermal measurements are carried out to verify the simulations and analysis.

Chapter 7 examines the magnetic field emitted by IH and ICH systems. Contribution [172] explores the relation between inductor currents, magnetic field and power in order to achieve advantageous designs.

Appendix E lists all of the contributions made throughout the dissertation.

8.2 Conclusion

The conclusions extracted from this dissertation are listed below:

- Overall, the adopted approach based on FEA simulations is accurate to the experimental measurements. Discrepancies appear due to the slight simulation overestimation of mutual impedance, which has further effects on equivalent impedance and power.
- The following figures of merit are able to assess the inductor-load systems: maximum power, power factor, power distribution, efficiency and emitted magnetic flux.
- IH systems of certain diameters are able to function at higher inductor-load distances than conventional arrangements with limitations. Low diameters are limited by efficiency, medium diameters are limited by power factor, and high diameters are limited by emitted magnetic flux.

- An additional inductor below the ferromagnetic load can be used to improve functionality at higher distances, hybridizing the IH and WPT technologies into what this dissertation calls ICH. The additional passive inductor distributes the losses between both inductors, it improves power factor at particular frequency ranges and it also reduces magnetic flux emissions depending on currents' amplitude and phase difference.
- ICH systems can be used to adapt different winding sizes to a single primary diameter. The same 180 mm diameter primary inductor offers good performance with secondary inductors and loads between 90 mm and 290 mm, with suitable power distribution.
- ICH systems can increase commercial cooktops' flexibility, as well as simplifying their layouts through the use of only one or two winding diameters, instead of the many possible variations.
- For high distance geometries, ICH systems achieve better efficiency and lower magnetic field emissions than comparable conventional IH systems.
- The secondary inductor of ICH systems can be used to feed additional electronics, such as additional IH windings to heat a second load.

8.3 Future research

At this point there is little research on ICH systems, which leaves a lot of space for future research.

- Substitute the primary inductor with multiple small transmitters, as with flexible or total active cooktops.
- Use different primary or secondary inductor shapes. For example, a rectangular secondary inductor could be used to adapt rectangular loads.
- Change primary inductor topology to allow voltage control to function at fixed frequency and maintain optimal parameters, such as power factor, power distribution or efficiency.
- Add secondary side topologies to increase control in normal situations and feeding additional electronics.
- Consider including a big secondary inductor within the cooktop, switching it on and off according to the detected load diameter.

Appendices

Appendix A

Electromagnetic theory

This appendix establishes the electromagnetic theory applied to the dissertation.

A.1 System electromagnetic modelling

The underlying principles of IH and ICH systems can be described with Maxwell's equations. Written in their differential form [15]:

$$\nabla \cdot \mathbf{D} = \rho, \tag{A.1}$$

$$\nabla \cdot \mathbf{B} = 0, \tag{A.2}$$

$$\nabla \times \mathbf{E} = -\partial_t \mathbf{B}, \tag{A.3}$$

$$\nabla \times \mathbf{H} = \mathbf{J} + \partial_t \mathbf{D}. \tag{A.4}$$

The electric field, $\mathbf{E}$, is generated by the charge density, ρ. In turn, the magnetic field, $\mathbf{H}$, is generated from the current density, $\mathbf{J}$. The sources of the electromagnetic fields are related by the continuity equation:

$$\nabla \cdot \mathbf{J} = -\partial_t \rho. \tag{A.5}$$

The simulated media considered throughout the dissertation are linear, homogeneous and isotropic. The displacement field, $\mathbf{D}$ and magnetic flux, $\mathbf{B}$ are related to $\mathbf{E}$ and $\mathbf{H}$ respectively through electric permittivity, ϵ, and magnetic

permeability, μ, resulting in the so-called constitutive relations:

$$\mathbf{D} = \epsilon \mathbf{E}, \tag{A.6}$$

$$\mathbf{B} = \mu \mathbf{H}. \tag{A.7}$$

Moreover, $\mathbf{J}$ is related to $\mathbf{E}$ through electric conductivity of the material, σ:

$$\mathbf{J} = \sigma \mathbf{E}. \tag{A.8}$$

$\mathbf{E}$ and $\mathbf{B}$ can be expressed in terms of the magnetic vector potential, $\mathbf{A}$ and the scalar electric potential, ϕ:

$$\mathbf{E} = -\partial_t \mathbf{A} - \nabla \phi, \tag{A.9}$$

$$\mathbf{B} = \nabla \times \mathbf{A}. \tag{A.10}$$

Additionally, to avoid the mathematical degree of freedom of $\mathbf{A}$, the Coulomb gauge is adopted:

$$\nabla \cdot \mathbf{A} = 0. \tag{A.11}$$

A.2 MQS approach

Further assumptions can be made for IH and ICH systems. The MQS approach states that $\mathbf{D}$ is constant or nearly constant, meaning that:

$$\partial_t \mathbf{D} \approx 0. \tag{A.12}$$

Therefore (A.4) is simplified to:

$$\nabla \times \mathbf{H} = \mathbf{J}. \tag{A.13}$$

Given the homogenous, isotropic media (A.7), the divergence of the magnetic field can be calculated from (A.2):

$$\mu \nabla \cdot \mathbf{H} = 0. \tag{A.14}$$

$\mathbf{A}$ can be directly related to $\mathbf{J}$ using (A.8), (A.9) and (A.13):

$$\nabla^2 \mathbf{A} - \mu \sigma \partial_t \mathbf{A} = -\mu \mathbf{J}_{\text{ext}}. \tag{A.15}$$

This equation enables the calculation of **A** through the diffusion field effects of the system's **J**. From there, due to the MQS approach, **E** can be calculated as:

$$\mathbf{E} = -\partial_t \mathbf{A}. \tag{A.16}$$

Moreover, the application of Coulomb's gauge (A.11) causes **E**'s divergence to be zero:

$$\nabla \cdot \mathbf{E} = \nabla \cdot (-\partial_t \mathbf{A}) = \partial_t \nabla \cdot \mathbf{A} = 0. \tag{A.17}$$

Consequently, **J**'s divergence is also zero:

$$\nabla \cdot \mathbf{J} = 0. \tag{A.18}$$

As a result, the currents have closed-loop characteristics.

The behaviour of the systems under the MQS approach can be modelled by resistances, which represent the dissipated losses, and inductances, which represent magnetic energy storage.

Appendix B

Twisted strands simulations

All windings simulated and prototyped in this dissertation use litz wire. For these applications, litz-wire structure favours the uniformity of driven current in the cross-sectional area of conductors, alleviating AC losses (skin and proximity effects) and improving the global efficiency of the application. These features are achieved by means of a special cable arrangement consisting of many isolated fine copper strands twisted together according to the manufacturing process. Often, the manufacturing process involves several twisting steps where bundles of moderate number of strands are successively twisted resulting in intricate cable structures. A mathematical description of the trajectories of copper strands is presented with the purpose of obtaining the cable losses by means of FEA simulations tools. Moreover, a nomenclature for these multilevel structures is also proposed. Parameters such as the number of twisting steps, number of strands, strand diameter or pitch length are included in this representation, allowing to compare the performance of different manufacturing solutions.

B.1 Litz wire description

Ac loss reduction is achieved when a thick cable is divided in several preferably isolated fine strands. If some transposition pattern is applied to strands, which favours their geometrical equivalence, additional loss reduction is achieved. Litz wires are wound by recursively twisting bundles of strands together in multiple levels. Usually, the innermost level has a moderate number of thin strands, which are twisted such that the trajectory of each strand corresponds to a helix. The twisting is repeated recursively on the bundles to form bundles of higher level, as is

Figure B.1: Litz wires with different number of strands and structure: $n_s = 38$ single bundle, $n_s = 76$ in two bundles of previous wire, $n_s = 156$ in two bundles of previous wire.

shown in Fig. B.1.

Magnetic design with litz wire requires an estimation of AC losses with respect to the cable parameters: number of strands, structure of cable and diameter of strands. Existing loss models essentially rely on three assumptions: equivalence of strands, orthogonality of AC loss mechanisms (skin and proximity effects), and widely spaced isolated and infinite strands. The preceding premises implicitly assume that cable structure is perfect and therefore current is equally shared in strands, which minimizes the Joule's effect losses. Accordingly, AC losses of litz wires are usually computed as the losses of a strand multiplied by the number of strands.

AC losses in a strand are calculated as the sum of copper losses due to skin and proximity effects, which in its turn can be obtained as exact solutions of Maxwell's equations for round geometry by applying the third premise as a boundary condition. Some aspects of litz-wire loss modelling are still pending of a satisfactory approach, specially those aspects related with the underlying structure of the cable. Details of construction of the wire, i.e. complex structures which can comprise several bundle levels (as it is shown in Fig. B.1) can become relevant. These reasons are

often mentioned when discrepancies between theory and measurements are found. Structure of litz wire and wire rope are, in general terms, identical. The basic element of both is a single thin metallic wire. A mathematical description of litz-wire arrangements is proposed, with the purpose of obtaining strand resistances and current densities by means of 3D FEA simulations. The mathematical description includes elements from wire rope descriptions, particularly the collision avoidance methods. A rigorous method and a simplified method have been tested for their solvability, accuracy and applicability to the current problem. Additionally, the simulated cases seek to determine the dependencies of the AC losses with respect to different constructive parameters (such as the number of strands per bundle and the insulation between strands). These dependencies show some manufacturing guidelines which can help to reduce cable losses.

B.2 Mathematical description

Electromagnetic analysis of litz wires under AC excitation conditions can be carried out by means of 3D FEA simulations. However, these 3D simulations present some challenges, mainly derived from the fact that litz wire is a multiscale structure where extremely different orders of magnitude can appear in the same system under study. For example, in real applications it is usual to find strands with diameters of microns whose total lengths can be up to several meters. Moreover, the use of wires with hundreds or thousands of isolated strands is also very common, manufactured in several bundling steps, whose analysis capturing the geometrical details is also challenging. Currently, realistic simulations of real applications with litz wires is almost unapproachable even with advanced computing facilities.

B.2.1 Nomenclature, definitions and assumptions

Each individual length of conductive metal is called a strand. Several strands can be twisted together to form bundles. Several bundles can in turn compose more complex bundles. The grouping of all bundles is called the (litz) wire.

Construction details of a litz wire can include many factors and, for this reason, the following basic assumptions are adopted:

- Only round strands are considered.
- Strands have no electrical contact, and the insulation material is the air.

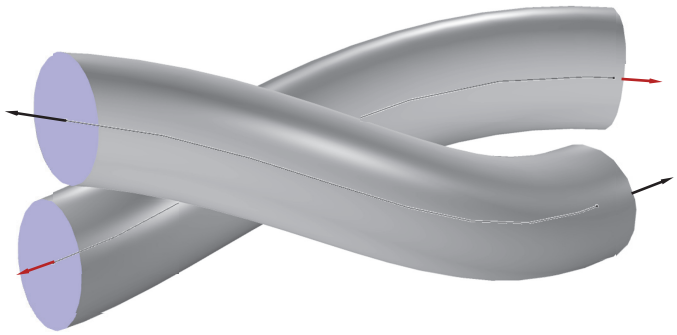

Figure B.2: Generation of strand domains.

- Smooth trajectories of both strands and bundles, which can be described in the Frenet-Serret frame, are considered.
- A bundling operation involves identical sub-bundles.

In COMSOL, the FEA tool, the domain of every strand can be generated by extruding a circle along a given trajectory as it is schematically shown in Fig. B.2. Therefore, it is necessary to describe mathematically the trajectory of every strand for simulating the cable. For this purpose, it is convenient to define some parameters in order to describe complex wire structures. Moreover, it is also interesting to define a nomenclature to properly denote structures made up of several bundles, which can in turn hold even smaller bundles.

In this work, the term bundle refers to the basic entity. The external radius of a bundle is denoted as r_b. Considering that a bundle, as a result of a twisting process, can include several concentric layers of strands, in general, it is considered that a bundle is placed in the n layer of a more general bundle and has a position radius, $r_{\mathrm{pos},n}$, with respect to the center of the bundle. Therefore, r_b can be calculated from the position of the outermost sub-bundle and its external radius: $r_b = r_{\mathrm{pos},n_{\max}} + r_{b,n_{\max}}$. The number of layers of a bundle is n_b. Other parameters of interest for describing a bundle are the bundle level, b_l, and the twisting level, t_l, which correspond to the number of bundling and twisting operations, respectively, conducted on a bundle in the manufacturing process of the cable.

Strands are placed in the deepest bundle level and, for convenience, they are considered bundles as well. A single straight strand corresponds to a bundle with $n_b = 0$, $b_l = 0$, and $t_l = 0$. Similarly, central bundles (or central strands) are placed in the layer $n = 0$ of a bundle and have one twisting level less than the rest of

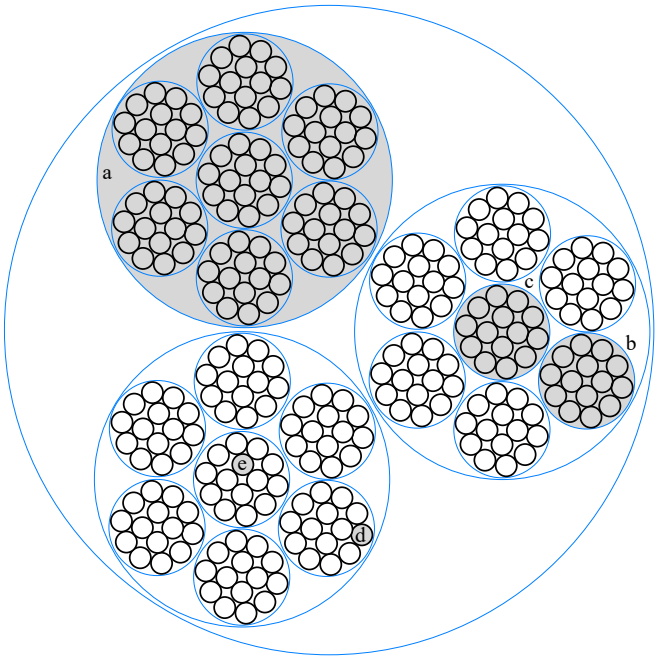

Figure B.3: Examples of array $\mathbf{N}_l$ for different bundles.

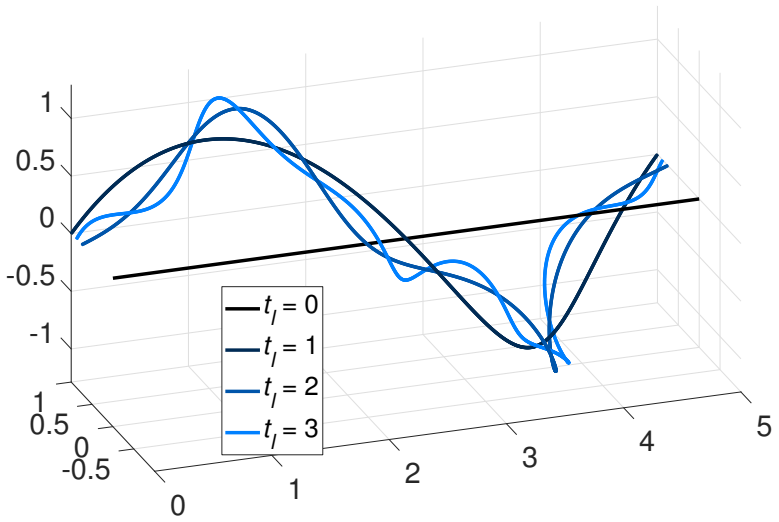

Figure B.4: Generation of helix bundle trajectories.

entities of the bundle.

According to the previous definitions, a bundle can be associated with an array $\mathbf{N}_l$ of b_l elements, where b_l is its bundle level. The i^{th} bundle level corresponds to the n^{th} layer of the i^{th} level where the bundle is placed. According to this definition, parameters b_l and t_l of a bundle can be obtained from $\mathbf{N}_l$. In particular, b_l is equal to the dimension of $\mathbf{N}_l$ and t_l corresponds to the number of elements of $\mathbf{N}_l$ higher than zero. Fig. B.3 shows some examples of values of $\mathbf{N}_l$ for different bundles for a cable of $14 \times 7 \times 3$ entities.

Regarding trajectories, it is considered that bundles describe circles along a path. In particular, if the path is simply a straight line, as it is schematically shown in Fig. B.4, the trajectory corresponds to a helix. Small bundles twisted together also describe helical trajectories, as it is schematically shown in Fig. B.4. In general, the trajectory of the $\mathbf{N}_l$ bundle can be mathematically described by considering that it successively describes t_l helices with respect to b_l trajectories.

B.2.2 Mathematical description of bundle trajectories

In general, bundles describe helices around a core according to its position radius, $r_{\text{pos},n}$, therefore, the case of straight bundles corresponds to $r_{\text{pos},n}$ corresponds to a helix whose parameterized equation is:

$$\begin{cases} x = \lambda\varphi \\ y = r_{\text{pos},n} \cdot \cos\varphi \\ z = r_{\text{pos},n} \cdot \sin\varphi \end{cases}, \tag{B.1}$$

where φ is the curve parameter that ranges from 0 to 2π rad for a single helix turn, λ is the angular pitch, $\lambda = \lambda/2\pi$, where λ is the pitch in a similar relation between linear and angular wavelength.

In order to describe the trajectory of bundles, it is convenient to adopt the Frenet-Serret frame in which smooth curves are described on the basis of three orthonormal unitary vectors (i.e. directional vectors) $\hat{\mathbf{t}}$, $\hat{\mathbf{n}}$, $\hat{\mathbf{b}}$ called tangent, normal and binormal, respectively. Moreover, as it has been mentioned, the manufacturing of a litz wire can be assimilated to a recursive process and the trajectory and position of a given bundle for a twist level can be described on the basis of the core trajectory of the previous twist level:

$$\mathbf{r}_{t_l} = \mathbf{r}_{t_l-1} + r_{\text{pos},n}\cos(pr_n \cdot \varphi) \cdot \hat{\mathbf{n}}_{t_l-1} + r_{\text{pos},n}\sin(pr_n \cdot \varphi) \cdot \hat{\mathbf{b}}_{t_l-1}, \tag{B.2}$$

where $\mathbf{r}_{t_l}$ is the position vector of the twist level t_l, pr_n is the ratio of the n^{th} layer pitch of the t_l^{th} twist level with respect to the global wire pitch and $\hat{\mathbf{n}}_{t_l-1}$ and $\hat{\mathbf{b}}_{t_l-1}$ are the normalized perpendicular vectors of the twist level $t_l - 1$. The parameter pr_n takes into account that different twist levels can have different pitches. In order for the wire to be periodic in 2π intervals of φ, all pr_n values have to be non-zero integers. Negative values change the lay of the bundle.

The tangent and normal vectors of each twist level can be obtained as follows:

$$\bar{\mathbf{t}}_{t_l} = \frac{\partial x_{t_l}}{\partial \varphi}\hat{\mathbf{x}} + \frac{\partial y_{t_l}}{\partial \varphi}\hat{\mathbf{y}} + \frac{\partial z_{t_l}}{\partial \varphi}\hat{\mathbf{z}}, \tag{B.3}$$

$$\bar{\mathbf{n}}_{t_l} = \frac{\partial (t_{t_l})_x}{\partial \varphi}\hat{\mathbf{x}} + \frac{\partial (t_{t_l})_y}{\partial \varphi}\hat{\mathbf{y}} + \frac{\partial (t_{t_l})_z}{\partial \varphi}\hat{\mathbf{z}}, \tag{B.4}$$

$$\hat{\mathbf{t}}_{t_l} = \frac{\bar{\mathbf{t}}_{t_l}}{\left|\bar{\mathbf{t}}_{t_l}\right|}, \tag{B.5}$$

$$\hat{\mathbf{n}}_{t_l} = \frac{\bar{\mathbf{n}}_{t_l}}{\left|\bar{\mathbf{n}}_{t_l}\right|}, \tag{B.6}$$

$$\hat{\mathbf{b}}_{t_l} = \hat{\mathbf{t}}_{t_l} \times \hat{\mathbf{n}}_{t_l}. \tag{B.7}$$

Apart from calculating the position vector, it is also convenient to obtain the rest of directional vectors because they are required to calculate the current density and losses in conductors. Considering the the twist level $t_l = 1$, the directional vectors are:

$$\hat{\mathbf{t}}_1 = \frac{\lambda}{\sqrt{\lambda^2 + r_{\text{pos},1}^2}}\hat{\mathbf{x}} - \frac{r_{\text{pos},1} \cdot \sin(pr_1 \cdot \varphi)}{\sqrt{\lambda^2 + r_{\text{pos},1}^2}}\hat{\mathbf{y}} + \frac{r_{\text{pos},1} \cdot \cos(pr_1 \cdot \varphi)}{\sqrt{\lambda^2 + r_{\text{pos},1}^2}}\hat{\mathbf{z}}, \tag{B.8}$$

$$\hat{\mathbf{n}}_1 = -\cos(pr_1 \cdot \varphi)\hat{\mathbf{y}} + \sin(pr_1 \cdot \varphi)\hat{\mathbf{z}}, \tag{B.9}$$

$$\hat{\mathbf{b}}_1 = \frac{r_{\text{pos},1}}{\sqrt{\lambda^2 + r_{\text{pos},1}^2}}\hat{\mathbf{x}} + \frac{\lambda \cdot \sin(pr_1 \cdot \varphi)}{\sqrt{\lambda^2 + r_{\text{pos},1}^2}}\hat{\mathbf{y}} - \frac{\lambda \cdot \cos(pr_1 \cdot \varphi)}{\sqrt{\lambda^2 + r_{\text{pos},1}^2}}\hat{\mathbf{z}}. \tag{B.10}$$

The position vector corresponding to the twist level $t_l = 2$ can be obtained using (B.2):

$$x_2 = \lambda \cdot pr_1 \cdot \varphi + r_{\text{pos},2}\frac{r_{\text{pos},1}}{\sqrt{\lambda^2 + r_{\text{pos},1}^2}}\sin(pr_2 \cdot \varphi) \tag{B.11}$$

$$\begin{aligned} y_2 = {} & r_{\text{pos},1} \cdot \cos(pr_1 \cdot \varphi) - r_{\text{pos},2} \cdot \cos(pr_1 \cdot \varphi) \cdot \cos(pr_2 \cdot \varphi) + \\ & + r_{\text{pos},2}\frac{\lambda \cdot \sin(pr_1 \cdot \varphi)}{\sqrt{\lambda^2 + r_{\text{pos},1}^2}}\sin(pr_2 \cdot \varphi) \end{aligned} \tag{B.12}$$

$$\begin{aligned} z_2 = {} & r_{\text{pos},1} \cdot \sin(pr_1 \cdot \varphi) - r_{\text{pos},2} \cdot \sin(pr_1 \cdot \varphi) \cdot \cos(pr_2 \cdot \varphi) - \\ & - r_{\text{pos},2}\frac{\lambda \cdot \cos(pr_1 \cdot \varphi)}{\sqrt{\lambda^2 + r_{\text{pos},1}^2}} \cdot \sin(pr_2 \cdot \varphi) \end{aligned} \tag{B.13}$$

The last expressions can be used to obtain the directional vectors $\hat{\mathbf{t}}_2$, $\hat{\mathbf{n}}_2$ and $\hat{\mathbf{b}}_2$ by means of (B.3)-(B.7). Moreover, analytical expressions for position and directional vectors of bundles with $t_l = 3$ have been also obtained for the simulations presented in section 3. In order to implement these expressions, the position radius of bundles is required.

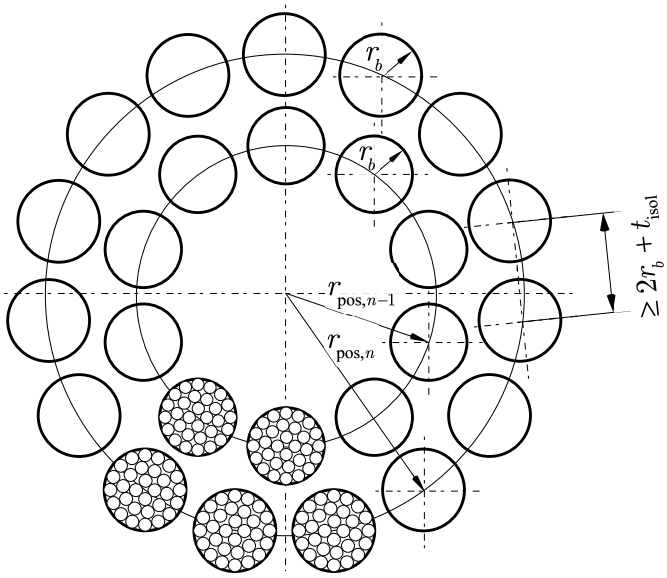

Figure B.5: Position radii of two consecutive layers of a bundle.

B.2.3 Collision detection methods

Bundles can be built outwards starting from their core, successively adding the required sub-bundle layers. Therefore, in order to avoid collision, $r_{\text{pos},n}$ has to satisfy two conditions:

- The sub-bundle position radius, $r_{\text{pos},n}$, should be greater than the sum of the sub-bundle's external radius, $r_{b,n}$, and the external radius of the previous layer, $r_{\text{pos},n-1} + r_{b,n-1}$.
- The bundle position radius should be big enough to place all bundles in the layer, assuming a regular distribution as shown in Fig. B.5.

Considering bundles composed of identical sub-bundles of radius r_b, the first condition can be easily expressed as:

$$r_{\text{pos},n} \geq 2 \cdot r_b + t_{\text{ins}} + r_{\text{pos},n-1}, \tag{B.14}$$

where $r_{\text{pos},n-1}$ is the position radius of a bundle placed in the $(n-1)$ layer, t_{ins} is the insulation distance between bundles and b_n is the number of bundles of the layer. The minimum insulation distance corresponds to the insulation thickness of strands, which is a standardised value dependent on the insulation grade.

There are several approaches to avoid overlapping between bundles in the same layer. The most rigourous seek to determine the minimum distance between bundles along their entire length. Others simplify the three-dimensional problem to a two-dimensional cross section, assuming that the resulting bundle sections will have

the shape of ellipses. In the case of litz wire, as opposed to cable rope, the bundles and strands do not need to be in physical contact, and in fact they are separated by an insulating layer to avoid electrical contact. A small error in the positioning radius will mean a smaller gap between bundles instead of physical overlap. Therefore, absolutely exact positioning is not strictly required. Nevertheless, both kinds of approaches were tested to be able to compare results.

In the case of litz wires, the bundle's external radius is an input parameter, as it can be calculated incrementally from the bundle composition down to the strand radius. The wire's pitch, λ, can be defined either directly, or indirectly with the helix angle, β, through the relation $\lambda = 2\pi r_{\mathrm{pos},n} \tan\beta$. Therefore, the collision detection methods need to have bundle external radius and pitch as input parameters and minimum bundle position radius as output.

B.2.3.1 Three dimensional method

The three-dimensional method expresses the trajectory of two consecutive bundles (A and B, for example) in the same layer in terms of their curve parameter, the angle $\varphi = \varphi_A$, their difference between curve angle, $\Delta\varphi = \varphi_B - \varphi_A$, and their in-layer angular separation, θ, given by the number of bundles in the layer, $\theta = 2\pi/b_n$. The segment with minimum distance between A and B for each value of φ is perpendicular to both trajectories, so this segment's length is simply the sum of the bundles' radius and gap between them. Since the position vector of the bundles are periodic with period 2π, the minimum distance can be found in any period length interval of φ. Consequently, the absolute limits of $\Delta\varphi$ are $[-2\pi, 2\pi]$ although the minimum distance is expected to be found in values closer to zero.

$$\vec{\mathbf{AB}} = \mathbf{p}_B(\varphi, \Delta\varphi, \theta, r_{\mathrm{pos,b}}) - \mathbf{p}_A(\varphi, r_{\mathrm{pos,b}}), \tag{B.15}$$

$$\min\left(\left\|\vec{\mathbf{AB}}(\varphi, \Delta\varphi, \theta, r_{\mathrm{pos,b}})\right\|\right) = 2r_b + t_{\mathrm{ins}}. \tag{B.16}$$

The equation can be transformed to output the bundle position radius:

$$r_{\mathrm{pos,b,min}} = \max\left(r_{\mathrm{pos,b}}(\varphi, \Delta\varphi, \theta, r_b, t_{\mathrm{ins}})\right). \tag{B.17}$$

Parameters θ, r_b and t_{ins} are known beforehand, so the function has to be maximized for inputs φ and $\Delta\varphi$. The implementation for a bundle of $t_l = 1$ is

rather straightforward. The vector $\vec{\mathbf{AB}}_1$ can be defined as:

$$\vec{\mathbf{AB}}_1 = \begin{pmatrix} \lambda\Delta\varphi \\ r_{\text{pos,b}}\left(\cos\left(\varphi+\Delta\varphi+\theta\right)-\cos\varphi\right) \\ r_{\text{pos,b}}\left(\sin\left(\varphi+\Delta\varphi+\theta\right)-\sin\varphi\right) \end{pmatrix}. \tag{B.18}$$

Moreover, its squared norm is:

$$\left\|\vec{\mathbf{AB}}_1\right\|^2 = \lambda^2\Delta\varphi^2 + 2r_{\text{pos,b}}^2\left(1-\cos\left(\Delta\varphi+\theta\right)\right). \tag{B.19}$$

Helices of $t_l = 1$ have a very regular trajectory, so the distance between two of the same $r_{\text{pos},b}$ and β is only dependent on the difference of position and not its absolute value. Isolating $r_{\text{pos},b}$:

$$r_{\text{pos,b,min}} = \max\left(\sqrt{\frac{(2r_b+t_{\text{ins}})^2-\lambda^2\Delta\varphi^2}{2(1-\cos(\Delta\varphi+\theta))}}\right). \tag{B.20}$$

As stated earlier, for simple helices the maximization function has only one input parameter, which will not be the case for higher levels where the axial tangent component is not constant. Although this is the simplest position radius expression, it is clearly non linear, and higher level expressions are even more intricate. Since analytical methods are not feasible, numerical ones are the only option. Fortunately, there are myriad numeric methods that can be used to maximize bounded, multiple input, non linear functions.

In this case, since Matlab's symbolic toolbox was already used to obtain the expressions for the position, tangent, normal and binormal vectors, it is also applied to deduce the expressions of $r_{\text{pos},b,\text{min}}$ for each t_l and eventually maximize them for each geometry case. The Matlab function used was *fmincon*, which minimizes non linear functions with any number of input arguments, user input constraints and bounds on the inputs. The default algorithm uses an interior point method where in each iteration it attempts a direct, linear approximation step. If the projected Hessian for said step is not positive definite, the algorithm performs a conjugate gradient step. In order to solve the maximization problem with a minimization algorithm, the input function is $-r_{\text{pos},b}$.

Most optimization algorithms require a convex function. A scalar function's convexity can be proven if its Hessian is positive definite (i.e. all eigenvalues are positive) but such a test was taking too long to compute in Matlab for $t_l > 1$. In

Table B.1

Parameters used for the convexity tests

t_l	λ	r_b	b_n	pr_2	pr_3	$r_{\text{pos,b,1}}$	$r_{\text{pos,b,2}}$
1	1	0.1	5	-	-	-	-
2	1	0.1	5	2	-	1	-
3	1	0.1	5	3	2	1	0.5

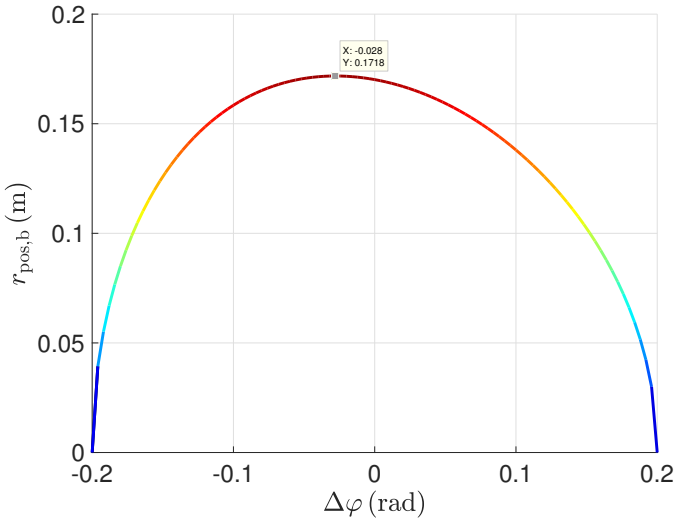

Figure B.6: Bundle position radius ($t_l = 1$) versus $\Delta\varphi$.

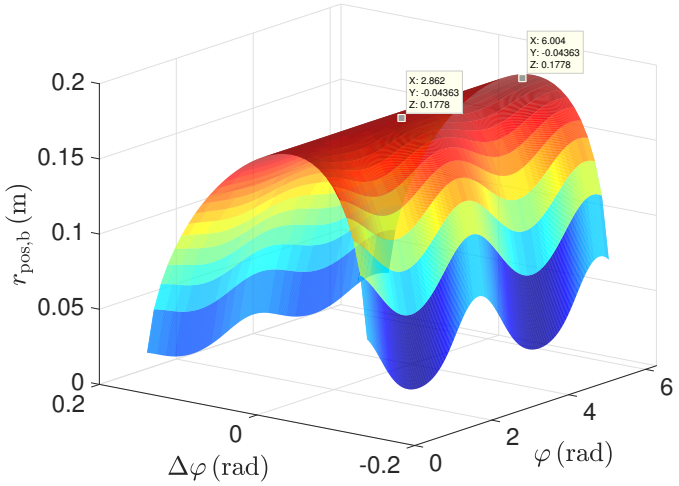

Figure B.7: Bundle position radius ($t_l = 2$) versus φ and $\Delta\varphi$.

order to determine function convexity, a test case for each t_l has been selected to plot $r_{\text{pos},b}$. The geometric parameters for each case appear in Table B.1.

The only function that is unquestionably convex is that of $t_l = 1$, as seen in Fig. B.6. The function for $t_l = 2$ is harder to determine (Fig. B.7), but all minima found are global minima, as the function is periodic with period $2\pi/pr_2$ in φ. Lastly, the function for $t_l = 3$ is simply not convex, as the global minimum is surrounded by

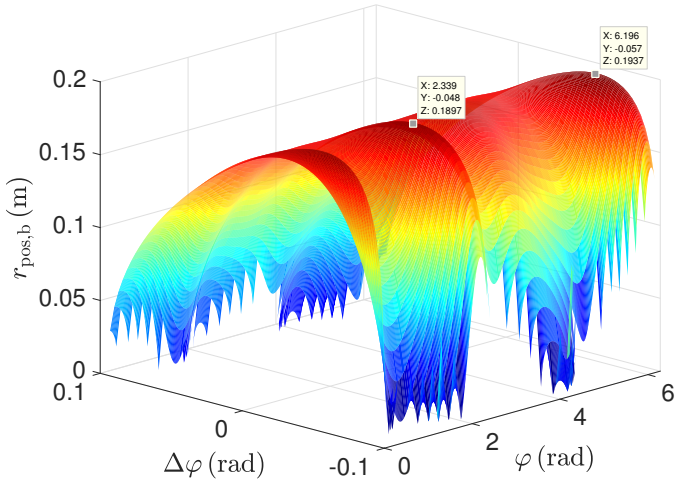

Figure B.8: Bundle position radius ($t_l = 3$) versus φ and $\Delta\varphi$.

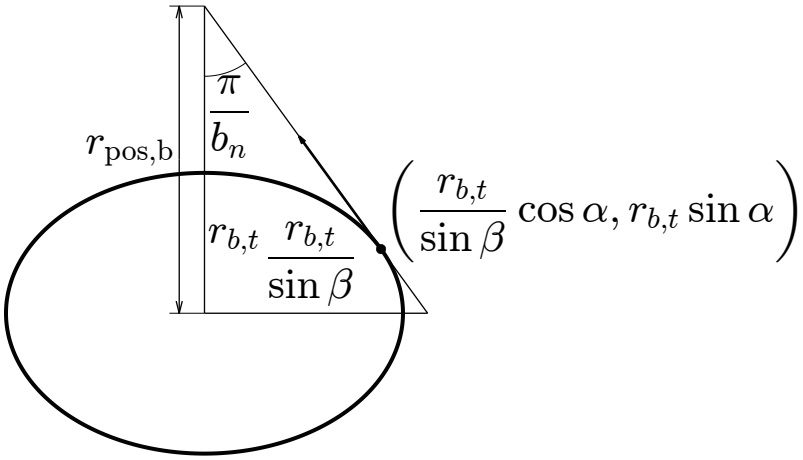

Figure B.9: 2D bundle section simplification.

local minima, and is difficult to reach (Fig. B.8).

B.2.3.2 Two dimensional method

The two-dimensional method assumes that the sub-bundle sections are created by cuts of the big bundle's normal plane with cylinders of radius $r_{b,t} = r_b + t_{\mathrm{ins}}/2$ and incident angle β, as shown in Fig. B.9. Each bundle layer is made up of identical, regularly spaced b_n ellipses with their small axis in the radial direction. Though β is used elsewhere for the main cable angle, in this case it is bundle specific. It can be calculated from the scalar product of the central bundle trajectory and the considered bundle's: $\hat{\mathbf{t}}_n \cdot \hat{\mathbf{t}}_{n-1} = \cos(\pi/2 - \beta)$. The semi-minor axis equals $r_{b,t}$ and the semi-major axis equals $r_{b,t}/\sin\beta$. In order for all ellipses to be tangent to one another, each ellipse, belong to the diagonal line that diverges π/b_n rad from the line that connects to the center of the ellipse and have the ellipse's tangent parallel to this line. The parametric equation of an ellipse with semi-major axis a and semi-minor

axis b can be expressed as:

$$\mathbf{p}_e = (a\cos\alpha, b\sin\alpha)\,, \tag{B.21}$$

where $\mathbf{p}_e$ is the position vector of a generic ellipse and α is the curve parameter. The ellipse tangent, $\bar{\mathbf{t}}_e$, can be obtained as the position vector gradient:

$$\bar{\mathbf{t}}_e = (-a\sin\alpha, b\cos\alpha)\,. \tag{B.22}$$

Therefore, α has to satisfy:

$$\frac{b\cos\alpha}{-a\sin\alpha} = \tan\left(\pi - \left(\frac{\pi}{2} - \frac{\pi}{b_n}\right)\right), \tag{B.23}$$

$$\tan\alpha = \tan\frac{\pi}{b_n}\sin\beta. \tag{B.24}$$

For the ellipse point to be in the diagonal line, this last condition has to be met:

$$\tan\frac{\pi}{b_n} = \frac{\frac{r_{b,t}}{\sin\beta}\cos\alpha}{r_{\text{pos,b}} - r_{b,t}\sin\alpha}, \tag{B.25}$$

$$r_{\text{pos,b}} = r_{b,t}\sqrt{1 + \frac{1}{\tan^2\frac{\pi}{b_n}\sin^2\beta}}. \tag{B.26}$$

If the input parameter is λ instead of β, the expression of $r_{\text{pos},b}$ becomes:

$$r_{\text{pos,b}} = \frac{r_{b,t}}{\sqrt{\left(1 + \frac{r_{b,t}^2}{\lambda^2}\right)\sin^2\frac{\pi}{b_n} - \frac{r_{b,t}^2}{\lambda^2}}} \tag{B.27}$$

The resulting expressions are much simpler than the 3D optimization process, but they become inaccurate as β decreases and the ration $r_{b,t}/r_{\text{pos},b}$ increases, as shown in Fig. B.10. The cuts were generated with the position vector for helices of $t_l = 2$, $\mathbf{r}_2(\varphi, \alpha)$, where φ is the parameter that sweeps the bundle's trajectory while α is the parameter that sweeps the bundle's normal angle. The combination of φ and α when they are not bound generates the external bundle surface. The cut with the plane $x = x_0$ provides the relation between φ and α that describes the parametric curve of the bundle surface contained in the plane:

$$x_0 = \lambda\varphi + r_b\cos\beta\sin\left(pr_2\varphi + \alpha\right). \tag{B.28}$$

$$\alpha = \arcsin\left(\frac{x_0 - \lambda\varphi}{r_b\cos\beta}\right) - pr_2\varphi. \tag{B.29}$$

For the solution to be real, φ must be bound between $(x_0 - r_b\cos\beta)/\lambda$ and $(x_0 + r_b\cos\beta)/\lambda$.

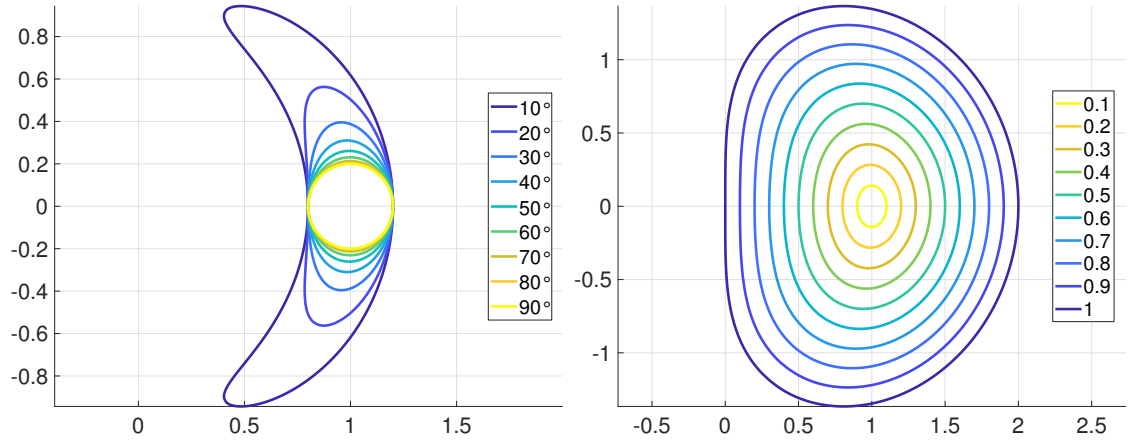

(a) (b)

Figure B.10: Real cross sections of bundles depending on (a) helix angle β (at ratio 0.2) (b) External and position radius ratio $r_{b,t}/r_{\text{pos,b}}$ (at β 45°).

Table B.2
Calculated $r_{\text{pos,b}}$ for the 2, 4, 4 case

	$r_{\text{pos,b,1}}$ (µm)	$r_{\text{pos,b,2}}$ (µm)	$r_{\text{pos,b,3}}$ (µm)
2D method	728.1	289.9	100.0
3D method	731.6	289.6	100.0
absolute difference	3.476	0.6808	0
relative difference	0.457%	0.235%	0%

Table B.3
Calculated $r_{\text{pos,b}}$ for the 4, 4, 2 case

	$r_{\text{pos,b,1}}$ (µm)	$r_{\text{pos,b,2}}$ (µm)	$r_{\text{pos,b,3}}$ (µm)
2D method	602.3	355.0	142.3
3D method	602.3	359.9	142.4
absolute difference	0	4.958	0.0824
relative difference	0%	1.38%	0.0579%

B.2.4 Method comparison for the simulations at hand

The minimum position radii were calculated for each bundle level for both simulation cases, $2 \times 4 \times 4$ and $4 \times 4 \times 2$, assuming zero insulation. The results are shown in Tables B.2 and B.3, respectively. The maximum relative and absolute difference found is 1.4 % and 5 µm, significant enough for problems that require zero tolerance, but adequate for magnetic field calculations where the separation between strands is big enough. For the main simulations, $t_{\text{ins}} = 30\,\mu\text{m}$, so $r_{\text{pos},b,2}$ from this example would increase around 22 µm using (B.27), completely avoiding collision between

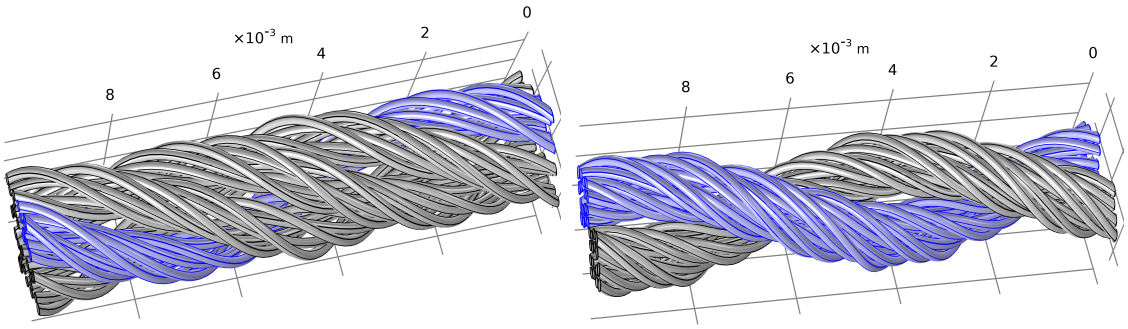

(a) (b)

Figure B.11: Geometry of the two simulated cables.

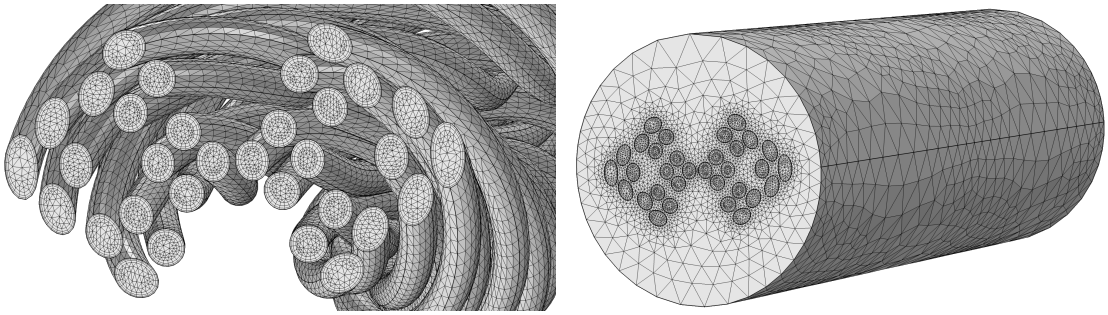

(a) (b)

Figure B.12: Mesh of the strands and air.

bundles. Since the 3D method was implemented for testing purposes and it is more accurate and much simpler to implement, so future simulations are encouraged to use this method.

B.3 Simulation model

The previous mathematical description is used to simulate two different cables with identical number of strands, i.e. $n_s = 32$, of diameter $\varnothing_s = 0.2\,\text{mm}$. Cables are arranged according to the bundling sequence $2 \times 4 \times 4$ and $4 \times 4 \times 2$. The first sequence corresponds to a cable of 4 external bundles composed of 4 bundles of a twisted pair of strands. The second sequence is a twisted pair of bundles whose internal structure consists of 4 bundles of 4 strands. An image of the simulated cables is shown in Fig. B.11, where one of the external bundles is highlighted for the sake of clarity.

As it was commented in section B.2, the commercial FEA software COMSOL is used. This software runs in a computer with a i7-3820 CPU (3.6 GHz clock rate) and 64 GB of RAM. In order to properly capture both skin and proximity effects, which

require fine meshing in the radial direction, a meshing strategy based on boundary layers is used. The strands' outer circumference is divided into 20 elements and their length is divided into 200 elements, converting the resulting rectangles into triangles. From the exterior surface, 3 boundary layers are generated inwards to better capture skin effects. The rest of the strands' interior as well as the outside air are meshed by free tetrahedra. The total number of elements are 1 553 317 for the $2 \times 4 \times 4$ cable and 1 444 346 for the $4 \times 4 \times 2$ cable. Fig. B.12 shows the mesh of the $4 \times 4 \times 2$ cable with the air hidden in (a) and shown in (b). The simulation of both configurations and all frequencies takes approximately 6 h, 30 min to complete and uses 58 GB of RAM. The 2D simulation used for comparison purposes also has boundary layer meshing, resulting in 115 324 triangle elements and taking about 3 min, 40 s in total.

The objective of the simulation is to obtain the AC resistance of cables and also to check if the proposed 3D description is advantageous with respect to 2D models, where the transposition of strands is not captured. The transposition should be reflected in an improvement of the equivalence among strands. AC resistance of cables is the consequence of AC losses due to two purely AC effects: skin and proximity. These effects are simulated by applying idfferent boundary conditions, which correspond to the different physical origin of skin and proximity effect refers to losses in a conductive material when it is under an external alternating magnetic field. Therefore, the applied boundary condition consists of an AC magnetic field perpendicular to the cable. Moreover, it is also assumed that the simulated cable is in the air and insulated from other elements. Voltage and field AC dependency is considered sinusoidal.

Loss dissipated in copper strands can be obtained by integrating the Joule's losses, which using the microscopic Ohm's law, $\mathbf{J} = \sigma_{\mathrm{Cu}}\mathbf{E}$, are expressed as:

$$P_s = \frac{1}{2}\int_{\Omega_s} \frac{\mathbf{J}\cdot\mathbf{J}^*}{\sigma_{Cu}} dv, \tag{B.30}$$

where $\mathbf{J}$ is the current density in the strand, $\mathbf{J}^*$ is its conjugated magnitude and Ω_s is the strand domain.

Total losses of cable corresponds to the sum of losses of all strands, $P_c = \sum_{n_s} P_s$. It is also interesting to connect losses with resistances. For this purpose, total current in the cable is required. As occurs with losses, the total current in the cable is the sum of currents in individual strand, i.e.:

$$I = \sum_{n_s} I_s = \sum_{n_s} \int_{S_s} \mathbf{J}\cdot\hat{\mathbf{n}}\cdot dS, \tag{B.31}$$

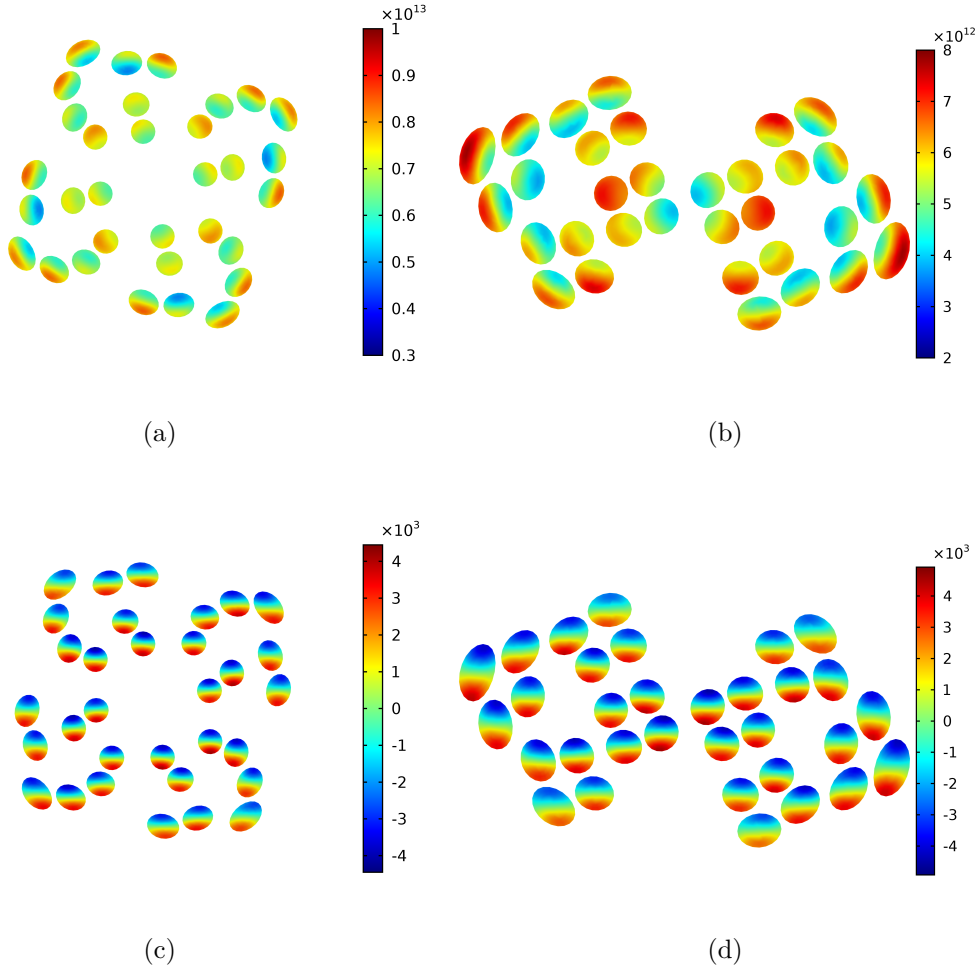

Figure B.13: Current density at 1 MHz for the two considered cable arrangements an ac loss effects. (a) Case $2 \times 4 \times 4$, skin effect. (b) Case $4 \times 4 \times 2$, skin effect. (c) Case $2 \times 4 \times 4$, proximity effect. (d) Case $4 \times 4 \times 2$, proximity effect.

where S_s is the cross section of the strand. The normal vector of a strand corresponding to a specific twisting level can be obtained from (B.6).

In order to compare then resistance of different arrangements, it is also convenient to obtain the power of the resistance per unit of length. The length of a strand can be calculated as follows:

$$l_s = \frac{1}{\pi r_s^2} \int_{\Omega_s} dv. \tag{B.32}$$

B.4 Simulation results

Fig. B.13 shows the simulation results of current density for the two considered arrangements: Fig. B.13 (a) and B.13 (c) for the $2 \times 4 \times 4$ cable, and B.13 (b) and B.13 (d) for the $4 \times 4 \times 2$ cable. The skin effect corresponds to the upper figures

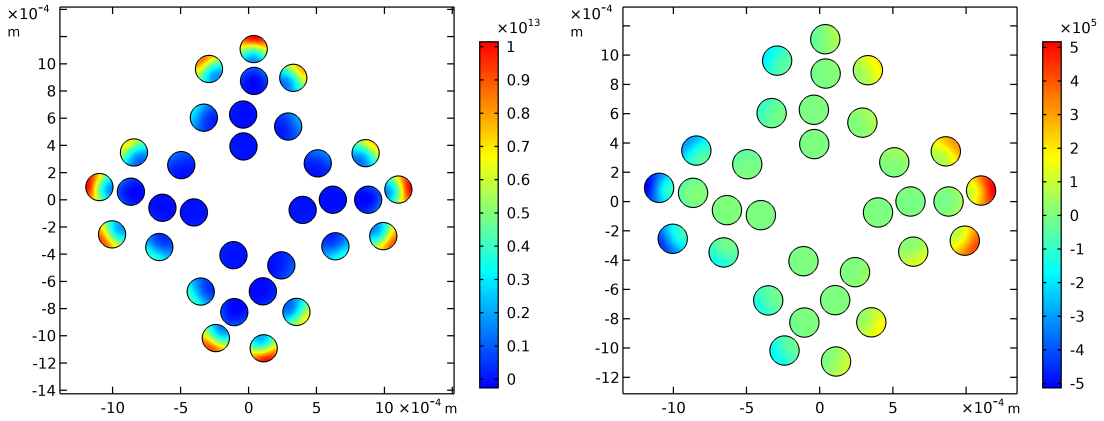

(a) (b)

Figure B.14: Current density at 1 MHz for a 2D finite element simulation. (a) Skin effect. (b) Proximity effect.

and the proximity effect results to the lower figures. The excitation frequency has been set to 1 MHz. At this frequency, a trade-off between making evident the AC losses and meshing requirements is achieved. Regarding skin effect and, in view of the scale of the color legend, it could be concluded that current is spread among strands. Regarding proximity effect, it is also observed that twisting leads to similar induced currents in all strands.

The effectiveness of the modeled cable structures is also shown when AC-loss results of 2D and 3D simulations are compared. The 2D simulated case corresponds to a cable with identical number of strands and similar arrangement. The frequency of simulations is also set at 1 MHz. Results are presented in Fig. B.14 (a) for the case of the skin effects and Fig. B.14 (b) for the case of proximity effect. As it is shown, in contrast with external strands, inner strands hardly carry current. This uneven current distribution causes the overestimation of the cable losses and resistance. Moreover, the effect of the non-twisting in the 2D simulation generates induced current whose round-trip path involves several strands, which does not occur when strands are twisted because, in this case, each strand carries an individual induced current, as it is shown in Fig. B.13 (b) and Fig. B.13 (c). Considering that proximity losses are proportional to the square of induced current density, and considering the results obtained in Figs. B.13 and B.14, this effect is also reflected in the overestimation of proximity losses. These results point the interest on having proper 3D models.

Qualitative results are intersting for examining the simulation results at a glance.

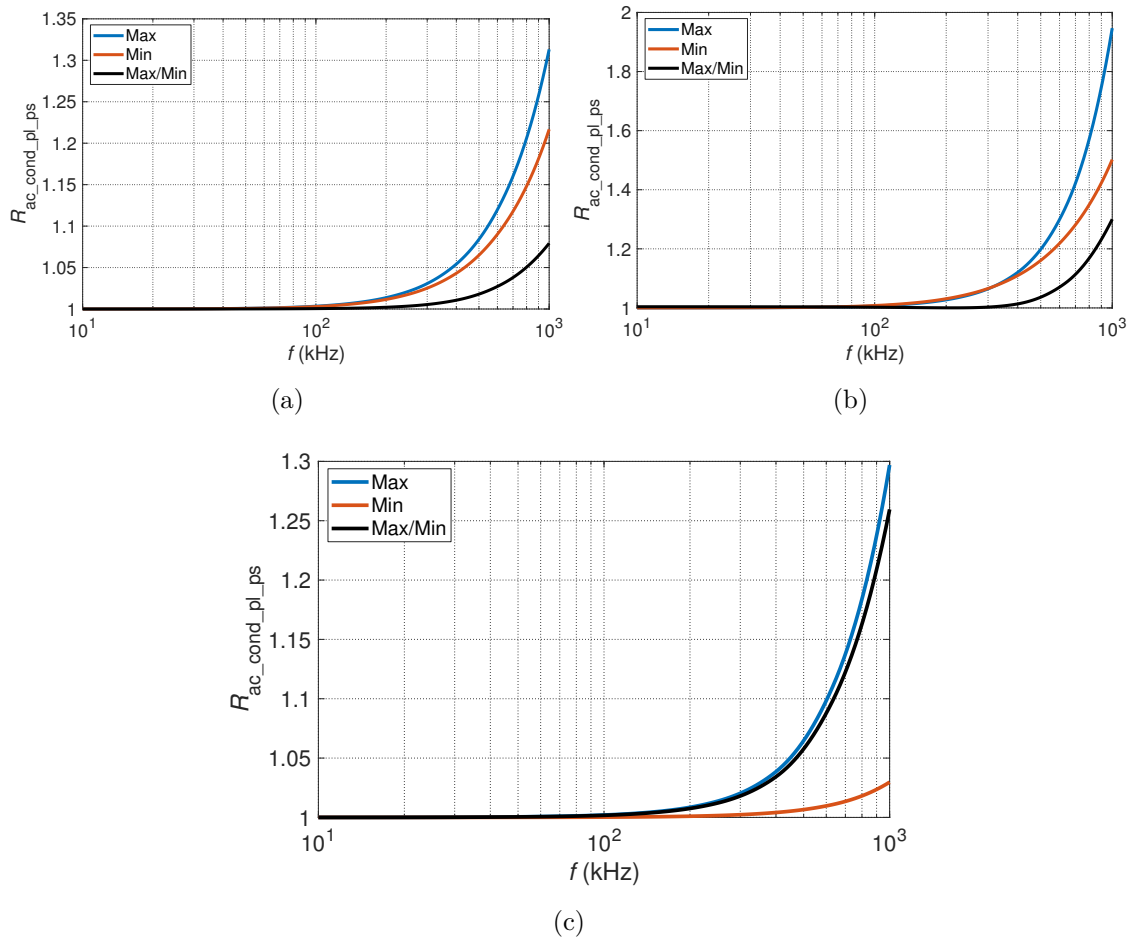

Figure B.15: Comparison of skin effect resistance of strands for different cases. (a) Case $2 \times 4 \times 4$. (b) Case $4 \times 4 \times 2$. (c) Case 2D

Moreover, quantitative results of the conduction resistance per strand length are also presented. Fig. B.15 shows the skin effect resistance for the different modeled cases, relative to the low frequency (near DC) result. In this figure, the maximum and minimum resistances of strands are also compared, which is a measure of its equivalence. The results show that for the $2 \times 4 \times 4$ case the difference between the maximum and minimum resistance values of strands is 8 %, whereas this value is about 25 % for the $4 \times 4 \times 2$ case and the 2D simulation. The length difference between the shortest and longest strands is 2.5 %, which can further separate the absolute resistance values in the 3D cases. The preceding results points that different arrangements could lead to different AC resistances and different equivalence of strands. This fact shows the practical interest of having a proper model for describing complex litz-wire cables.

These contributions have been presented in [173] and [174].

Appendix C

Measurement post processing

This appendix establishes how oscilloscope voltage and current measurements are transformed into impedance values.

Fundamentally, there are two approaches that can be undertaken.

- Fourier transformations
- Energy balance

The Fourier transformation method takes the measured voltage and current waveforms and extracts their first harmonic component at the switching frequency. The transformed voltages and currents are phasors, whose division produces impedance with real and imaginary components. The discrete Fourier transform (DFT) is used, as the oscilloscope waveforms are discrete points over a consistent sample rate. Additionally, the fast Fourier transform (FFT) can be used without accuracy loss:

$$V_k = 2 \sum_{n=0}^{N-1} v_n e^{-j2\pi kn/N} \; \forall \; k = [0, N/2], \tag{C.1}$$

where v_n is the voltage of the nth time sample of N total samples, V_k is the transformed voltage of bin k, where k is the frequency bin that can be converted to actual frequency through the sample frequency, F_s:

$$f_k = kF_s/N. \tag{C.2}$$

The multiplication by 2 in (C.1) is due to the DFT calculations generating frequency-symmetrical values from bin $N/2+1$ to N, which are folded in the middle to obtain the actual values. The frequency bin closest to the first harmonic, k_{h1},

can be calculated as:

$$k_{h1} = \text{round}\left(f_{h1}N/F_s\right). \tag{C.3}$$

Considering that frequency bins are discrete, higher F_s increases the precision of k_{h1} to be as close as possible to f_{h1}.

The current fourier transform, I_k, is obtained with the same formula as (C.1):

$$I_k = 2\sum_{n=0}^{N-1} i_n e^{-j2\pi kn/N} \;\forall\; k = [0, N/2]. \tag{C.4}$$

Winding impedance can be calculated from the Fourier transformations of its voltage and current waveforms, $V_{w,k_{h1}}$ and $I_{w,k_{h1}}$ respectively:

$$Z_{\text{eq}} = V_{w,k_{h1}}/I_{w,k_{h1}}, \tag{C.5}$$

$$R_{\text{eq}} = \Re\left(Z_{\text{eq}}\right), \tag{C.6}$$

$$L_{\text{eq}} = \Im\left(Z_{\text{eq}}\right)/\omega. \tag{C.7}$$

The energy balance method considers not only the first harmonic, but the total energy dissipated and stored by the system. Dissipated power and apparent power are calculated separately, and estimations of resistance and inductance can be obtained. Average power, P, is obtained from instant power, p_n, calculated as:

$$p_n = v_n \cdot i_n, \tag{C.8}$$

$$P = \frac{\sum_{n=1}^{N} p_n}{N}. \tag{C.9}$$

Apparent power, S, can be calculated from the rms values of voltage and current:

$$V_{\text{rms}} = \sqrt{\frac{\sum_{n=1}^{N} v_n^2}{N}}, \tag{C.10}$$

$$I_{\text{rms}} = \sqrt{\frac{\sum_{n=1}^{N} i_n^2}{N}}, \tag{C.11}$$

$$S = V_{\text{rms}} I_{\text{rms}}. \tag{C.12}$$

Reactive power, Q, can be calculated from S and P:

$$Q = \sqrt{S^2 - P^2}. \tag{C.13}$$

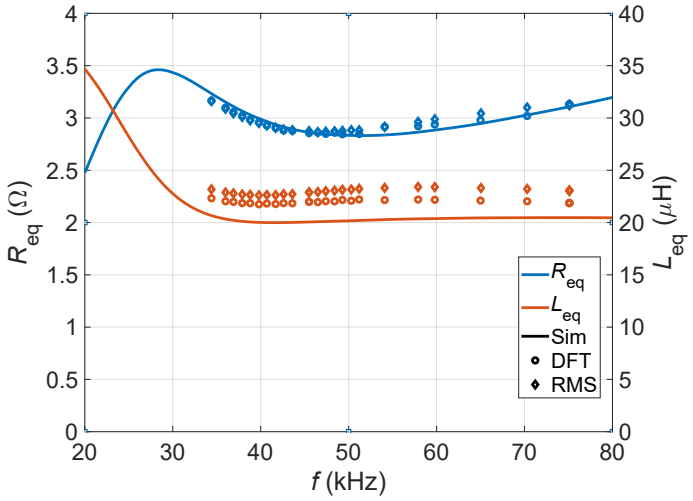

Figure C.1: Simulated and calculated impedance from waveform captures, using either the DFT method or rms method.

Winding resistance and inductance can be obtained from P and Q respectively:

$$R_{\text{eq}} = \frac{P}{I_{\text{rms}}^2}, \tag{C.14}$$

$$L_{\text{eq}} = \frac{Q}{\omega I_{\text{rms}}^2}. \tag{C.15}$$

Fig. C.1 shows the differences between the two methods and compares them with simulated values. As might be expected, the rms method produces higher values, as it includes all harmonics, whereas the DFT method only considers the first harmonic. Nevertheless, the difference is very slight for R_{eq} and a maximum 5 % for L_{eq}. As a result, first harmonics are accurate enough to describe the impedance of a system, and considering that FEM simulations generate first order harmonics more easily, it is more convenient and expedient to use the DFT method.

The resonant capacitor C can also be estimated from voltage and current measurements. Though C is known beforehand, it serves as an indication of the accuracy of the measurements, and sometimes to detect capacitor degradation. As capacitor voltage, v_c, is not typically measured directly, it can be obtained from the difference between inverter output voltage, v_o, and primary winding voltage, $v_{w,1}$:

$$v_c = v_o - v_{w,1}. \tag{C.16}$$

The Fourier transform of v_c, V_c, is used to obtain C:

$$C = \frac{1}{\omega \Im\left(\frac{V_c}{I_w}\right)} \tag{C.17}$$

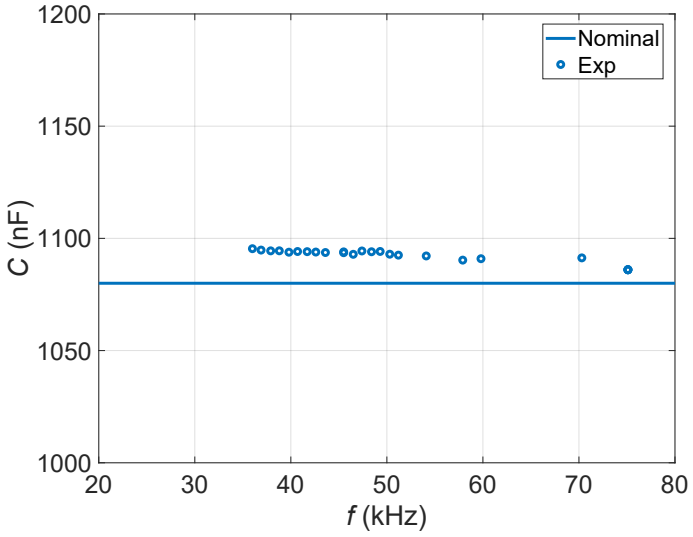

Figure C.2: Simulated and measured capacitance.

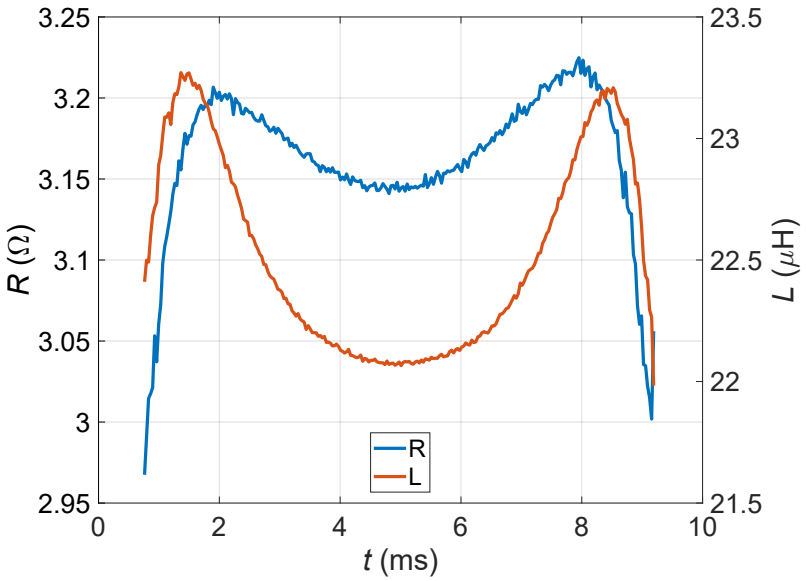

Figure C.3: Measured intra-cycle R and L.

Fig. C.2 shows an example of capacitor calculation.

All previous calculations are applied to waveforms containing an integer number of mains half-cycles, typically one or two. In order to observe the change of system impedance with current, and consequently magnetic field strength, H, the impedance calculations can be carried out over waveform segments within a half-cycle. Individual transistor commutations generally include a small number of oscilloscope samples, which provides very little resolution in the frequency bins. To minimize the issue, several commutations can be included in the DFT, sliding the "window" commutation by commutation. The resulting impedance is an average of each considered window.

Fig. C.3 shows intra-cycle measurements of R and L, where the lower values at the center represent the saturation of the ferromagnetic material.

Appendix D

Experimental results comparison

Experimental results are presented in each individual chapter throughout the dissertation. As a result, comparisons between the systems can be onerous to the reader. Therefore, this appendix includes the relevant experimental figures from previous chapters.

D.1 Experimental setups

First, pictures of the experimental setups are repeated to review system geometry.

The IuW prototypes were composed of two systems with $\varnothing_{w,\text{ext}} = 180\,\text{mm}$ and $d_{\text{load}} = 20\,\text{mm}$ and one system with $\varnothing_{w,\text{ext}} = 210\,\text{mm}$ and $d_{\text{load}} = 34\,\text{mm}$, represented in Fig. D.1 (a).

The same diameter ICH prototype represented in Fig. D.1 (b) uses $\varnothing_{w1,\text{ext}} = \varnothing_{w2,\text{ext}} = 180\,\text{mm}$ and $d_{w1l} = 50\,\text{mm}$, more than double of the same diameter IuW system.

The big receiver ICH system represented in Fig. D.1 (c) uses the same primary inductor as the previous prototype with $\varnothing_{w2,\text{ext}} = 290\,\text{mm}$ and d_{w12} ranging from 6 to 40 mm. A value of $d_{w12} = 30\,\text{mm}$ is represented in Fig. D.1 (c).

The multiple loads, single transmitter ICH system represented in Fig. D.1 (d) has $\varnothing_{w1,\text{ext}} = \varnothing_{w2,\text{ext}} = \varnothing_{w3,\text{ext}} = 210\,\text{mm}$ and $d_{w12} = 10\,\text{mm}$.

The small receiver ICH system represented in D.1 (e) uses $\varnothing_{w1,\text{ext}} = 180\,\text{mm}$, $\varnothing_{w2,\text{ext}} = 100\,\text{mm}$ and d_{w12} ranging from 6 mm to 40 mm.

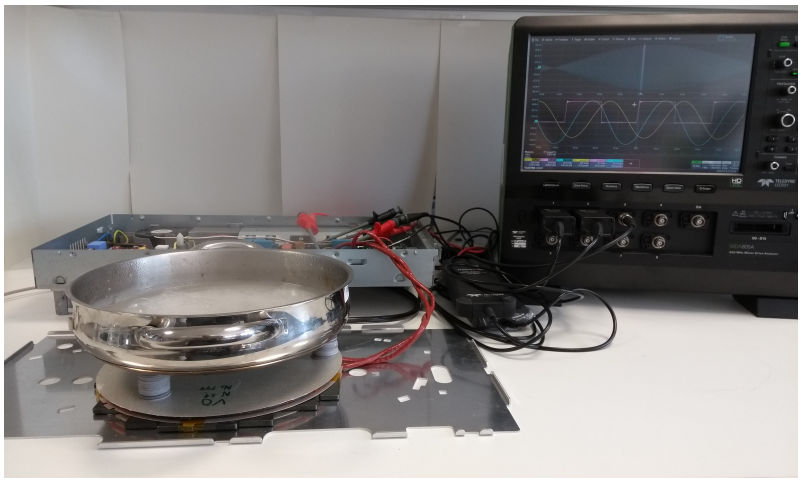

(a)

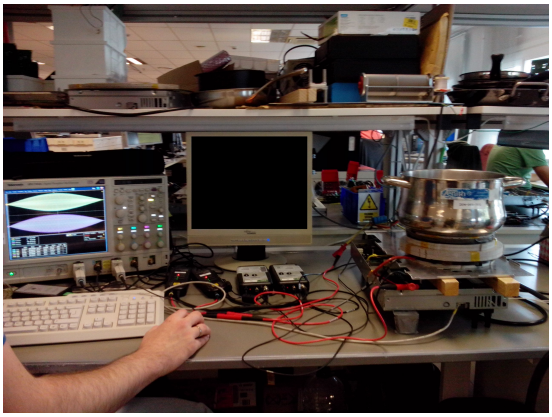

(b)

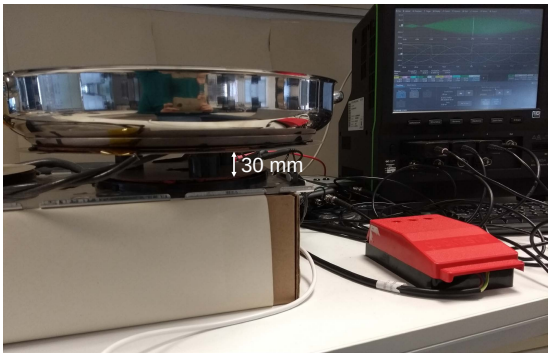

(c)

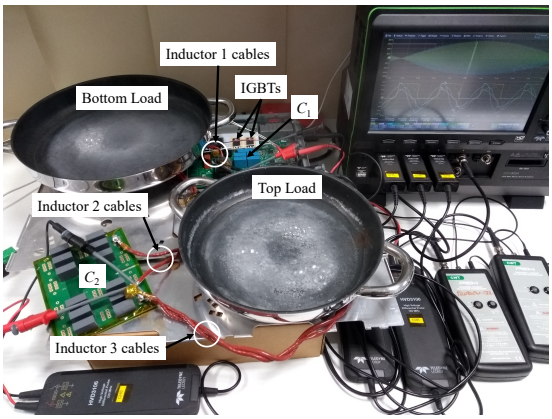

(d)

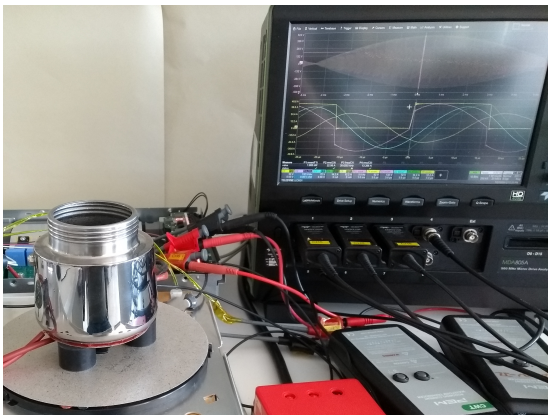

(e)

Figure D.1: (a) IuW experimental setup with the 210 mm ⌀ inductor. (b) Same diameter ICH experimental setup. (c) Big secondary ICH experimental setup. (d) Multiple-loads ICH experimental setup with both bottom and top loads boiling water. (e) Small secondary ICH experimental setup.

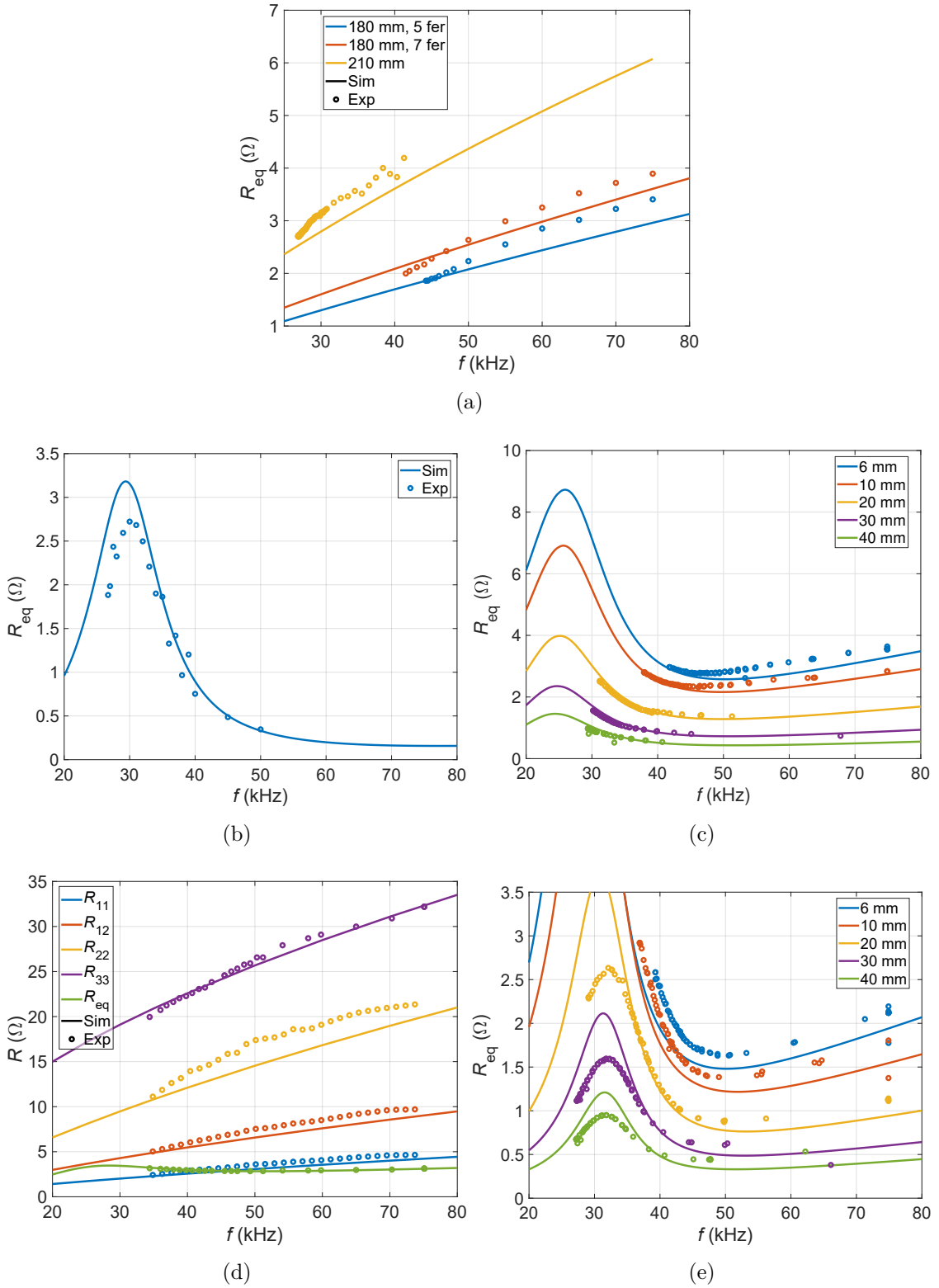

Figure D.2: Resistance experimental measurements: (a) the three IuW inductors, (b) same diameter ICH system, (c) big secondary ICH system, (d) multiple loads ICH system: (e) small secondary ICH system.

D.2 Equivalent impedance measurements

Next, equivalent impedance measurements are shown for comparison.

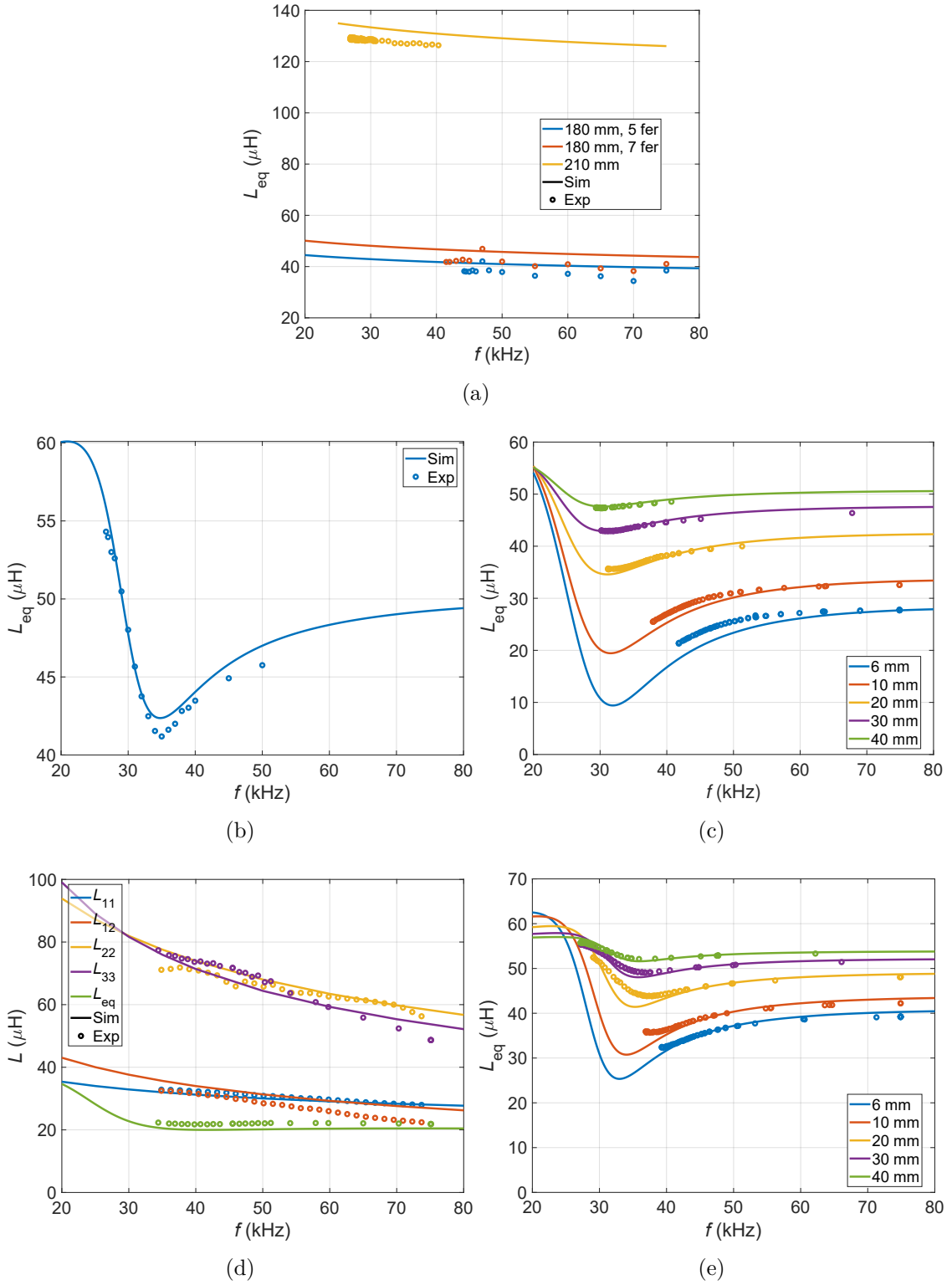

Figure D.3: Inductance experimental measurements: (a) the three IuW inductors, (b) same diameter ICH system, (c) big secondary ICH system, (d) multiple loads ICH system, (e) small secondary ICH system.

IuW system impedance is shown in Fig. D.2 (a) and Fig. D.3 (a). In order to achieve $P = 3700\,\mathrm{W}$ near resonance, a $R_{\mathrm{eq}} \approx 2.8\,\Omega$ is needed and all systems come

close. The smaller inductor systems have slightly lower R_{eq} which will cause higher currents for the same power. High L_{eq} values with similar R_{eq} values causes low PF_{ind}, which is related to more pronounced power-frequency peaks.

Impedance of the same diameter ICH system is represented in Fig. D.2 (b) and Fig. D.3 (b). The effect of the secondary inductor causes R_{eq} to increase near $f_{0,2}$ and L_{eq} to decrease. Therefore, PF_{ind} improves at the desired frequency, with a clear advantage over single inductor IuW systems.

The impedance of the big receiver ICH system is represented in Fig. D.2 (c) and Fig. D.3 (c). The better power distribution is achieved in frequencies above $f_{0,2}$, whereas the R_{eq} peak and L_{eq} valley are close to $f_{0,2}$. Therefore, this system is not able to fully take advantage of ICH impedance improvement in favor of distribution improvement.

Impedance of the multiple loads single transmitter ICH system is represented in Fig. D.2 (d) and Fig. D.3 (d). Similar to the previous case, maximum power ratio in the top load is achieved at frequencies above the L_{eq} minimum, whereas optimum impedance occurs slightly below. Consequently, this system also sacrifices impedance optimality in favor of higher power in the top load.

The impedance of the small receiver ICH system is represented in Fig. D.2 (e) and Fig. D.3 (e). Power distribution is barely affected in this case, so the design takes full advantage of the R_{eq} peak and L_{eq} valley to improve power factor at high power.

D.3 Power and current measurements

Power and current IuW measurements are represented in Fig. D.4 (a) and Fig. D.5 (a). The power peaks are very pronounced, and current is slightly higher for the systems with smaller diameter.

Power and current measurements of the same diameter ICH system are represented in Fig. D.4 (b) and Fig. D.5 (b). The impedance extrema generate a second lump in the power curve, which drives down the current.

Power and current measurements of the big receiver ICH system are represented in Fig. D.4 (c) and Fig. D.5 (c). At low distances, the R_{eq} peak slightly reduces maximum power, while at high distances, the ICH positive effect on impedance is lessened. As distance increases, the required current for each power point increases.

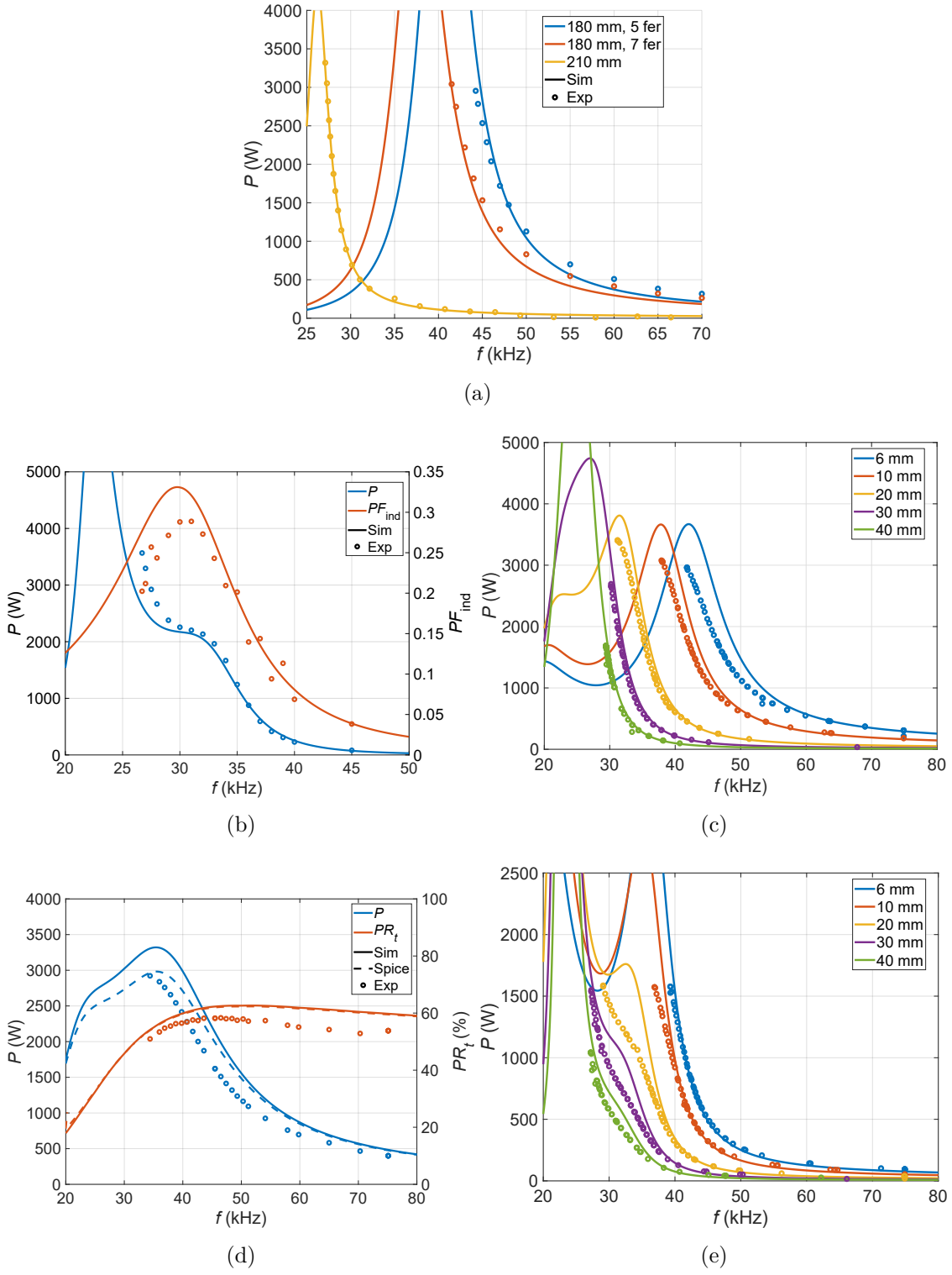

Figure D.4: Power measurements of: (a) the three IuW inductors, (b) same diameter ICH system, (c) big secondary ICH system, (d) multiple loads ICH system with connected receiver, (e) small secondary ICH system.

Power and current measurements of the multiple loads single transmitter ICH system are represented in Fig. D.4 (d) and Fig. D.5 (d). Due to the low distance, the power curve is fairly wide, and currents are relatively small. The top load power

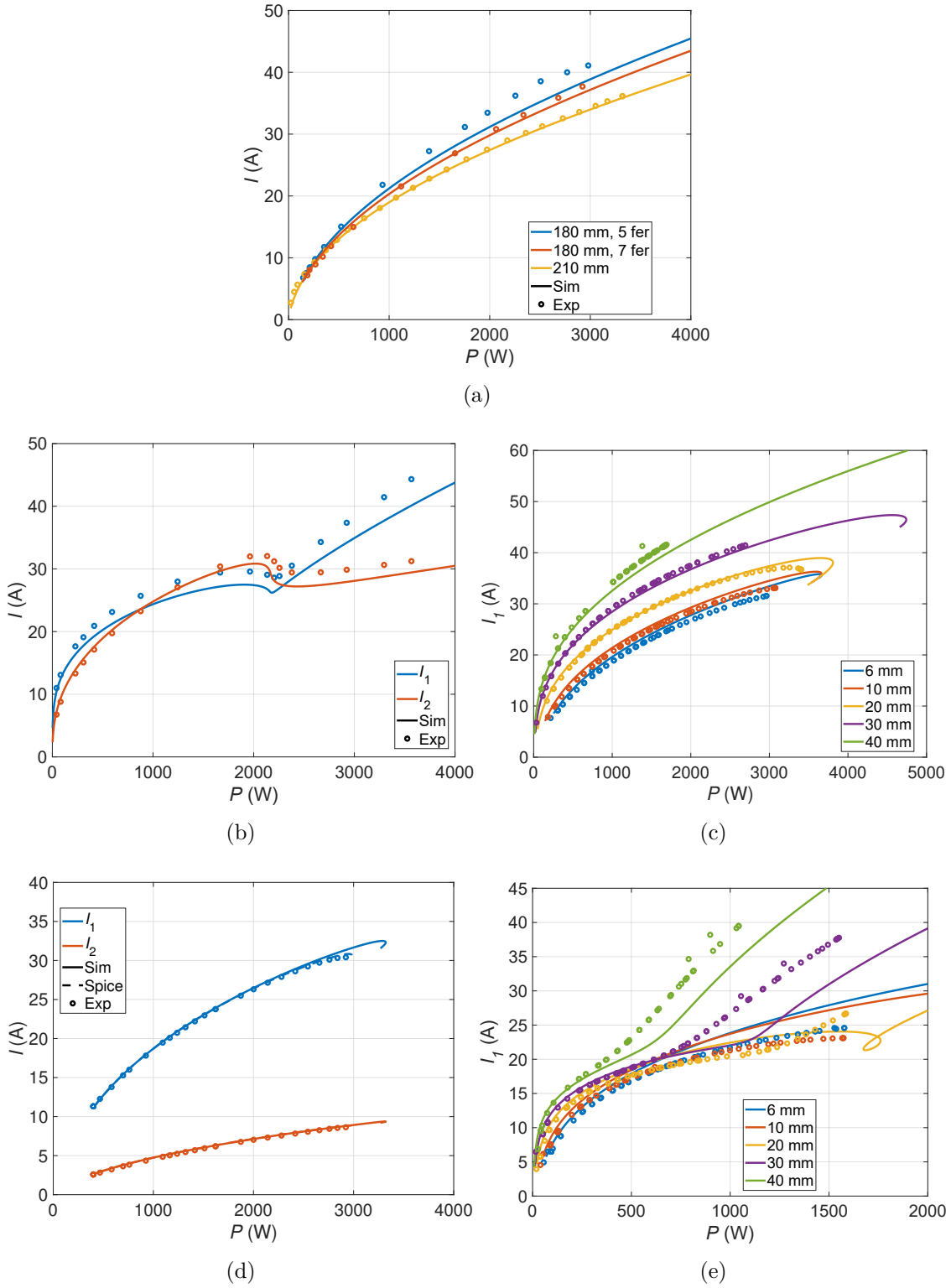

Figure D.5: Current measurements of: (a) the three IuW inductors, (b) same diameter ICH system, (c) big secondary ICH system, (d) multiple loads ICH system with connected receiver, (e) small secondary ICH system.

ratio is maintained for all the power range.

Power and current measurements of the small receiver ICH system are

represented in Fig. D.4 (e) and Fig. D.5 (e). The small load diameter causes relatively high current for all distances. At medium and lower distances, the optimum impedance values are achieved at the maximum power. At 30 mm and above, the effect is lessened, and current for each power point increases significantly.

Appendix E

List of contributions

Throughout the development of the dissertation, several contributions have been made in terms of conference papers, journal articles and patents.

E.1 Conference papers

E. Plumed, I. Lope, J. Acero, and J. M. Burdío, "Evaluación de sistemas de calentamiento por inducción doméstica con mayor distancia a la carga," *24th Seminario Anual de Automática, Electrónica Industrial e Instrumentación (SAAEI 2017)*, July, 2017.

E. Plumed, J. Acero, J. M. Burdío, and I. Lope, "Design method for domestic induction heating systems with a larger load distance," in *IECON 2017 - 43rd Annual Conf. IEEE Industrial Electronics Society*, Oct. 2017, pp. 3785–3790.

E. Plumed, I. Lope, J. Acero and J. M. Burdío, "Evaluación de sistemas inductores para aplicación simultánea de transferencia de energía y calentamiento por inducción," in *25th Seminario Anual de Automática, Electrónica Industrial e Instrumentación (SAAEI 2018)*, July, 2018.

E. Plumed, I. Lope, J. Acero, and J. M. Burdío, "Inductor system evaluation for simultaneous wireless energy transfer and induction heating," in *IECON 2018 - 44th Annual Conf. IEEE Industrial Electronics Society*, Oct. 2018, pp. 3509–3514.

E. Plumed, J. Acero, I. Lope and C. Carretero, "3D Finite Element Simulation of Litz Wires with Multilevel Bundle Structure," in *IECON 2018 - 44th Annual Conf. IEEE Industrial Electronics Society*, Oct., 2018, pp. 3479-3484.

E. Plumed, J. Acero, I. Lope and C. Carretero, "Simulación 3D por Elementos Finitos de Cables de Litz con Estructura de Mazos Multinivel", in *26th Seminario Anual de Automática, Electrónica, Industrial e Instrumentación (SAAEI 2019)*, July, 2019.

E. Plumed, I. Lope, J. Acero, and J. M. Burdío, "Design of a three inductor system with one externally fed for an inductively coupled heating application," in *IECON 2019 - 45th Annual Conf. IEEE Industrial Electronics Society*, vol. 1, Oct. 2019, pp. 5070–5074.

E. Plumed, I. Lope, J. Acero, J. M. Burdío, "Diseño de un sistema de tres inductores con uno alimentado externamente para una aplicación de calentamiento por inducción acoplado," in *27th Seminario Anual de Automática, Electrónica, Industrial e Instrumentación (SAAEI 2020)*, September, 2020.

E. Plumed, I. Lope, J. Acero and J. M. Burdío, "Domestic induction heating system with standard primary inductor for reduced-size and high distance cookware," in *IEEE Applied Power Electronics Conf. and Expo. (APEC) 2021*, pp. 2842-2847, June 2021.

E.2 Journal articles

E. Plumed, J. Acero, I. Lope, and J. M. Burdío, "Design methodology of high performance domestic induction heating systems under worktop," *IET Power Electron.*, Oct. 2019.

E. Plumed, I. Lope, C. Carretero, and J. Acero, "A recursive methodology for modelling multi-stranded wires with multilevel helix structure," *Appl. Math. Model*, vol. 83, pp. 76 – 89, 2020.

E. Plumed, I. Lope, and J. Acero, "Induction heating adaptation of a different-sized load with matching secondary inductor to achieve uniform heating and enhance vertical displacement," *IEEE Trans. Power Electron.*, vol. 36, no. 6, pp. 6929–6942, Jun. 2021.

E. Plumed, I. Lope, J. Acero, and J. M. Burdío, "Induction heating of two magnetically independent loads with a single transmitter," *IEEE Tran. Power Electron.*, 2021, Early Access.

E. Plumed, I. Lope, and J. Acero, "EMI reduction via resonator coils in glassless integrated domestic induction systems," *IEEE Access*, vol. 9, pp. 128147–128156,

2021.

E.3 Patents

J. Acero, D. Antón, C. Carretero, P. Hernández, S. Llorente, I. Lope, and E. Plumed, "Cooking system," WO patent WO2019166909, Feb. 18, 2020. [Online]. Available: https://worldwide.espacenet.com/patent/search/family/065818046/publication/WO2019166909A1?q=pn=WO2019166909A1

T. Cabeza, J. Lasobras, S. Llorente, E. Plumed, J. Rivera, and J. Serrano, "Household appliance system," WO patent WO2021104849, Jun. 03, 2021. [Online]. Available: https://worldwide.espacenet.com/patent/search/family/068808252/publication/WO2021104849A1?q=pn=WO2021104849A1

T. Cabeza, S. Llorente, E. Plumed, and J. Rivera, "Kochfeldvorrichtung," WO patent WO2021069213A1, Aug. 05, 2021. [Online]. Available: https://worldwide.espacenet.com/patent/search/family/069701129/publication/DE102021200406A1?q=pn=DE102021200406A1

T. Cabeza, J. Lasobras, S. Llorente, E. Plumed, and J. Rivera, "Induction energy transmission system," DE patent DE102021200406A1, Apr. 15, 2021. [Online]. Available: https://worldwide.espacenet.com/patent/search/family/068503016/publication/WO2021069213A1?q=pn=WO2021069213A1

Bibliography

[1] E. J. Davies and P. G. Simpson, "Induction heating for industry," *Electronics and Power*, vol. 25, no. 7, pp. 508–515, 1979.

[2] H. Matsuki, T. Satoh, K. Murakami, T. Hoshino, T. Yanada, and S. Kikuchi, "Local hyperthermia based on soft heating method utilizing temperature-sensitive ferrite rod," *IEEE Trans. Magn.*, vol. 26, no. 5, pp. 1551–1553, 1990.

[3] X. Wang, J. Tang, and L. Shi, "Induction heating of magnetic fluids for hyperthermia treatment," *IEEE Trans. Magn.*, vol. 46, no. 4, pp. 1043–1051, 2010.

[4] J. Acero, J. M. Burdío, L. A. Barragán, D. Navarro, R. Alonso, J. Ramón, F. Monterde, P. Hernández, S. Llorente, and I. Garde, "Domestic induction appliances," *IEEE Ind. Appl. Mag.*, vol. 16, no. 2, pp. 39–47, Mar. 2010.

[5] I. Millán, J. M. Burdío, J. Acero, O. Lucía, and S. Llorente, "Series resonant inverter with selective harmonic operation applied to all-metal domestic induction heating," *IET Power Electron.*, vol. 4, no. 5, pp. 587–592, May 2011.

[6] J. Davies and P. Simpson, *Induction heating handbook*. McGraw-Hill Companies, 1979.

[7] P. Guerrier, K. K. Nielsen, and J. H. Hattel, "Temperature dependence and magnetic properties of injection molding tool materials used in induction heating," *IEEE Trans. Magn.*, vol. 51, no. 9, pp. 1–7, 2015.

[8] J. P. Jordan, "Design of electronic heaters for induction heating," *Proceedings of the IRE*, vol. 32, no. 8, pp. 449–452, 1944.

[9] General Electric Co., U.S. patent US3 786 219A, 1974.

[10] Matsushita Electric Ind. Co. Ltd., Japan patent JPS5 251 131A, 1977.

[11] O. Lucía, J. Acero, C. Carretero, and J. M. Burdío, "Induction heating appliances: Toward more flexible cooking surfaces," *IEEE Ind. Electron. Mag.*, vol. 7, no. 3, pp. 35–47, Sep. 2013.

[12] J. Acero, R. Alonso, J. M. Burdío, and L. A. Barragán, "Enhancement of induction heating performance by sandwiched planar windings," *Electron. Lett.*, vol. 42, no. 4, pp. 241–242, 2006.

[13] G. A. Covic and J. T. Boys, "Inductive power transfer," *Proc. IEEE*, vol. 101, no. 6, pp. 1276–1289, Jun. 2013.

[14] J. Acero, R. Alonso, J. M. Burdío, L. A. Barragán, and D. Puyal, "Frequency-dependent resistance in litz-wire planar windings for domestic induction heating appliances," *IEEE Trans. Power Electron.*, vol. 21, no. 4, pp. 856–866, 2006.

[15] J. Stratton, *Electromagnetic Theory*. McGraw-Hill, New-York, 1941.

[16] W. Hurley and J. Kassakian, "Induction heating of circular ferromagnetic plates," *IEEE Trans. Magn.*, vol. 15, no. 4, pp. 1174–1181, 1979.

[17] R. Albanese and G. Rubinacci, "Solution of three dimensional eddy current problems by integral and differential methods," *IEEE Trans. Magn.*, vol. 24, no. 1, pp. 98–101, 1988.

[18] W. G. Hurley and M. C. Duffy, "Calculation of self and mutual impedances in planar magnetic structures," *IEEE Trans. Magn.*, vol. 31, no. 4, pp. 2416–2422, 1995.

[19] J. Acero, "Estudio teórico y experimental del calentamiento por inducción de cualquier material conductor," Ph.D. dissertation, Universidad de Zaragoza, 2005.

[20] J. Acero, O. Lucía, I. Millán, L. A. Barragán, J. M. Burdío, and R. Alonso, "Identification of the material properties used in domestic induction heating appliances for system-level simulation and design purposes," in *IEEE Applied Power Electronics Conf. and Expo. (APEC) 2010*. IEEE, 2010, pp. 439–443.

[21] C. Carretero, "Análisis de sistemas de múltiples bobinados aplicados a sistemas de calentamiento por inducción doméstico," Ph.D. dissertation, Universidad de Zaragoza, 2010.

[22] E. E. Kriezis, T. D. Tsiboukis, S. M. Panas, and J. A. Tegopoulos, "Eddy currents: theory and applications," *Proc. IEEE*, vol. 80, no. 10, pp. 1559–1589, 1992.

[23] M. N. O. Sadiku, *Numerical Techniques in Electromagnetics*. Boca Raton: CRC Press, 2000.

[24] A. E. Ruehli, "Equivalent circuit models for three-dimensional multiconductor systems," *IEEE Trans. Microw. Theory Techn.*, vol. 22, no. 3, pp. 216–221, 1974.

[25] T. Miyoshi and G. Maeda, "Finite element analysis of leakage magnetic flux from an induction heating system," *IEEE Trans. Magn.*, vol. 18, no. 3, pp. 917–920, 1982.

[26] I. Mayergoyz, M. Chari, and A. Konrad, "Boundary Galerkin's method for three-dimensional finite element electromagnetic field computation," *IEEE Trans. Magn.*, vol. 19, no. 6, pp. 2333–2336, 1983.

[27] T. Nakata, N. Takahashi, Y. Kawase, H. Funakoshi, and S. Ito, "Finite element analysis of magnetic circuits composed of axisymmetric and rectangular regions," *IEEE Trans. Magn.*, vol. 21, no. 6, pp. 2199–2202, 1985.

[28] J. Jin, *The Finite Element Method in Electromagnetics*. Wiley-IEEE Press, 2002.

[29] J. Sakellaris, G. Meunier, A. Raizer, and A. Darcherif, "The impedance boundary condition applied to the finite element method using the magnetic vector potential as state variable: a rigorous solution for high frequency axisymmetric problems," *IEEE Trans. Magn.*, vol. 28, no. 2, pp. 1643–1646, Mar. 1992.

[30] J. Acero, O. Lucía, C. Carretero, I. Lope, and C. Díez, "Efficiency improvement of domestic induction appliances using variable inductor-load distance," in *IEEE Applied Power Electronics Conf. and Expo. (APEC) 2012*, Feb. 2012, pp. 2153–2158.

[31] J. Lammeraner and M. Stafl, *Eddy Currents*. London U. K.: Illiffe Books, 1966.

[32] J. A. Ferreira, "Analytical computation of AC resistance of round and rectangular litz wire windings," *IEE Proc-B*, vol. 139, pp. 21–25, Jan. 1992.

[33] M. Bartoli, N. Noferi, A. Reatti, and M. K. Kazimierczuk, "Modeling litz-wire winding losses in high-frequency power inductors," in *IEEE Pow. Electr. Spec. Conf, (PESC) 1996*, vol. 2, 1996, pp. 1690–1696 vol.2.

[34] X. Tang and C. R. Sullivan, "Stranded wire with uninsulated strands as a low-cost alternative to litz wire," in *IEEE Pow. Electr. Spec. Conf, (PESC) 2003*, vol. 1, 2003, pp. 289–295 vol.1.

[35] J. Acero, R. Alonso, J. M. Burdío, L. A. Barragán, and C. Carretero, "A model of losses in twisted-multistranded wires for planar windings used in domestic induction heating appliances," in *IEEE Applied Power Electronics Conf. and Expo. (APEC) 2007*, Feb. 2007, pp. 1247–1253.

[36] J. A. Ferreira, "Appropriate modelling of conductive losses in the design of magnetic components," in *21st Annual IEEE Conference on Power Electronics Specialists*, 1990, pp. 780–785.

[37] J. A. Ferreira, "Improved analytical modeling of conductive losses in magnetic components," *IEEE Trans. Power Electron.*, vol. 9, pp. 127–131, Jan. 1994.

[38] C. Carretero, J. Acero, and R. Alonso, "TM-TE decomposition of power losses in multi-stranded litz-wires used in electronic devices," *Progress In Electromagnetics Research, PIER*, vol. 123, no. 1, pp. 83–103, Jan. 2012.

[39] G. Brown, C. Hoyler, and R. Bierwirth, *Theory and Application of Radio-frequency Heating*. D. Van Nostrand Company, Incorporated, 1947. [Online]. Available: https://books.google.es/books?id=_E4hAAAAMAAJ

[40] P. L. Dowell, "Effects of eddy currents in transformer windings," *Proc. Inst. Electr. Eng.*, vol. 113, no. 8, pp. 1387–1394, 1966.

[41] R. L. Stoll, "Approximate formula for the eddy-current loss induced in a long conductor of rectangular cross-section by a transverse magnetic field," *Proc. Inst. Electr. Eng.*, vol. 116, no. 6, pp. 1003–1008, 1969.

[42] A. M. Urling, V. A. Niemela, G. R. Skutt, and T. G. Wilson, "Characterizing high-frequency effects in transformer windings-a guide to several significant articles," in *IEEE Applied Power Electronics Conf. and Expo. (APEC) 1989*, 1989, pp. 373–385.

[43] M. C. Duffy and W. G. Hurley, "High frequency effects in planar magnetics: inclusive of skin effect," in *IEEE Pow. Electr. Spec. Conf, (PESC) 1995*, vol. 2, 1995, pp. 645–650 vol.2.

[44] W. G. Hurley, E. Gath, and J. G. Breslin, "Optimizing the AC resistance of multilayer transformer windings with arbitrary current waveforms," *IEEE Trans. Power Electron.*, vol. 15, no. 2, pp. 369–376, 2000.

[45] A. Reatti and M. K. Kazimierczuk, "Comparison of various methods for calculating the ac resistance of inductors," *IEEE Trans. Magn.*, vol. 38, no. 3, pp. 1512–1518, 2002.

[46] R. Wojda and M. Kazimierczuk, "Winding resistance of litz-wire and multi-strand inductors," *IET Electr. Power App.*, vol. 5, no. 2, pp. 257–268, Feb. 2012.

[47] R. P. Wojda and M. K. Kazimierczuk, "Analytical optimization of solid–round-wire windings," *IEEE Trans. Ind. Electron.*, vol. 60, no. 3, pp. 1033–1041, Mar. 2013.

[48] R. P. Wojda and M. K. Kazimierczuk, "Analytical winding size optimisation for different conductor shapes using Ampère's law," *IET Power Electron.*, vol. 6, no. 6, pp. 1058–1068, 2013.

[49] A. Phung, G. Meunier, O. Chadebec, X. Margueron, and J. Keradec, "High-frequency proximity losses determination for rectangular cross-section conductors," *IEEE Trans. Magn.*, vol. 43, no. 4, pp. 1213–1216, 2007.

[50] J. Acero, C. Carretero, R. Alonso, and J. M. Burdío, "Quantitative evaluation of induction efficiency in domestic induction heating applications," *IEEE Trans. Magn.*, vol. 49, no. 4, pp. 1382–1389, Apr. 2013.

[51] J. Acero, C. Carretero, I. Lope, R. Alonso, and J. Burdío, "Analytical solution of the induced currents in multilayer cylindrical conductors under external electromagnetic sources," *Appl. Math. Model*, 2016. [Online]. Available: http://dx.doi.org/10.1016/j.apm.2016.07.031

[52] K. Umetani, S. Kawahara, J. Acero, H. Sarnago, O. Lucía, and E. Hiraki, "Analytical formulation of copper loss of litz wire with multiple levels of twisting using measurable parameters," *IEEE Trans. Ind. Appl.*, vol. 57, no. 3, pp. 2407–2420, 2021.

[53] J. Acero, P. Hernández, J. M. Burdío, R. Alonso, and L. A. Barragán, "Simple resistance calculation in litz-wire planar windings for induction cooking appliances," *IEEE Trans. Magn.*, vol. 41, no. 4, pp. 1280–1288, 2005.

[54] I. Lope, J. Acero, and C. Carretero, "Analysis and optimization of the efficiency of induction heating applications with litz-wire planar and solenoidal coils," *IEEE Trans. Power Electron.*, vol. 31, no. 7, pp. 5089–5101, Jul. 2016.

[55] J. Gyselinck, R. V. Sabariego, and P. Dular, "Time-domain homogenization of windings in 2-D finite element models," *IEEE Trans. Magn.*, vol. 43, no. 4, pp. 1297–1300, 2007.

[56] R. V. Sabariego, P. Dular, and J. Gyselinck, "Time-domain homogenization of windings in 3-D finite element models," *IEEE Trans. Magn.*, vol. 44, no. 6, pp. 1302–1305, 2008.

[57] A. Rosskopf, E. Bar, and C. Joffe, "Influence of inner skin- and proximity effects on conduction in litz wires," *IEEE Trans. Power Electron.*, vol. 29, no. 10, pp. 5454–5461, Oct. 2014.

[58] R. Faraji-Dana and Y. Chow, "Edge condition of the field and AC resistance of a rectangular strip conductor," *IEE Proc-H*, vol. 137, no. 2, pp. 133–140, 1990.

[59] A. W. Loth and F. C. Lee, "Two-dimensional skin effect in power foils for high-frequency applications," *IEEE Trans. Magn.*, vol. 31, no. 2, pp. 1003–1006, 1995.

[60] I. Lope, J. Acero, J. M. Burdío, C. Carretero, and R. Alonso, "Design and implementation of PCB inductors with litz-wire structure for conventional-size large-signal domestic induction heating applications," *IEEE Trans. Ind. Appl.*, vol. 3, no. 51, pp. 2434–2442, Jun. 2015.

[61] I. Lope, "Printed circuit board inductors applied to domestic induction heating," Ph.D. dissertation, Universidad de Zaragoza, 2015.

[62] R. Scapolan, A. Gagnoud, and Y. Terrail, "3-D multistrands inductor modeling: Influence of complex geometrical arrangements," *IEEE Trans. Magn.*, vol. 50, no. 2, pp. 949–952, Feb. 2014.

[63] J. Acero, I. Lope, J. M. Burdío, C. Carretero, and R. Alonso, "Loss analysis of multistranded twisted wires by using 3D-FEA simulation," in *IEEE Workshop on Control and Modeling for Power Electronics (COMPEL) 2014*, Jun. 2014.

[64] R. Zhang, J. White, J. Kassakian, and C. Sullivan, "Realistic litz wire characterization using fast numerical simulations," in *IEEE Workshop on Control and Modeling for Power Electronics (COMPEL) 2014*, Jun. 2014.

[65] R. Y. Zhang, J. K. White, and J. G. Kassakian, "Fast simulation of complicated 3-D structures above lossy magnetic media," *IEEE Trans. Magn.*, vol. 50, no. 10, Oct. 2014.

[66] A. Rosskopf, E. Bar, C. Joffe, and C. Bonse, "Calculation of power losses in litz wire systems by coupling FEM and PEEC method," *IEEE Trans. Power Electron.*, vol. 31, no. 9, pp. 6442–6449, Sep. 2016.

[67] S. Ehrlich, H. Rossmanith, M. Sauer, C. Joffe, and M. März, "Fast numerical power loss calculation for high-frequency litz wires," *IEEE Trans. Power Electron.*, vol. 36, no. 2, pp. 2018–2032, 2021.

[68] L. Meng, K. W. E. Cheng, and K. W. Chan, "Systematic approach to high-power and energy-efficient industrial induction cooker system: Circuit design, control strategy, and prototype evaluation," *IEEE Trans. Power Electron.*, vol. 26, pp. 3754–3765, 2011.

[69] L. C. Meng, K. W. E. Cheng, K. W. Chan, and Y. Lu, "Variable turn pitch coils design for heating performance enhancement of commercial induction cooker," *IET Power Electron.*, vol. 5, no. 1, pp. 134–141, Jan. 2012.

[70] L. C. Meng, K. W. E. Cheng, and S. L. Ho, "Multicoils design for induction cookers with applying switched exciting method," *IEEE Trans. Magn.*, vol. 48, pp. 4503–4506, 2012.

[71] C. Carretero, O. Lucía, J. Acero, R. Alonso, and J. M. Burdío, "Frequency-dependent modelling of domestic induction heating systems using numerical methods for accurate time-domain simulation," *IET Power Electron.*, vol. 5, no. 8, pp. 1291–1297, Sep. 2012.

[72] H. Sarnago, O. Lucía, A. Mediano, and J. M. Burdío, "Modulation scheme for improved operation of an RB-IGBT-based resonant inverter applied to

domestic induction heating," *IEEE Trans. Ind. Electron.*, vol. 60, no. 5, pp. 2066–2073, May 2013.

[73] N. Mohan and T. M. Undeland, *Power electronics: converters, applications, and design.* John Wiley & Sons, 2007.

[74] P. Vishnuram, G. Ramachandiran, S. Ramasamy, and S. Dayalan, "A comprehensive overview of power converter topologies for induction heating applications," *Int. Trans. Electr. Energy Syst.*, vol. 30, no. 10, p. e12554, Aug. 2020. [Online]. Available: https://onlinelibrary.wiley.com/doi/abs/10.1002/2050-7038.12554

[75] O. Lucía, P. Maussion, E. J. Dede, and J. M. Burdío, "Induction heating technology and its applications: Past developments, current technology, and future challenges," *IEEE Trans. Ind. Electron.*, vol. 61, no. 5, pp. 2509–2520, May 2014.

[76] H. Sarnago, O. Lucía, A. Mediano, and J. M. Burdío, "High-efficiency parallel quasi-resonant current source inverter featuring SiC metal-oxide semiconductor field-effect transistors for induction heating systems with coupled inductors," *IET Power Electron.*, vol. 6, no. 1, pp. 183–191, Jan. 2013.

[77] T. Mishima, C. Takami, and M. Nakaoka, "A new current phasor-controlled ZVS twin half-bridge high-frequency resonant inverter for induction heating," *IEEE Trans. Ind. Electron.*, vol. 61, no. 5, pp. 2531–2545, May 2014.

[78] T. Mishima and M. Nakaoka, "A load-power adaptive dual pulse modulated current phasor-controlled ZVS high-frequency resonant inverter for induction heating applications," *IEEE Trans. Power Electron.*, vol. 29, pp. 3864–3880, 2014.

[79] V. Esteve, J. Jordán, E. Sanchis-Kilders, E. J. Dede, E. Maset, J. B. Ejea, and A. Ferreres, "Enhanced pulse-density-modulated power control for high-frequency induction heating inverters," *IEEE Trans. Ind. Electron.*, vol. 62, no. 11, pp. 6905–6914, Nov. 2015.

[80] H. Sarnago, J. M. Burdío, and O. Lucía, "High-performance and cost-effective ZCS matrix resonant inverter for total active surface induction heating appliances," *IEEE Trans. Power Electron.*, vol. 34, no. 1, pp. 117–125, Jan. 2019.

[81] H. Sarnago, P. Guillén, J. M. Burdío, and O. Lucía, "Multiple-output ZVS resonant inverter architecture for flexible induction heating appliances," *IEEE Access*, vol. 7, pp. 157 046–157 056, 2019.

[82] H. Sarnago, O. Lucía, A. Mediano, and J. M. Burdío, "Dual-mode-operation half-bridge resonant converter for improved-efficiency induction heating system," in *IEEE Applied Power Electronics Conf. and Expo. (APEC) 2012*. IEEE, 2012, pp. 2184–2188.

[83] O. Lucía, J. M. Burdío, I. Millán, J. Acero, and L. A. Barragán, "Efficiency-oriented design of ZVS half-bridge series resonant inverter with variable frequency duty cycle control," *IEEE Trans. Power Electron.*, vol. 25, no. 7, pp. 1671–1674, 2010.

[84] J. Villa, J. I. Artigas, J. R. Beltrán, A. D. Vicente, and L. A. Barragán, "Analysis of the acoustic noise spectrum of domestic induction heating systems controlled by phase-accumulator modulators," *IEEE Trans. Ind. Electron.*, vol. 66, no. 8, pp. 5929–5938, Aug. 2019.

[85] International Commission on Non-Ionizing Radiation Protection (ICNIRP), "Guidelines for limiting exposure to time-varying electric, magnetic, and elctromagnetic fields (up to 300 GHz)," *Health Phys.*, vol. 74, no. 4, 1998. [Online]. Available: https://journals.lww.com/health-physics/Fulltext/1998/04000/GUIDELINES_FOR_LIMITING_EXPOSURE_TO_TIME_VARYING.13.aspx

[86] ——, "ICNIRP statement on the "Guidelines for limiting exposure to time-varying electric, magnetic, and electromagnetic fields (up to 300 GHz)"," *Health Phys.*, vol. 97, no. 3, 2009. [Online]. Available: https://journals.lww.com/health-physics/Fulltext/2009/09000/ICNIRP_STATEMENT_ON_THE__GUIDELINES_FOR_LIMITING.9.aspx

[87] ——, "Guidelines for limiting exposure to time-varying electric and magnetic fields (1 Hz to 100 kHz)," *Health Phys.*, vol. 99, no. 6, 2010. [Online]. Available: https://journals.lww.com/health-physics/Fulltext/2010/12000/GUIDELINES_FOR_LIMITING_EXPOSURE_TO_TIME_VARYING.26.aspx

[88] ——, "Guidelines for Limiting Exposure to Electromagnetic Fields (100 kHz to 300 GHz)," *Health Phys.*, vol. 118, no. 5, 2020.

[Online]. Available: https://journals.lww.com/health-physics/Fulltext/2020/05000/Guidelines_for_Limiting_Exposure_to.2.aspx

[89] *IEC 62233 Measurement methods for electromagnetic fields of household appliances and similar apparatus with regard to human exposure*, International Electrotechnical Commission (EIC) Std., 2005. [Online]. Available: https://webstore.iec.ch/publication/6618

[90] *UNE-EN 62233 Métodos de medida de los campos electromagnéticos de los aparatos electrodomésticos y análogos en relación con la exposición humana*, Asociación Española de Normalización y Certificación (AENOR) Std., 2009. [Online]. Available: https://www.en.aenor.com/

[91] C. Viellard, A. Romann, U. Lott, and N. Kuster, "B-field exposure from induction cooking appliances," *Zurich, July*, 2006.

[92] C. Carretero, R. Alonso, and J. Acero, "Interference emission estimation of domestic induction cookers based on finite-element simulation," *IEEE Trans. Electromagn. Compat.*, vol. 58, no. 4, pp. 993–999, 2016.

[93] M. K. Kazimierczuk, *High-frequency magnetic components*. John Wiley & Sons, 2009.

[94] W. Hurley and W. Wölfle, *Transformers and Inductors for Power Electronics. Theory, Design and Applications*. United Kingdom: John Wiley & Sons, 2013.

[95] J. Garnica, R. A. Chinga, and J. Lin, "Wireless power transmission: From far field to near field," *Proc. IEEE*, vol. 101, no. 6, pp. 1321–1331, Jun. 2013.

[96] Z. Zhang, H. Pang, A. Georgiadis, and C. Cecati, "Wireless power transfer: An overview," *IEEE Trans. Ind. Electron.*, vol. 66, pp. 1044–1058, Feb. 2019.

[97] J. Huang, Y. Zhou, Z. Ning, and H. Gharavi, "Wireless power transfer and energy harvesting: Current status and future prospects," *IEEE Trans. Wireless Commun.*, vol. 26, no. 4, pp. 163–169, Aug. 2019.

[98] M. Budhia, G. A. Covic, and J. T. Boys, "Design and optimization of circular magnetic structures for lumped inductive power transfer systems," *IEEE Trans. Power Electron.*, vol. 26, no. 11, pp. 3096–3108, 2011.

[99] T. Kan, T.-D. Nguyen, J. C. White, R. K. Malhan, and C. C. Mi, "A new integration method for an electric vehicle wireless charging system using LCC

compensation topology: Analysis and design," *IEEE Trans. Power Electron.*, vol. 32, pp. 1638–1650, 2017.

[100] B. A. Reese, R. Joseph, and C. R. Sullivan, "Improved litz-wire designs for the MHz range," in *IEEE Workshop on Control and Modeling for Power Electronics (COMPEL) 2018*, Jun. 2018.

[101] C. R. Sullivan, "Optimal choice for number of strands in a litz-wire transformer winding," *IEEE Trans. Power Electron.*, vol. 14, no. 2, pp. 283–291, Mar. 1999.

[102] C. Sullivan and R. Zhang, "Simplified design method for litz wire," in *IEEE Applied Power Electronics Conf. and Expo. (APEC) 2014*, Mar. 2014, pp. 2667–2674.

[103] Q. Deng, J. Liu, D. Czarkowski, M. K. Kazimierczuk, M. Bojarski, H. Zhou, and W. Hu, "Frequency-dependent resistance of litz-wire square solenoid coils and quality factor optimization for wireless power transfer," *IEEE Trans. Ind. Electron.*, vol. 63, no. 5, pp. 2825–2837, May 2016.

[104] C. R. Sullivan, "Computationally efficient winding loss calculation with multiple windings, arbitrary waveforms, and two-dimensional or three-dimensional field geometry," *IEEE Trans. Power Electron.*, vol. 16, no. 1, pp. 142–150, Jan. 2001.

[105] C. Carretero, "Coupling power losses in inductive power transfer systems with litz-wire coils," *IEEE Trans. Ind. Electron.*, vol. 64, no. 6, pp. 4474–4482, Jun. 2017.

[106] M. Albach, "Two-dimensional calculation of winding losses in transformers," in *IEEE Pow. Electr. Spec. Conf, (PESC) 2000*, 2000, pp. 1639–1644.

[107] F. Tourkhani and P. Viarouge, "Accurate analytical model of winding losses in round litz wire windings," *IEEE Trans. Magn.*, vol. 37, no. 1, pp. 538–543, Jan. 2001.

[108] H. Hamalainen, J. Pyrhonen, J. Nerg, and J. Talvitie, "AC resistance factor of litz-wire windings used in low-voltage high-power generators," *IEEE Trans. Ind. Electron.*, vol. 61, no. 2, pp. 693–700, Feb. 2014.

[109] D. Barth, B. Klaus, and T. Leibfried, "Litz wire design for wireless power transfer in electric vehicles," in *Proc. IEEE Wireless Power Transfer Conference (WPTC'17)*, May 2017.

[110] R. Wojda and M. Kazimierczuk, "Winding resistance and power loss of inductors with litz and solid-round wires," *IEEE Trans. Ind. Appl.*, vol. 54, no. 4, pp. 3548–3557, Jul. 2018.

[111] J. Gyselinck and P. Dular, "Frequency-domain homogenization of bundles of wires in 2-D magnetodynamic FE calculations," *IEEE Trans. Magn.*, vol. 41, no. 5, pp. 1416–1419, May 2005.

[112] A. Stadler, "The optimization of high frequency inductors with litz-wire windings," in *Proc. of the IEEE 8th International Conference on Compatibility and Power Electronics (CPE), 2013*, Jun. 2013, pp. 209–213.

[113] A. Delgado, G. Salinas, J. A. Oliver, J. A. Cobos, and J. Rodriguez-Moreno, "Equivalent conductor layer for fast 3-D finite element simulations of inductive power transfer coils," *IEEE Trans. Power Electron.*, vol. 35, no. 6, pp. 6221–6230, 2020.

[114] H. Rossmanith, M. Doebroenti, M. Albach, and D. Exner, "Measurement and characterization of high frequency losses in nonideal litz wires," *IEEE Trans. Power Electron.*, vol. 26, no. 11, pp. 3386–3394, Nov. 2011.

[115] C. R. Sullivan and R. Y. Zhang, "Analytical model for effects of twisting on litz-wire losses," in *IEEE Workshop on Control and Modeling for Power Electronics (COMPEL) 2014*, Jun. 2014.

[116] S. Hiruma and H. Igarashi, "Fast 3-D analysis of eddy current in litz wire using integral equation," *IEEE Trans. Magn.*, vol. 53, no. 6, Jun. 2017.

[117] T. Guillod, J. Huber, F. Krismer, and J. Kolar, "Litz wire losses: Effects of twisting imperfections," in *IEEE Workshop on Control and Modeling for Power Electronics (COMPEL) 2017*, Jul. 2017.

[118] L. Makong, A. Kameni, F. Bouillault, and P. Masson, "3-D equivalent model to compute the electro-magnetic behavior of twisted multi-filamentary superconductors wires," *IEEE Trans. Magn.*, vol. 54, no. 3, pp. 1–4, Mar. 2018.

[119] J. Hou, Q. Chen, Z. Zhang, S. Wong, and C. K. Tse, "Analysis of output current characteristics for higher order primary compensation in inductive power transfer systems," *IEEE Trans. Power Electron.*, vol. 33, no. 8, pp. 6807–6821, Aug. 2018.

[120] R. Bosshard, "Multi-objective optimization of inductive power transfer systems for EV charging," Ph.D. dissertation, ETH Zurich, 2015.

[121] S. Valtchev, B. Borges, K. Brandisky, and J. B. Klaassens, "Resonant contactless energy transfer with improved efficiency," *IEEE Trans. Power Electron.*, vol. 24, no. 3, pp. 685–699, 2009.

[122] R. Laouamer, M. Brunello, J. P. Ferrieux, O. Normand, and N. Buchheit, "A multi-resonant converter for non-contact charging with electromagnetic coupling," in *IECON 1997 - 23rd Annual Conf. IEEE Industrial Electronics Society*, vol. 2, 1997, pp. 792–797 vol.2.

[123] B. Ji, K. Hata, T. Imura, Y. Hori, S. Shimada, and O. Kawasaki, "MPPT control for PV based wireless power transfer system in lunar rover by secondary side converter," in *2019 IEEE PELS Workshop on Emerging Technologies: Wireless Power Transfer (WoW)*, June 2019, pp. 105–110.

[124] Y. Lyu, F. Meng, G. Yang, B. Che, Q. Wu, L. Sun, D. Erni, and J. L. Li, "A method of using nonidentical resonant coils for frequency splitting elimination in wireless power transfer," *IEEE Trans. Power Electron.*, vol. 30, no. 11, pp. 6097–6107, 2015.

[125] R. Bosshard, J. W. Kolar, J. Mühlethaler, I. Stevanović, B. Wunsch, and F. Canales, "Modeling and η-α-Pareto optimization of inductive power transfer coils for electric vehicles," *IEEE Trans. Emerg. Sel. Topics Power Electron.*, vol. 3, no. 1, pp. 50–64, Mar. 2015.

[126] J. Yin, D. Lin, T. Parisini, and S. Y. Hui, "Front-end monitoring of the mutual inductance and load resistance in a series–series compensated wireless power transfer system," *IEEE Trans. Power Electron.*, vol. 31, no. 10, pp. 7339–7352, Oct. 2016.

[127] K. Song, Z. Li, J. Jiang, and C. Zhu, "Constant current/voltage charging operation for series–series and series–parallel compensated wireless power transfer systems employing primary-side controller," *IEEE Trans. Power Electron.*, vol. 33, no. 9, pp. 8065–8080, Sep. 2018.

[128] U. Iruretagoyena, A. Garcia-Bediaga, L. Mir, H. Camblong, and I. Villar, "Bifurcation limits and non-idealities effects in a three-phase dynamic IPT system," *IEEE Trans. Power Electron.*, vol. 35, no. 1, pp. 208–219, Jan. 2020.

[129] M. Kim, H. Park, and J. Jung, "Practical design methodology of IH and IPT dual-functional apparatus," *IEEE Trans. Power Electron.*, vol. 35, no. 9, pp. 8897–8901, 2020.

[130] J. Dai and D. C. Ludois, "A survey of wireless power transfer and a critical comparison of inductive and capacitive coupling for small gap applications," *IEEE Trans. Power Electron.*, vol. 30, no. 11, pp. 6017–6029, 2015.

[131] *Wireless Power Transfer for Light-Duty Plug-in/Electric Vehicles and Alignment Methodology J2954*, SAE International Std. J2954, 2020.

[132] R. Bosshard, J. Mühlethaler, J. W. Kolar, and I. Stevanović, "Optimized magnetic design for inductive power transfer coils," in *IEEE Applied Power Electronics Conf. and Expo. (APEC) 2013*, 2013, pp. 1812–1819.

[133] J. Kim, J. Kim, S. Kong, H. Kim, I. Suh, N. P. Suh, D. Cho, J. Kim, and S. Ahn, "Coil design and shielding methods for a magnetic resonant wireless power transfer system," *Proc. IEEE*, vol. 101, no. 6, pp. 1332–1342, 2013.

[134] H. Moon, S. Kim, H. H. Park, and S. Ahn, "Design of a resonant reactive shield with double coils and a phase shifter for wireless charging of electric vehicles," *IEEE Trans. Magn.*, vol. 51, no. 3, pp. 1–4, 2015.

[135] A. Tejeda, C. Carretero, J. T. Boys, and G. A. Covic, "Ferrite-less circular pad with controlled flux cancelation for EV wireless charging," *IEEE Trans. Power Electron.*, vol. 32, no. 11, pp. 8349–8359, 2017.

[136] M. G. S. Pearce, M. J. O'Sullivan, C. Carretero, G. A. Covic, and J. T. Boys, "Optimising ferrite-less pad reflection winding with a multi-objective genetic algorithm," in *2019 IEEE PELS Workshop on Emerging Technologies: Wireless Power Transfer (WoW)*, 2019, pp. 1–6.

[137] C. Carretero, O. Lucía, J. Acero, and J. M. Burdío, "FEA tool based model of partly coupled coils used in domestic induction cookers," in *IECON 2011 - 37th Annual Conf. IEEE Industrial Electronics Society*, Nov. 2011, pp. 2533–2538.

[138] H. N. Pham, H. Fujita, K. Ozaki, and N. Uchida, "Estimating method of heat distribution using 3-D resistance matrix for zone-control induction heating systems," *IEEE Trans. Power Electron.*, vol. 27, pp. 3374–3382, 2012.

[139] J. Acero, C. Carretero, O. Lucía, R. Alonso, and J. M. Burdío, "Mutual impedance of small ring-type coils for multiwinding induction heating

appliances," *IEEE Trans. Power Electron.*, vol. 28, no. 2, pp. 1025–1035, Feb. 2013.

[140] C. Carretero, O. Lucía, J. Acero, and J. M. Burdío, "First harmonic equivalent impedance of coupled inductive loads for induction heating applications," in *IECON 2012 - 38th Annual Conf. IEEE Industrial Electronics Society*, Oct. 2012, pp. 427–432.

[141] C. Carretero, O. Lucía, J. Acero, and J. M. Burdío, "Computational modeling of two partly coupled coils supplied by a double half-bridge resonant inverter for induction heating appliances," *IEEE Trans. Ind. Electron.*, vol. 60, no. 8, pp. 3092–3105, Aug. 2013.

[142] ——, "Phase-shift modulation in double half-bridge inverter with common resonant capacitor for induction heating appliances," *IET Power Electron.*, vol. 8, no. 7, pp. 1128–1136, 2015.

[143] C. Carretero, J. Acero, R. Alonso, and J. M. Burdío, "Normal-mode decomposition of surface power distribution in multiple-coil induction heating systems," *IEEE Trans. Magn.*, vol. 52, no. 2, pp. 1–8, 2016.

[144] J. Serrano, J. Acero, I. Lope, C. Carretero, and J. M. Burdío, "A flexible cooking zone composed of partially overlapped inductors," *IEEE Trans. Ind. Electron.*, vol. 65, no. 10, pp. 7762–7771, Oct. 2018.

[145] J. Serrano, I. Lope, and J. Acero, "Nonplanar overlapped inductors applied to domestic induction heating appliances," *IEEE Trans. Ind. Electron.*, vol. 66, no. 9, pp. 6916–6924, Sep. 2019.

[146] R. C. M. Gomes, M. A. Vitorino, D. A. Acevedo-Bueno, and M. B. de Rossiter Corrêa, "Multiphase resonant inverter with coupled coils for AC-AC induction heating application," *IEEE Trans. Ind. Appl.*, vol. 56, pp. 551–560, 2020.

[147] W. Han, K. T. Chau, and Z. Zhang, "Flexible induction heating using magnetic resonant coupling," *IEEE Trans. Ind. Electron.*, vol. 64, no. 3, pp. 1982–1992, Mar. 2017.

[148] W. Han, K. T. Chau, Z. Zhang, and C. Jiang, "Single-source multiple-coil homogeneous induction heating," *IEEE Trans. Magn.*, vol. 53, no. 11, pp. 1–6, Nov. 2017.

[149] W. Han, K. T. Chau, C. Jiang, and W. Liu, "All-metal domestic induction heating using single-frequency double-layer coils," *IEEE Trans. Magn.*, vol. 54, no. 11, pp. 1–5, Nov. 2018.

[150] J. Edminister, *Theory and Problems of Electric Circuits*, ser. Schaum's outline series. McGraw-Hill, 1965. [Online]. Available: https://books.google.es/books?id=XYQpAQAAMAAJ

[151] C. Carretero, J. Acero, R. Alonso, J. M. Burdío, and F. Monterde, "Modeling mutual impedances of loaded non-coaxial inductors for induction heating applications," *IEEE Trans. Magn.*, vol. 44, no. 11, pp. 4115–4118, 2008.

[152] J. Acero, C. Carretero, I. Millán, O. Lucía, R. Alonso, and J. M. Burdío, "Analysis and modeling of planar concentric windings forming adaptable-diameter burners for induction heating appliances," *IEEE Trans. Power Electron.*, vol. 26, no. 5, pp. 1546–1558, 2011.

[153] J. Acero, C. Carretero, I. Millán, R. Alonso, O. Lucía, and J. M. Burdío, "Experimental setup for inductive efficiency measurements of domestic induction systems based on energy balance," in *IECON 2010 - 36th Annual Conf. IEEE Industrial Electronics Society*, 2010, pp. 114–119.

[154] G. Zulauf and J. M. Rivas-Davila, "Single-turn air-core coils for high-frequency inductive wireless power transfer," vol. 35, no. 3, pp. 2917–2932, 2020.

[155] A. L. F. Stein, P. A. Kyaw, and C. R. Sullivan, "Wireless power transfer utilizing a high-Q self-resonant structure," *IEEE Trans. Power Electron.*, vol. 34, no. 7, pp. 6722–6735, 2019.

[156] C.-S. Wang, G. Covic, and O. Stielau, "Power transfer capability and bifurcation phenomena of loosely coupled inductive power transfer systems," *IEEE Trans. Ind. Electron.*, vol. 51, no. 1, pp. 148–157, 2004.

[157] R. Bosshard, J. W. Kolar, and B. Wunsch, "Control method for inductive power transfer with high partial-load efficiency and resonance tracking," in *2014 International Power Electronics Conference (IPEC-Hiroshima 2014 - ECCE ASIA)*, 2014, pp. 2167–2174.

[158] F. J. López-Alcolea, J. Vázquez del Real, P. Roncero-Sánchez, and A. Parreño, "Modeling of a magnetic coupler based on single- and double-layered

rectangular planar coils with in-plane misalignment for wireless power transfer," *IEEE Trans. Power Electron.*, vol. 35, no. 5, pp. 5102–5121, 2020.

[159] N. Khan, H. Matsumoto, and O. Trescases, "Wireless electric vehicle charger with electromagnetic coil-based position correction using impedance and resonant frequency detection," *IEEE Trans. Power Electron.*, vol. 35, no. 8, pp. 7873–7883, 2020.

[160] I. Lope, C. Carretero, J. Acero, R. Alonso, and J. M. Burdío, "Frequency-dependent resistance of planar coils in printed circuit board with litz structure," *IEEE Trans. Magn.*, vol. 50, no. 12, pp. 1–9, 2014.

[161] E. Plumed, J. Acero, J. M. Burdío, and I. Lope, "Design method for domestic induction heating systems with a larger load distance," in *IECON 2017 - 43rd Annual Conf. IEEE Industrial Electronics Society*, Oct. 2017, pp. 3785–3790.

[162] E. Plumed, J. Acero, I. Lope, and J. M. Burdío, "Design methodology of high performance domestic induction heating systems under worktop," *IET Power Electron.*, Oct. 2019.

[163] E. Plumed, I. Lope, J. Acero, and J. M. Burdío, "Inductor system evaluation for simultaneous wireless energy transfer and induction heating," in *IECON 2018 - 44th Annual Conf. IEEE Industrial Electronics Society*, Oct. 2018, pp. 3509–3514.

[164] E. Plumed, I. Lope, and J. Acero, "Induction heating adaptation of a different-sized load with matching secondary inductor to achieve uniform heating and enhance vertical displacement," *IEEE Trans. Power Electron.*, vol. 36, no. 6, pp. 6929–6942, Jun. 2021.

[165] E. Plumed, I. Lope, J. Acero, and J. M. Burdío, "Design of a three inductor system with one externally fed for an inductively coupled heating application," in *IECON 2019 - 45th Annual Conf. IEEE Industrial Electronics Society*, vol. 1, Oct. 2019, pp. 5070–5074.

[166] E. Plumed, I. Lope, J. Acero, and J. M. Burdío, "Induction heating of two magnetically independent loads with a single transmitter," *IEEE Tran. Power Electron.*, 2021, Early Access.

[167] J. Acero, D. Antón, C. Carretero, P. Hernández, S. Llorente, I. Lope, and E. Plumed, "Cooking system," WO patent WO2 019 166 909, Feb. 18, 2020.

[Online]. Available: https://worldwide.espacenet.com/patent/search/family/065818046/publication/WO2019166909A1?q=pn=WO2019166909A1

[168] T. Cabeza, J. Lasobras, S. Llorente, E. Plumed, J. Rivera, and J. Serrano, "Household appliance system," WO patent WO2 021 104 849, Jun. 03, 2021. [Online]. Available: https://worldwide.espacenet.com/patent/search/family/068808252/publication/WO2021104849A1?q=pn=WO2021104849A1

[169] T. Cabeza, S. Llorente, E. Plumed, and J. Rivera, "Kochfeldvorrichtung," WO patent WO2 021 069 213A1, Aug. 05, 2021. [Online]. Available: https://worldwide.espacenet.com/patent/search/family/069701129/publication/DE102021200406A1?q=pn=DE102021200406A1

[170] T. Cabeza, J. Lasobras, S. Llorente, E. Plumed, and J. Rivera, "Induction energy transmission system," DE patent DE102 021 200 406A1, Apr. 15, 2021. [Online]. Available: https://worldwide.espacenet.com/patent/search/family/068503016/publication/WO2021069213A1?q=pn=WO2021069213A1

[171] E. Plumed, I. Lope, J. Acero, and J. M. Burdío, "Domestic induction heating system with standard primary inductor for reduced-size and high distance cookware," in *IEEE Applied Power Electronics Conf. and Expo. (APEC) 2021*, 2021, pp. 2842–2847.

[172] E. Plumed, I. Lope, and J. Acero, "EMI reduction via resonator coils in glassless integrated domestic induction systems," *IEEE Access*, vol. 9, pp. 128 147–128 156, 2021.

[173] E. Plumed, J. Acero, I. Lope, and C. Carretero, "3D finite element simulation of litz wires with multilevel bundle structure," in *IECON 2018 - 44th Annual Conf. IEEE Industrial Electronics Society*, Oct. 2018, pp. 3479–3484.

[174] E. Plumed, I. Lope, C. Carretero, and J. Acero, "A recursive methodology for modelling multi-stranded wires with multilevel helix structure," *Appl. Math. Model*, vol. 83, pp. 76 – 89, 2020. [Online]. Available: http://www.sciencedirect.com/science/article/pii/S0307904X20301050